The Dissertation Committee for Mikhail Nikolaevich Gladkikh
certifies that this is the approved version of the following
dissertation:

A Priori Prediction of Macroscopic Properties of Sedimentary Rocks Containing Two Immiscible Fluids

Committee:

Steven L. Bryant,
Supervisor

Roger T. Bonnecaze

Luis A. Caffarelli

Clint N. Dawson

Kitty L. Milliken

A Priori Prediction of Macroscopic Properties of Sedimentary Rocks Containing Two Immiscible Fluids

by

Mikhail Nikolaevich Gladkikh, B.S.; M.S.

Dissertation

Presented to the Faculty of the Graduate School of
the University of Texas at Austin
in Partial Fulfillment
of the Requirements
for the Degree of

Doctor of Philosophy

The University of Texas at Austin

May 2005

Dum vires annique sinunt,
tolerate labores:
Iam veniet tacito
tarda senecta pede.

Publius Ovidius Naso.

Acknowledgements

I wish to express sincere gratitude and appreciation to my advisor, Dr. Steven Bryant, without whose guidance, inspiration, and ideas this work would be impossible. I am grateful to Dr. Mukul Sharma for many helpful discussions and collaboration. I am thankful to Dr. Roger Bonnecaze for sharing his extensive knowledge in surface phenomena. I wish to express my gratitude to Dr. Kitty Milliken for introducing and guiding me into the difficult subject of geology of sedimentary rocks. I have benefited from many enlightening discussions with Dr. David Herrick and Dr. Lev Tabarovsky.

I am grateful to all of the members of my committee for helpful suggestions, comments and references. I am thankful to Dr. Clint Dawson for his advice on my graduate study in Computational and Applied Mathematics and on my research work. I would like to thank Dr. Luis Caffarelli for his inspiring classes in applied mathematics.

I am grateful to Prof. Finney for the access to his sphere packing coordinates. I wish to express my special gratitude to National Water Research Institute and Dr. Ronald Linsky for supporting me during my graduate study.

This work would be impossible without the help, love, understanding and patience from my parents and my wife Larisa.

Finally, I would like to acknowledge all the people who contributed to this work and whom I may have forgotten to mention here.

Support for the research described here came from EPA (Science to Achieve Results (STAR) program, R827116/01/0), UT Austin's Research Consortium on Formation

Evaluation (member companies are Anadarko, Baker Atlas, ConocoPhillips, ExxonMobil, Halliburton, Instituto Mexicano del Petroleo, Shell, Schlumberger, Total), and DOE (grant #DE-FC26-04NT15518).

A Priori Prediction of Macroscopic Properties of Sedimentary Rocks Containing Two Immiscible Fluids

Publication No.________________

Mikhail Nikolaevich Gladkikh, Ph.D.
The University of Texas at Austin, 2005.

Supervisor: Steven L. Bryant

The processes in porous media governed by capillary forces, such as drainage and imbibition cycles, infiltration from surface water, flow, transport, adsorption and dissolution of contaminants, are of great importance in soil science, subsurface geochemistry, petroleum engineering, and hydrology.

The methodology proposed in this work is devoted to the pore-scale modeling of such processes. The goal is to be able to make *a priori* predictions of the macroscopic properties of model sedimentary rocks, such as capillary pressure curves, interfacial area, relative permeabilities and electrical properties. The idea is to conduct a theoretical investigation in a simple but physically representative model porous medium. The model is a random packing of equal spheres for which the coordinates of the centers have been measured. Knowledge of the coordinates determines the grain space and the void space in the packing, thereby overcoming a long-standing difficulty for theoretical approaches to pore-level modeling. Geological processes, such as isopachous and pore-filling cementation, are simulated in the sphere pack, thus creating simple models of sedimentary rocks with predetermined pore space geometry.

Despite the simplicity of the model porous medium, it is a powerful tool for investigation of the flow and transport in soils and sedimentary rocks. In particular it allows *a priori* predictions of macroscopic behavior. This capability is the most important aspect of the approach. Because there are no arbitrarily prescribed parameters, the predictions can be compared directly to experiments, providing a much stronger test than is possible with many other modeling approaches.

For example, knowledge of the pore space geometry and wettability conditions allows computing the exact configuration of liquid phases in porous media. This capability enables the simulation of imbibition of a wetting phase into the model porous medium using a physically consistent dynamic criterion for the imbibition of individual pores. This approach allows *a priori*, quantitative prediction of the configuration of fluid phases during imbibition. This in turn allows a quantitative understanding of how different macroscopic processes and parameters (e.g. relative permeabilities or resistivity index) depend on the geologic (e.g. type and amount of cement) and physical (e.g. wettability) features of porous media.

Table of Contents

List of Figures

Chapter I

1.1 Introduction

The properties of porous media have a great importance for the modeling and understanding of different flow processes in the subsurface, such as oil recovery, drainage and imbibition, infiltration from surface water, and the migration of contaminant in groundwater. Because of the great influence of these processes on the environment and industry, there have been numerous attempts to model them at the microscopic scale and to predict the behavior of the subsurface. Many of these attempts model the porous medium as a *network* with *sites* (pore bodies) and *bonds* (pore throats) and some parameters, prescribed to the network in advance, for instance, *coordination number* of the sites or *size distribution* of pore bodies and pore throats. By simulating transport processes in such networks one can describe the behavior of the desired unknowns (e.g. relative permeabilities, residual NAPL saturation, dissolution rates etc). Unfortunately, the predictive capability of this approach is limited by the presence of prescribed parameters, which usually cannot be determined independently of the phenomena of interest.

The methodology proposed in this work is also devoted to the pore-scale modeling of the flow and transport processes in the subsurface, but it differs from the above approaches significantly. The idea is to conduct a theoretical investigation in a simple but physically representative model porous medium. The model is a random packing of equal spheres for which the coordinates of the centers have been measured (*Finney pack*, [38]). Knowledge of the coordinates determines the grain space and the void space in the packing, thereby overcoming a long-standing difficulty for theoretical approaches. It is also possible to simulate geologic processes in the sphere pack, such as isopachous and pore-filling cementation, thus creating simple models of sedimentary rocks with predetermined pore space geometry.

Although a network representation of pore space is used for numerical calculations, this approach differs from many network models in that the features of the network are extracted *directly* from the geometry of the model porous medium. For the purpose of extracting the network from the Finney packing the Delaunay tessellation [94] is used, which subdivides a set of points by grouping four nearest neighbors together. Applied to the sphere centers of the Finney pack, this procedure subdivides the volume of the packing into tetrahedral cells, thus creating a simple network. All geometrical features of such network follow directly from the known coordinates of the sphere centers. The topology of the network arises naturally: since each cell is a tetrahedron, it has four neighbors, resulting in a lattice of connectivity four.

Despite the simplicity of the model porous medium, it is a powerful tool for investigation of the processes which occur in soils and sedimentary rocks. In particular it allows *a priori* predictions of macroscopic behavior that have been validated by experimental data. This capability is the most important aspect of the approach. Because there are no prescribed parameters, the predictions can be tested directly against experiments. If the predictions do not fit the data, we can conclude that the model does not account for some essential part of the physical situation, and then seek a more realistic model. On the other hand, a successful prediction allows some confidence that the model can be taken as a reasonable approximation of the actual situation, and thus has a predictive capability and can be used to explain other observations.

For example, knowledge of the pore space geometry and wettability conditions (the value of the contact angle) allows computing the exact configuration of liquid phases in porous media (pendular rings around grain contacts, and menisci in pore throats). Then the imbibition of a wetting phase in this model porous medium is simulated by the means of the Melrose criterion for imbibition of a single pore [95], which suggests that the wetting phase spontaneously jumps into the pore body when the meniscus touches a pendular ring. This approach allows *a priori*, quantitative prediction of the configuration of fluid phases in porous media during imbibition. This in turn allows a quantitative understanding of how different macroscopic processes and parameters (for example, relative permeabilities or interfacial area) depend on the geologic (e.g. type and amount of cement) and physical (e.g. wettability) features of porous media.

1.2 Major Contributions

In this work the following major contributions are made:

1) The algorithm for imbibition, based upon the pore-level Melrose criterion [95] for the imbibition of a single pore, Haines' treatment [56] of snap-off at pore throats as coalescence of pendular rings, and accurate computation of the phases' configuration, is developed;
2) A strong case is made that the dynamic Melrose criterion [95] is the correct criterion for the imbibition of a single pore. Several independent forms of evidence, including physical consistency with drainage criteria, dynamic behavior, dependence on wettability conditions, distribution of residual NW phase, and theoretical analysis of the stability of two-dimensional liquid wedges, are gathered in support of this criterion;
3) Predictions of a displacement cycle (drainage followed by imbibition) in model sedimentary rocks containing two immiscible fluids are made. The methodology developed is able to predict the configuration of phases at any stage of drainage or imbibition in model rocks of various geological properties (two types of cementation are modeled: isopachous (uniform layers of cement) and pore-filling) and physical conditions (wettability of the rock, specified by the value of contact angle). The predictions are generally in a good agreement with existing experiments.
4) The model of two-phase flow [13] and electric current flow [16] in model porous media is extended to include accurate geometric description of phase interfaces and applied to compute relative permeabilities of two-phase flow and electrical properties of model rocks during imbibition. The influence of

geological (i.e. amount and type of cement) and physical (i.e. wettability) conditions on these macroscopic parameters is quantified and compared with experimental evidences.

5) *A priori* predictions of the behavior of interfacial area between two immiscible phases during imbibition in model rocks are made. The predictions are consistent with the thermodynamic analysis. The simulations show the influence of geological and wettability conditions on interfacial area.

1.3 Outline

The outline of this work is as follows.

Chapter I presents the overview of the history of pore-scale modeling and literature review, followed by the description of the methodology used to create physically representative model sedimentary rocks.

Chapter II is devoted to the algorithms developed for the simulation of fluid displacement processes (drainage and imbibition) in model rocks containing two immiscible fluids, description of the geometry of liquid phases and pore-level events; and finally presents the theoretical analysis of the stability of liquid wedges in the two-dimensional case.

Chapter III presents the results of the simulations of drainage and imbibition as capillary pressure curves, influence of cementation and wettability on these curves, and their comparison with existing experimental data. Several forms of evidence in support of the suggested criterion for the imbibition of a single pore [95] are also presented in this Chapter.

Chapter IV is devoted to the modeling of two-phase and electric current flow in the model rocks and presents predictions of macroscopic petrophysical parameters, such as relative permeabilities of two-phase flow, electrical resistivity index and electrical efficiency during both drainage and imbibition. The comparison of these parameters with existing experimental data as well as quantification of the influence of cementation and wettability on these parameters is also presented in this Chapter.

Chapter V is devoted to the thermodynamic analysis and predictions of the behavior of interfacial area between two immiscible phases during both drainage and imbibition in model porous media. The comparison of predicted trends with experimental data and quantification of the influence of cementation and wettability on interfacial area are also presented in this Chapter.

Finally, Chapter VI draws some conclusions and suggests possible directions of future work.

1.4 History of Pore-Scale Modeling and Literature Review

The importance of the processes of immiscible two-phase displacement (i.e. drainage and imbibition) in different branches of soil science, agriculture, petroleum engineering and geology is hard to overestimate. The early series of works by Haines [55 – 57] established a solid basis for the understanding of physical nature of pore-scale processes, which occur during fluid displacement in porous media. Haines carried out a set of drainage and imbibition experiments in a random packing of glass beads and gave a complete description of observed events (including the hysteresis in capillary behavior). In order to understand and quantify the drainage (displacement of wetting phase (W) by nonwetting (NW)) and imbibition (displacement of NW by W) he suggested the notion of “critical curvature”. The idea is that one phase displaces another from the given pore when certain critical curvature (or, interchangeably, capillary pressure) of the interface is achieved. This critical curvature is a characteristic parameter for the given *pore throat* in the case of drainage and for the *pore body* in the case of imbibition. The drainage critical curvature can be estimated, according to Haines, as a curvature of the sphere that just passes through the given pore throat. The imbibition critical curvature was estimated by Haines as the curvature of the sphere that just touches the grains that form the pore. He was also the first who explained and actually observed the phenomenon of the “snap-off” at pore throats, which was caused by the coalescence of pendular rings existing around grain contacts [56].

In 1941 Leverett [81] presented theoretical approach for the modeling of capillary pressure curves for clean, unconsolidated sands, which combined physical properties of the liquids along with the characteristics of the sands (porosity and permeability) into the so–called *Leverett's J-function.* This function is actually a scaled capillary pressure curve and in theory is the same for all clean and unconsolidated sands. Although Leverett's theory did not provide ways for the understanding of pore-level mechanisms, it has gained a huge success in petroleum engineering. Other interesting micro scale theories suggested include the pore-doublet model by Chatzis and Dullien [23] and pore-level analysis of trapped oil mobilization by Stegemeier [123].

In 1949 Purcell [115] made the first attempt in simulating pore-scale events and proposed a model of fluid displacements in porous media, which idealized the pore space as a bundle of capillary tubes and provided simple analytical solutions to macro scale properties, such as capillary pressure curves and permeability. The underlying description of porous media was certainly far away from the real pore geometry, but this was the first step in such a modeling, which sought to establish the connection between capillary effects and macro scale properties of porous media.

Purcell's "bundle of capillary tubes model" failed to incorporate the interconnectivity of the pore space. The idea of representing the porous media as a network with *sites* (pores), connected by *bonds* (pore throats) arose as the next step in pore scale modeling with the pioneering works of Fatt [34 – 36], which established the appearance and long history of *network models.* They have been used to study a wide range of the properties in different flow processes, such as relative permeabilities [39, 82, 116]; capillary pressure hysteresis [62, 69, 80, 97, 98]; relationships between capillary pressure, saturation and interfacial areas [11, 117]; non-Darcy behavior [130]; electrical resistivity [83]; properties of three-phase flow [37, 84, 127]; dynamic effects in multiphase flow [2, 22, 42]. However, without complete geometric description of porous media and due to the complexity of pore space morphology, all these models used simplified structures, such as convenient shapes of pore bodies and pore throats (e.g., cubes and cylindrical tubes), regular lattice (e.g. cubic), randomly distributed parameters (e.g. pore body and pore throat radii) and so on. Thus, the topology of pore space was completely defined by arbitrarily choosing a lattice and without any connection to real porous media. Several approaches were used to identify the pore structure and fit model parameters to the experimentally measured properties. Such models, being fitted in this fashion, were limited in their predictive power and could not be compared directly with the experimental results.

One of the approaches, which are used to overcome this difficulty, is the application of direct mapping methods that obtain pore network structure independently. These imaging techniques include thin section analysis [28, 128], Wood's metal casts [30, 124, 131], and non-destructive techniques such as nuclear magnetic resonance [71] and X-ray microtomography [26, 78, 79, 114]. The latter allows obtaining three-dimensional images of porous media systems at the scale of about 10 microns. An interesting technique based on electron microtomography imaging of water in soil was proposed by Gvirtzman *et al* [53]. Methods based on the reconstruction of sedimentary rocks [70, 106] were applied for predicting various rock/fluid properties [6, 61, 107, 110, 126]. Other examples of the physically representative methods include predictions of drainage [64], predictions of permeabilities and residence time distributions for mechanical dispersion in packed beds [125], and electrical conductivity [21]. Lattice-gas and lattice-Boltzmann simulations [25, 93, 109, 119, 120] are widely used, but demand a huge machine time and can be used only in relatively small digitized samples.

All the above approaches either demand intensive experimental studies (thin sections, microtomography, NMR) to extract network model parameters, or construct a computer representation of the porous media which represents the real media only in terms of some statistical parameters.

A completely different approach is to use simple, but *physically representative* porous media whose geometry is known, which was first proposed by Mason in 1971

[85]. The idea is based upon extracting a network model of pore space from the packing of equal spheres for which coordinates of the centers has been measured (*Finney packing*, [38]). The existence of such data makes the pore space geometrically predetermined. This allows us to understand and quantify physical events, which govern different processes in porous media. Mellor [94] used the Delaunay tessellation for extracting the network and measure geometric properties of Finney packing. The Delaunay tessellation subdivides a set of points by grouping four nearest neighbors together, and is a procedure complementary to the constructing of Voronoi polyhedra. Following these pioneering works, several studies have used this physically representative simple porous medium to model different pore scale processes. Bryant *et al* [17 – 20] simulated compaction and cementation in the Finney pack to model a broader group of porous materials. They performed dynamic modeling of fluid flow and have found the quantitative agreement between predicted and measured permeabilities in sandstones. They also demonstrated the effect of pore scale spatial correlations on transport properties. Bryant and Blunt [13] obtained good agreement with the experimental data for the modeling of relative permeabilities of two-phase flow, and Bryant and Pallatt [16] similarly predicted the behavior of electrical properties of sedimentary rocks (formation factor and resistivity index during drainage). Mason and Mellor [87] applied this approach to investigate drainage and imbibition in this physically representative porous media. Bryant and Johnson [14, 15] and Gladkikh and Bryant [43] modeled the behavior of interfacial areas between phases during drainage and imbibition respectively. Similar pore-level ideas were used to explain the relationship between capillary pressure, wettability and interfacial areas [49].

The series of works [14, 15, 88 – 90, 92, 99, 100, 113] have established a good understanding of the physics, thermodynamics and capillary phenomena that govern the process of drainage. Yet for the process of imbibition, due to the lack of the knowledge of governing physics, the Haines insphere imbibition criterion [56] is still widely used. This is despite the fact that Mason and Mellor [87] showed that for the physically representative porous media (Finney pack), this criterion leads to the inconsistent and intractable set of imbibition curvatures. Moreover, to our knowledge, nobody has tried to incorporate the complete mathematical description of the liquid phases and interfaces between them into the model, thus making possible quantitative *a priori* predictions of different pore-level processes (such as capillary pressure hysteresis during drainage and imbibition) and their properties, as well as investigation of parameters that influence such processes. In this work we propose an approach similar to the methods described above. Unlike them, it is based upon pore level physical events and complete geometric description of the phases within the Finney packing.

Prediction of imbibition in simple granular materials was the basis for our earlier published papers [44 – 48]. In this work we present the results of simulations of capillary pressure hysteresis and quantify the influence of wettability and different types of cementation on capillary pressure curves. We also present the results of modeling single- and two-phase flow in the Finney pack, as well as electric current flow. The methodology allows making *a priori* predictions of corresponding macroscopic properties of rocks (capillary curves, relative permeabilities, interfacial area, and electrical properties) and investigating the influence of geologic (cementation) and physical (wettability) conditions on them.

1.5 Physically Representative Pore-Scale Model of Porous Media

In 1899 Slichter [122] and subsequently in 1928 Hackett and Strettan [54] suggested taking a random packing of equal spheres as the model of “ideal soil”. Though this approach is surely oversimplified, nevertheless, it captures many essential features of the pore space of real sediments, namely, the locations of the grains, pores and pore throats. Thus, the “ideal soil” model allows constructing simple, but *physically representative* sediments and geometry of their pore spaces (Figs. 1 and 2).

Fig. 1 shows an image of Fontainebleau sandstone – clean, well-sorted and lightly consolidated. Fig. 2 depicts the model porous medium – a subset of Finney's dense random packing of equal spheres. On the first glance, there is nothing in common between the porous media shown in Figs. 1 and 2. However, they do share one common property – namely, the random spatial positions of grains. Moreover, it turns out that this property is very important and is the one that governs properties of sedimentary rocks of interest to us. Thus, given a sufficiently large number of grains in the packing, we can obtain *physically representative* model porous media and make predictions of their macroscopic behavior, which will be valid for the sandstone in Fig. 1 as well.

Fig. 1 Fontainebleau sandstone

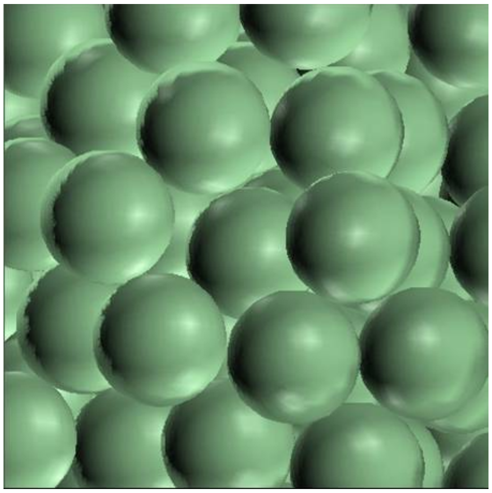

Fig. 2 Random dense packing of equal spheres

The first application of this approach became possible after Finney [38] measured spatial coordinates of the centers of about 8,000 equal spheres, in order to build a model of the liquid state of matter. His model is a spherical conglomerate of spherical particles of equal size, and we will call this conglomerate *Finney pack*. The packing has a porosity of 36.2%. Fortunately, the power of Finney's data for the modeling of porous media was recognized and applied by Mason [85] and Mellor [94], who proposed the network model extracted from the Finney pack.

The common way of constructing a network model of porous media as a lattice of sites (pores), connected by bonds (pore throats) usually assumes random assigning of different network attributes, such as coordination number, distribution of pore throat and pore body sizes etc. Such features of real porous media (and a random sphere packing, as a physically representative simple porous media), though, are not randomly distributed [18, 20, 112, 131] and are hard to measure. A completely different and natural way of constructing a network model of porous media from the Finney's geometric data is a *Delaunay tessellation* of the sphere centers. Applied to points in *n*–dimensional space, Delaunay tessellation finds sets of *n*+ 1 nearest neighbor. Thus it subdivides the volume of the Finney packing into tetrahedra (Fig. 3). Each vertex of the tetrahedron is the center of a sphere. The void space in this tetrahedron corresponds naturally to a pore body. The cross-sectional area of the void goes through a minimum in the plane containing three sphere centers, so the void area in each face of the tetrahedron corresponds naturally to a pore throat.

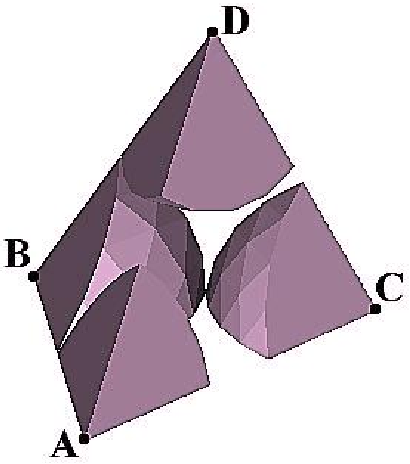

Fig. 3 Tetrahedral cell within the Finney pack, resulting from Delaunay tessellation. The apices of the tetrahedron (points *A, B, C* and *D*) are the centers of four nearest neighbor spheres. Only the sections of the spheres contained within the tetrahedron are shown.

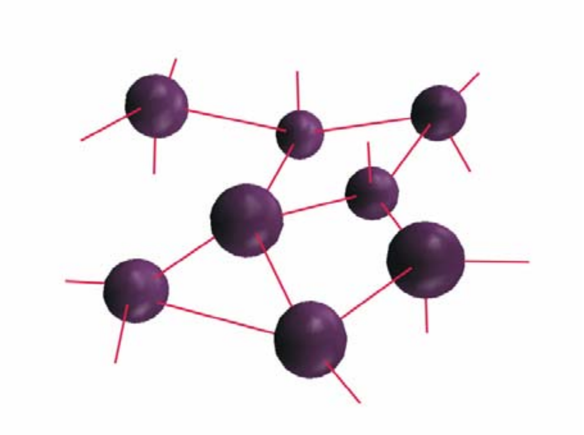

Fig. 4 Schematic representation of a network model. The spheres correspond to the internal regions of tetrahedral cells and should not be confused with spherical grains in Fig. 2. The bonds, which connect spheres, correspond to cell faces. Each site has four neighbors.

Thus, a simple network is built (Fig. 4): its “sites” (*pore bodies*, shown in Fig. 4 as spheres) correspond to the internal regions of tetrahedral Delaunay cells and its “bonds” (*pore throats,* shown in Fig. 4 by lines) correspond to the faces of those cells. (Note that spheres in Fig. 4 are just representations of pore bodies and correspond to the internal regions of actual Delaunay tetrahedra, shown in Fig. 3. They should not be confused with the actual spherical grains, shown in Fig. 2). All geometrical features of these pore bodies and throats (such as their volume, area etc) follow directly from the known coordinates of the sphere centers. The topology of the network arises naturally: since each cell is a tetrahedron, it has four neighbors, resulting in a lattice of connectivity four. However, the network is completely irregular; there is no evidence of any crystalline structure such as the diamond lattice [94]. In this work the central 3,367 spheres of the Finney pack were used, which yield a network with about 15,000 pores and 30,000 pore throats. More detailed description of the Finney pack and the network obtained from it by Delaunay tessellation can be found elsewhere [38, 85, 87, 94].

Further, it is desirable to create simple models of sedimentary rocks from the model sediment shown in Fig. 2. Bryant *et al* [17 – 19] simulated results of geological processes, such as compaction and cementation, in the Finney pack, and predicted trends of permeability decreasing with decrease in porosity. In this work we follow their approach in modeling results of isopachous cementation (Figs. 5 and 6), when cement grows as layers of uniform size on the surfaces of grains.

Moreover, the use of smooth spheres in the Finney pack allows accommodating the degree of roughness of the surfaces of real grains (cf. Figs. 1 and 2). If the capillary pressure is not very high, all the micro pores and micro fractures of grain surfaces will contain W phase, which therefore smoothes rough surfaces of grains. To displace W phase from such micro cavities, capillary pressure has to reach sufficiently large value. We assume that during displacement processes, considered in this work, this large value of capillary pressure is not reached, since the size of the smallest pores in the packing is still several orders of magnitude larger than the size of micro features of grain surfaces responsible for its roughness.

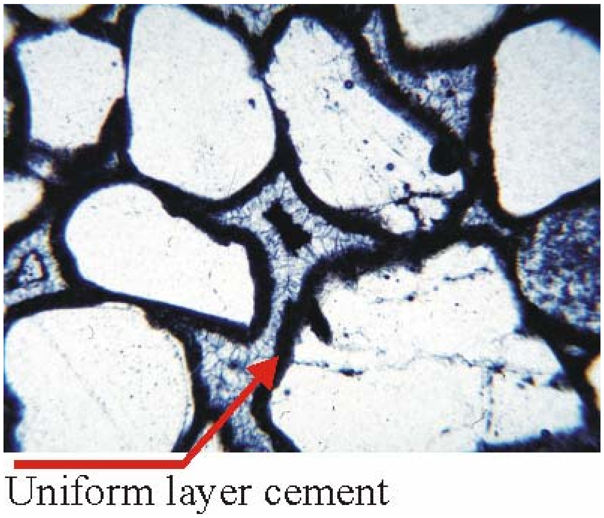

Fig. 5 Sandstone containing isopachous cement (black uniform layers around grains, shown by the arrow).

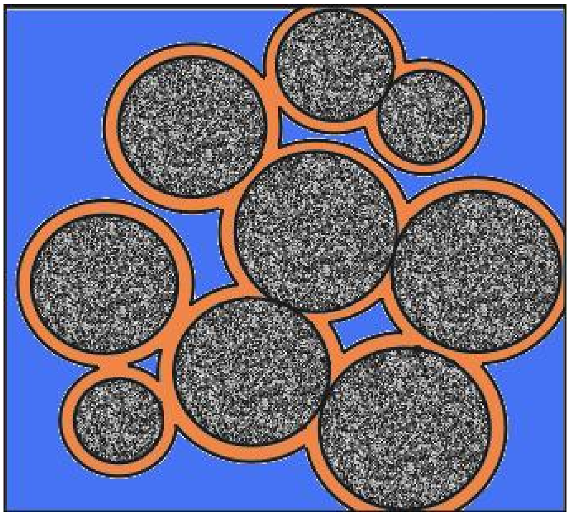

Fig. 6 Model cemented porous media (isopachous cement – shown with orange color). 2D-slice through the cemented packing.

Fig. 5 shows the sandstone sample with isopachous cement, which occurs as uniform layers on grain surfaces (black layers around grains on Fig. 5). Following the idea of Bryant *et al* [17 – 19], we model this type of cement in the packing by increasing sphere radii and allowing spherical grains to grow in size and interpenetrate into each other (Fig. 6). The increase in radius can be either the same for each sphere (*uniform isopachous cementation*) or taken as random (from some pre-determined distribution) for each spherical grain. Thus we can create physically representative model sandstones with isopachous cement, having a wide range of porosities. This will allow us making predictions of such important properties as permeability – porosity and electrical efficiency – porosity relationships.

Another type of cementation, which we consider in this work, is pore-filling (Figs. 7 and 8). In this case cement completely fills whole pores and occurs usually as patches containing clusters of neighboring pores (patches of white color in Fig. 7). We model the results of pore-filling cementation in the Finney pack by allowing tetrahedral pores (shown in Fig. 3) be completely filled with cement. In order to grow cement in clusters of pores, we 1) define desired porosity; 2) specify maximal allowed cluster size (in number of pores); 3) determine the number of seed pores and the size of the cluster, corresponding to each seed, and distribute them randomly throughout the packing; 4) mark each seed pore as cemented and cement each of its neighboring pores, then the pores, neighboring to them, and so on, until the needed cluster size is reached. As might be expected in advance, the dependence between porosity and number fraction of pores filled with cement is linear.

This algorithm provides us with a different type of model for cemented rocks and allows us making similar predictions as for the case of models with isopachous cement.

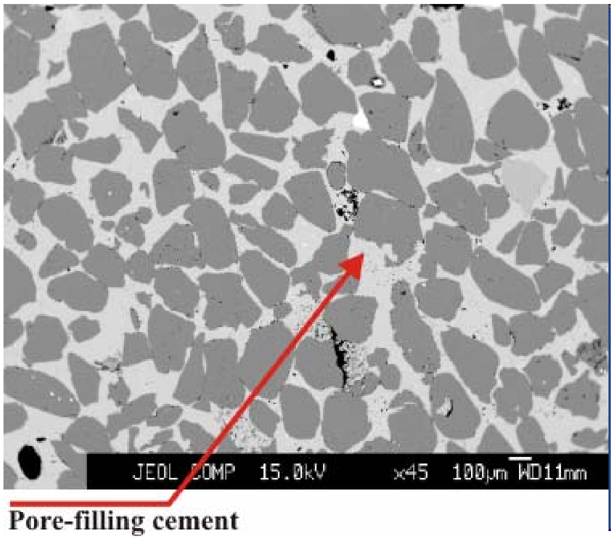

Fig. 7 Pore-filling cement in the sandstone (patches of white, shown by the arrow).

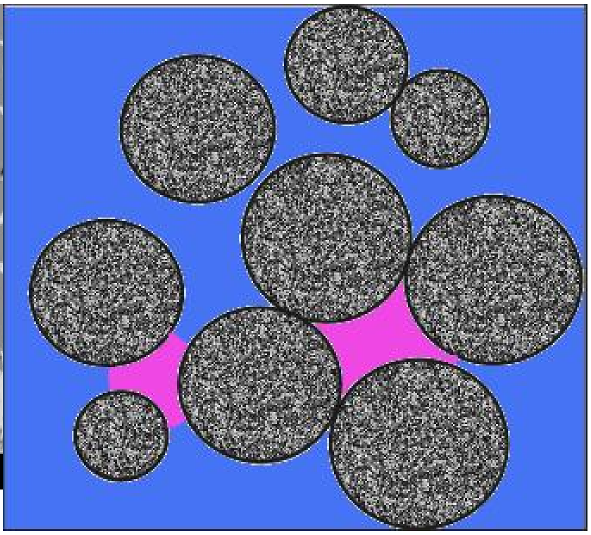

Fig. 8 Model cemented porous media (pore-filling cement – shown with pink color). 2D-slice through the cemented packing.

Chapter II

2.1 Model of Fluid Displacement

2.1.1 Capillarity and Wetting Phase Morphology

In this work we consider displacements of one phase by another within the Finney pack. One of the phases is wetting (W) and another one is non-wetting (NW) (for example, they can be water (wetting) and air (non-wetting), or water (wetting) and oil (non-wetting). The phases are immiscible. When viscous and body forces are negligible, the configuration of the phases within the packing is governed by the Young – Laplace [1] equation, which relates capillary pressure to the curvature of the interface between two phases:

$$P_C = \gamma C, \qquad (1)$$

where $P_c = P_{nw} - P_w$ is the pressure difference between NW and W phases (*capillary pressure)*; γ is the interfacial tension between them and C is the sum of the two principal curvatures, or twice the mean curvature of the interface:

$$C = \frac{1}{r_1} + \frac{1}{r_2},$$

where r_1 and r_2 are the corresponding principal radii of curvature. For brevity we refer to C as "curvature". Because of Eq. (1), we use the terms "capillary pressure" and "curvature" interchangeably. In spite of the fact that equation (1) describes a static configuration, it is commonly applied to the displacement of one immiscible phase by another, when that displacement occurs sufficiently slowly for capillary forces to dominate, and throughout this work it is supposed that this condition is satisfied.

In the simulations, presented in this work, we consider actual physical experiment (Fig. 9). Given a dry sample of sedimentary rock with defined geological properties (i.e. grain size, type and amount of cement, porosity and so on) we fill its pore volume 100% with the W phase. Then we apply pressure difference between the phases and thus force *drainage* (displacement of W phase by NW phase) to happen. At some critical value of capillary pressure (*entry pressure)* NW phase first enters the packing. When the capillary pressure is increased further and reaches the value of *percolation threshold*, rapid invasion of the packing by NW phase occurs – small change in curvature leads to large decrease of W phase saturation. Increasing the pressure difference between phases by some finite increment, we wait until at each increment the equilibrium configuration of phases is reached, at which point the measured incremental volumes of fluids that enter and leave the sample allow us to determine the volume fraction of pore space (*saturation*) occupied by each fluid in the sample. At some high value of pressure difference, the saturation in the sample changes no more with the increase in curvature. This means that the *irreducible W phase saturation* is reached; remaining W phase is trapped within the pore space and is hydraulically disconnected from the W phase reservoir.

Starting from this irreducible W phase configuration, we reverse the process and gradually decrease the applied pressure, so that spontaneous *imbibition* (displacement of the NW phase by the W phase) occurs. Again, at some critical value of curvature (entry pressure) W phase penetrates into the pore space; when curvature reaches percolation threshold rapid invasion of the pore space by the W phase occurs. At the end of imbibition (zero capillary pressure) the sample is not 100% saturated with the W phase, because some *residual* NW phase saturation is also present (its value is usually of order of 10 – 20% of the pore volume).

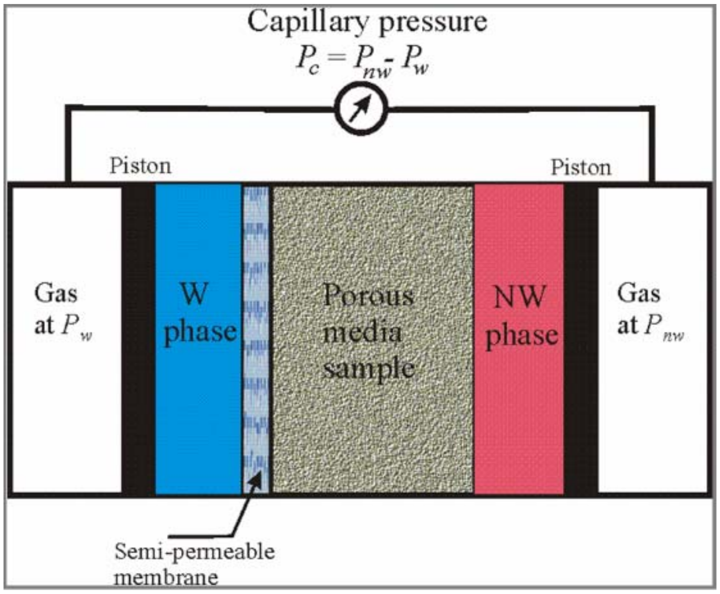

Fig. 9 The schematic of the experimental setup for drainage and imbibition in porous media sample.

In the simulations described in this work we model numerically this actual physical experiment described above, using physically representative model sedimentary rock, obtained from the Finney pack, as a porous media sample. We consider the phases to be incompressible and immiscible.

It is necessary to define the terminology of possible configurations of the phases and the interfaces between them in the packing. We consider three distinct W phase morphologies, which exist during both drainage and imbibition (Figs. 10 and 11).

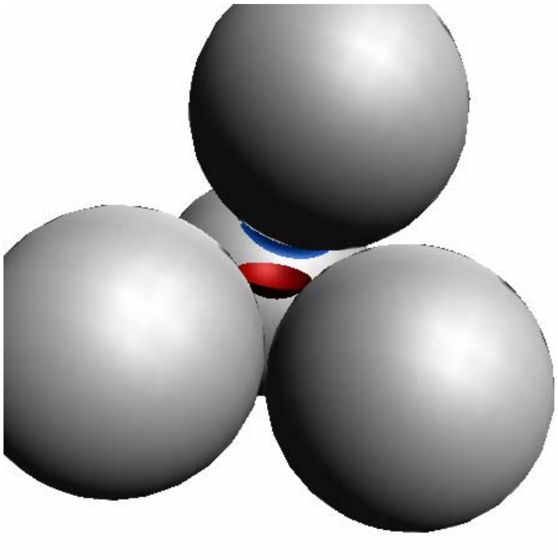

Fig. 10 Four grains and tetrahedral pore, which is formed by them. The blue shape is the pendular ring, which fills the gap between two grains. The red spherical cap is the interface of the meniscus, which is assumed to have locally spherical shape. Everything below this cap is W phase, above – NW phase.

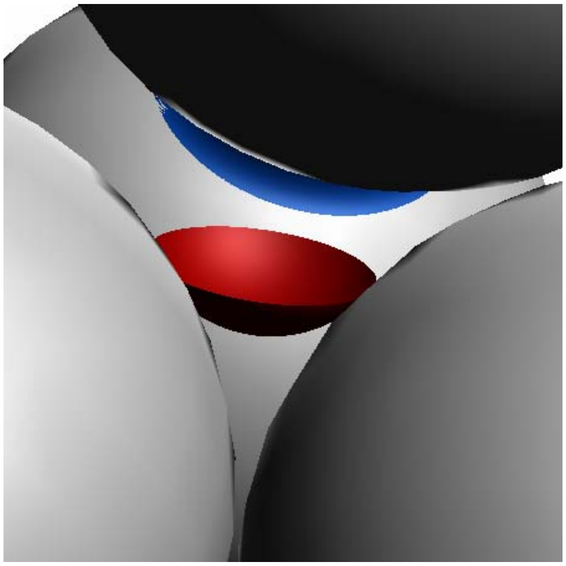

Fig. 11 Zoomed view of the configuration shown in Fig. 10

1) *Pendular ring* (shown by blue color in Figs. 10 and 11) at *grain contact*. We define *grain contact* as a pair of neighboring grains, which need not actually touch. Grain contacts coincide with the edges of tetrahedral pores (Fig. 3). It is clear that each pore in the packing thus has six associated grain contacts, and each pore throat, three. W phase supported within the gap between two spheres is often called a *liquid bridge*; for brevity we use the term "rings" to refer to liquid bridges as well. Pendular rings always exist when two spheres actually touch. If a gap separates the two spheres, a pendular ring can exist only at curvatures below a critical value that depends upon the value of the gap between spheres. The geometry of such rings will be discussed below in detail (section 2.2.1).
2) W phase completely occupies pore space within tetrahedral pore. This provides the main contribution to the W phase saturation during both drainage and imbibition. During drainage W phase initially fills all the pore bodies and retracts as NW phase invades the packing; though some pores filled with the W phase

can be trapped and contribute to irreducible W phase saturation. During imbibition W phase invades the pore space and completely fills pore bodies.

3) *Meniscus* at the pore throat that connects a pore completely filled with W phase and a neighboring pore which contains NW phase. The first pore is a natural candidate for drainage, and the second for imbibition, depending on what process we consider. Meniscus is shown by red color in Figs. 10 and 11 and is assumed to have locally spherical shape. Its geometry is discussed below in details (section 2.2.3).

2.1.2 Model of Drainage

We consider drainage as a quasi-static bond invasion percolation process [135]. In this work we follow the approach, suggested first by Mason and Mellor [87] and extended by Bryant and Johnson [14, 15] to include behavior of different W phase morphologies (pendular rings, menisci and *lenses* of W phase) during drainage and account for irreducible W phase saturation.

Drainage is modeled in the network, extracted from the Finney pack and represented by bonds (pore throats) and sites (pore bodies) (Fig. 4). Each pore throat is assigned a *critical curvature* for drainage in advance. The pores connected with W and NW phase reservoirs (they define the “boundary” of the packing – see Fig. 9 and section 2.1.4) are defined. The algorithm for the drainage simulation proceeds with the incremental change of curvature and finding new equilibrium configuration (when some pores drain as a result of increase in curvature), which corresponds to new value of curvature applied. Pores connected with NW phase reservoir are initial candidates for drainage and are drained if currently applied curvature is greater than drainage critical curvature for the pore throat that connects this pore to the NW phase reservoir. Any other pore in the interior of the packing is allowed to drain only if 1) its immediate neighbor (that shares the pore throat with the given pore; each tetrahedral pore has four immediate neighbors –

Figs. 3 and 4) is already drained and 2) current curvature is larger than the critical value for the pore throat which connects the given pore to this neighbor. This algorithm is straightforward and its more detailed description can be found in [87]. During drainage we account for the formation of *lenses* of W phase at pore throats as well. Each pore throat connects two neighboring pores. If both these pores are drained through one of their pore throats, different from the throat in consideration, the W phase can remain at the pore throat in the form of lens. We treat this lens as a double-sided meniscus and compute its volume and surface area similarly (see section 2.2.3 for the geometry of meniscus).

It is worth mentioning here that we consider neither drainage nor imbibition as reversible thermodynamic processes. In fact, the irreversibility of the movement of the interfaces during displacement processes is well-known (*Haines' jumps*, [56, 57, 99]). We use the term "quasi-static" in a macroscopic sense: we wait until the new static equilibrium configuration of phases is achieved in the packing as a result of the change in applied curvature. Thus, we model displacement processes as a sequence of equilibrium points in curvature-saturation domain. For the detailed discussion of thermodynamics and irreversibility of displacement processes in porous media see [99].

The most important task in drainage algorithm is to define drainage critical curvatures of pore throats. Haines [56] in 1927 suggested approximating the critical curvature by the curvature of the sphere that just passes through the pore throat (which is called after him *Haines' face insphere* approximation):

$$C_H^{dr} = \frac{2\cos\theta}{r_t}, \tag{2}$$

where θ - contact angle of W-NW-solid interface (see below, section 2.1.5) and r_t – radius of sphere that just passes through the pore throat. Another technique for the computation of pore throat drainage critical curvatures was invented by Mayer and Stowe [92], and further developed by Princen [113]. The resulting set of so-called *MSP critical* *curvatures* is computed analytically. These curvatures are exact for the case of 2D-geometry (considering wedges of liquid between uniform semi-infinite rods), but are not very accurate for the case of spherical grains (see also [88 – 90]). In this work we use Haines' face insphere approximation to compute drainage critical curvatures. The reason for this choice is that both Haines' face insphere and MSP criteria introduce errors of similar magnitude to drainage capillary curve when compared to experimental data (see section 3.1.1) and therefore Haines' face insphere approximation, being much simpler to compute numerically, is preferable.

The algorithm, similar to described above, was developed further by Bryant and Johnson [14, 15] to include accurate computation of fluid configurations (pendular rings of W phase at grain contacts, menisci between phases, *lenses* (double-sided menisci) of W phase at pore throats) and account for irreducible W phase saturation. In this work we apply the same strategy as described in Bryant and Johnson [15]. As a criterion for the entrapment of W phase we apply case 3 (intermediate connectivity of W phase) from their work. This criterion allows achieving more realistic configuration and value of saturation of irreducible W phase.

2.1.3 Model of Imbibition

In this work we model imbibition considering pore-level events that occur within pores with fluid interfaces (menisci and pendular rings, Figs. 10 and 11). Imbibition proceeds with an incremental decrease of the curvature of the interface, starting from initial condition (irreducible W phase saturation at drainage end-point). This decrease allows W phase to penetrate back into the packing.

In order to simulate imbibition, we implement the following algorithm. The pores connected with W and NW phase reservoirs (they define the "boundary" of the packing – see Fig. 9 and section 2.1.4) are defined. The algorithm for the imbibition simulation proceeds with incremental decrease of curvature and finding new equilibrium configuration of pendular rings, menisci and completely imbibed pores. Pores, connected with W phase reservoir are initial candidates for the imbibition and are imbibed when *Melrose criterion* (see section 2.3.1), applied to them, is satisfied. Any other pore in the interior of the packing, which contains NW phase and is not contained within any *cluster of trapped pores* (see section 2.3.2), is considered for pore level events (imbibition and *snap-off* (see section 2.2.2)) that can occur within it. If *Melrose criterion* (see section 2.3.1) for imbibition, applied to the given pore, is satisfied, then this pore is checked to determine whether it is contained in a cluster of pores connected to an *exit pore* (see section 2.1.4). The existence of such a cluster implies a continuous path of pores containing NW phase from the candidate pore to the NW phase reservoir. If this condition is not met, the pore cannot be imbibed; the pore and other pores containing NW phase that are connected to it are added to the list of pores containing *trapped NW phase* (for the implementation of NW phase entrapment see below, section 2.3.2). Since we consider the phases to be incompressible, everything within such trapped cluster of pores becomes frozen, in the sense that all pendular rings and menisci within the cluster cannot change or move. Otherwise, the considered pore becomes imbibed (completely filled with W phase) and menisci arise at all pore throats, which connect this pore to its non-imbibed neighbors.

Trapped cells and newly imbibed cells are removed from the list of candidates, and this list is re-checked against the criteria for imbibition and snap-off as described above. When no pore level event (that is, imbibition or snap-off) can happen, it means that an equilibrium configuration has been reached at current curvature. Then volumes of the phases are computed, which provides the values of phase saturations at current curvature. This completes one iteration of the algorithm, and the curvature can be decreased again.

Historically, similarly to drainage (which is considered as *bond* invasion percolation process), imbibition was considered as *site* invasion percolation problem [135]. In order to simulate such a process, one needs to specify *imbibition critical curvatures* for pore bodies (similarly to drainage critical curvatures of pore throats). The first (and the simplest) attempt to define this critical curvature was made by Haines [56] as

$$C_H^{imb} = 2 / R_{in}, \qquad (3)$$

where R_{in} is the radius of the sphere inscribed into the pore body (such a sphere would touch each of four pore grains – Fig. 12). Such defined imbibition critical curvature is called *Haines' insphere* curvature.

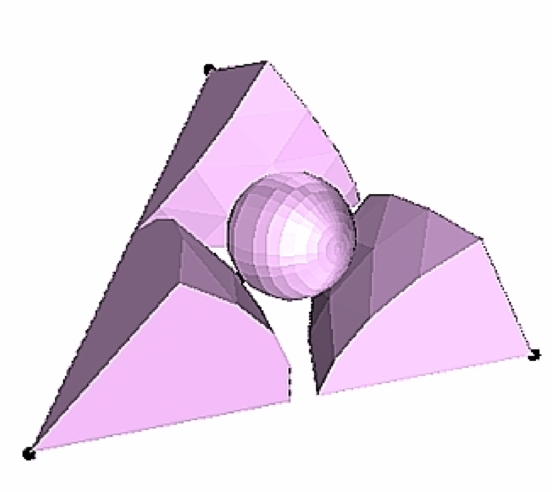

Fig. 12 Illustration of Haines' insphere criterion for imbibition. Sphere, inscribed into the pore is shown; imbibition critical curvature for the pore is taken as the curvature of this sphere. Parts of three grains that form the tetrahedral pore are also shown; the fourth (upper) grain is removed for the purposes of clarity (compare with Fig. 3)

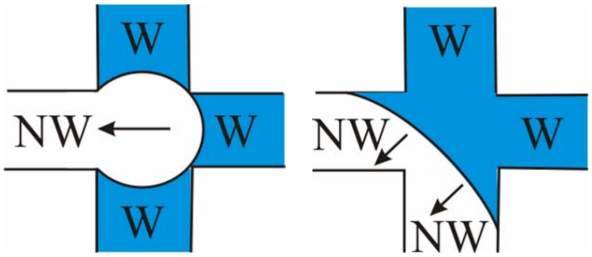

Fig. 13 Illustration of Lenormand and Zarcone [80] observation in 2D-case. The pore to the left has three immediate neighbors filled with W phase and is imbibed earlier (at larger curvature) than the pore to the right, that has only two immediate neighbors filled with W phase.

Unfortunately, the set of Haines' insphere curvatures, computed for the pores in the Finney pack, would allow *negative hysteresis* for some pores, that is, their critical curvature for drainage would be less than their critical curvature for imbibition (as was shown by Mason and Mellor, [87], see also below, section 3.2.2). In order to avoid this nonphysical effect, Mason and Mellor [87] proposed to modify the Haines insphere curvature as:

$$C_{MM}^{imb} = C_H^{imb} - 1.6 / R_{grain}, \tag{4}$$

where R_{grain} is the radius of spherical grain. This empirical modification was specific to a random packing of equal spheres. Eq. (4) says that each pore has a fixed, predetermined critical curvature at which it will imbibe (if W phase is present in a neighboring pore). However, there is experimental evidence (Lenormand and Zarcone, [80]) that the more already imbibed neighbors the pore has, the sooner (that is, at larger curvature) this pore will be imbibed (see illustration in Fig. 13). This contradicts the notion of a predetermined critical curvature for imbibition. A modification of Haines' estimate that attempts to account for this dynamic feature of imbibition was proposed by Jerauld and Salter [69]:

$$C_{JS}^{imb} = C_H^{imb} / N_{NW}, \tag{5}$$

where N_{NW} is the number of the immediate neighbors, which contain NW phase. While qualitatively reasonable, the estimate given by Eq. (5) is essentially empirical.

Instead, in this work we propose to use the criterion for imbibition of a single pore, suggested by Melrose [95]. This *Melrose criterion* is dynamic (we cannot tell in advance the curvature at which each pore is imbibed) and based upon the physical events that happen during imbibition at pore scale. This criterion is described in details below (section 2.3.1).

2.1.4 Boundary Conditions for the Displacement

In order to simulate the displacement process, both drainage and imbibition, it is necessary to define *entrance* and *exit* pores. The *entrance* pores are the pores through which the displacing phase enters the packing. During drainage they are assumed to be always connected with the NW phase reservoir (NW phase enters the packing through them), and during imbibition – with the W phase reservoir (W phase enters the packing through them). The *exit* pores are the pores through which the displaced phase leaves the packing. During drainage they assumed to be always connected with the W phase reservoir (W phase leaves the packing through them), and during imbibition with the NW phase reservoir (NW phase leaves the packing through them). The pores that are actual surface pores of the Finney packing are natural choices for entrance and exit pores. However, Mason and Mellor [87] have shown that the Finney packing, being a spherical conglomerate has a high ratio of surface pores to internal pores in comparison with samples typically used in the laboratory. Consequently simulations in which a large fraction of the surface pores are taken as W phase entrances do not give a sharp *percolation threshold* (that is, very fast invasion of a large volume of the sample, once the curvature reaches its specific percolation value). In order to replicate the percolation behavior of real samples, Mason and Mellor [87] proposed to diminish the number of entrance cells. Using this technique, they obtained percolation threshold at a dimensionless (i.e. for grain radius equal to 1) curvature of about 4.1, which is close to the values observed during experiments. When making a comparison to the experiments, the number of entrance pores can be taken correspondingly to the actual ratio of surface to internal pores in the experimental sample, which is estimated from the grain size and sample geometry. This eliminates the uncertainty in the choice of this parameter, which depends only on the macroscopic geometry of the sample. The choice for the exit pores as actual surface pores of the Finney pack is consistent with most practical situations. The influence of different choices for exit pores during imbibition and drainage (e.g. some fraction of the surface pores, a random selection of pores from within the packing, etc) on the residual NW-phase saturation is interesting but is beyond the scope of this work. The choice of the exit pores also depends only upon the geometry of the sample.

2.1.5 Physical Constraints: Wettability

Physical conditions of porous media have a great importance on displacement processes. In this work we consider the influence of *wettability* condition, which is specified by the contact angle of W-NW-solid interface [1] (Figs. 14 and 15):

$$\gamma_{S-NW} = \gamma_{S-W} + \gamma_{W-NW} \cos\theta, \qquad (6)$$

where $\gamma_{S-NW}, \gamma_{S-W}, \gamma_{W-NW}$ are interfacial tensions of solid-NW, solid-W and W-NW interfaces correspondingly; θ is the contact angle (Fig 15). Eq. (6) is called the Young – Dupre contact angle equation [1]. Eq. (6) and the value of contact angle θ govern the shapes of local interfaces (i.e. pendular rings and menisci) between phases during displacement in the equilibrium configuration.

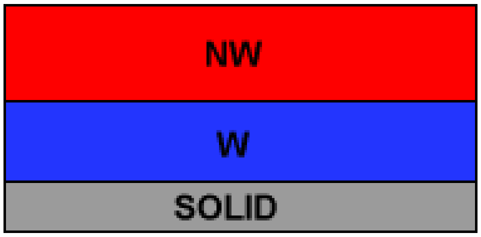

Fig. 14 Spreading of W phase upon solid surface of the grain (value of contact angle θ of W-NW-solid interface is zero).

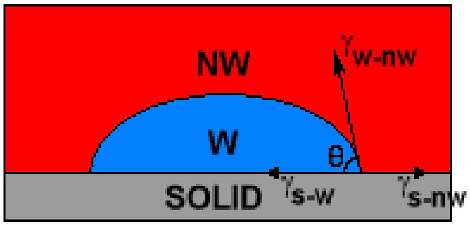

Fig. 15 Formation of a drop of W phase on solid surface of the grain. The contact angle of W-NW-solid interface has non-zero value θ.

Further, if the value of contact angle is zero, W phase spreads upon the surface of solid grain and thin film is formed (Fig. 14). Thus, in this case NW phase is never in direct contact with the grain surface, upon which the thin film of the W phase exists at any stage of displacement. If the contact angle has non-zero value, then such a film cannot be formed and the W phase exists on the grain surface in the form of the drop (Fig. 15).

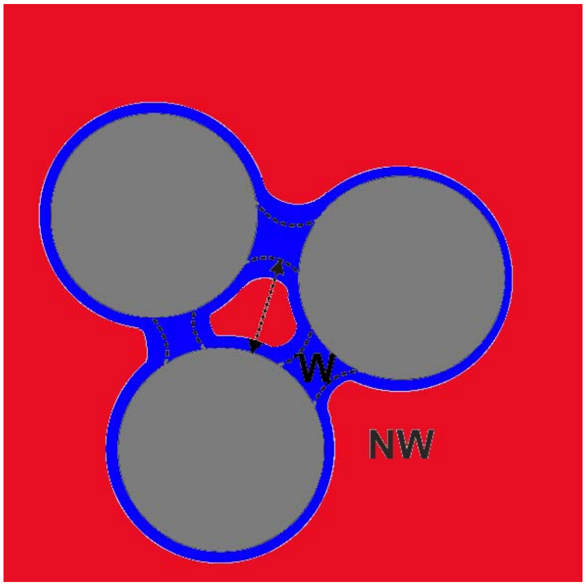

Fig. 16 Influence of W phase connectivity. Pendular rings in the case of disconnected W phase (shown by dotted lines) remain isolated and do not advance within the pore space when capillary pressure increases during drainage or decreases during imbibition. Pendular rings in the case of connected W phase (shown by blue color) are hydraulically connected to the bulk through thin films around grains and adjust their shape to the current curvature.

The condition of the wettability of the system naturally specifies the condition of the *connectivity* of the W phase. If the value of contact angle θ is zero, and W phase spreads upon grain surfaces, thin films of W phase exist (Fig. 14) and W phase is hydraulically connected through these films. This provides the complete hydraulic connectivity of the W phase throughout the whole packing at any stage of displacement; we say the W phase is *completely connected*. Here hydraulic connectivity implies that W phase can be moved into any part of the packing. At small W phase saturations the movement may require transmission through thin films of W phase on grain surfaces (Fig. 16).

An important consequence of complete connectivity is that all pendular rings in the packing are surfaces of curvature equal to the currently applied value. Thus they adjust their shape immediately when a change in capillary pressure is applied. In particular, all the rings will grow and advance along grain surfaces as the curvature decreases during imbibition and will shrink and retreat along grain surfaces as the curvature increases during drainage. Complete connectivity is thus a limiting case. Because films have small conductance, the time required for rings to adjust can be quite large in practice.

On the other hand, if W phase does not possess complete connectivity, then a pendular ring becomes "trapped" during drainage (that is, loses its connection to the bulk volume) and remains a surface whose curvature is held constant at the value at which it was trapped. (For convenience in treating trapped volumes we have assumed incompressible phases and zero interphase mass transfer.) The trapped ring contributes to the irreducible wetting phase saturation. If imbibition starts from this drainage endpoint, such a ring cannot grow until it becomes connected to the bulk volume of W phase again. Such re-connection happens when the W phase imbibes pores neighboring to this ring. So, the existence of thin films on grain surfaces causes qualitatively different behavior during displacement processes. Different configurations of the system for both cases of W phase connectivity are shown in Fig. 16. Pendular rings for the case of the disconnected W phase (shown by dotted lines) remain isolated and do not change shape; whereas for the case of the connected W phase (shown by blue color) they are hydraulically connected to the bulk of W phase through the thin films and adjust their shape to the current capillary pressure.

2.2 Geometry of Liquid Phases

As was pointed out above, we assume that W phase exists in three different configurations: pendular rings (liquid bridges) at grain contacts; pores, completely filled with W phase; and menisci between phases. Below we consider geometry of two configurations (pendular rings and menisci) in detail.

2.2.1 Pendular Rings at Grain Contacts

Pendular rings play a crucial role in this approach to simulating displacement processes. Indeed, at small W phase saturations (early stages of imbibition or late stages of drainage) the most part of W phase exists in the form of such rings, which occupy the space between solid grains (Fig. 17). Moreover, their swelling as curvature decreases is an essential part of the Melrose imbibition criterion (see section 2.3.1). Quantifying their geometry in some detail is therefore necessary.

This is one of the classical problems concerning the configuration of a mass of liquid which exists in a gap between two solid surfaces, formulated first by Plateau [104]. Knowing all geometric features of such rings we can include their contribution to imbibition or drainage capillary pressure curves (since the curvature defines capillary pressure and total volume of rings defines W phase saturation). We also need to investigate the stability of these rings for two situations: when they are isolated, and when they come in contact with other interfaces. This will establish the basis for the different pore level physical events that happen as a result of the contact between interfaces.

Grain particles are assumed to be equal spheres with radius *R* (Fig. 17). The known values are the gap *h* (half of the distance between sphere surfaces) and current curvature *C* of the liquid bridge surface (since the curvature (or pressure) controls displacement process and can be measured). In an ideal soil about half the pairs of nearest neighbor grains are in contact, so that $h = 0$.

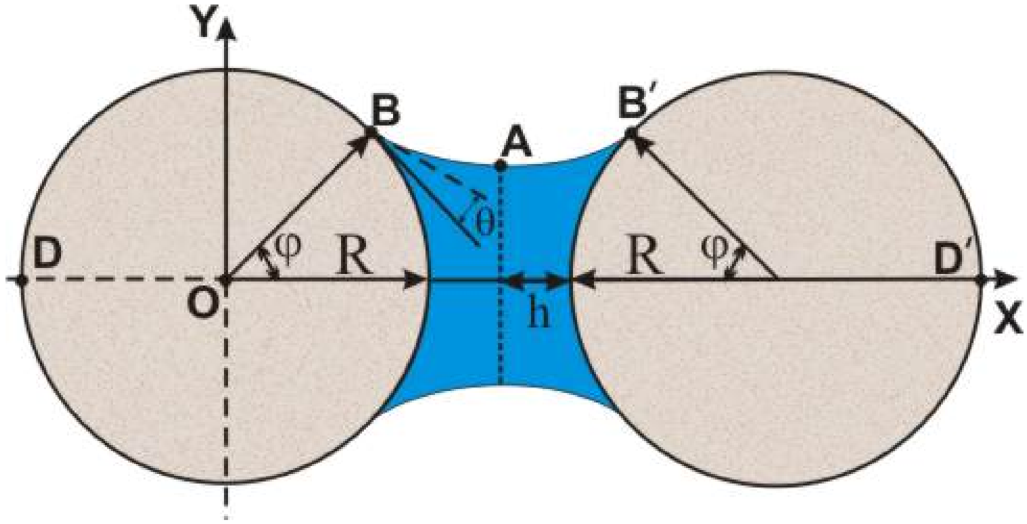

Fig. 17 Pendular ring between two equal spheres; we use the term to denote liquid bridges as well as rings. θ – contact angle; φ - filling angle; h – half the gap between spherical grains.

One way to solve this problem is to approximate the liquid bridge as a surface, which has two principal radii of revolution – *toroidal* approximation. This approach admits an analytical solution (i.e. equation for the shape of the ring) for the given h and C. The formulae for the toroidal shape can be found elsewhere [40, 55, 72, 118].

The true shape of the liquid bridge is governed by the condition that its surface must have constant curvature everywhere. This condition produces a surface known as the *nodoid*.

Let us consider an immersion from a 2-dimensional domain to the 3-dimensional Euclidean space, which produces the shape of nodoid. Let D be a domain in the (u, v)-plane and $\boldsymbol{X}$ a C^∞ map from D to the 3 –dimensional Euclidean space $\mathbf{R}^3$. We will work in dimensionless Euclidean coordinates, so that the radius of the spheres R=1. (And thus the curvature C of the surface (Eq. (1)) will be written in the units of $1/R$). Let us write then

$$X(u,v) = (x(u,v), y(u,v), z(u,v)) \in R^3, (u,v) \in D.$$

Since the liquid bridge (Fig. 17) is the axisymmetric surface, we will seek the equations of the mapping in the form:

$$\begin{cases} x = u, \\ y = f(u)\cos v, \\ z = f(u)\sin v, \end{cases} \tag{7}$$

where (x, y, z) – coordinates in 3-dimensional Euclidean space (Fig. 17); (u, v) – coordinates in the domain D: $0<v<2\pi; 0<u<L$ (where L is the distance between the points B and B' in Fig. 17); $y=f(x)$ is the equation of the curve BAB', which bounds the surface of the ring.

Differentiating (7), we obtain:

$$X_u(u,v) = (1, f'\cos v, f'\sin v);$$
$$X_v(u,v) = (0, -f\sin v, f\cos v). \tag{8}$$

And for the second derivatives:

$$\begin{aligned} X_{uu}(u,v) &= (0, f''\cos v, f''\sin v); \\ X_{uv}(u,v) &= (0, -f'\sin v, f'\cos v); \\ X_{vv}(u,v) &= (0, -f\cos v, -f\sin v). \end{aligned} \tag{9}$$

The first fundamental form of the nodoid is:

$$I_X = Edu^2 + 2Fdudv + Gdv^2,$$

where

$$\begin{aligned} E &= \langle X_u, X_u \rangle = 1 + (f')^2; \\ F &= \langle X_u, X_v \rangle = 0; \\ G &= \langle X_v, X_v \rangle = f^2. \end{aligned} \tag{10}$$

Next, we can compute the outward unit normal vector to the surface of the ring:

$$\vec{n} = -\frac{X_u \wedge X_v}{|X_u \wedge X_v|}.$$

Since

$$X_u \wedge X_v = (f'f, -f\cos v, -f\sin v),$$

and

$$\left|X_u \wedge X_v\right| = \sqrt{\left(f'f\right)^2 + f^2} = f\sqrt{1+\left(f'\right)^2},$$

we have

$$\vec{n} = \left(-\frac{f'}{\sqrt{1+\left(f'\right)^2}}, \frac{\cos v}{\sqrt{1+\left(f'\right)^2}}, \frac{\sin v}{\sqrt{1+\left(f'\right)^2}}\right). \tag{11}$$

Then we can compute the second fundamental form of the nodoid as:

$$\Pi_X = Ldu^2 + 2Mdudv + Ndv^2,$$

where

$$\begin{aligned} L &= \left\langle X_{uu}, \vec{n}\right\rangle = \frac{f''}{\sqrt{1+\left(f'\right)^2}}; \\ M &= \left\langle X_{uv}, \vec{n}\right\rangle = 0; \\ N &= \left\langle X_{vv}, \vec{n}\right\rangle = -\frac{f}{\sqrt{1+\left(f'\right)^2}}. \end{aligned} \tag{12}$$

Then, in terms of Eq. (1), curvature C (twice the mean curvature of the interface) is computed as:

$$C=\frac{GL+EN-2FM}{EG-F^2}=\frac{\dfrac{f^2 f''}{\sqrt{1+(f')^2}}+\left(1+(f')^2\right)\dfrac{-f}{\sqrt{1+(f')^2}}}{f^2\left(1+(f')^2\right)}= \tag{13}$$

$$=\frac{f''}{\left(1+(f')^2\right)^{3/2}}-\frac{1}{f\sqrt{1+(f')^2}}.$$

So we have the following differential equation for the function *y=f(x)* that defines the shape of the nodoid:

$$C=\frac{f''}{\left(1+(f')^2\right)^{3/2}}-\frac{1}{f\sqrt{1+(f')^2}}=const. \tag{14}$$

Let's make a substitution

$$Q=(f')^2+1,$$

then from (13) we obtain:

$$\frac{dQ}{df}-\frac{2Q}{f}=2CQ^{3/2}. \tag{15}$$

This equation may be integrated to yield

$$\frac{2f}{\sqrt{\left(1+(f')^2\right)}}+Cf^2=K=const. \tag{16}$$

This leads to the following differential equation for the function $y=f(x)$:

$$f' = -\sqrt{\frac{4f^2}{\left\{K - Cf^2\right\}^2} - 1}. \tag{17}$$

This equation is integrated for chosen values of curvature C and filling angle φ. Boundary conditions at point B are specified by filling angle φ and contact angle θ:

$$x_B = \cos\varphi, \qquad y_B = \sin\varphi, \qquad y'_B = \cot(\varphi + \theta). \tag{18}$$

Integration is stopped when the boundary condition at the point A is met, that is, $y' = 0$. The constant K is evaluated from Eq. (16) at point B, which yields

$$K = 2\sin\varphi\sin(\varphi + \theta) + C\sin^2\varphi. \tag{19}$$

Equation (17) is integrated numerically using predictor – corrector scheme with explicit Euler method as the predictor and trapezoidal rule as the corrector. Dimensionless step-size in X direction is chosen to be equal to 10^{-5} to provide stability of the numerical method.

The technique, described above, allows to find point A (it will be the point where the integration is stopped – see Fig. 17), that is, to find the separation h for the given values of curvature C and filling angle φ. Unfortunately, during the simulation of the displacement process (drainage or imbibition) the value of filling angle φ is unknown, but we can measure the value of separation h instead. To resolve this complexity we need to integrate (17) for the whole range $(0, \pi/2)$ of filling angles and find the solution, which corresponds to the given value of separation.

In order to find the set of solutions corresponding to the given values of curvature and separation, we compute first a map of solution to Eq. (17) for a rectangular grid of values of C and φ. Values of C in the range (0, 20) with the increment of 0.1 and values of φ in the range $(0, \pi/2)$ with the increment 0.005 were used.

If we fix the value of separation in Eq. (17) and integrate it to find the set of filling angles for the range of curvatures, we obtain the *curves of constant separation.* These curves are shown in Fig. 18. The separation is presented in the dimensionless form as $s = 1.0 + h/R$.

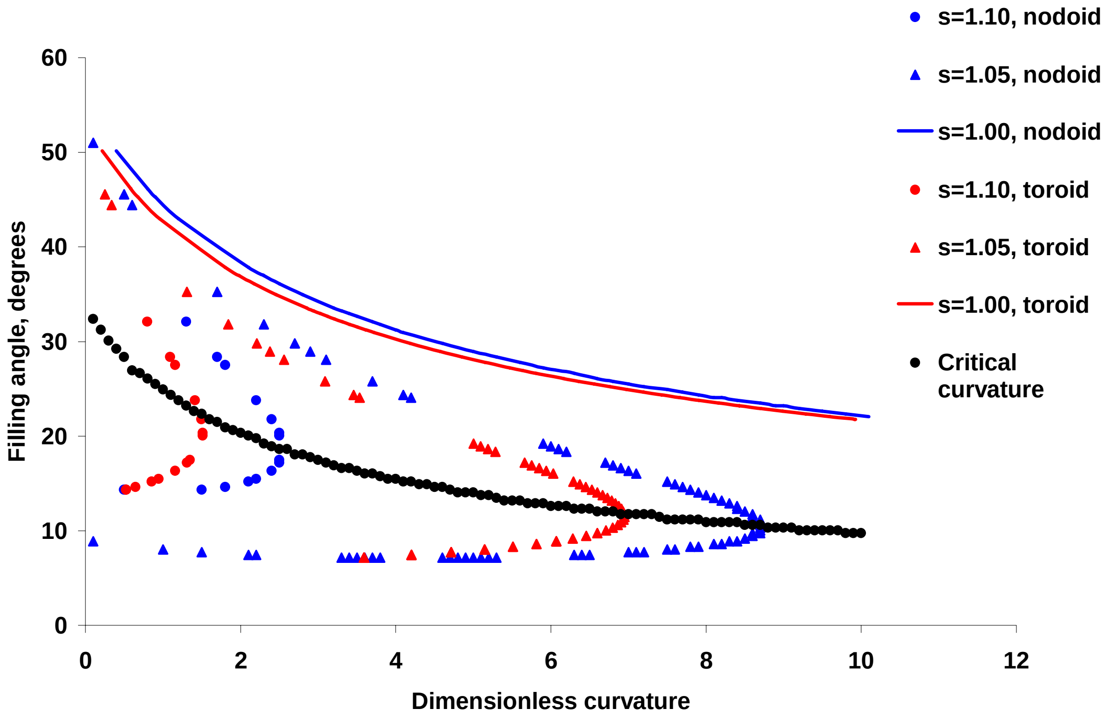

Fig. 18 Curves of constant separation. Solutions for true shape of nodoid and toroidal approximation are shown.

In Fig. 18 one can see that for each curve, corresponding to the given separation s (except for the case of $s = 1.0$, corresponding to grains in contact) there exist two solutions: to each value of dimensionless curvature C correspond two values of filling angle φ. The major problem is to find the criterion for the stability of these solutions and separate stable solutions from unstable ones. This problem received a lot of attention in the literature, but the stability criterion has not been resolved yet. Some authors [32, 77, 86] considered related problem of stability of the liquid bridge having a fixed *volume* and suggested semi-empirical criteria based on experimental and numerical support. The problem of our interest (the geometry of a liquid bridge having specified values of curvature and separation), however, differs from the one considered in the literature and seems even more complicated. No theoretical work or experimental evidences have been gathered for this problem. We suggest that the solution that corresponds to smaller value of filling angle (lower branch of the curves in Fig. 18) is mechanically unstable. We prefer this solution because of several reasons; one of them is that there is a continuity in the solution as we increase the separation from *1.0* (only one solution exists) by some infinitesimal value). More work has to be done to verify the stability of solutions rigorously.

Fig. 18 suggests that to separate mechanically stable solutions from unstable ones, we need to find the value of *critical curvature* for each separation *s.* This critical curvature can be defined as the curvature at which two solutions converge and only one solution exists (Fig. 18). A liquid bridge can exist only at curvatures smaller than critical value; if the curvature is greater than the critical one the liquid bridge does not exist. Mechanically unstable liquid bridges correspond to the points below critical curvature curve in Fig. 18, as long as stable configurations lie above this curve.

In Fig. 18 the curves for the toroidal approximation are presented also. The error associated with this approximation is very small for the curve with $s=1.0$ (spheres in contact) but increases with an increase in s and is larger for the values of curvatures near the critical.

If we now fix the value of the curvature C in Eq. (17) and integrate it to find the set of separations h for the range of filling angles, we obtain *curves of constant curvature*. These curves are shown in Fig .19.

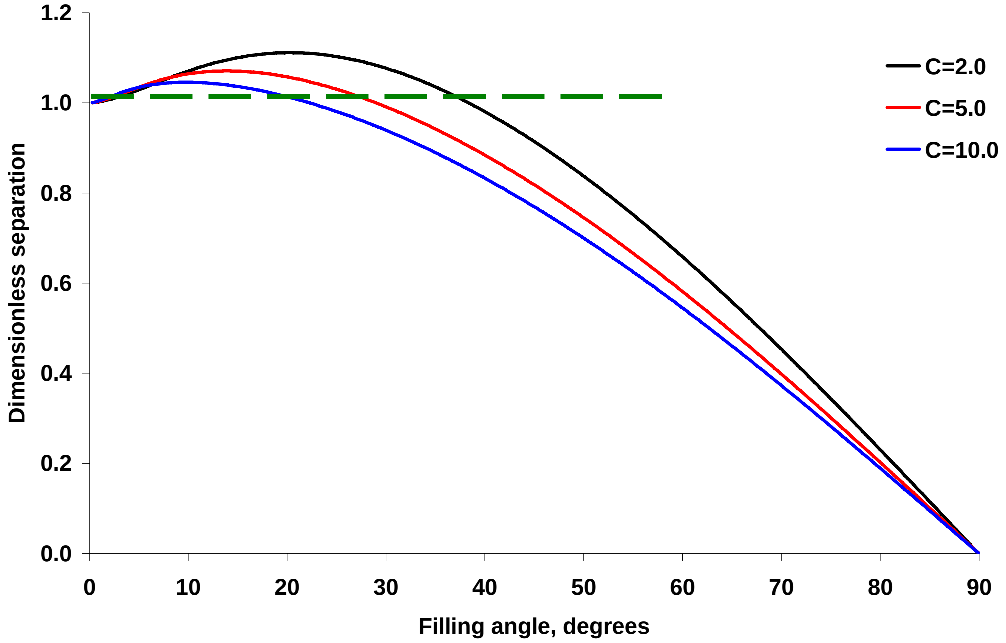

Fig. 19 Curves of constant curvature. The dotted green line represents the existence of two different solutions for the filling angle for the fixed value of separation.

Results presented in Fig. 19 show that for the same value of separation s (if it is greater than *1.0*) two different values of filling angle can exist. Moreover, with the decrease of filling angle φ from *0* to $\pi/2$ the separation increases at the beginning from *1.0* (grains in contact) to some maximal value and then decreases monotonically to zero. (Case when $s<1.0$ means that two spheres penetrate into each other, nevertheless the solution for the liquid bridge still exists. Maximal possible separation is going to *1.0* as curvature is approaching infinity, which could be expected in advance. The results for $s<1.0$ represent model consolidated porous media: the grains overlap as a result of isopachous cementation process (see Figs. 5 and 6)). According to the empirical stability criterion that we have chosen for the curves of constant separation (Fig. 18) we distinguish between stable (separation decreases with the increase in filling angle) and unstable (separation increases with the increase of filling angle) solutions for the curves of constant curvature in Fig. 19. This also illustrates the existence of *critical separation* for the given value of curvature, namely, the liquid bridge of fixed curvature can exist only at separations less than this critical value (experimentally it means that if we place the pendular ring of fixed curvature between two spherical grains in contact with each other and start to move them apart, the liquid bridge will break and disappear when the distance between grains will reach its critical value). This provides additional support for our stability criterion. Let us consider the following imaginary experiment: we fix some value of curvature and place liquid bridge between two accreted spheres (separation *s* is less than *1.0*). In this case only one solution for the shape of the liquid bridge exists (Fig. 19). If we now start to move the spheres apart from each other (we can say that their outer shells dissolve, for example), the filling angle of the bridge decreases as the separation increases (Fig. 19). When separation reaches the value of *1.0* (spheres just touch each other) plus some infinitesimal increment, there are two solutions for the filling angle, one of which (and we consider it to be stable) is continuous with the whole previous process and another one (which we consider unstable) goes to zero (Fig. 19), which means that the liquid bridge essentially ceases to exist at this point. The latter effect may be considered as non-physical. This is illustrated in Fig. 19 by dotted green line, which corresponds to the constant separation equal to the value *1.0* plus some infinitesimal increment. This line intersects the curves of constant curvature at two points – one point corresponds to some finite filling angle (stable) and another one goes to zero (unstable).

Thus, using the above definitions of critical curvatures and separations, we can find the dependence between their values. The results are shown in Fig. 20 together with the critical curve of toroidal approximation.

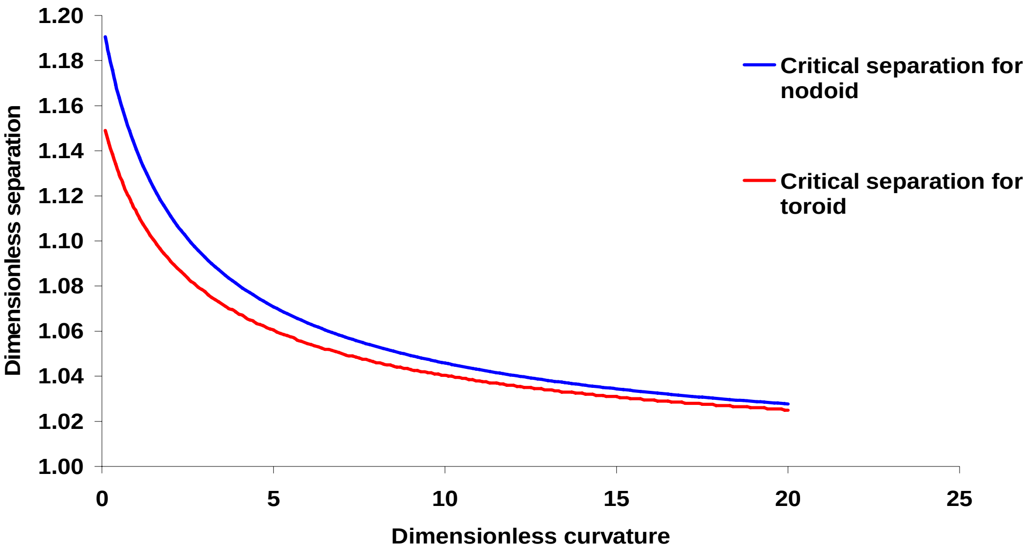

Fig. 20 Critical separation as a function of curvature.

The curves in Fig. 20 show that toroidal approximation underestimates the value of critical separation for the given curvature and also the value of the critical curvature for the given separation. It means that the nodoid will still exist at the values of curvatures and separations, where the toroid breaks and ceases to exist.

Further, it is necessary to calculate surface area and volume of a liquid bridge for different separations and curvatures and compare them with the values of toroidal shape. Area and volume of the nodoid were computed by numerical integration of appropriate integrals of the curve *f (x),* obtained from the solution of (17), assuming the nodoid as a body of revolution of this curve:

$$S = 2\pi \int_{X_D}^{X_{D'}} f \sqrt{1 + (f')^2}\, dx, \quad V = \pi \int_{X_D}^{X_{D'}} f^2 dx. \tag{20}$$

Numerical integration is employed using trapezoidal rule. The values of area and volume for toroid are calculated analytically [40, 72, 96, 118]. The obtained results for surface areas are shown in Fig. 21 and for volumes in Fig. 22. In these figures we also observe two different values of surface area or volume of liquid bridge for the given separation, which tells us about two different solutions, one of which (with the increase in separation from *1.0* to the critical value and the corresponding increase in surface area or volume – the lower branch of the curves) is mechanically unstable. It is interesting that the error in volume, associated with toroidal approximation, is not large and reaches its maximal value of about 10% near the critical point. The error in surface area achieves the maximum of about 50% at the same point. Also, the error in volume decreases as spheres begin to overlap, but the error in surface area starts to increase in this case and for the small *s* increases dramatically. This tells us that for the problems, where the calculation of surface areas is needed (for instance, in modeling of transport processes in porous media), toroidal approximation must be avoided and the integration of exact equation (17) must be used instead to obtain surface areas of liquid bridges.

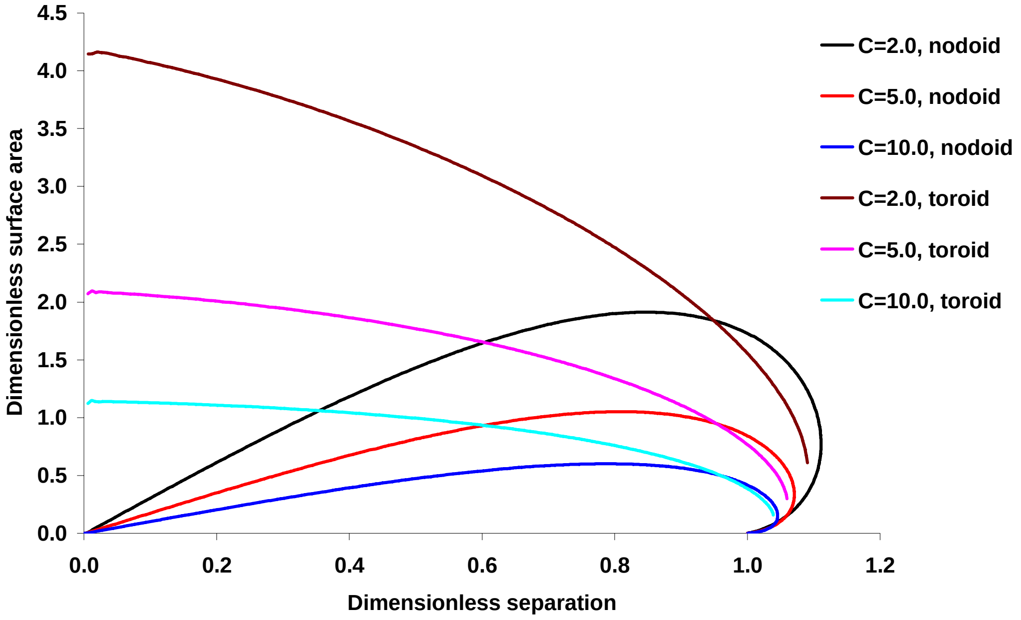

Fig. 21 Surface area of the liquid bridge for the true shape of nodoid and toroidal approximation.

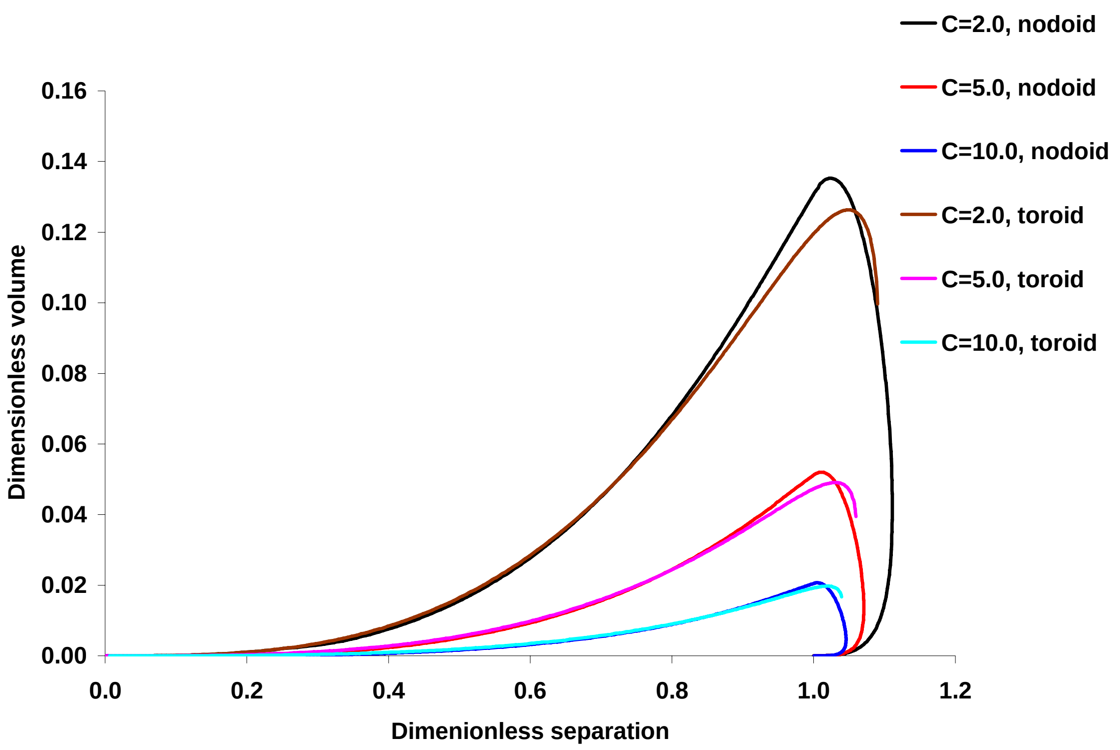

Fig. 22 Volume of the liquid bridge for both the true shape of nodoid and toroidal approximation.

2.2.2 Coalescence of Pendular Rings

To this point we have considered the liquid bridge in isolation. In dense packing of equal spheres the average sphere has approximately eight contacts that will support liquid bridges [9]. The presence of multiple rings on a single sphere raises the problem of their stability when they come into contact with each other. This will lead to their *coalescence* as the volume of the rings increases during imbibition. The effect was thoroughly analyzed by Haines [56] and is often called *snap-off* of NW phase in pore throats, because it leads to full closure of pore throats (bonds of the network – faces of tetrahedral cells, Fig. 3) with the W phase. The stages of coalescence of pendular rings are shown in

Figs. 23 and 24.

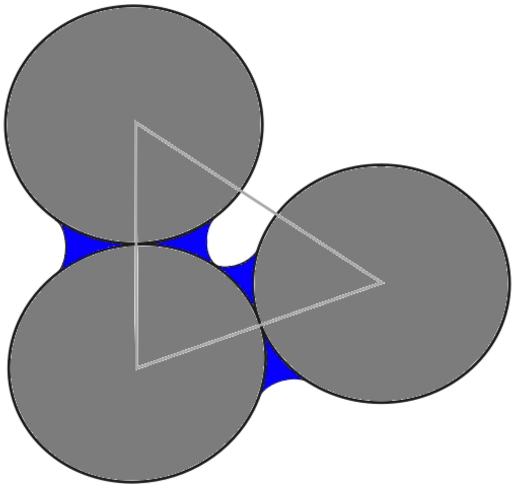

Fig. 23 Initial stage of coalescence. 2D slice of the pore throat by the plane that contains grain centers. The pore throat is the void area within the face of a Delaunay tetrahedron, shown by grey triangle. Two pendular rings just touch each other. W phase is shown by blue color; NW phase - by white in the middle of the pore throat.

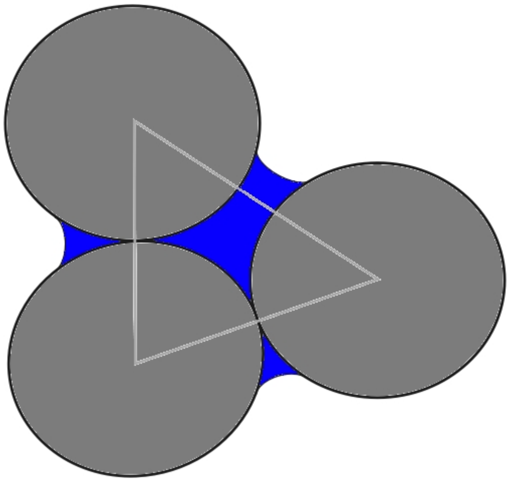

Fig. 24 Final stage of coalescence. Pore throat is full of W phase.

Consider a pore throat between three spherical grains. In a random packing, the three spheres usually are not all in point contact, though at least one pair of spheres is almost always in contact. Point contacts and near-contacts will support pendular rings of W phase.

With decreasing curvature (and, thus, increasing W phase saturation) pendular rings grow and at some point they will just touch each other (Fig. 23) This results in the instability of the interface and leads to the closure of the pore throat and complete filling of it by W phase [56], causing "snap-off" of NW phase. At this final stage of coalescence the pore throat is full of W phase, which is shown in Fig. 24, and the previously continuous volume of NW phase now exists in two distinct blobs (not shown) in the pores connected by the throat.

Using the exact calculations of ring geometry described above, it is straightforward to obtain the *coalescence curvature* for each pore throat in the packing, i.e. curvature at which neighboring pendular rings will coalesce. Not all throats in the model porous medium are formed by three spheres in contact. The mutual disposition of these three spheres is different for each pore throat, which gives different coalescence curvatures for different throats. These coalescence curvatures have *a priori* character, that is, they are obtained *independent* of the actual imbibition and thus, represent the properties of the pore throats only. Further, it is assumed in these calculations, that each ring is formed at the very moment when the current curvature reaches a value smaller than the critical value for the given ring. This idealized assumption is obviously not true during imbibition, since there may not be enough volume of W phase nearby to form a ring even if the current curvature is smaller than the critical one.

The distribution of such dimensionless coalescence curvatures for the case of the value of contact angle = 0 degrees is shown in Fig. 25. The case with three grains in actual contact with each other provides the pore throat with the highest possible coalescence curvature, which dimensionless value for the case of the value of contact angle = 0 degrees is about 4.5. Not all throats in the model porous medium are formed by three spheres in contact; most in fact have gaps between at least one pair of spheres. The range of relative locations of pore-throat-defining spheres accounts for the distribution in Fig. 25.

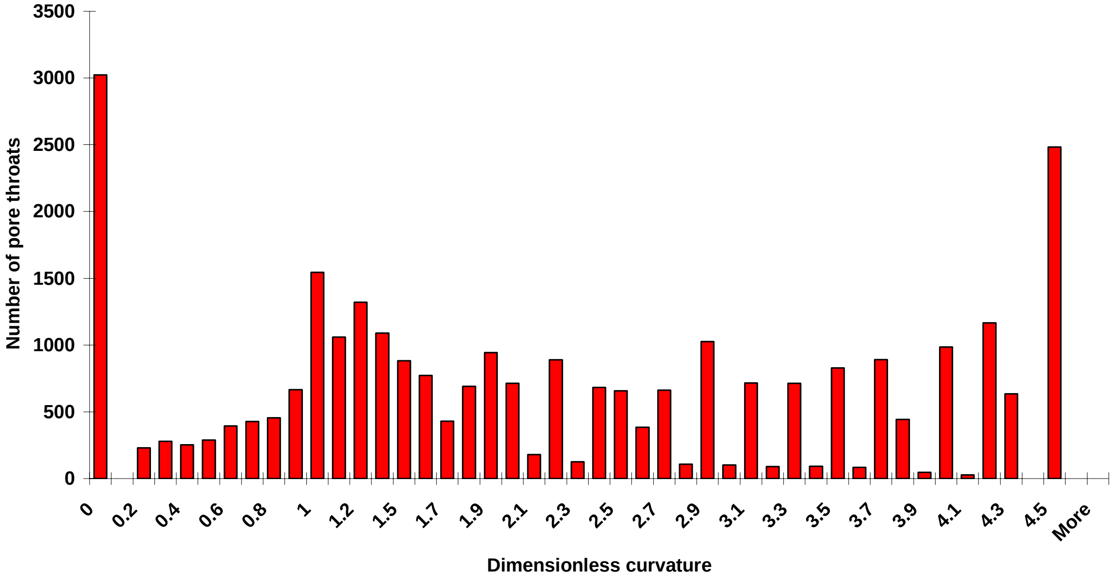

Fig. 25 Distribution of the *a priori* dimensionless coalescence curvatures for the pore throats in the Finney packing for zero contact angle. Maximal possible coalescence curvature of about 4.5 corresponds to the case of three grains in actual contact with each other.

Since coalescence of pendular rings leads to the closure of pore throats to NW phase, it diminishes NW phase connectivity and so not only increases W phase saturation, but also increases the likelihood of entrapment of NW phase. This qualitative argument has led to the conventional wisdom that these snap-offs are one of the key features of the imbibition process and strongly affect the value of residual NW phase saturation [2, 69, 80]. But the results of simulations presented below (see section 3.3.2) show that the influence of snap-off in a bead pack is negligible. This is readily explained by the lesser values of coalescence curvatures in comparison with the curvatures, at which main part of imbibition events happens. This means that by the time the capillary pressure (current curvature) has been reduced enough to initiate coalescence, much of the packing has already been imbibed. These results will be explained below in more detail.

2.2.3 Menisci between Phases

When W phase penetrates into the packing, it completely fills some of the pores. Thus, in the throats, which connect pores filled with the W phase with ones filled with the NW phase, the interface between phases appears in the form of *meniscus* (Figs. 10, 11, 26 and 27). The equilibrium shape of the meniscus is defined by the condition that its surface must have constant curvature (equal to currently applied value) at each point. The boundary conditions are specified by the positions of spherical grains and physical constraints (e.g. wettability condition). Unfortunately, the geometry of the medium itself is very complicated, so “mathematics of calculating displacement curvatures in sphere packings is close to intractable" (Mason and Morrow, [88]). One possible way to overcome this difficulty is to consider 2D geometry instead of 3D or search for the equilibrium shape of the meniscus between cylindrical rods instead of spherical grains. Attempts in this direction were made by Mayer and Stowe [92], Princen [113], Mason *et al* [90] etc.

To overcome this difficulty, we propose to use *locally spherical approximation* for the shape of meniscus. In Figs. 26 and 27, W phase occupies the pore space below the meniscus. The meniscus extends into the volume between each pair of grains and, in fact, in the immediate vicinity of the grain contacts the shape of the meniscus resembles a liquid bridge. Far from the contacts in the vicinity of center of the pore throat, we assume that the meniscus has *locally spherical shape*. It means that the meniscus is assumed to be a segment of a sphere (spherical cap) whose radius corresponds to the current curvature C of the interface (Figs. 26 and 27):

$$R_{men} = 2 / C. \tag{21}$$

The actual meniscus shape will be a hybrid of the spherical cap and the pendular ring. The approximation of Eq. (21) avoids the difficulty of computing the true shape; it is reasonable except at small curvatures (approaching residual NW saturation) when it leads to overlap of pairs of menisci in some pores.

The calculations of the geometry of such locally spherical meniscus are as follows. First, we define point N (Figs. 26 and 28), which lies in the plane, defined by the centers of three grains (points A, B and C in Fig. 28), which form the given pore throat. This point N is defined as the point, equidistant from the centers of these three grains (Fig. 28). Then, the center of the meniscus' sphere (point O in Figs. 26 and 27) is assumed to lie on the line, which contains point N and is perpendicular to the plane {ABC}, introduced above.

Next, the geometry of meniscus is calculated as follows. Knowing the position of line ON and the radius of the meniscus' sphere, (Eq. (21)), we can find the coordinates of the point O from the condition that the meniscus' sphere just touches three spherical gains (points K, L and M, where meniscus just touches the grains, are shown in Figs. 26 and 27). Thus, the meniscus has a dynamic behavior, that is, its shape and location change with the change in curvature.

In Fig. 29 two-dimensional slice by the plane {AON} is shown. Here OK = OF = R_{men} – radius of meniscus' sphere, AK = R_{grain} – grain radius, θ – contact angle. Let's denote also d = ON and L = AO. From the triangle AKO we have:

$$L = \left(R_{grain}^2 + R_{men}^2 + 2R_{grain}R_{men}\cos\theta\right)^{1/2}, \qquad (22)$$

and

$$d = \left(L^2 - r_{pl}^2\right)^{1/2}, \qquad (23)$$

where r_{pl} = AN = BN = CN (Fig. 28). If previous calculations yield that $r_{pl} > L$, we obtain the condition, under which the meniscus will "fall" through the pore throat, formed by spheres with the centers at A, B and C, and, thus, cannot exist. In this case we set the volume and surface area of the meniscus and the angle ψ of the meniscus' rise (Fig. 29) all equal to zero.

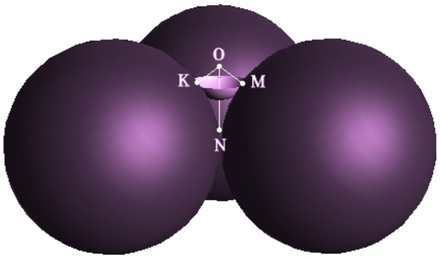

Fig. 26 Pore throat, formed by three grains (purple color), containing meniscus (light spherical cap in the middle). Meniscus has locally spherical shape. N is the point, equidistant from the grain centers and lying in the same plane as those centers. Vector ON is perpendicular to this plane. Point O is the center of the sphere, which defines meniscus.

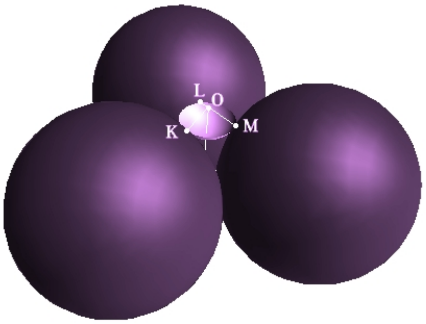

Fig. 27 Another point of view to the meniscus, shown in Fig 26. Meniscus touches spherical grains at points K, L and M**.**

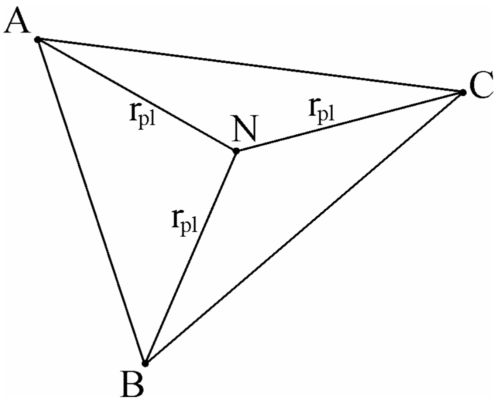

Fig. 28 Plane, formed by the grain centers A, B and C. Point N lies in this plane and is equidistant from grain centers: AN=BN=CN= $r_{pl.}$

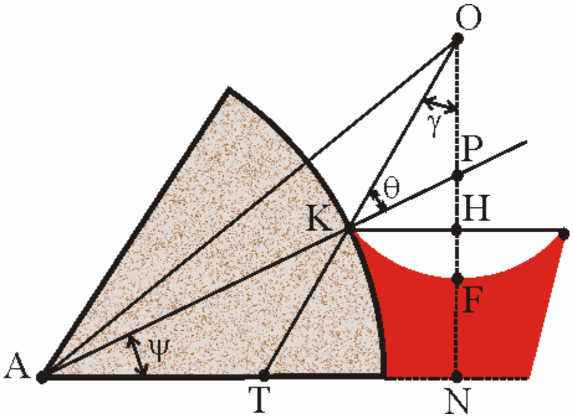

Fig. 29 Geometry of meniscus (shown by red). A – center of the grain; O – center of the meniscus' sphere. OK = OF = R_{men} – radius of meniscus' sphere (Eq. (21)). θ – contact angle (angle between normal vectors to the surfaces of the grain and the meniscus). ψ - angle of the meniscus' rise.

Next, coordinates of point O (center of meniscus' sphere) are found from the condition that the vector ON is perpendicular to the plane {ABC}. This condition gives two sets of the coordinates for the point O; we choose that which yields smaller distance to the center of the fourth grain of the given tetrahedral pore (not shown in Figs. 26 and 27).

Further, simple geometrical computations (Fig. 29) yield following results for the meniscus' angles:

$$\gamma = \arcsin\left(\frac{r_{pl}}{L}\right) - \arccos\left(\frac{L^2 + R_{men}^2 - R_{grain}^2}{2LR_{men}}\right), \tag{24}$$

$$\psi = \frac{\pi}{2} - \gamma - \theta. \tag{25}$$

Next, from the triangles OKH and OTN, we have

$$h = R_{grain}(1 - \cos\gamma), \tag{26}$$

where h = HF is the height of the meniscus' spherical cap. The coordinates of point K on the grain surface are found from the conditions, that (1) vector AT is collinear to vector AN (which yields coordinates of point T), and (2) vector OK is collinear to vector OT.

Similar calculations provide the coordinates of points L and M on the surfaces of two other grains (Figs. 26 and 27).

The volume of the meniscus is computed then as follows:

$$V_{men} = V_{PABC}^{tetr} - V_{ABCP}^{SA} - V_{BACP}^{SA} - V_{CABP}^{SA} - V_{PKLM}^{\sec tor}, \tag{27}$$

where V_{PABC}^{tetr} - volume of the tetrahedron with vertices P, A, B and C; $V_{ABCP}^{SA}, V_{BACP}^{SA}, V_{CABP}^{SA}$ - volumes of the part of the grains, comprised within the solid angles with vertices at corresponding grain centers A, B and C, and edges formed by the segments connecting these vertices with three other points (B, C and P for the solid angle with vertex at grain center A, etc); $V_{PKLM}^{\sec tor}$ - volume of the spherical sector, formed by the point P and points K, L and M on the surface of the meniscus sphere (Figs. 26 and 27). It is computed as follows:

$$V_{PKLM}^{\sec tor} = V_{OKLM}^{SA} - (V_{OKLM}^{tertr} - V_{PKLM}^{tetr}), \tag{28}$$

where V_{OKLM}^{SA} - volume of the part of the meniscus' sphere, comprised within the solid angle with vertex at point O and edges OK, OL and OM; $V_{OKLM}^{tertr}, V_{PKLM}^{tetr}$ - volumes of tetrahedra OKLM and PKLM respectively.

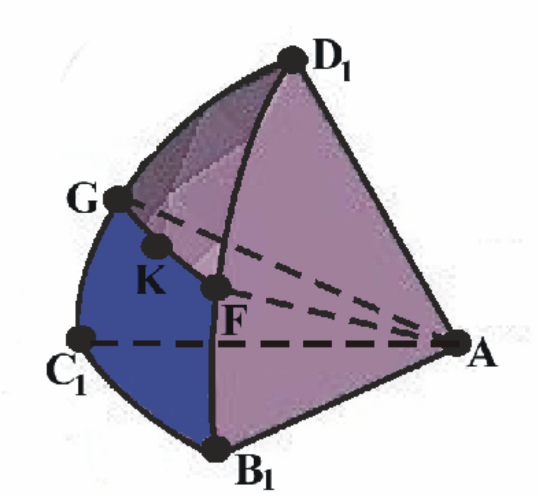

Fig. 30 Area of contact between the meniscus and surface of the grain (shown by blue color). A – center of the grain; B_1, C_1, and D_1 – points on the grain surface, which lie on the corresponding edges of the tetrahedral cell AB, AC and AD (Fig. 3). K – point of contact between meniscus' sphere and grain (Figs. 26 – 27). Plane {GKF} is parallel to the plane {AB_1C_1}.

Similar geometric considerations are applied to find the surface area of the meniscus and the area of contact between meniscus and grain surfaces, which is essential if the interfacial areas are the objects of interest (Fig. 30).

Surface area of the meniscus is computed as an area of a sector OKLM on the surface of meniscus' sphere (the surface area of the spherical cap, shown on Figs. 26 and 27).

The area of contact between meniscus and grain surface is computed as follows (Fig. 30). First, we find the plane, which is parallel to the plane {ABC} and contains point K of contact between the grain and the meniscus (Figs. 26 – 30). Next, we compute the coordinates of points G and F, which lie on the intersection of this new meniscus' plane with the planes {ACD} and {ABD} correspondingly, with the condition that these points lie on the surface of the grain with the center in point A as well. Further, we compute the surface of the grain, comprised within the pore, as the surface of the solid angle with vertex in A and edges AB_1, AC_1, and AD_1 (Fig. 30). The area of contact between meniscus and grain surface is then estimated as the difference between the surface area of this solid angle minus the surface area of the solid angle with vertex in A and edges AF, AG and AD_1.

2.3 Pore-Level Physical Events

2.3.1 Melrose Criterion for the Imbibition of a Pore

The most important step in the simulation of imbibition is to define the criterion for the imbibition of a single pore. As was pointed out above (section 2.1.3), the use of critical curvatures prescribed in advance for every pore in the packing does not reflect actual physical processes, which take place in the porous medium. For example, this approach does not account for the many different routes, by which actual pores are imbibed. A dynamic approach that considers these pore level processes directly is needed, and for that purpose we use the *Melrose criterion* [95]. This criterion is applied as follows. In the equilibrium configuration of the phases in the packing, corresponding to currently applied value of curvature, we know the geometry and location of every pendular ring and meniscus in the packing; this defines the configuration of W phase within every pore. Let's assume for simplicity that for some current curvature, a given pore has the meniscus in one of its pore throats and also has one pendular ring at a grain contact, which is not associated with this throat. This configuration is shown in Fig. 31. (Note that each pore throat (face of the tetrahedral pore in Fig. 3) has three edges, each of which corresponds to the grain contact. The presence of the meniscus at this face (throat) leads to the formation of pendular rings at each of these three edges (if such rings do not exist already and the current curvature is below the critical value for the separation of the grain contact). In this sense, these three edges are associated with the pore throat. Because the pore is a tetrahedral cell, it follows that each pore throat of the tetrahedral cell (Fig. 3) also has three edges that are not associated with it but are contained in the same cell. For example, in Fig. 3, for the throat, formed by the grains with centers in points A, B and C, three grain contacts, associated with this throat are AB, AC and BC; three grain contacts, not associated with this throat are AD, BD and CD. A pendular ring is also possible at each non-associated grain contact.

It is obvious, that the only interesting effect within the pore can happen when the meniscus at the pore throat comes in contact with one of the rings existing at the grain contact not associated with this throat. Further we consider only these types of interface contacts as leading to the imbibition event according to Melrose criterion.

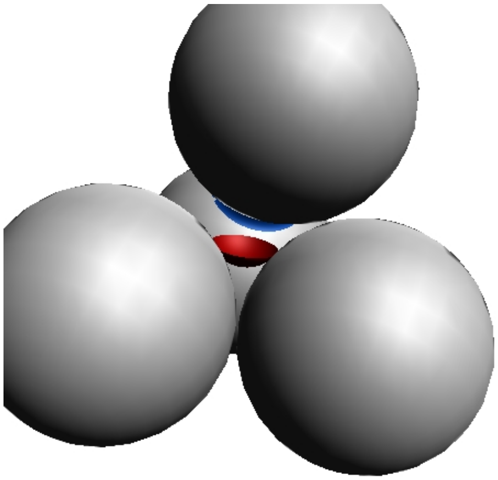

Fig. 31 Configuration of phases in the pore prior to the imbibition event. Meniscus at the pore throat, formed by three lower grains and pendular ring, independent of this meniscus, are shown.

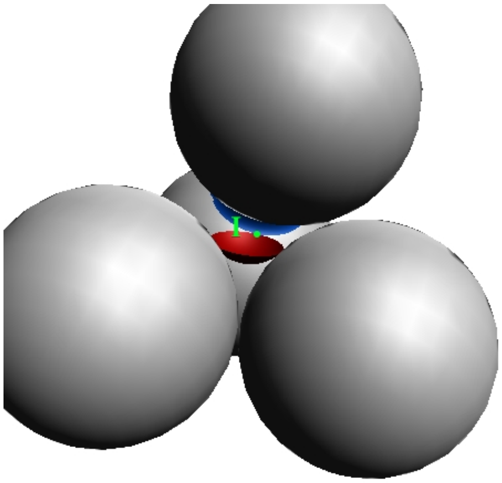

Fig. 32 At some value of current curvature ring and meniscus come into contact at point I (green color) on the surface of the grain. This results in the instability of the interface and leads to the imbibition event – W phase completely fills the pore.

Let us consider what happens if the curvature is decreased further. The dependence of the geometry of both meniscus and pendular ring on the current curvature causes their swelling as the curvature of the interface increases – both pendular ring and meniscus grow and advance into the pore space. Their new locations follow from the calculations described above.

Further decreases in curvature cause further growth and advance, until at some value of curvature the meniscus and ring touch at some point I (Fig. 32) on the surface of the corresponding grain. An infinitesimal decrease in curvature leads to the mechanical instability of the interface (the mathematical basis for this statement is established below, section 2.4), which, in turn, results in the imbibition event: the ring and meniscus merge to form a single surface, and the NW phase spontaneously withdraws from the pore, leaving the pore completely filled with the W phase. This situation is illustrated also in Figs. 33 and 34, which show the configuration prior to the imbibition event (Fig. 33) and unstable configuration after the meniscus and ring came in contact (Fig. 34).

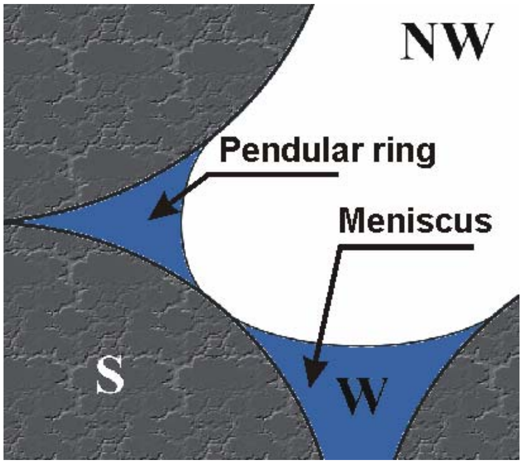

Fig. 33 Configuration, prior to the imbibition event. 2D slice of the pore space through the center of the pore. Solid grains are shown by the textured surface; W phase – by blue color and NW phase – by white. Meniscus and pendular ring are distinct.

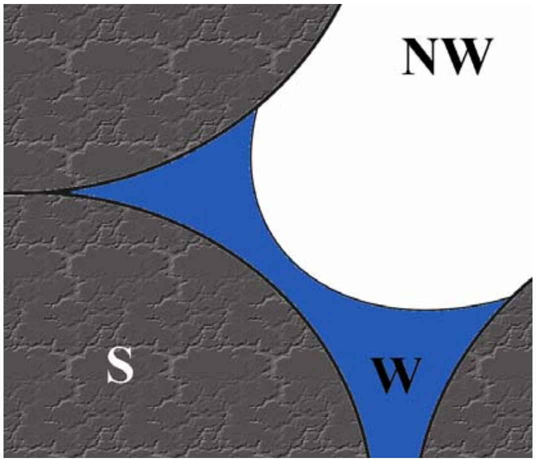

Fig. 34 Unstable configuration, which leads to the imbibition event. Pendular ring and meniscus are now in contact and form one whole interface. The interface will retreat from the pore until the pore walls can accommodate the global curvature.

The extension of this idea to the other possible configurations of menisci and liquid bridges in a pore is straightforward. At a given curvature and for a given pore, we catalog all the menisci and rings in that pore. For each meniscus, we test for contact with independent rings (i.e. rings held at grain contacts not associated with the pore throat containing the meniscus.). If any of the tests are positive, then the Melrose criterion is satisfied and the pore is then allowed to imbibe.

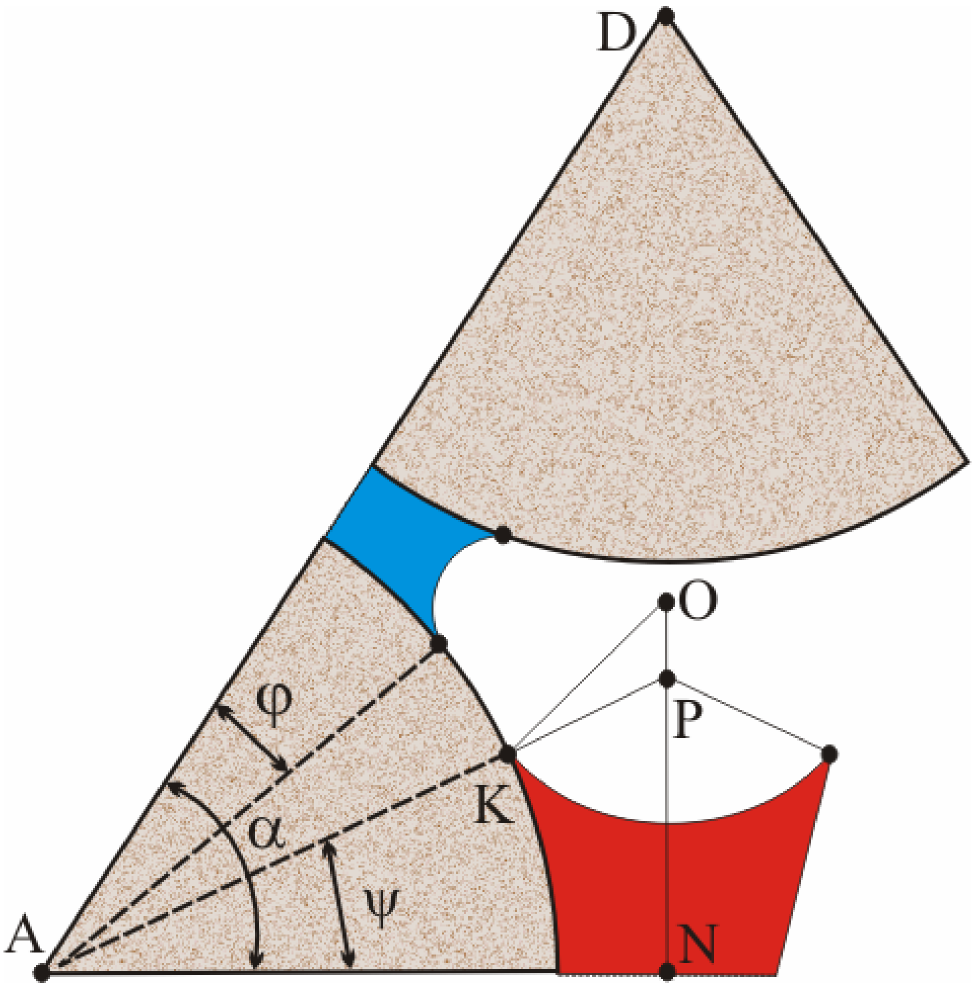

Fig. 35 Numerical implementation of Melrose criterion. Plane that dissects the pore through the grain centers A, D and center of meniscus sphere O is shown. Point P lies on the intersection of the vector ON and the normal vector to the grain surface at point K (cf. Fig. 29). Imbibition of the pore occurs if $\varphi + \psi > \alpha$.

Numerical implementation of the Melrose criterion is as follows. First, we compute the filling angle φ of the pendular ring (Figs. 10, 11 and 17) and the angle ψ of the meniscus' rise (Fig. 29, Eq. (25)). Further, we calculate angle α between the grain contact (edge) (AD in Fig. 35) containing pendular ring and its projection on the plane {ABC} (Figs. 26 – 29), defined by the grain centers, which form the pore throat with the meniscus. (The edge AD will not necessarily lie in the plane defined by the vectors AN and ON, as shown in Fig. 35. In this case we assume that the angle ψ of the meniscus' rise is the same in the plane defined by the edge AD and the height of the tetrahedron dropped from the vertex D, as it is in the plane {AON}). We consider angle α to be obtuse if both angles at the corresponding faces of the tetrahedron (angles DAC and DAB in Fig.3) are obtuse; otherwise angle α is taken to be acute. Pendular ring and meniscus come into contact and touch each other, if

$$\varphi + \psi > \alpha. \tag{29}$$

This condition is checked every time the pore is considered as a candidate for imbibition.

2.3.2 Entrapment of NW phase

During imbibition, NW phase can be *trapped* inside the pore bodies, which results in the *residual NW phase saturation* at the end of the imbibition (at zero curvature of bulk W phase). The structure and magnitude of this residual saturation is very important, for example, in environmental studies, when it represents the residual contaminant saturation in soil or an aquifer. NW-phase can be trapped in one pore body or in several neighboring pore bodies (*trapped cluster of pores*) due to the loss of connectivity with the exit pores, i.e. with the pores connected to the NW phase reservoir. NW phase connectivity is updated after each successful imbibition event (snap-off or imbibition of a pore).

In Fig. 36 one possible way of entrapment of NW phase is represented. In this figure W phase is shown by purple color and NW phase by yellow. In configuration I the central and upper pores are not imbibed yet and contain NW phase. Suppose that the upper cell has an exit pore as a neighbor, so NW phase in configuration I is connected to the NW phase reservoir and thus is not trapped. Suppose further that the imbibition event, according to the Melrose criterion, occurs first in the upper pore (with the meniscus advancing from the pore containing W phase on the right). At the moment when this upper pore is imbibed, the central pore loses its connection to the NW phase reservoir and becomes trapped.

Thus, using the strategy for the entrapment, described above, we obtain residual NW phase distribution. The description of this distribution and comparison with the experiments is presented below (section 3.2.6).

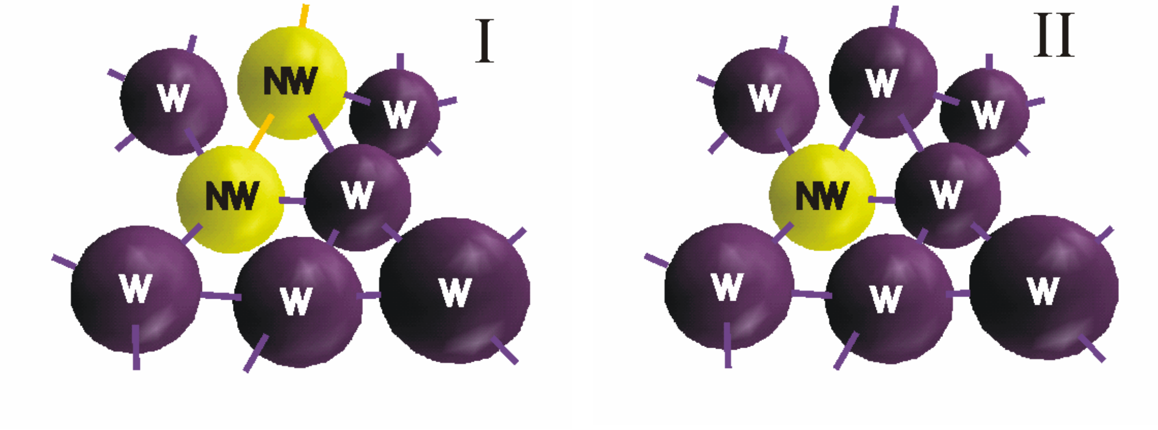

Fig. 36 One of possible ways of entrapment of NW phase. In configuration I, both pores containing NW phase are connected to NW phase reservoir (not shown). An imbibition event occurs in the upper pore containing NW phase before the central pore. Thus it imbibes first, in this case with the meniscus advancing from the pore, containing W phase, at the right. NW phase in the upper pore retreats into NW phase reservoir. Thus NW phase in the central pore becomes trapped, configuration II. This is the situation for most of the residual NW saturation, though many clusters of a several pores containing NW also get trapped.

2.4 Theoretical Investigation of the Stability of Menisci

2.4.1 The Wedge of Liquid between Two Cylindrical Rods

We have seen that the Melrose criterion relies on the idea that contact between two W-NW interfaces leads to instability. This idea is intuitively appealing, but it would be useful to place it on a more rigorous foundation. Unfortunately the problem of theoretical investigation of the pore-level events (instability and merger of menisci and pendular rings) in the packing of spherical particles is extremely complicated and close to intractable. Instead of trying to approach this problem directly, we consider first a simple case: the stability of two-dimensional liquid bridges, or the wedges between cylindrical rods (Fig. 37).

First we need to find the shape of such a wedge from the condition that the mean curvature of its surface is constant at every point. For simplicity in the following analysis we will limit ourselves to the case when the contact angle θ (cf. Fig. 17) of solid-liquid interface is equal to zero.

Let us consider (similar to the problem of the 3-dimensional pendular ring, Fig. 17) an immersion from a 2-dimensional domain to the 3-dimensional Euclidean space. Let *D* be a domain in the *(u,v)*-plane and ***X*** a C^{∞} map from *D* to the 3 –dimensional Euclidean space $\mathbf{R}^3$.

We will seek the equations of the mapping in the form:

$$\begin{cases} x = u, \\ y = f(u), \\ z = v. \end{cases} \tag{30}$$

Where *(x, y, z)* – coordinates in 3-dimensional Euclidean space (Fig. 37); *(u, v)* – coordinates in the domain *D:* $0<u<\gamma$; $0<v<L$ (where *L* is height of the wedge – Fig. 37);

$y=f(x)$ is the equation of the curve in (x, y) plane, which bounds the wedge.

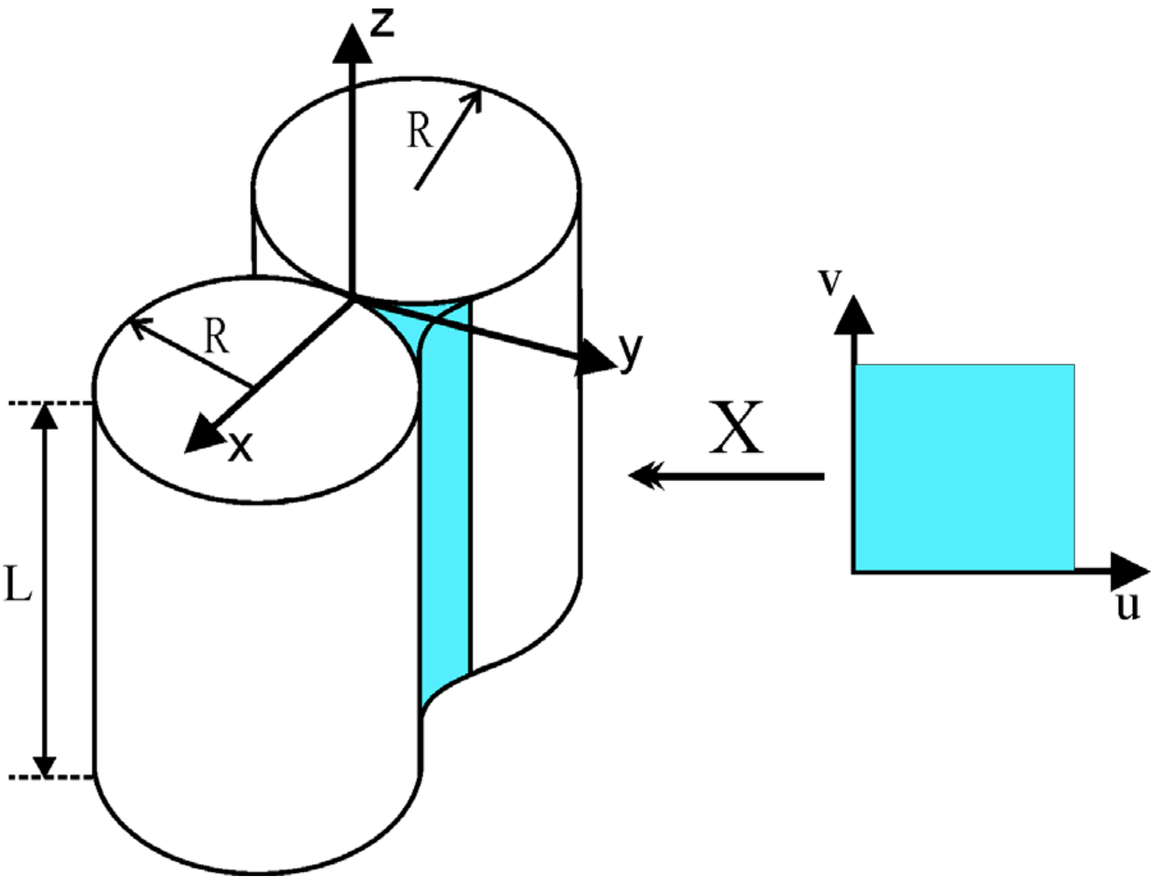

Fig. 37 The wedge of liquid between two solid cylinders.

Differentiating (30), we obtain:

$$X_u(u,v) = (1, f', 0);$$
$$X_v(u,v) = (0,0,1). \tag{31}$$

And for the second derivatives:

$$
\begin{aligned}
X_{uu}(u,v) &= (0, f'', 0); \\
X_{uv}(u,v) &= (0,0,0); \\
X_{vv}(u,v) &= (0,0,0).
\end{aligned}
\tag{32}
$$

The first fundamental form of the wedge is:

$$I_X = Edu^2 + 2Fdudv + Gdv^2,$$

where

$$
\begin{aligned}
E &= \langle X_u, X_u \rangle = 1 + (f')^2; \\
F &= \langle X_u, X_v \rangle = 0; \\
G &= \langle X_v, X_v \rangle = 1.
\end{aligned}
\tag{33}
$$

Next, we can compute the outward unit normal vector to the surface of the wedge:

$$\vec{n} = -\frac{X_u \wedge X_v}{|X_u \wedge X_v|}.$$

Since

$$X_u \wedge X_v = (f', -1, 0),$$

and

$$|X_u \wedge X_v| = \sqrt{1 + (f')^2},$$

we have

$$\vec{n} = \left(-\frac{f'}{\sqrt{1+(f')^2}}, \frac{1}{\sqrt{1+(f')^2}}, 0 \right). \tag{34}$$

Then we can compute the second fundamental form of the wedge as:

$$\Pi_X = L du^2 + 2M du dv + N dv^2,$$

where

$$\begin{aligned} L &= \langle X_{uu}, \vec{n} \rangle = \frac{f''}{\sqrt{1+(f')^2}}; \\ M &= \langle X_{uv}, \vec{n} \rangle = 0; \\ N &= \langle X_{vv}, \vec{n} \rangle = 0. \end{aligned} \tag{35}$$

Then, the curvature *C* (twice the mean curvature of the interface), is computed as:

$$C = \frac{GL + EN - 2FM}{EG - F^2} = \frac{\frac{f''}{\sqrt{1+(f')^2}}}{1+(f')^2} = \frac{f''}{\left(1+(f')^2\right)^{3/2}}. \tag{36}$$

Let's denote $f' = g$, then we can integrate (36) and obtain

$$\int \frac{dg}{\left(1+g^2\right)^{3/2}} = \int C dx = Cx + K, \tag{37}$$

where *K=const.* Let's make the substitution $g = \sinh \phi$, then from (37) we have

$$\int \frac{\cosh \phi d\phi}{\left(1+\sinh^2 \phi\right)^{3/2}} = \int \frac{d\phi}{\cosh^2 \phi} = \tanh \phi = \frac{g}{\sqrt{g^2+1}},$$

and we obtain

$$g(x) = \pm \frac{Cx+K}{\sqrt{1-(Cx+K)^2}}. \quad (38)$$

Since, from symmetry, $f'(0) = g(0) = 0$, from (38) we have $K = 0$, and

$$g(x) = \pm \frac{Cx}{\sqrt{1-(Cx)^2}}. \quad (39)$$

Let us denote $1/C \equiv r$, then we have

$$g(x) = \pm \frac{x}{\sqrt{r^2 - x^2}},$$

and

$$f(x) = \int g(x)dx = \int \frac{xdx}{\sqrt{r^2 - x^2}} = K_1 \pm \sqrt{r^2 - x^2},$$

which we can write as

$$\left(y - K_1\right)^2 + x^2 = r^2. \quad (40)$$

This means that the curve $y = f(x)$ is an arc of the circle with the center at $(0, K_1)$ and radius $r = {}^{1}\!/_{C}$. So the wedge of the liquid between two cylindrical rods in Fig. 37 has a cylindrical shape.

2.4.2 Stability of Two Merging Wedges

Since the wedge has a cylindrical shape, it is convenient now to work in cylindrical coordinates. We need to consider the problem of the stability of two liquid wedges when they just touch each other, which in our simplified geometry (essentially two-dimensional) is analogous to the problem of the merging of two pendular rings (coalescence, see above) and ring and meniscus (Melrose criterion, see section 2.3.1) in the case of the geometry of spherical grains. This problem is illustrated in Figs. 38 and 39.

Let’s consider now the system of three cylindrical rods of height L and two liquid wedges between them (Figs. 38 and 39). We start from the initial position, shown in Fig. 38, and move the top and right rods towards each other, keeping the center rod fixed, so that two wedges will just touch each other (Fig. 39). Our goal is to investigate the stability of the wedges when they are isolated (Fig. 38) and just touch each other (Fig. 39). Both these situations are similar, since an isolated wedge is the part of the cylinder (as was shown above), and two wedges that just touch each other form similar shape (the contact angle is zero, so two wedges in Fig. 39 form one continuous surface). What changes is the value of the angle (denoted γ in Fig. 39) that defines which part of the cylindrical surface we need to consider (for the whole cylinder this angle is equal to 2π).

There is the well known result [1] for the stability of the whole cylinder ($\gamma = 2\pi$), which tells that the cylinder is stable if its height is greater than the length of its circumference: $L \geq 2\pi r$. Our goal is to investigate the stability of cylindrical surface for the case $\gamma < 2\pi$.

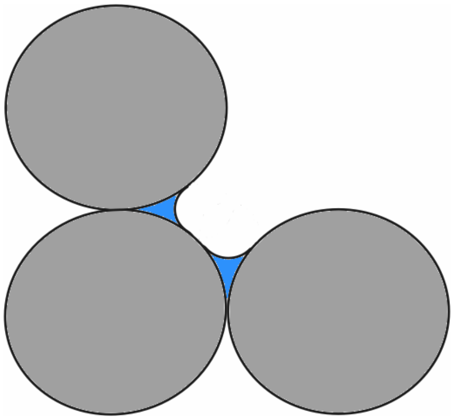

Fig. 38 The system of three solid cylindrical rods and two wedges of liquid; each wedge is identical to that shown in Fig. 37**.**

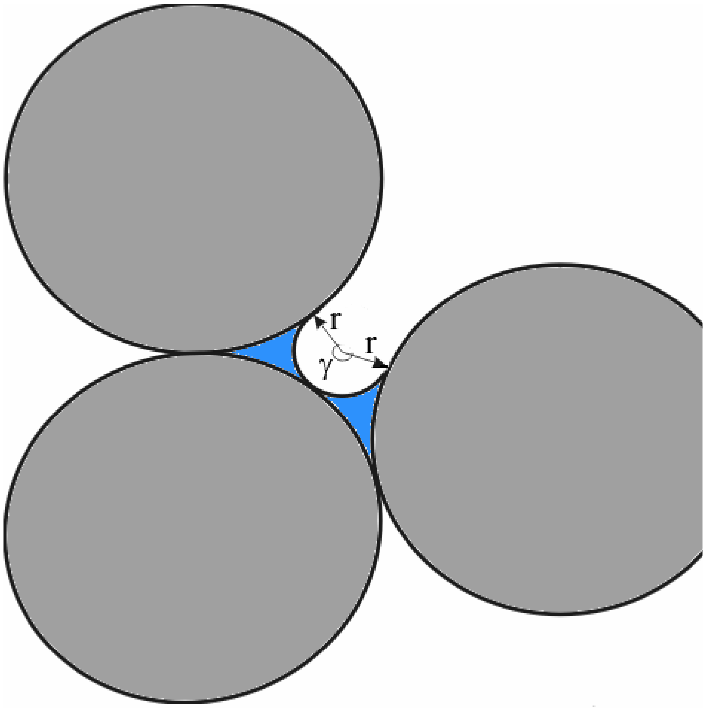

Fig. 39 The rods are brought together from the initial position shown in Fig. 38, so that the wedges just touch each other.

Similar to the analysis above, we will seek the mapping in the form:

$$\begin{cases} x = r\cos u, \\ y = r\sin u, \\ z = v. \end{cases} \tag{41}$$

Here *(x, y, z)* – coordinates in 3-dimensional Euclidean space (Fig. 37); *(u, v)* – coordinates in the domain *D: 0<u<γ; 0<v<L*.

Differentiating (41), we obtain:

$$\begin{aligned} X_u(u,v) &= (-r\sin u, r\cos u, 0); \\ X_v(u,v) &= (0,0,1). \end{aligned} \tag{42}$$

And for the second derivatives:

$$\begin{aligned} X_{uu}(u,v) &= (-r\cos u, -r\sin u, 0); \\ X_{uv}(u,v) &= (0,0,0); \\ X_{vv}(u,v) &= (0,0,0). \end{aligned} \tag{43}$$

The first fundamental form of the wedge is:

$$I_X = Edu^2 + 2Fdudv + Gdv^2,$$

where

$$\begin{aligned} E &= \langle X_u, X_u \rangle = r^2; \\ F &= \langle X_u, X_v \rangle = 0; \\ G &= \langle X_v, X_v \rangle = 1. \end{aligned} \tag{44}$$

Next, we can compute the inward unit normal vector to the surface of the wedge:

$$\vec{n} = \frac{X_u \wedge X_v}{|X_u \wedge X_v|}.$$

Since

$$X_u \wedge X_v = (r\cos u, r\sin u, 0),$$

and

$$|X_u \wedge X_v| = r,$$

we have

$$\vec{n} = (-\cos u, -\sin u, 0). \tag{45}$$

Then we can compute the second fundamental form of the wedge as:

$$\Pi_X = Ldu^2 + 2Mdudv + Ndv^2,$$

where

$$\begin{aligned} L &= \langle X_{uu}, \vec{n} \rangle = r; \\ M &= \langle X_{uv}, \vec{n} \rangle = 0; \\ N &= \langle X_{vv}, \vec{n} \rangle = 0. \end{aligned} \tag{46}$$

Then, the curvature C (twice the mean curvature of the interface), is computed as:

$$C = \frac{GL + EN - 2FM}{EG - F^2} = \frac{1}{r}. \tag{47}$$

Now we can apply the theorem for the stability of surfaces of constant mean curvature [74]:

> *For a constant mean curvature surface* $X : M \to R^3$, *a necessary and sufficient condition for X to be stable is that the inequality*
>
> $$\int_D \left(-\Delta\lambda - |B|^2 \lambda\right)\lambda dM \geq 0 \tag{48}$$

holds for any relatively compact domain D of M and any function λ in F_D.

Here F_D is a set of piecewise differentiable functions λ on D satisfying

$$\int_D \lambda dM = 0, \qquad \lambda|_{\partial D} = 0. \tag{49}$$

And $|B|^2$ is the square of the length of the second fundamental form of X:

$$|B|^2 = g^{ij} g^{kl} h_{ik} h_{jl}, \tag{50}$$

where

$$\begin{pmatrix} g_{11} & g_{12} \\ g_{21} & g_{22} \end{pmatrix} = \begin{pmatrix} E & F \\ F & G \end{pmatrix}; \qquad \begin{pmatrix} h_{11} & h_{12} \\ h_{21} & h_{22} \end{pmatrix} = \begin{pmatrix} L & M \\ M & N \end{pmatrix},$$

and (g^{ij}) is the inverse matrix of the matrix (g_{ij}).

For our problem,

$$\begin{pmatrix} g_{11} & g_{12} \\ g_{21} & g_{22} \end{pmatrix} = \begin{pmatrix} r^2 & 0 \\ 0 & 1 \end{pmatrix}; \quad \begin{pmatrix} g^{11} & g^{12} \\ g^{21} & g^{22} \end{pmatrix} = \begin{pmatrix} 1/r^2 & 0 \\ 0 & 1 \end{pmatrix}; \quad \begin{pmatrix} h_{11} & h_{12} \\ h_{21} & h_{22} \end{pmatrix} = \begin{pmatrix} r & 0 \\ 0 & 0 \end{pmatrix}, \tag{51}$$

and

$$|B|^2 = g^{ij} g^{kl} h_{ik} h_{jl} = \frac{1}{r^2}\frac{1}{r^2} r^2 = \frac{1}{r^2}. \tag{52}$$

Further, in cylindrical coordinates (with r = *const)* we have

$$\Delta\lambda = \frac{1}{r^2}\lambda_{uu} + \lambda_{vv}\,. \tag{53}$$

So, from the stability theorem and (52)-(53) it follows that we need to consider an eigenvalue problem for the operator $L\lambda$*:*

$$L\lambda = -\frac{1}{r^2}\lambda_{uu} - \lambda_{vv} - \frac{1}{r^2}\lambda = \mu\lambda. \tag{54}$$

The result of the stability theorem then implies that if the negative eigenvalues μ are possible then the surface is unstable.

We will apply the method of the separation of variables and will seek eigenfunctions in the form $\lambda = A(u)B(v)$. Then, the boundary condition on λ (49) results in:

$$\lambda\,|_{\partial D} = 0 \Rightarrow \begin{cases} A(0) = A(\gamma) = 0; \\ B(0) = B(L) = 0. \end{cases} \tag{55}$$

From (54) we obtain:

$$-\frac{1}{r^2}A''B - B'' - \frac{1}{r^2}AB - \mu AB = 0;$$

and further,

$$-\frac{A''}{A} = \frac{r^2 B''}{B} + 1 + \mu r^2 = const, \tag{56}$$

since the left-hand side depends only on u and right-hand side depends only on v.

Next, consider the resulting eigenvalue problem for $A(u)$:

$$-A''(u)=\xi A(u). \tag{57}$$

The general solution to this problem is

$$A(u)=C_1\sin\sqrt{\xi}u+C_2\cos\sqrt{\xi}u.$$

Taking into account boundary conditions (55): $A(0)=A(\gamma)=0$, we obtain finally:

$$\xi=\frac{\pi^2k^2}{\gamma^2};\qquad A(u)=\sin\frac{\pi k}{\gamma}u,\qquad k=1,2,... \tag{58}$$

Then, from (58) and (56) we obtain the eigenvalue problem for the function *B(v)*:

$$-B''=\eta B,\qquad \text{where}\quad \eta=\mu+\frac{1}{r^2}-\frac{\pi^2k^2}{\gamma^2}. \tag{59}$$

Taking into account boundary conditions (55): $B(0)=B(L)=0$, we obtain, similarly to *A(u)*:

$$\eta=\frac{\pi^2n^2}{L^2};\qquad B(v)=\sin\frac{\pi n}{L}v,\qquad n=1,2,... \tag{60}$$

So, for the eigenvalues of the initial problem (54) we have

$$\mu_{n,k}=\frac{\pi^2n^2}{L^2}+\frac{\pi^2k^2}{\gamma^2}-\frac{1}{r^2}. \tag{61}$$

Next, we need to check if negative eigenvalues $\mu_{n.k}$ in (61) are possible so that the integral condition on λ in (49) is satisfied.

The smallest eigenvalue in (61) is $\mu_{1,1}=\frac{\pi^2}{L^2}+\frac{\pi^2}{\gamma^2}-\frac{1}{r^2}$, the corresponding eigenfunction is $\lambda_{1,1}(u,v)=\sin\frac{\pi}{\gamma}u\cdot\sin\frac{\pi}{L}v$, but

$$\int_D \lambda_{1,1}dM=\int_u\int_v \sin\frac{\pi}{\gamma}u\cdot\sin\frac{\pi}{L}v\cdot\sqrt{EG-F^2}\,dudv=$$
$$=r\int_u \sin\frac{\pi}{\gamma}u\left(\frac{L}{\pi}\int_0^{\pi}\sin t dt\right)du=\frac{Lr}{\pi}\int_u \sin\frac{\pi}{\gamma}du\cdot\left(-\cos t\,|_o^{\pi}\right)>0.$$

The next smallest eigenvalue is $\mu_{2,1}=\frac{4\pi^2}{L^2}+\frac{\pi^2}{\gamma^2}-\frac{1}{r^2}$, the corresponding eigenfunction is $\lambda_{2,1}(u,v)=\sin\frac{\pi}{\gamma}u\cdot\sin\frac{2\pi}{L}v$, and

$$\int_D \lambda_{2,1}dM=\int_u\int_v \sin\frac{\pi}{\gamma}u\cdot\sin\frac{2\pi}{L}v\cdot\sqrt{EG-F^2}\,dudv=$$
$$=r\int_u \sin\frac{\pi}{\gamma}u\left(\frac{L}{2\pi}\int_0^{2\pi}\sin t dt\right)du=\frac{Lr}{2\pi}\int_u \sin\frac{\pi}{\gamma}du\cdot\left(-\cos t\,|_o^{2\pi}\right)=0.$$

So, $\mu_{2,1}$ is indeed the smallest eigenvalue of the problem (54), which satisfies the conditions (49).

Now, if we consider the limiting 2-dimensional case and set $L\rightarrow\propto$, we have as the condition on μ:

$$\mu=\frac{\pi^2}{\gamma^2}-\frac{1}{r^2}<0, \tag{62}$$

and so, we can write the condition for the instability of two-dimensional liquid wedge:

$$\gamma > \pi r, \qquad or \qquad \gamma > \frac{\pi}{C}, \tag{63}$$

where C – twice mean curvature of the surface, Eq. (47).

2.4.3 Interpretation of the Stability Analysis for the Wedges

Thus, the presented analysis allows interpreting pore-level events, such as coalescence of pendular rings and Melrose criterion for the imbibition of a single pore, in two-dimensional geometry in the following way. Suppose that two wedges in Fig. 38 have the same curvature C, which is small enough to provide their stability according to criterion (63). When we bring two rods together and make wedges touch each other, everything that influences their stability remains the same, except angle γ, since now they form one continuous body and this angle becomes twice larger than it has been for the isolated wedge. If now this new value 2γ is large enough to exceed the right-hand side of Eq. (63), the new surface becomes unstable and we have two-dimensional analogue of the coalescence of two pendular rings.

Now let us consider this simple geometrical problem to see if this indeed could be the case. Fig. 40 shows the situation when two wedges just touch each other; the angle of their continuous surface, corresponding to the Eq. (63), is equal to γ. We will consider the problem in the dimensionless form, that is, for the radii of the rods are all equal to 1, and the radius of the wedge r is expressed then in the units of the rods radii.

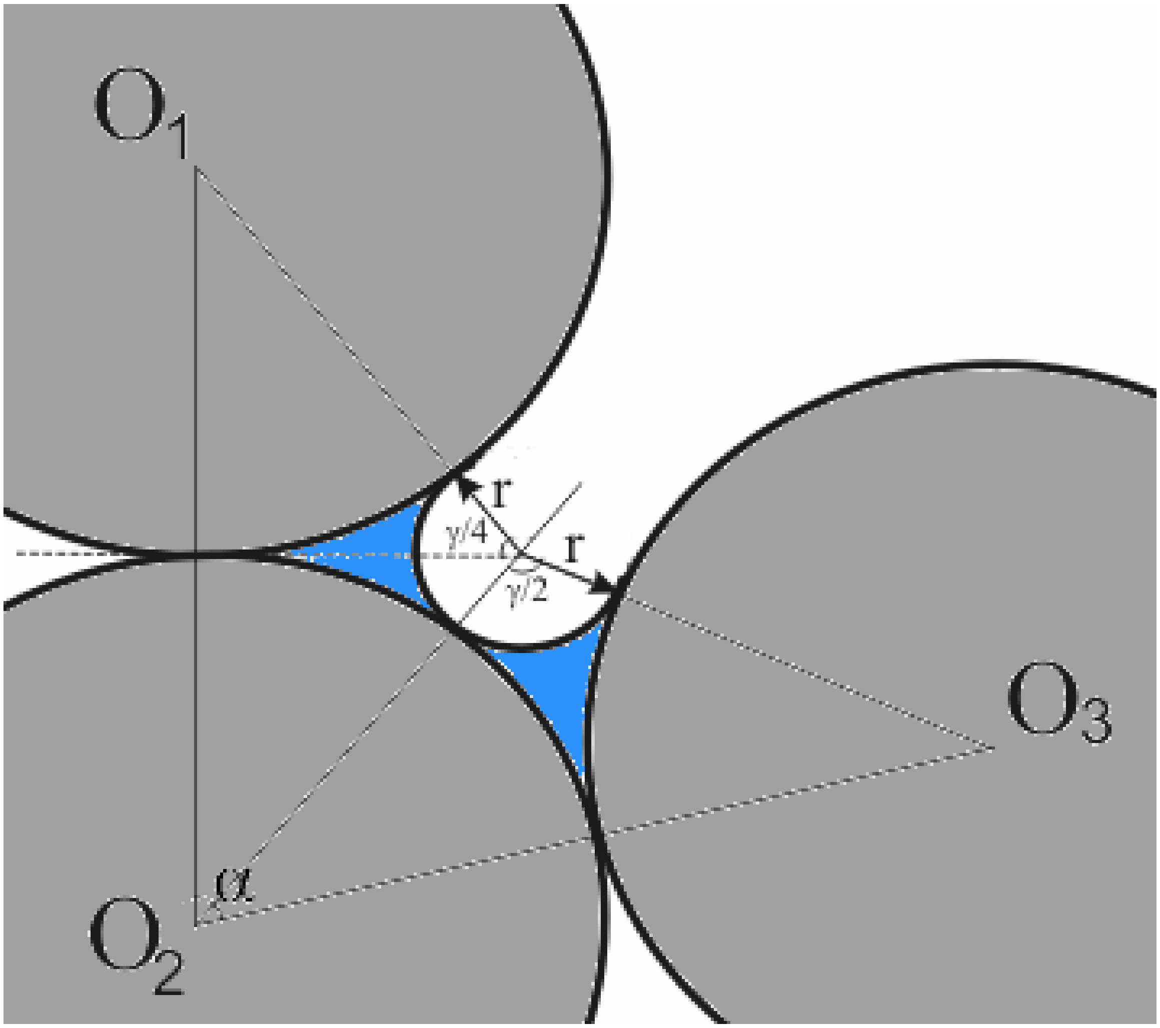

Fig. 40 The geometry of two liquid wedges that just touch each other and three cylindrical rods.

From Fig. 40 it is easy to see that

$$\sin\frac{\gamma}{4} = \frac{1}{1+r},$$

which yields the condition for the instability

$$\gamma = 4\arcsin\frac{1}{1+r} > \pi r. \tag{64}$$

Numerical calculation of Eq. (64) gives the critical values for r and γ:

$$r_{crit} = 0.77; \qquad \gamma_{crit} = 2.40.$$

And since the angle α (Fig. 40) is equal to

$$\alpha = 2\arccos\frac{1}{1+r},$$

we can conclude that the configuration, shown in Fig. 40, when two wedges just touch each other, is unstable if the angle α is less than the critical value

$$\alpha < \alpha_{crit} = 1.94 = 0.62\pi. \tag{65}$$

Eq. (65) gives a critical condition for the behavior of the pore throat shown in Fig. 40. For any value of angle α, less than critical, the configuration of the touching wedges is unstable; the stable configuration is possible only for the larger values of α.

This analysis provides simple, but useful insight to the pore level events in 3D geometry of the interfaces between spherical grains and allows interpreting the results of the intersection between two pendular rings (coalescence) and meniscus and ring (imbibition of a pore). In practice, during imbibition, the rods do not move, but the wedges adjust their shapes and grow in size as a response to the current curvature. Since the pore throats in the packing are of different geometries, the analysis for the case of moving rods corresponds to the different geometric situations that can be encountered in the real packing. Each pore throat, therefore, similarly to Eq. (65), behaves according to some critical condition that will define whether it is possible to accommodate touching wedges as a stable configuration.

Similarly to condition (65), we cannot conclude that any intersection between two pendular rings or between ring and meniscus during imbibition in the Finney pack will always lead to the instability of the interface; it is most likely that some condition, similar to that of (65), has to be derived for the actual 3D geometry. Whether derivation of such condition is theoretically possible remains uncertain and is the subject of future research.

Chapter III

This chapter presents the results of simulations (as capillary pressure curves) of displacement processes (drainage and imbibition) in the Finney pack and comparison with existing experimental data. When such a comparison is shown, the simulations were performed with boundary conditions (i.e. number of entrance and exit pores), physical constraints (i.e. wettability condition) and geological data (i.e. amount of cement) consistent with the actual experimental sample. The simulations were made using the algorithms, described above.

3.1 Results: Drainage Capillary Curves

3.1.1 Comparison between Predicted and Experimental Drainage Capillary Curves

Let us begin with the prediction of drainage. Drainage capillary curves were simulated using algorithms described above. Fig. 41 presents the comparison between the results of drainage simulation in an unconsolidated packing and experimental data by Haines [57].

Haines [57] made the series of displacement experiments (drainage following by imbibition) for the medium, which is called “glistening dew” and is actually a packing of glass beads of diameter 0.038 cm. He observed the existence of thin films on grain surfaces, which, at least, yields the value of contact angle equal to zero. During simulations, we set the value of the contact angle equal to zero. Two cases are possible for zero contact angle: first, the case that thin films exist and serve to connect hydraulically all W phase throughout the packing. Second is the limiting case when the existing thin films in the grain surfaces are not hydraulically conductive and thus W phase does not possess hydraulic connectivity throughout the packing. The simulations presented in Fig. 41 were made using this second case. (This is contrary to what was said in section 2.1.5 about the influence of thin films. We make this simulation here on purpose to investigate such limiting case. We also believe that such behavior is more consistent with conditions of Haines' experiment, since together with direct observations of thin films he also achieved irreducible W phase saturation during drainage, which in the case of completely connected W phase goes to zero as curvature goes to infinity: each local morphology of the W phase is connected to the bulk by hydraulically connected thin films and therefore can be displaced, although in practice there is a time scale limitation for this [15, 31]. The ratio of entrance to internal pores in the sample used by Haines was about 0.1; we took the same ratio of pores for the Finney packing in our simulations, so the number of entrances was about 200 during simulations. Fig. 41 depicts two kinds of drainage simulation: one using Haines' face insphere criterion (see above, section 2.1.2), another – using MSP criterion (section 2.1.2).

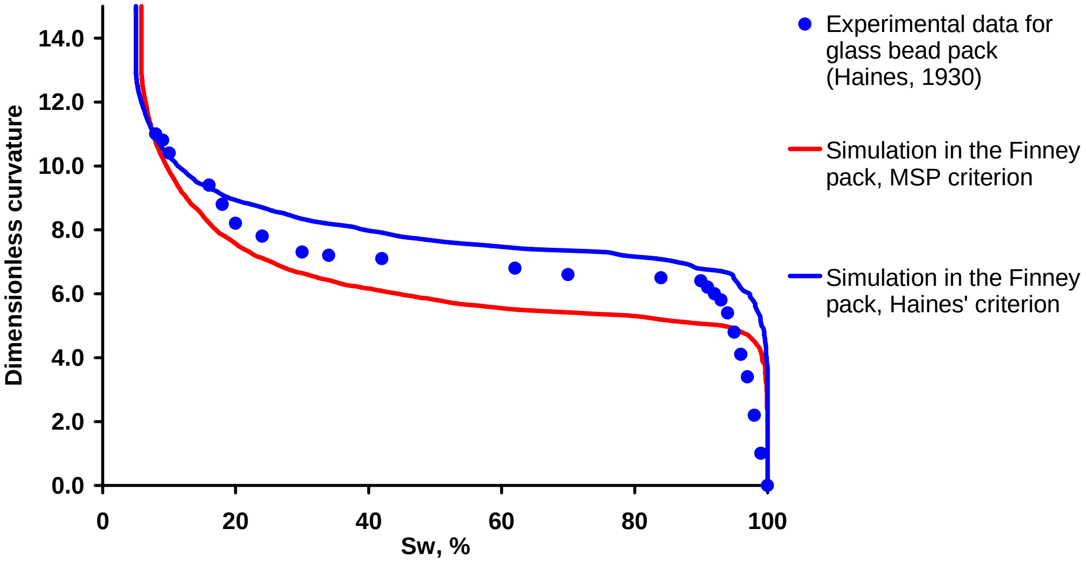

Fig. 41 Comparison between the simulations of drainage in the Finney pack using different drainage criteria and experimental data. Contact angle = 0 degrees. W phase is not hydraulically connected.

As one can see from Fig. 41, experimental data fall in between two simulated curves. Haines' face insphere criterion, being conservative (it finds the maximal sphere that just passes through the pore throat, but actual pore throat is not of the circular cross-section (Fig. 3) and therefore some part of its cross-sectional area is neglected by this criterion), overestimates the value of percolation curvature (the curvature, at which rapid penetration of the NW phase into the packing occurs and most part of the packing drains – Fig. 41). MSP criterion, on the other hand, being essentially two-dimensional, underestimates the percolation threshold value. Both criteria provide similar values of irreducible W phase saturation, consistent with experimental data [15].

From the comparison, presented in Fig. 41, we can notice that both criteria yield the discrepancy with experimental data, and the error associated is of similar magnitude but different signs for these two criteria. It can be concluded that both criteria fail to predict the behavior of simple porous media during drainage accurately, therefore work still has to be done in understanding the mechanisms of drainage and their application in real 3D geometry of sphere pack for the successful *a priori* prediction of drainage [20, 94]. In this work we prefer simple Haines' insphere criterion in comparison with computationally intense MSP technique, considering the fact that they provide predictions of drainage capillary pressure curves of similar accuracy.

3.1.2 Influence of Wettability on Drainage Capillary Curves

As an influence of wettability here and everywhere below we consider the influence of different values of contact angle. The values of contact angle can change within the interval between 0 and 90 degrees, so that identities of W and NW phases do not change. The "influence of wettability" in this sense corresponds to the change between strongly and weakly wetting behavior (cf. Figs. 14 and 15). When we consider thus defined "influence of wettability" for the parameters corresponding to both W and NW phase (for example, relative permeabilities), we indicate explicitly which of the phases is meant.

The prediction of the influence of wettability (specified by the value of contact angle) on drainage capillary curves is shown in Fig. 42. The simulations were made in the unconsolidated Finney pack using Haines' face insphere drainage criterion. The number of entrances was chosen to be equal to 9 in order to achieve sharp percolation threshold (see section 2.1.4).

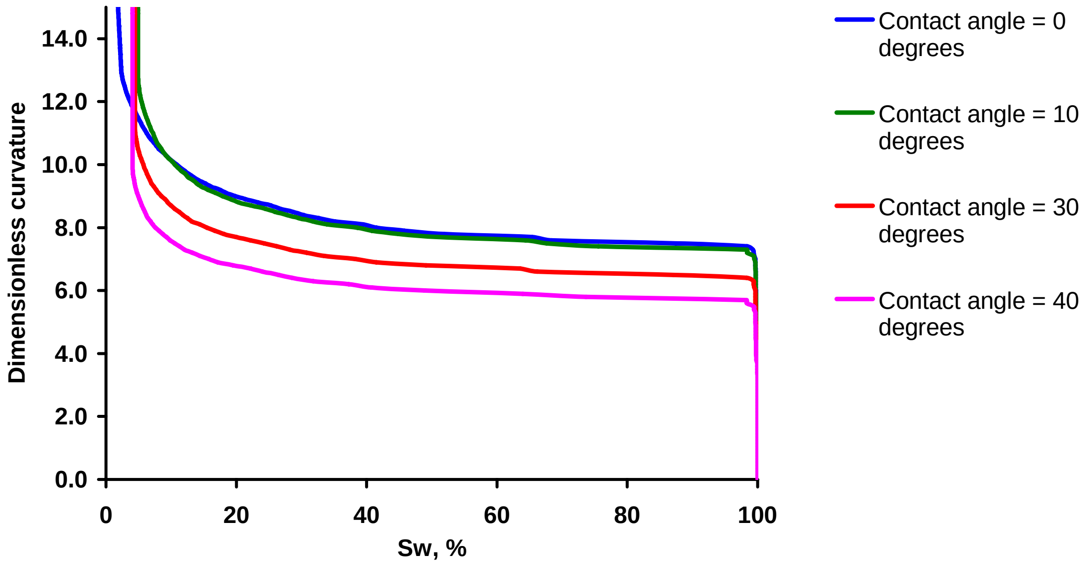

Fig. 42 Influence of wettability on simulated drainage capillary curves.

As can be easily seen from Eq. (2), which defines Haines' face insphere drainage criterion that we use, influence of wettability on drainage capillary curves in this case is trivial – shift in capillary pressure is linear with the cosine of contact angle θ. This is illustrated in Fig. 42, where all the curves (in the sense of macroscopic behavior) can be obtained from each other by using the scaling factor of $\cos\theta$ (except for the region of large curvatures, where the difference in irreducible W phase saturation is governed by the different shapes of the interfaces at different wettability conditions, which is not linear with $\cos\theta$). This scaling technique is known in the literature for a long time [7, 10, 12, 22, 123] and first appeared in so called "bundle of capillary tubes" models, where porous media were represented as a set of non-intersecting cylindrical capillaries having distribution of radii corresponding to the measured distribution of pore throat sizes [115]. It is still widely used to quantify the influence of wettability on displacement capillary curves, especially in mercury porosimetry [7, 12, 132].

3.2 Results: Imbibition Capillary Curves

3.2.1 Comparison between Predicted and Experimental Imbibition Capillary Curves

Simulations of imbibition in the Finney packing were conducted with the algorithms described above. The comparison between predicted capillary curves and experimental data in unconsolidated media is presented in Fig. 43. The predictions were made with conditions consistent with those reported for the considered experiments. Imbibition starts from the drainage endpoint (irreducible W phase saturation); value of contact angle is zero; number of pores connected with W-phase reservoir is about 200 (which is about 10% of overall number of pores in the packing); actual surface pores were taken as exits in order to define entrapment criterion for NW phase. Melrose criterion is used for the imbibition of a single pore.

For the comparison, we took the data for the imbibition capillary curves from the works of Haines [57] and Leverett [81]. Experiments of Haines were described in the preceding section. Fig. 43 shows good agreement between predicted capillary curves and those obtained experimentally by Haines. In order to estimate the influence of the W phase connectivity via thin films on grain surfaces, two limiting cases are shown in Fig. 43. One is for complete W phase connectivity, and the other for the case of no W phase connections via films, even though the films exist (this case was also considered in the preceding section for drainage). In the case of complete connectivity, the initially present pendular rings grow with every decrement in dimensionless curvature. This causes the smooth approach to the percolation threshold in Fig. 43, in contrast with the sharper onset of imbibition when connections through films are neglected (these conditions are the same as were set for the drainage simulations in Fig. 41).

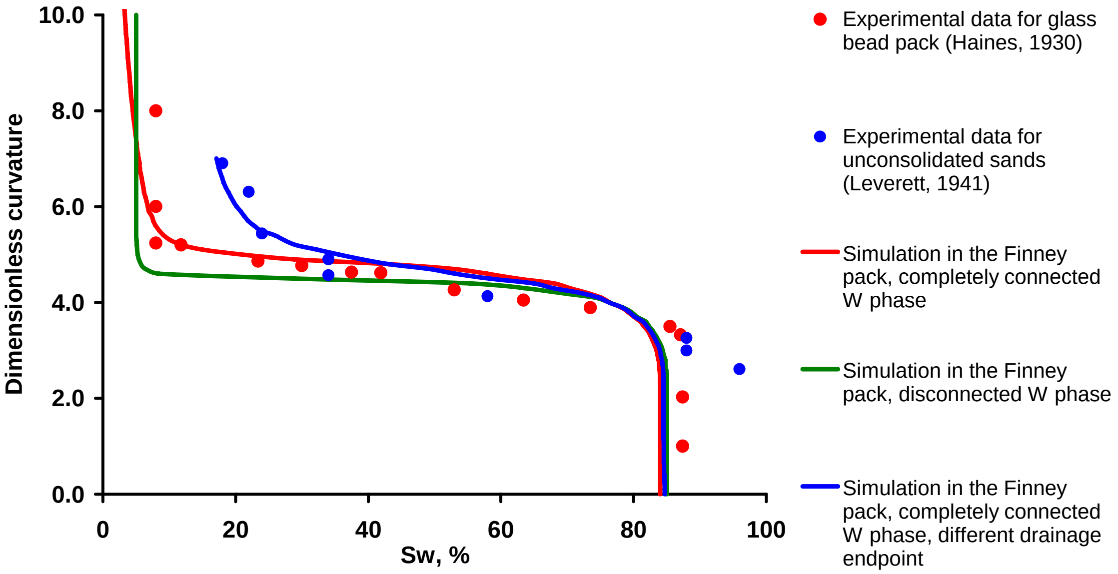

Fig. 43 Comparison between predicted imbibition capillary curves (Melrose criterion) and experimental data. Contact angle =0 degrees.

In the early stages (large values of curvature), Haines' data are consistent with the no-connectivity-via-films simulation: the W saturation does not change as the capillary pressure decreases until a sharp percolation threshold is reached. The difference between simulation (green curve in Fig. 43) and experiment is probably due to larger value of irreducible W phase saturation during experiment. Subsequently the data fall on or between the two predicted curves.

Data reported by Leverett [81] for different unconsolidated sands are also shown in Fig. 43. We simulated his experiment as described above, except the drainage endpoint was taken to be at higher W phase saturation: each grain contact supports the pendular ring, if its separation is smaller than the critical for the endpoint curvature 7.0, and in addition all the pores with inscribed radius (see above, section 2.1.3, where this radius is used to define Haines' insphere criterion for imbibition) less than 0.28 are filled with the

W phase. Such specified drainage endpoint yields irreducible W phase saturation of about 17%, which is the value consistent with the experiment of Leverett. The simulation and the data show the same percolation behavior as Haines'. The agreement is significant: no adjustable parameters enter the calculations. We conclude that the Melrose criterion for imbibition of a single pore is able to predict correct *macroscopic* behavior of the porous medium.

The comparison of theory and experiment in Fig. 43 suggests that the W phase connectivity varied during the experiment or was intermediate between the two simulated extremes. (We have ruled out several alternative explanations. The approximations underlying Eq. (21) do not affect the location of the percolation threshold, so that error is unlikely to alter the predicted curves. Extensive simulations have shown that the choice of pores connected to the W phase reservoir does not matter: multiple realizations with 200 entrance pores yield indistinguishable imbibition curves. The number of pores in the Finney pack (about 15,000) is statistically representative of the pore space in the larger packings used in laboratory experiments).

We speculate that practical applications may require an *effective* W phase connectivity, which could be defined in terms of a characteristic length scale. Suppose that two volumes of W phase are connected only by a thin film. If the path length through the film between the volumes exceeds some critical distance, the two volumes would be effectively disconnected and behave as though no film were present. On the other hand, if the distance between the two volumes is less than this characteristic length, they behave as though connected (would have the same curvature). The characteristic length for the condition of complete connectivity described above would be infinite; the value would be zero for the condition of disconnected W phase. A nonzero finite length would cause a pendular ring to be "frozen" at its initial curvature until the imbibing W phase advanced to within that distance of the ring. At that point, flow through the W phase film would allow the ring to adjust to the current curvature and thereby increase in volume.

The concept of a threshold separation at which W phase volumes are effectively disconnected can be recast in terms of a characteristic time scale. If flow through a thin film is very slow compared to the rate of change of capillary pressure during an experiment, then volumes of W phase connected only by thin films would behave as though disconnected. We have not attempted to estimate length scales or time scales for effective connectivity in this work, though the model porous medium does provide the geometric information necessary for making such estimates.

3.2.2 Physical Consistency of Melrose Criterion

It is instructive to consider whether the Melrose criterion for imbibition is physically consistent at the pore level with criteria for drainage. In particular we need to check that *negative hysteresis* does not occur in individual pores. Negative hysteresis means that a pore would drain at *smaller* curvature than the value at which the pore is imbibed. This situation is clearly non-physical, so it provides a good test of independently computed estimates of critical curvature.

Mason and Mellor [87] showed an example of negative hysteresis using the Haines criterion for the imbibition of a single pore [56] and the MSP (see above, sections 2.1.2 and 3.1.1) criterion for drainage of a pore throat [92, 113]. The Haines criterion states that when dimensionless curvature becomes equal to the curvature of the largest sphere that just passes through the pore throat (Eq. (2)), NW phase will spontaneously withdraw from that pore. This critical curvature for imbibition is readily computed for every pore in the Finney packing, since the locations of the four spheres defining each pore are known. Similarly, the critical curvatures for drainage can be computed for every pore throat in the Finney packing from the known locations of the three spheres defining each throat. Mason and Mellor [87] analyzed the cumulative number fraction of pores, which are drained and imbibed at particular curvature. (This analysis corresponds to the drainage and imbibition of a hypothetical disaggregated packing.) They found that a majority of individual pores would drain at smaller curvatures than at which they would imbibe. This inadmissible behavior was the basis for their modification of the Haines' criterion for imbibition (section 2.1.3, Eq. (4)). Namely, if the Haines dimensionless critical curvatures for imbibition are decreased by a constant value of 1.6, this negative hysteresis is removed. Not coincidentally, this modification improves the fit to experimental data.

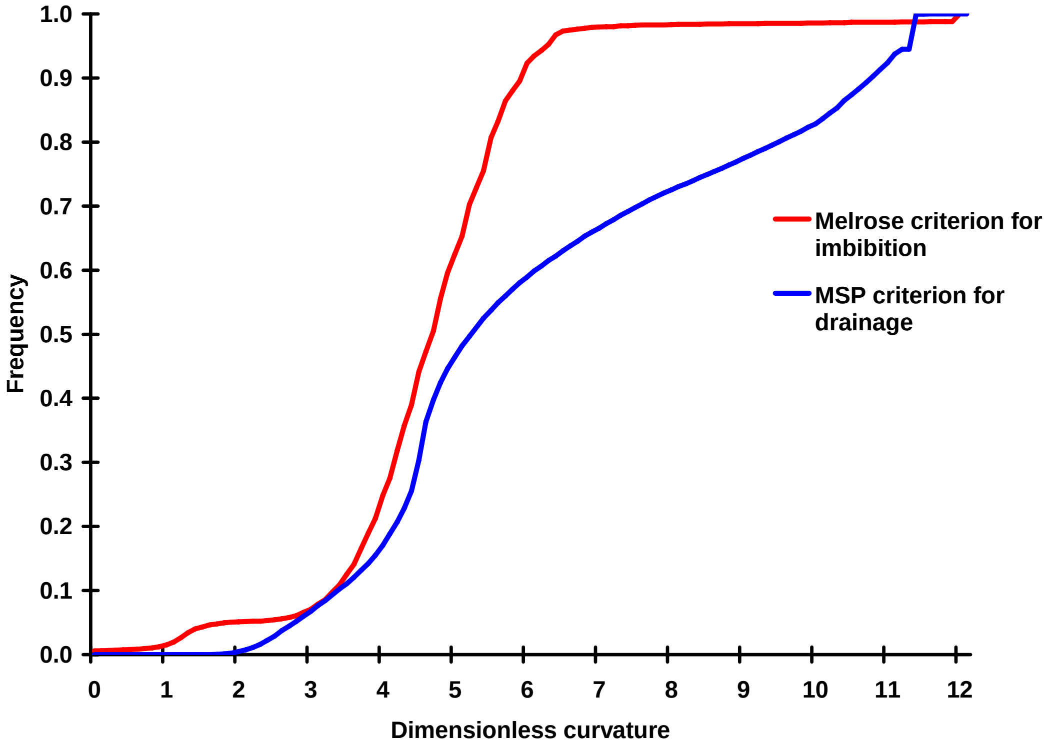

Fig. 44 Comparison between MSP drainage and Melrose imbibition critical curvatures for pores in the Finney pack. The cumulative distribution of imbibition curvatures lies to the left of the distribution of drainage curvatures except for a few pores in the neighborhood of $C = 3$ and $C > 11$. Thus the Melrose criterion avoids the problem of "negative hysteresis", an important independent test of physical consistency.

We made similar calculations for the Melrose criterion for imbibition. The results are shown in Fig. 44. Unlike the Haines' criterion, the Melrose criterion is dynamic. Thus we cannot compute in advance the dimensionless curvature at which any given pore will imbibe. Instead we computed the four critical curvatures corresponding to imbibition of the pore through each of its faces (pore throats). Thus each pore has four *a priori* critical curvatures for imbibition, corresponding to each of its pore throats. Taking each of the faces of a particular pore in turn, we assumed that a meniscus was present in the throat and that a pendular ring existed at each grain contact not associated with that throat. The Melrose criterion is readily applied to these configurations. Once the critical curvature was determined for a configuration, we checked that the pendular rings would in fact exist at that curvature; if not, that configuration was discarded from the analysis. The critical curvatures for drainage were computed using the MSP method as described in [87].

Fig. 44 shows that, unlike Haines' insphere, the Melrose criterion does not lead to massive negative hysteresis – the overlap between the curves for drainage and imbibition is very small. Moreover, this overlap occurs at 1) small dimensionless curvatures (very few pores in the neighborhood of $C = 3$), which are below the percolation thresholds for both drainage and imbibition [87]; and at 2) very large curvatures $C > 11$. The overlap at large curvatures is due to the fact that Delaunay tessellation applied to the Finney pack results in some tetrahedral pores (their number is small, about 1% of the total number of pores in the packing) that are almost flat and close to degenerate. When we consider disaggregated set of pores, as was described above, we assume that W phase exists at each of the four faces of the tetrahedral pore in consideration. Since the pore is flat, the angle α (Fig. 35) is very small, and any existing pendular ring would immediately satisfy Melrose criterion (given by Eq. (29)) regardless of the value of the angle ψ of meniscus' rise (Fig. 35). This means that such degenerate pores will be imbibed immediately when one of their neighbors is imbibed; but at large curvatures (critical curvatures for disaggregated set $C > 11$) the W phase would never come close to these flat tetrahedral pores, because their neighbors are not degenerate and would be imbibed at much smaller curvatures. This effect is therefore simply an artifact of our computation technique for the *disaggregated* set and should be disregarded as non-physical.

Thus we can conclude that simulations of drainage and imbibition in the actual Finney packing with the MSP and Melrose criteria do not exhibit negative hysteresis.

These considerations provide independent support for the validity of the Melrose criterion at the pore level. We do not show similar comparison between Haines’ face insphere critical curvatures for drainage and Melrose imbibition curvatures. It is obvious that Haines’ face insphere criterion yields the set of critical curvatures larger than MSP approach (Fig. 41) and thus the curve for disaggregated set in Fig. 44, corresponding to Haines’ face insphere criterion would lie further to the right of the MSP curve (shown by red in Fig. 44). The analysis in this case is therefore redundant.

3.2.3 Influence of Wettability on Imbibition Capillary Curves

Fig. 45 depicts results of imbibition simulations in the unconsolidated Finney pack for different wettability conditions (different values of contact angle). The simulations were made in the unconsolidated Finney pack using Melrose criterion for the imbibition of a single pore. The number of entrances was chosen to be equal to 11 in order to achieve sharp percolation threshold (see section 2.1.4). All the actual surface pores of the Finney pack were chosen as exits to define criterion for the NW phase entrapment (see section 2.3.2).

The predictions in Fig. 45 show that increasing the contact angle has two effects: 1) shifting the imbibition curve down to smaller values of dimensionless curvatures; and 2) decreasing the residual NW phase saturation. The second effect is qualitatively correct: at the contact angle of 90 degrees difference between phases disappears (neither phase can be considered W or NW), and the displacing phase can enter all the pores simultaneously. Thus in this case the residual NW phase saturation must vanish.

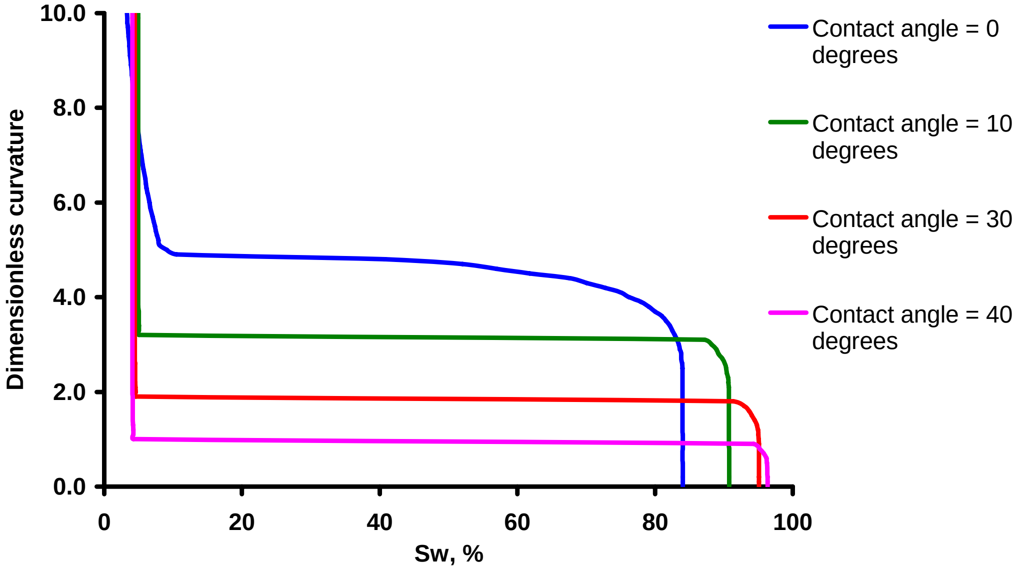

Fig. 45 Influence of wettability on imbibition capillary curves. Predictions for the unconsolidated Finney pack.

Experiments performed in media with independently measured value of contact angle are consistent with the predicted trends. Morrow *et al* [102] carried out water-decane imbibition experiments in columns of crushed dolomite. The wettability (value of advancing contact angle) in their experiments was controlled by the concentration of octanoic acid in the decane (which was a NW phase). When the value of contact angle was changed from 0 degrees to 49 degrees, the value of percolation threshold capillary pressure was decreased by a factor of two. Hamon and Bennes [58] performed waterflooding in water-wet Fontainebleau sandstone. Their experimental data show strong correlation between residual gas saturation and Amott wettability index (namely, residual gas saturation increases with the increase in wettability index). This trend is qualitatively consistent with the predictions shown in Fig. 45.

The shift in both predicted and experimental capillary curves is significant. In classical applications of the Young-Laplace equation (1), e.g. “bundle of capillary tubes” models [115], uniform wettability changes can be accounted for simply by scaling the critical curvature values by the factor of $cos\theta$. Recalling that $cos(40°) = 0.7$ and $cos(49°)$

= 0.66, we would then expect the percolation thresholds in Fig. 44 and in the experiments of Morrow *et al* to decrease by only 30% to 50%. The data indicate that the influence of contact angle on fluid interfaces in sphere packs is more complex than bundle of tubes interpretations admit. Others (e.g. Ioannidis *et al*, [66]) have shown that models that account for contact angle and nontrivial asymmetry in pore space geometry also yield nonlinear dependence on $cos\theta$. The predictions with the Melrose criterion account for the contact angle directly *and* for dynamic interface movement in realistic grain-scale geometry. The combination leads to a nonlinear dependence of macroscopic behavior on $cos\theta$ which is consistent with observations. This provides significant additional independent support for adopting the Melrose criterion.

Further, the smaller value of the residual NW phase saturation observed in the experiment by Morrow *et al* at larger contact angle (49 degrees), is also consistent with the predictions. The results of other experiments, obtained for the different types of porous media (teflon [101], crushed galena [59]) also qualitatively support the predicted influence of wettability on the imbibition capillary curves (shift to the smaller dimensionless curvatures and decrease in residual NW phase saturation with the increase of the contact angle).

3.2.4 Dynamic Character of Melrose Criterion

To illustrate the dynamic character of Melrose criterion, we present in Fig. 46 the frequency distributions of critical curvatures at which imbibition could happen in individual pores. The distributions shown are for the contact angles equal to 0 and 30 degrees. These curvatures are the same as those computed and discussed for the comparison between MSP and Melrose criteria and whose cumulative distribution is shown in Fig. 44 for the case of contact angle = 0 degrees.

The distributions cover a wide range of values. In fact, even a single pore can exhibit a wide range of critical curvatures: the values depend on which pore throat contains the meniscus whose advance leads to the imbibition event. During imbibition simulation we cannot know in advance (at the beginning of the simulation, say) from what side the W phase front approaches any given pore. Nor will we know in advance which pore throats contain menisci and which grain contacts contain pendular rings when a pore becomes a candidate for imbibition. Thus we cannot know in advance which of the possible curvatures of Fig. 46 will be realized during imbibition. Although the distribution of values at which imbibition events *could* happen is broad, the range of curvatures at which imbibition events *do* happen is narrow. This is manifest in the percolation threshold of Fig. 45: most pores are imbibed at curvatures between 4.5 and 5 (contact angle = 0 degrees) and between 1.8 and 1.9 (contact angle = 30 degrees).

In this case the percolation threshold is the consequence of two phenomena. One is accessibility: a pore cannot imbibe until a meniscus reaches at least one of its throats, regardless of its critical curvature. This is intrinsic to capillary-controlled displacements in porous media. The other is particular to the Melrose criterion: even after a meniscus arrives in a pore throat, the imbibition event will depend on whether pendular rings are present, whether they are connected to the W phase reservoir, etc. The latter conditions convolve accessibility and connectivity.

The dependence of imbibition curvature on the dynamic local situation is familiar (cf. Lenormand and Zarcone, [80]). But unlike other dynamic criteria, the Melrose criterion cannot be readily applied in a traditional network model. Interface movement under the Melrose criterion occurs as an inherent feature of the particular pore space, directly connected to its geometry and internal conditions (such as wettability). Therefore direct application of the critical curvatures given by the Melrose criterion in particular pore space geometry (for example, in the Finney pack) would not necessarily provide the correct behavior of some artificially constructed network. Thus, it would be a non-trivial problem to predict the percolation threshold only from the distributions of possible imbibition curvatures, shown in Fig. 46.

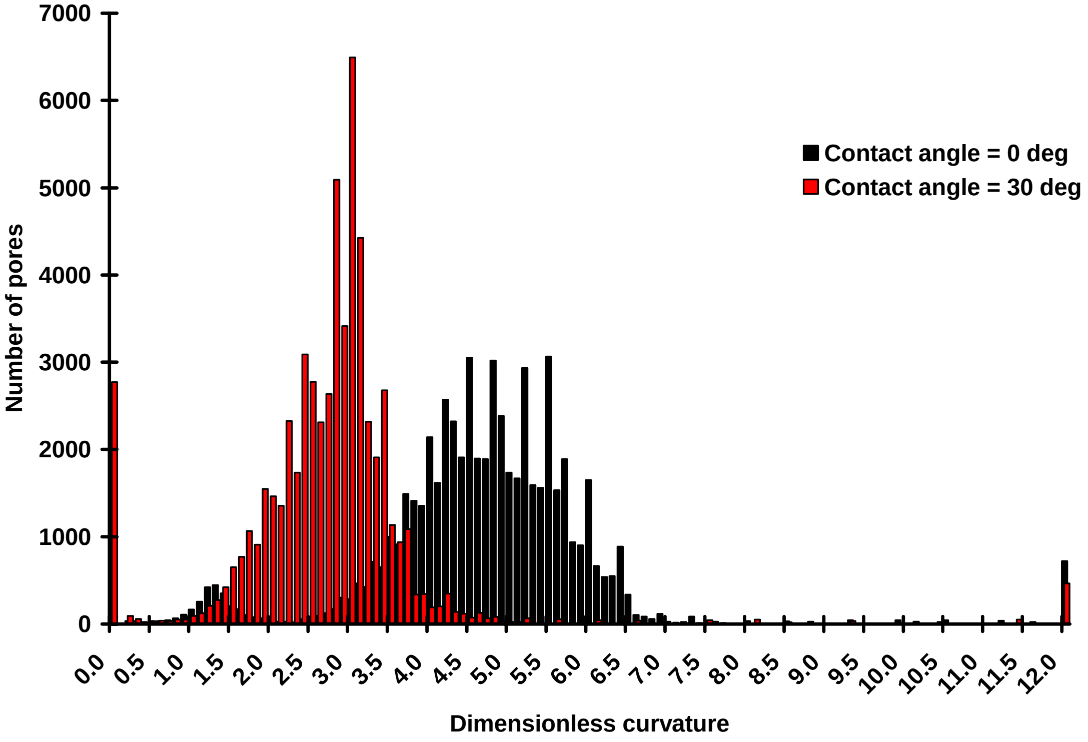

Fig. 46 Distributions of the dimensionless imbibition curvatures at which the pores in the Finney packing could imbibe, based on the Melrose criterion. Two distributions, corresponding to contact angles of 0 and 30 degrees are shown (cf. corresponding imbibition capillary curves in Fig. 45). The spikes at the value of curvature of 12 correspond to all the pores, where imbibition event happens at curvature 12 or higher (tetrahedral pores, close to flat, which were discussed in section 3.2.2).

3.2.5 Influence of Wettability on W Phase Topology

We have seen that increase in contact angle results in two effects: shift of capillary curve to smaller dimensionless curvatures and decrease in residual NW phase saturation. The first is readily explained by the Young-Laplace equation (1) and the behavior of fluid interfaces (menisci and pendular rings) in realistic pore space. The second can be explained if we consider topology of the W phase. Here we characterize the topology of a fluid configuration by the average *coordination number*, the average number of imbibed immediate neighbors adjacent to an imbibed pore. This measure ignores pendular rings and thin films. Because the pores correspond to Delaunay tetrahedra, the maximum coordination number in our model porous medium is four (see section 1.5). The evolution of W phase coordination number during imbibition is shown in Fig. 47 for different situations.

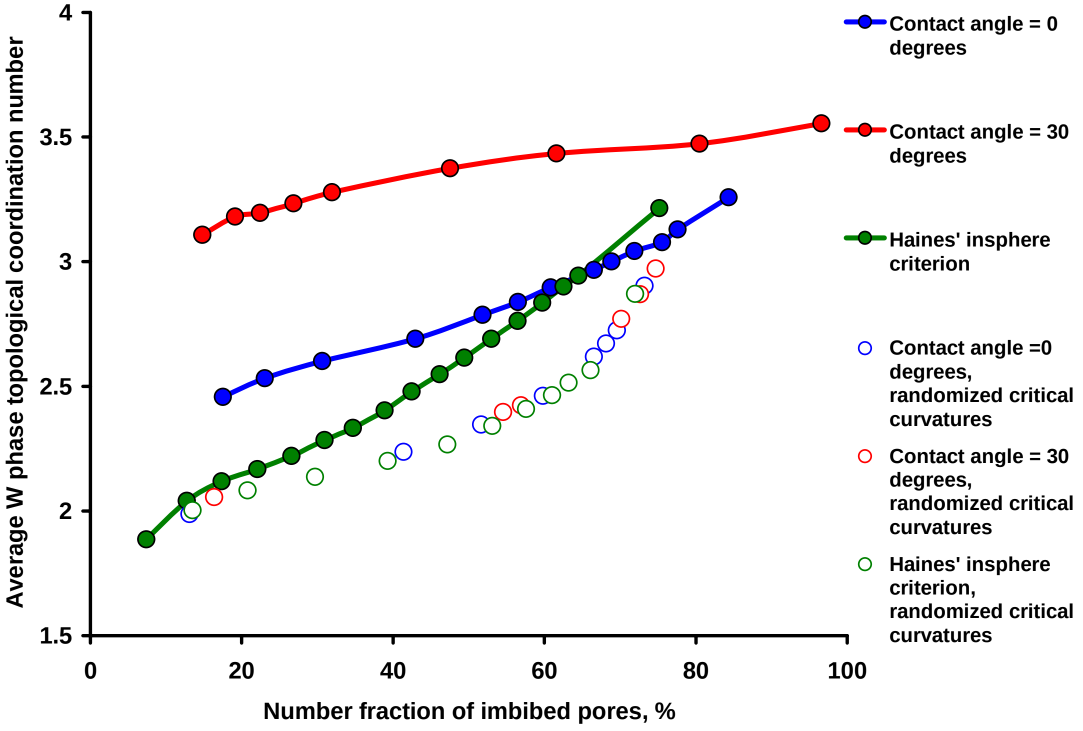

Fig. 47 Influence of wettability on W phase topology during imbibition is strongly related to the spatial correlation of pore-space geometry.

First, we compare the behavior for different values of contact angle (0 and 30 degrees). The average W phase coordination number is *consistently larger* at any W phase saturation for the *larger* value of contact angle (30 degrees). This means that at larger contact angles W phase invades as *compact body* (each imbibed pore on average has at least 3 imbibed neighbors – Fig. 47). In contrast, at zero contact angle the W phase configuration exhibits many more *dendritic branches* with a lot of dead ends (a dead end is an imbibed pore that has only one imbibed neighbor). For the latter case clusters of pores within the packing can be surrounded more easily by imbibed pores and thereby lose their connection to the exits, which leads to larger values of residual NW phase saturation.

For comparison, average W phase coordination number during imbibition simulated with Haines' insphere criterion is also shown in Fig. 47. It differs significantly at early stages of imbibition from the curves obtained using Melrose criterion. Near the endpoint it yields a W phase configuration with average connectivity similar to that obtained by Melrose criterion for zero contact angle. On the axes of this plot, the Haines criterion curve is independent of contact angle, because the *sequence* of pore level imbibition events computed with this criterion will be exactly the same for any wettability condition; this criterion suggests the scaling of capillary pressure by $\cos\theta$ with the change of the contact angle. This is an important observation; the W phase topology influences properties such as relative permeability and electrical resistivity. Thus criteria derived from the application of Eq. (1) to cylindrical capillaries, which result in linear dependence between capillary pressure and cosine of contact angle, are unlikely to be helpful in explaining the effect of wettability on such properties.

The Melrose criterion is inseparable from the pore space geometry. Thus we anticipate a strong interdependence with the spatial correlation inherent in the pore geometry of granular materials [18, 20, 112, 131]. To illustrate this dependence, Fig. 47 also shows average W phase coordination number during simulations with *randomized* values of imbibition critical curvatures. To conduct these simulations, we take exactly the same values of critical curvatures, at which pores in the packing were actually imbibed, and assign those values randomly throughout the pores in the whole packing. As shown in Fig. 47, all influence of wettability disappears for this case – average coordination number is the same for both 0 and 30 degrees contact angles (and, moreover, the same for randomized Haines' insphere criterion) and is much smaller than non-randomized one. Although such choice of curvatures to randomize is not exactly the right one for the comparison with non-randomized case (such set of curvatures would include the effect of percolation and therefore guarantee that imbibition simulation would be different), it does provide very important information. Fig. 47 shows that all three (0 degrees, 30 degrees, Haines insphere) randomized sets of curvatures lead to the same topology of W phase during imbibition at any value of W phase saturation. Evidently this topology is characteristic of site invasion percolation in random 3D networks of connectivity four. This topology is not characteristic of an imbibition process, however, as shown by comparing it with the non-randomized simulations (Fig. 47). Random networks do not account for spatial correlations in pore space geometry and therefore will not exhibit the strong effect of contact angle during imbibition.

We are not aware of experimental data that can be directly compared to predictions in Fig. 47. But from these results we can predict qualitatively, for example, the influence of wettability on relative permeability to the wetting phase during two-phase flow in the packing. Predictions in Fig. 47 suggest that relative permeability to the W phase should be larger at larger values of contact angle (since average coordination number of the W phase is larger – Fig. 47; this qualitative observation is confirmed by the simulations of two-phase flow in the Finney pack – see section 4.5.2). Indeed, existing experimental data (see, for example, Owens and Archer [108] and Hamon and Bennes [58]) exhibit this trend, providing strong support for the presented approach.

3.2.6 Residual NW Phase Distribution

Another interesting comparison concerns distribution of residual NW phase. Many researchers have visualized and quantified the distribution of residual NW phase blobs (see, for example, [24, 91, 124]). For the comparison with our predictions we took the data from Johns and Gladden [71] and Prodanovic *et al* [114]. Johns and Gladden [71] explored dissolution of octanol ganglia in random packings of glass ballotini and measured residual NW phase area by magnetic resonance imaging (MRI). Prodanovic *et al* [114] analyzed three dimensional images of residual NW phase in Berea sandstone obtained from X-ray microtomography. Fig. 48 shows the comparison of cluster size distribution of pores, containing residual NW phase, between predictions of this work (for values of contact angle 0 and 30 degrees, 200 entrance pores) and these experimental data.

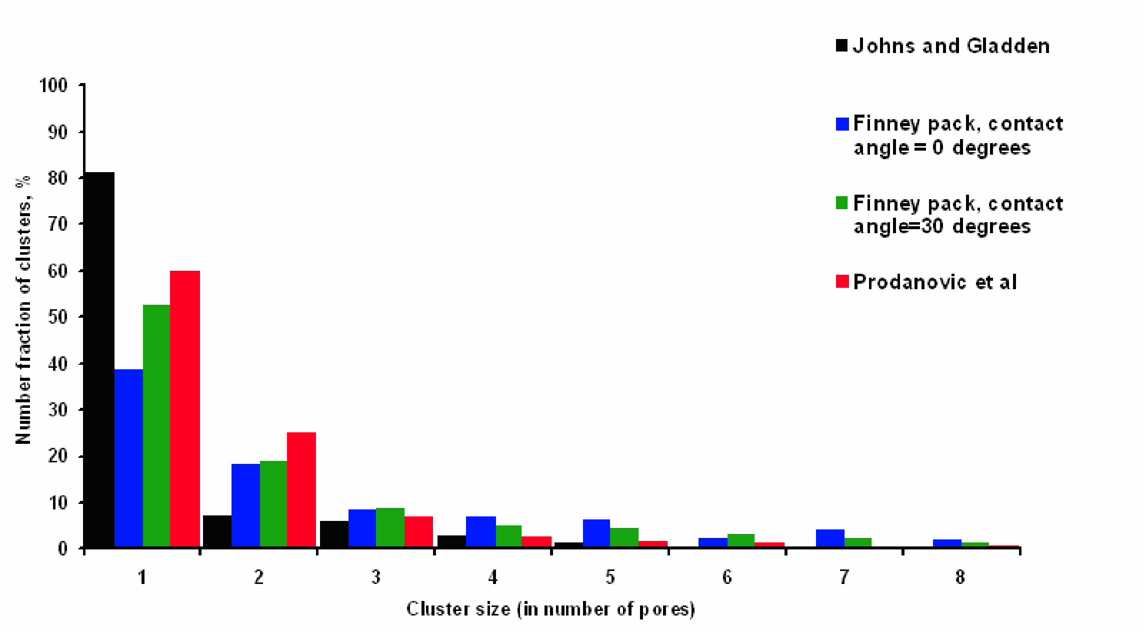

Fig. 48 Distribution of cluster sizes of pores, containing residual NW phase.

As discussed above, NW phase can be trapped as clusters of one pore (singlets) or several pores. Fig. 48 shows the distribution of size (in number of pores) of such clusters. The four histograms (two predicted and two experimental) are similar, all showing most clusters trapped as singlets. Data from Johns and Gladden [71] show no large clusters, whereas our simulations yield a few large clusters with more than 100 pores (We do not show the tail of the distribution in Fig. 48 for the purposes of better presenting data). The number of singlets (60%) and doublets (25%) in the data from Prodanovic *et al* [114] is close to our predictions and is similar to other observations [91]. Moreover, Prodanovic *et al* observed the existence of large clusters of pores with residual NW phase, which is also consistent with our predictions. The number of such clusters (containing more than 9 pores) was very small (less than 1%), but they occupied considerable amount of pore volume (the distribution of *pore volumes* with residual NW phase in their experiments is very broad and spans several orders of magnitude). The data from other sources [24, 91] also confirm the existence of large clusters.

A possible explanation for the difference between the data from Johns and Gladden [71] and our predictions and the data by Prodanovic *et al* [114] follows from the comparison between predicted histograms for different values of contact angle. As shown in Fig. 48, the character of W phase invasion depends on wettability: at smaller contact angles W phase invades as dendritic branches of smaller average coordination number. This type of invasion leads to the entrapment of large clusters of pores containing NW phase. The amount of singlets in this case is less than 40% of the overall number of trapped clusters (Fig. 48). For larger contact angles, though, W phase invades as compact body, which makes the entrapment of such large clusters much harder, while at the same time the number of singlets dramatically increases (Fig. 48). So, even though the *total* number of trapped *clusters* is less for the case of zero contact angle, the number of trapped *pores*, and, thus, the value of residual NW phase saturation, is significantly larger due to the existence of large clusters. This explains the difference between residual NW phase saturations for different simulations in Fig. 48 and provides another reason for the distribution, observed by Johns and Gladden (Fig. 48), where the absence of large clusters and the abundance of singlets might be attributable to a large value of contact angle. The cumulative distributions of blob diameters [24] and volumes [91] also qualitatively support our predictions of the structure of residual NW phase. Unfortunately, we are not aware of the existence of experimental data where residual NW phase distribution was measured with independently controlled wettability. But we can conclude that the Melrose criterion, acting in the pore geometry and inseparably tied to it, allows making predictions of the behavior of different parameters during imbibition (W phase topological coordination number, Fig. 47; structure of residual NW phase, Fig. 48) that can be tested during experiments and cannot be obtained without actual imbibition simulation in sufficiently detailed and physically representative pore space geometry.

3.3 Capillary Pressure Hysteresis: Unconsolidated Media

Let us consider now simulation of the whole hysteresis cycle (primary drainage followed by imbibition) in the unconsolidated Finney pack. Fig. 49 presents the results of such simulation and its comparison with experimental data reported by Haines [57] (see sections 3.1.1 and 3.2.1). Simulations were made using Haines' face insphere criterion for drainage and Melrose criterion for imbibition. Boundary (200 entrance pores) and wettability conditions (contact angle = 0 degrees) were consistent with those during Haines' experiment (see also Figs. 41 and 43). Fig. 49 illustrates good agreement between simulations and experimental data, especially for the case of imbibition.

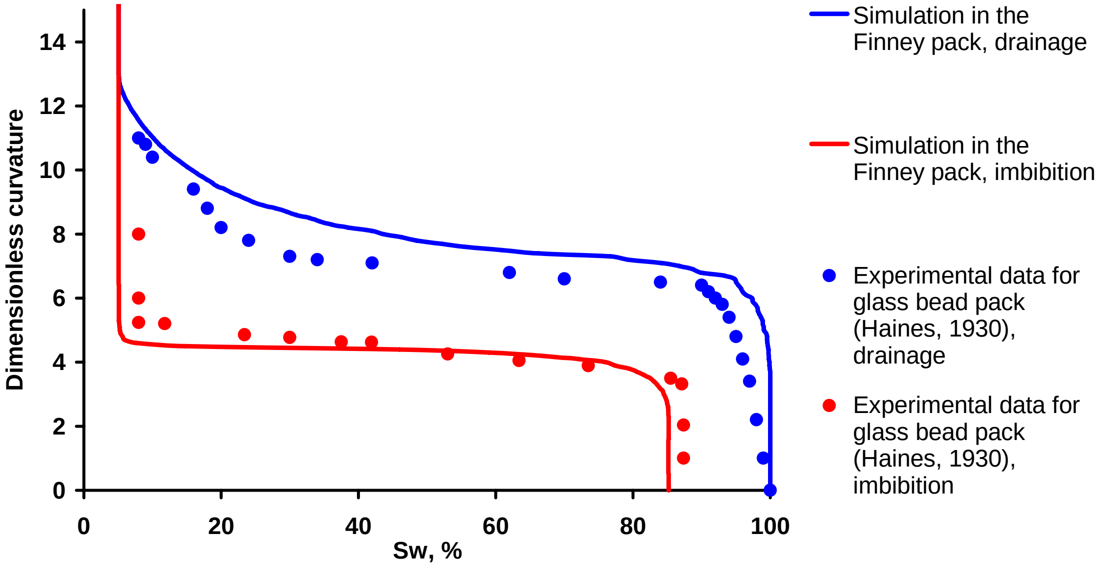

Fig. 49 Comparison between predicted hysteresis in capillary pressure in the unconsolidated Finney pack and experimental data for glass bead pack by Haines [57]. The drainage simulation starts from a 100% wetting phase saturation; the imbibition simulation starts with the fluid configuration obtained at the end of the drainage simulation.

3.3.1 Influence of Wettability

We illustrate in Fig. 50 the influence of wettability on the hysteresis in capillary pressure in the unconsolidated Finney pack. These simulations are the same as were shown in Figs. 42 and 45. The influence of wettability on imbibition part of capillary curves is much larger, than on drainage part (see sections 3.1.2 and 3.2.3). This leads to the stronger effect of hysteresis for large values of contact angle.

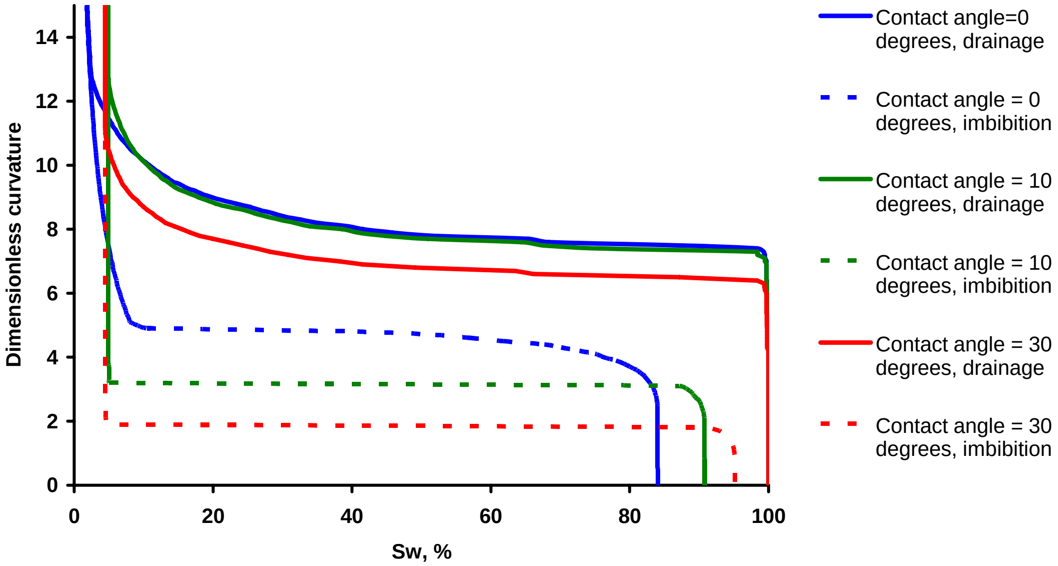

Fig. 50 Influence of wettability on the hysteresis in capillary pressure in the unconsolidated Finney pack.

3.3.2 Influence of Snap-off

It is interesting to quantify the influence of snap-off at pore throats (which we treat as a coalescence of pendular rings, see section 2.2.2). It has long ago been assumed in the literature that snap-off is crucial in imbibition [2, 69, 80]. Two major effects are a consequence of snap-off. First is that early blocking of pore throats leads to the earlier percolation (that is, percolation would happen at larger curvatures). This happens because W phase that fills pore throats as a result of snap-offs will create new candidates for imbibition (pores that share the throat that has been snapped-off). Second is an increase in the residual NW phase saturation (since the connectivity of the NW phase decreases as W phase at blocked pore throats disconnects bulk NW phase).

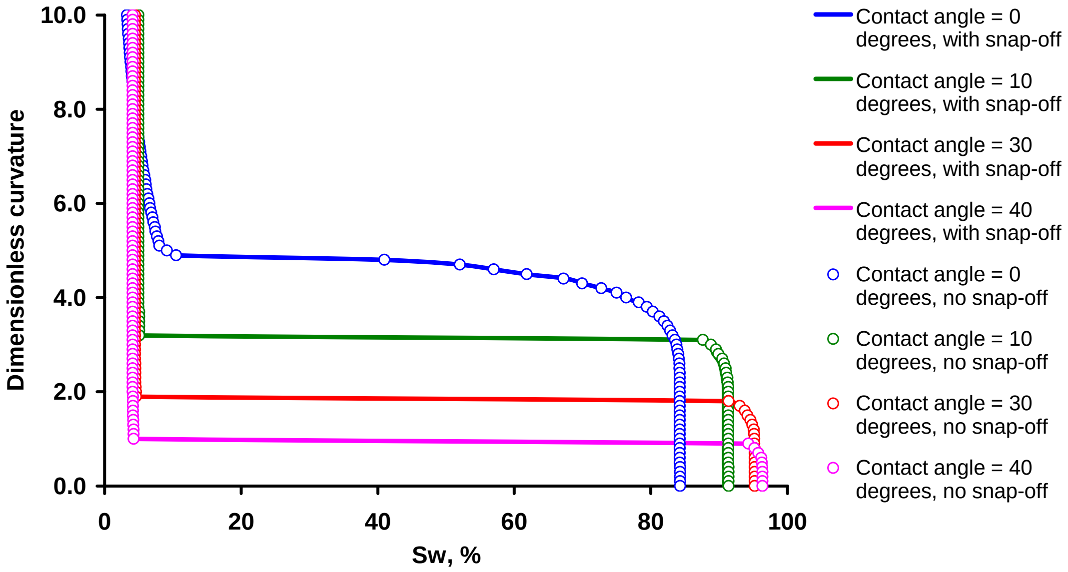

Fig. 51 Influence of snap-off (coalescence of pendular rings) on the imbibition capillary curves in an unconsolidated Finney pack.

Fig. 51 presents the results of imbibition simulation in the unconsolidated Finney pack for different wettability conditions with and without accounting for the snap-off effect. As one can see from Fig. 51, the influence of snap-off is negligible for any value of contact angle during imbibition, contrary to common knowledge. The reason for this is that the values of the curvatures, at which coalescence in an unconsolidated packing starts to occur, are relatively small (see the distribution of such curvatures for the contact angle = 0 degrees in Fig. 25, where the largest curvature of snap-off, corresponding to the pore throat formed by three grains in contact, is equal to 4.5). Thus when the curvature becomes small enough in an imbibition experiment for the coalescence to happen, most of the pores in the packing are already imbibed (compare with the set of *a priori* imbibition curvatures in Fig. 46 and imbibition capillary curves in Fig. 45). Thus we can conclude that our simulations predict the effect of the snap-off in an unconsolidated media during imbibition to be negligible.

3.4 Capillary Pressure Hysteresis: Media with Isopachous Cement

We illustrate in Figs. 52 – 54 the influence of isopachous cementation on the hysteresis in capillary pressure for different wettability conditions. This type of cementation was modeled as described in section 1.5 (see Figs. 5 and 6) by uniform increase of grain radii until the desired porosity was reached.

It must be noted here that the predictions made in this work for media with isopachous cement are true only for the range of porosities considered. When increase in grain radius becomes large, isopachous cement starts to block pore throats completely [17-19]. This effect might lead to a qualitatively different behavior of properties of interest when degree of isopachous cementation is very high (the blocking of pore throats by cement first occurs at porosity of about 12%). Overall, this is subject of future research.

Generally, the effect of isopachous cementation is the shift of both drainage and imbibition capillary curves up to larger values of dimensionless curvature. This may be expected in advance, because isopachous cementation reduces the sizes of pore throats and bodies and therefore larger pressure is needed to displace the phase from the pore space.

This effect is qualitatively the same for any wettability condition, although larger values of contact angle tend to separate drainage and imbibition capillary curves more, which is the consequence of the criteria used and their dependence on the wettability conditions (see sections 3.1.2 and 3.2.3).

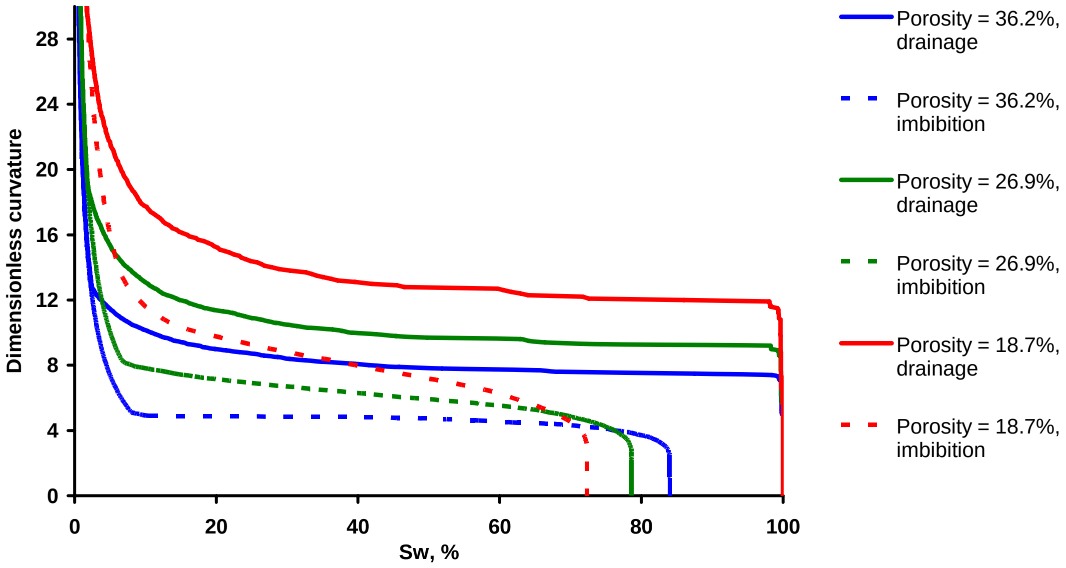

Fig. 52 Influence of isopachous cementation on the hysteresis in capillary pressure in the Finney pack. Contact angle =0 degrees.

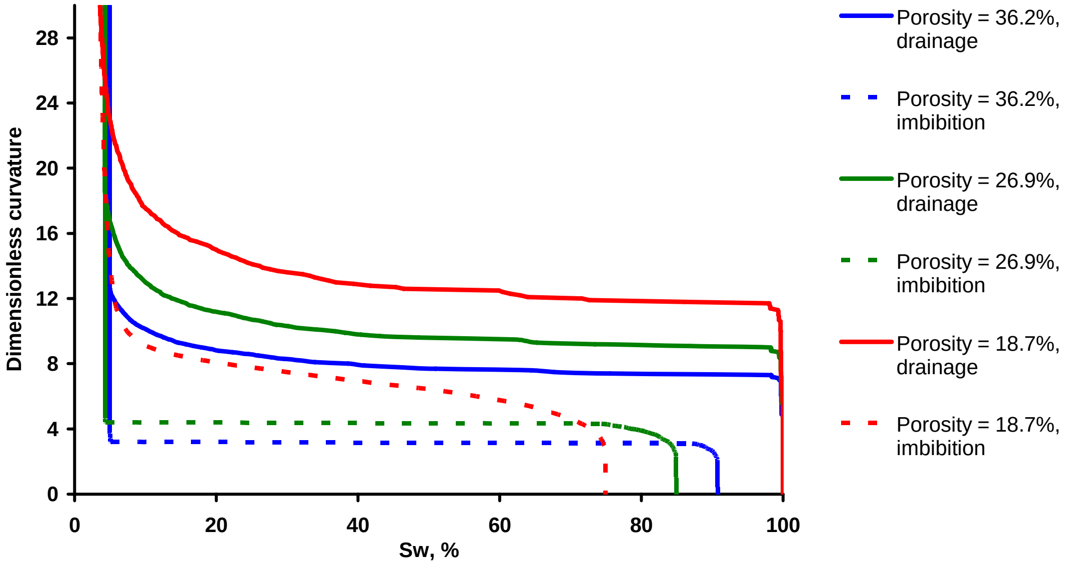

Fig. 53 Influence of isopachous cementation on the hysteresis in capillary pressure in the Finney pack. Contact angle =10 degrees.

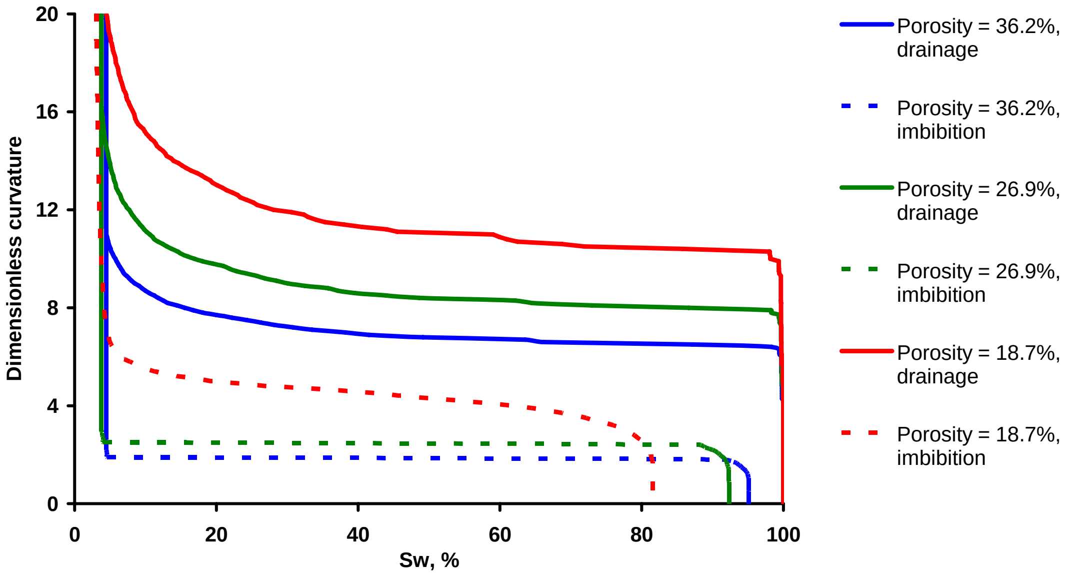

Fig. 54 Influence of isopachous cementation on the hysteresis in capillary pressure in the Finney pack. Contact angle =30 degrees.

Another effect of isopachous cementation is that it leads to the increase in the residual NW phase saturation for any value of contact angle (Figs. 52 – 54). This is qualitatively supported by the experimental data by Hamon and Bennes [58]. They carried out waterflooding in the Fontainebleau sandstone, which is a strongly water-wet outcrop rock. The variability of porosity in Fontainebleau sandstone is due to the different degree of isopachous quartz cementation. Their data show increase in residual gas saturation as porosity of the samples decreases as a result of isopachous cementation. The predicted trends (Figs. 52 – 54) are consistent with these experimental observations.

3.4.1 Influence of Wettability

It is interesting also to quantify the influence of wettability (specified by the value of contact angle) in the Finney pack with isopachous cement. Figs. 55 and 56 show hysteresis in capillary pressure for different wettability conditions (contact angle is equal to 0, 10 and 30 degrees) in the packing with different amount of isopachous cement (Fig. 55 – porosity 26.9%, Fig. 56 – porosity 18.7%). Qualitatively, the influence of wettability is the same as was shown for the unconsolidated media (cf. Figs. 42 and 45).

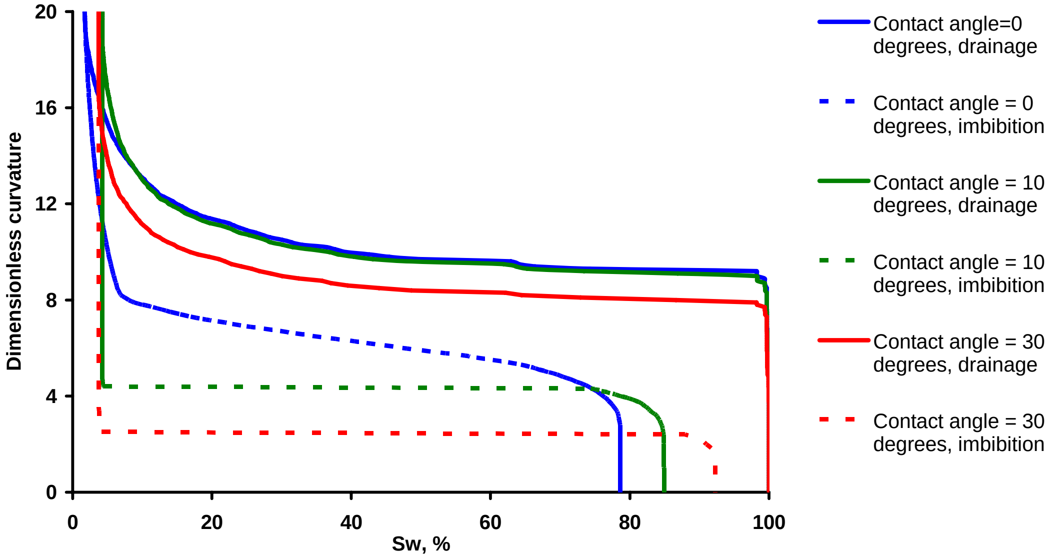

Fig. 55 Influence of wettability on the hysteresis in capillary pressure in the cemented Finney pack. Isopachous cement, porosity = 26.9%.

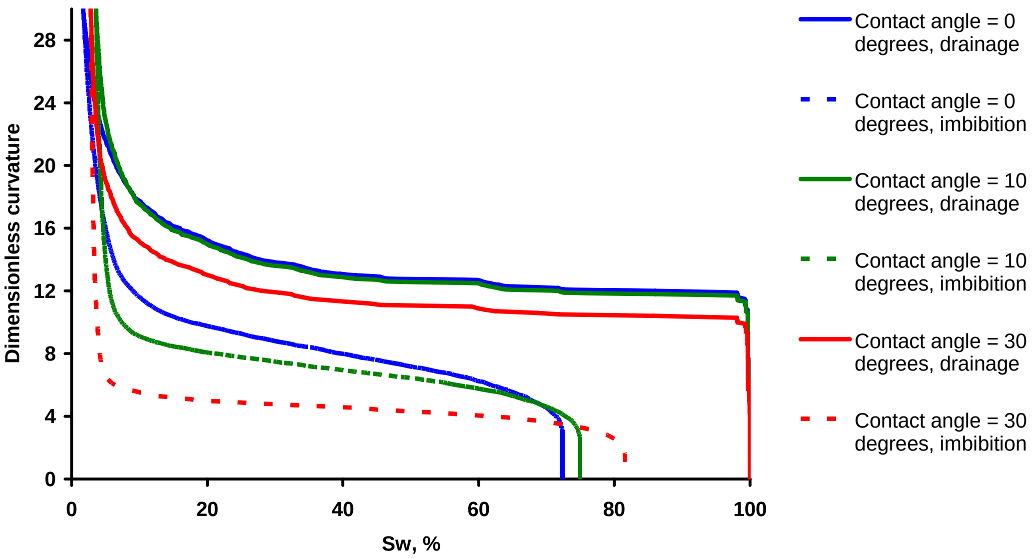

Fig. 56 Influence of wettability on the hysteresis in capillary pressure in the cemented Finney pack. Isopachous cement, porosity = 18.7%.

3.4.2 Influence of Snap-off

The influence of snap-off during imbibition in cemented Finney pack (isopachous cement, porosity = 18.7%) is shown in Fig. 57. In contrast to its negligible effect in the unconsolidated packing (Fig. 51), snap-off has stronger impact on capillary curves in the packing with isopachous cement (Fig. 57). The effect is also stronger for the smaller values of contact angle (Fig. 57). Snap-off not only forces the percolation to occur earlier (at larger curvatures, which is evident for the capillary curve corresponding to the value of contact angle = 0 degrees, in Fig. 57 shown by blue color), but also increases the value of residual NW phase saturation (in Fig. 57 this effect is profound for all capillary curves). Both these results agree with conventional wisdom of the influence of snap-off, but our predictions show that the effect of snap-off affects imbibition capillary pressure curves only for highly cemented pack and small values of contact angle (cf. Figs. 51 and 57).

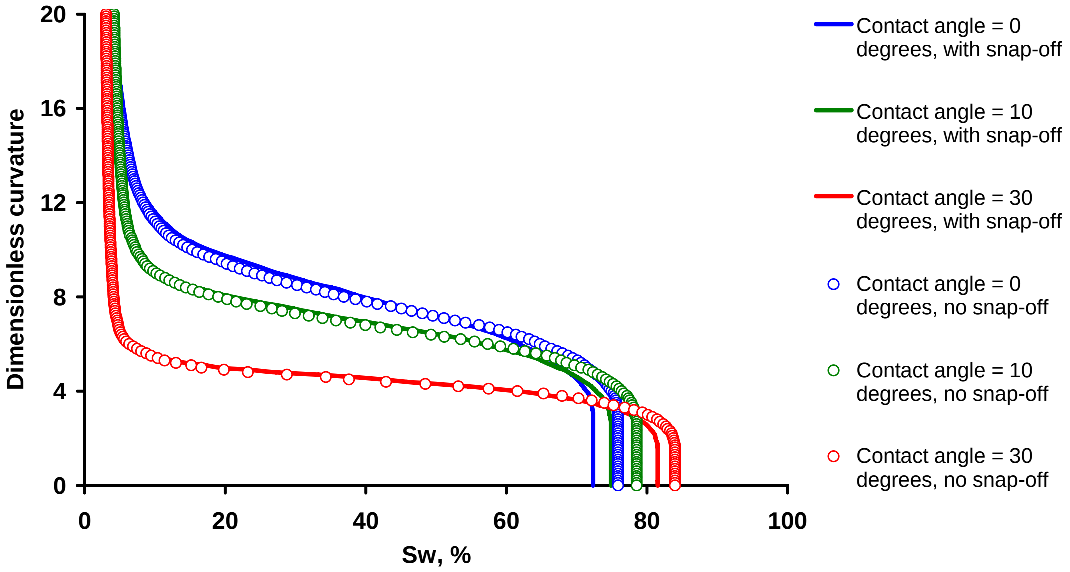

Fig. 57 Influence of snap-off (coalescence of pendular rings) on the imbibition capillary curves in the cemented media. Predictions for the Finney pack (isopachous cement, porosity = 18.7%).

3.5 Capillary Pressure Hysteresis: Media with Pore-Filling Cement

Figs. 58 – 60 depict the influence of pore-filling cementation on hysteresis in capillary pressure for different wettability conditions. This type of cementation was modeled using technique described in section 1.5 above (see Figs. 7 and 8). Maximal cluster size was chosen to be 10 pores.

One effect of pore-filling cementation is the shift of drainage capillary curves up to larger values of dimensionless curvatures (similar to isopachous cementation, Figs. 52 – 54). This is explained by the fact that the connectivity of the pore space (being equal to 4 for the unconsolidated packing) is diminished by the pores completely filled with cement. Therefore this type of cementation has an effect on pore space, qualitatively different from isopachous cementation (Figs. 52 – 54), which decreases pores and throats in size. The effect of pore-filling cement on pore space is the change in percolation behavior of the pore network due to its diminished connectivity. The investigation of this change for different sizes of maximal allowed cluster size of cemented pores is instructive but out of scope of this work. Overall it can be concluded from Figs. 52 – 54 (isopachous cement) and Figs. 58 – 60 (pore-filling cement) that mechanisms that influence percolation behavior by reducing connectivity of pores has a stronger effect than mechanisms that uniformly reduce sizes of pores and throats.

Also, increase in the amount of pore-filling cement pushes the imbibition capillary curve down to smaller values of dimensionless curvature, although the effect is small. This is another result of poorer connectivity of the pore space: presence of cemented pores (and therefore their pore throats) reduces the number of menisci that can be present within a neighboring uncemented pore as compared with the non-cemented case. The number of different combinations of pendular rings and menisci that could lead to imbibition of the pore according to the Melrose criterion decreases (see also sections

2.1.3 and 3.2.4). Thus most pores are imbibed at curvatures smaller than they are imbibed in the non-cemented packing.

Another effect is that during imbibition, increase in the amount of pore-filling cement leads to the increase in the residual NW phase saturation, which is also due to the poorer connectivity of the pore space: the presence of the pores filled with cement increases the likelihood of the entrapment of the pores containing NW phase.

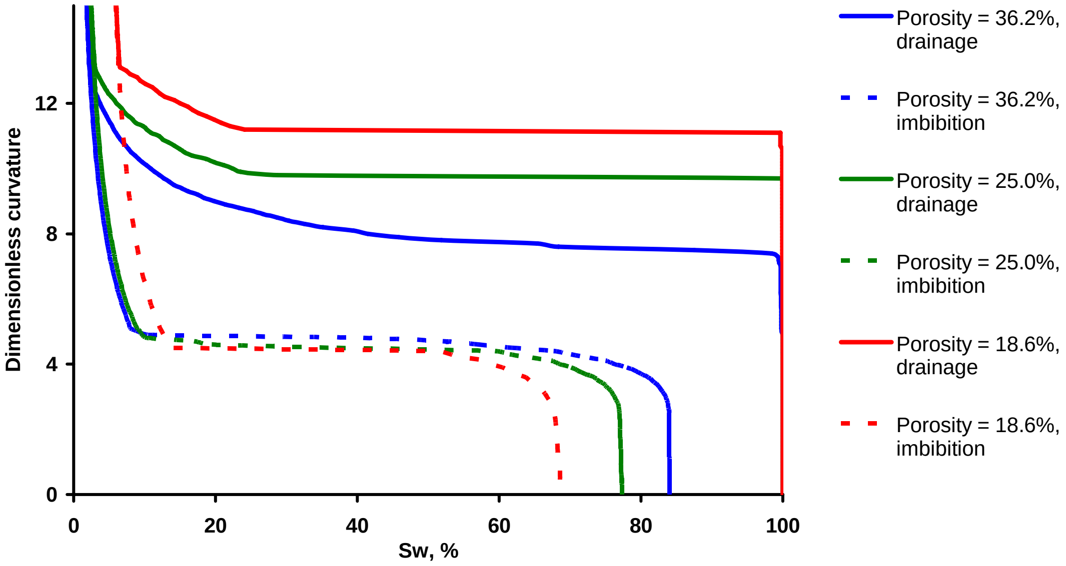

Fig. 58 Influence of pore-filling cementation on the hysteresis in capillary pressure in the cemented Finney pack. Contact angle =0 degrees.

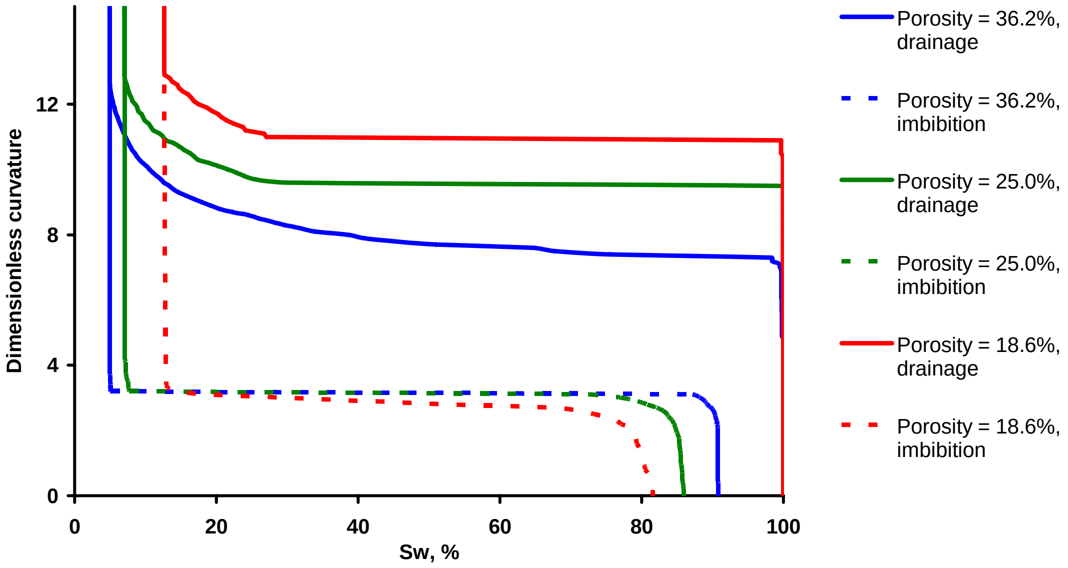

Fig. 59 Influence of pore-filling cementation on the hysteresis in capillary pressure in the cemented Finney pack. Contact angle =10 degrees.

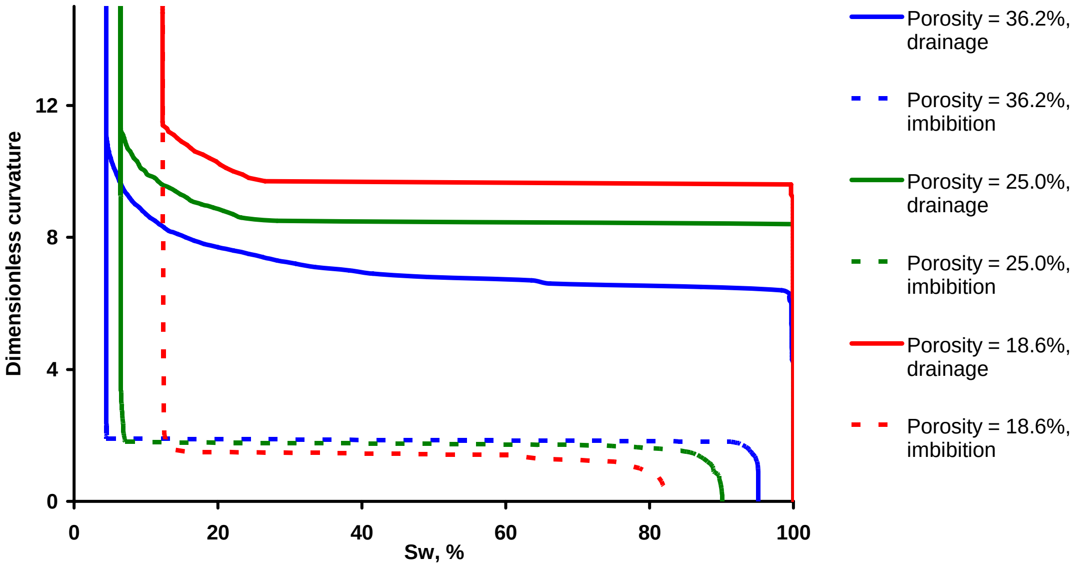

Fig. 60 Influence of pore-filling cementation on the hysteresis in capillary pressure in the cemented Finney pack. Contact angle =30 degrees.

3.5.1 Influence of Wettability

The influence of wettability (specified by the value of contact angle) on the hysteresis in capillary pressure in the Finney pack with pore-filling cement is shown in Figs. 61 and 62 (the values of contact angle are equal to 0, 10 and 30 degrees) Fig. 61 shows data for the packing with porosity 25.0%, Fig. 62 – porosity 18.6%. Qualitatively, the influence of wettability is the same as was shown for the non-cemented media (cf. Figs. 42 and 45).

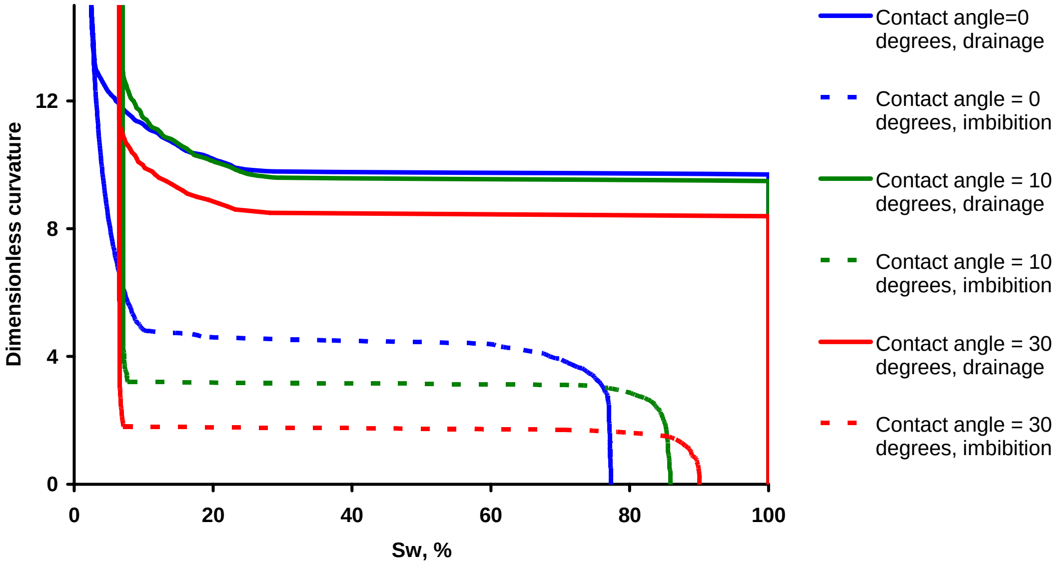

Fig. 61 Influence of wettability on the hysteresis in capillary pressure in the cemented Finney pack. Pore-filling cement, porosity = 25.0%.

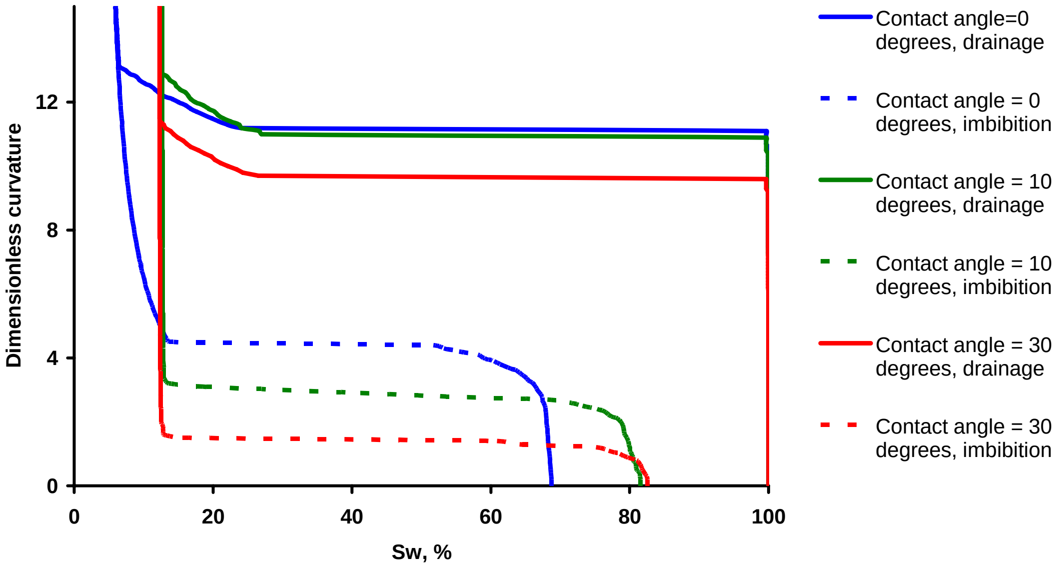

Fig. 62 Influence of wettability on the hysteresis in capillary pressure in the cemented Finney pack. Pore-filling cement, porosity = 18.6%.

Chapter IV

This chapter is dedicated to the simulation of the petrophysical properties of sedimentary rocks, namely, permeability of single-phase flow, relative permeabilities of two-phase flow and electrical properties (resistivity and efficiency) when one fluid phase is a conductor. These properties are fundamental to formation evaluation and many other aspects of petroleum, geological, hydrological and environmental engineering.

4.1 Model of Two-Phase Flow

4.1.1 Network model

We begin with the description of the methodology for the modeling of two-phase flow in model porous media. In this work we follow the approach proposed and developed by Bryant and Blunt [13] and Bryant *et al* [17 – 19].

The algorithm is applied as follows. For each value of dimensionless curvature (during either drainage or imbibition), when static equilibrium configuration of fluid phases is achieved and the geometry and distribution of phases within the packing are known, we simulate two-phase flow in the natural network extracted from the packing by Delaunay tessellation (Figs. 3 and 4). We consider the flow of each phase independently. The phases occupy different sub-networks (parts of the whole network), and the interaction between those networks and fluids within them is neglected. For each phase, each site of the corresponding sub-network (pore body), which corresponds to the internal region of the Delaunay tetrahedron (Fig. 3), is specified by the value of the *flow potential* (or pressure). Each bond of the network (pore throat, face of the tetrahedral cell in Fig. 3), is assigned the value of *hydraulic conductance*. The value of hydraulic conductance for the W phase is a function only of throat geometry, and for the NW phase depends also on the presence of pendular rings at grain contacts, associated with the given pore throat (for the computation of hydraulic conductances, see below, section 4.1.2). The potential drop due to flow within sites (pore bodies) is neglected.

Then the problem of two-phase flow is solved as follows. Because the Finney pack is a spherical conglomerate, it is convenient to impose a spherically symmetric pressure gradient on the network. To do this, pores in a small spherical region at the center of the pack are assigned a fixed potential (P = 1, say), and pores at the external surface of the packing are assigned a different potential (P = 0). We assume that viscous forces are negligibly small in comparison with capillary forces and compute total steady flow Q_i of the phase i through the corresponding sub-network by solving the system of linear equations of mass balance at each site using the method of conjugate gradients. Relative permeability to a phase is then follows from the spherical form of Darcy's law:

$$k_{r,i} = \frac{Q_i \mu}{4\pi K \dfrac{dP}{d\left(1/r\right)}}, \tag{66}$$

where μ is the fluid viscosity and K - absolute permeability of the packing.

4.1.2 Computation of Pore Throat Conductances

The calculations of pore throat conductances are as follows. We approximate the flow through the pore throat by the Poiseuille's equation [1] for the flow through cylindrical tube:

$$q = \frac{\pi r^4}{8\mu l} \Delta P \tag{67}$$

where q is the volumetric flow rate through the tube; ΔP – pressure drop across the tube;

r – tube radius; l – tube length; μ - fluid viscosity. Since the actual pore throats of the Finney packing are not cylindrical tubes, we use some approximations for l and r. For the latter we compute *effective* value r_{eff} for each pore throat, which is calculated from the known geometry of the throat (see below).

Each pore throat in the packing is shared by two pores. We compute hydraulic conductance of the given pore throat only if both these pores contain one phase (that is, they both contain W phase or both contain NW phase). In this case the hydraulic conductance of the pore throat to the corresponding phase has non-zero value. Applying this rule to the fluid configurations obtained at any stage of drainage or imbibition, we obtain a subdivision of the whole network into two parts, each of which conducts only one phase.

The effective radius of the pore throat is computed in the narrowest cross-section, corresponding to the face of the Delaunay tetrahedron (Figs. 63 and 64). Here the triangle *ABC* is the face of the Delaunay tetrahedral cell (cf. Fig. 3), *O* is the center of the circle, inscribed into the pore throat, with the radius $r_{in} = OM = OK = ON$. The effective radius of the pore throat is computed as

$$r_{eff} = \frac{1}{2}(r_{in} + r_a), \tag{68}$$

where $r_a = \sqrt{\dfrac{A}{\pi}}$ and A is the cross-sectional area of the pore throat, available for the flow. For the flow of the W phase, this area is the area of the triangle *ABC* (Fig. 63), minus the area of the circular sectors *CEG*, *BGF* and *ADF*, contained in this triangle, which represent the cross-sectional areas of corresponding grains. For the case of the NW phase flow we also need to account for the presence of the pendular rings of the W phase (Fig. 64), which decreases the area available for the flow of the NW phase and thus its effective radius and conductance.

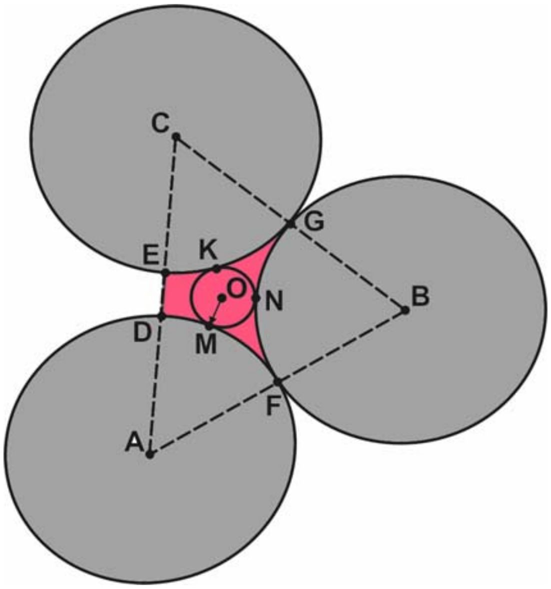

Fig. 63 Pore throat conductance to the flow of the W phase. The cross-section of the pore in the narrowest constriction (face of the tetrahedron, Fig. 3) is shown.

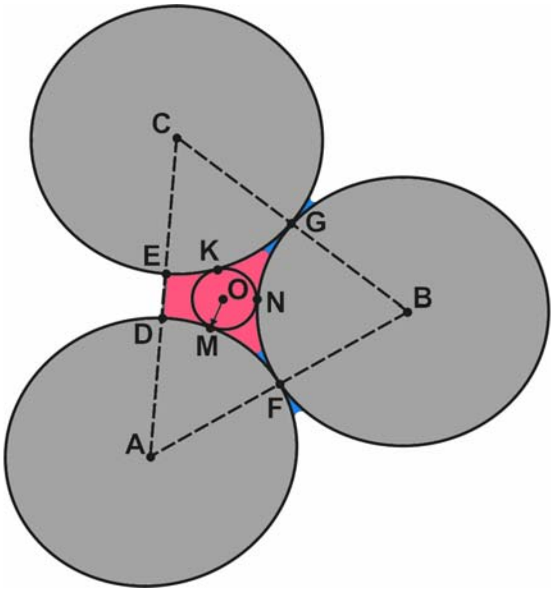

Fig. 64 Pore throat conductance to the flow of the NW phase. The cross-section of the pore in the narrowest constriction (face of the tetrahedron, Fig. 3) is shown. Pendular rings of W phase, shown by blue color at grain contacts (points *G* and *F*) decrease the cross-sectional area of the pore throat, available for the flow of the NW phase, thus decreasing its effective radius and therefore conductance.

The effective length of the tube may be taken naturally as the distance between centers of the corresponding pore bodies (sites). The center of the pore body is defined as the center of the sphere, inscribed into the corresponding tetrahedral pore, which just touches four grains that form this pore (this is the same sphere that defines Haines' insphere criterion for imbibition, see Fig. 12). However, such definition of the effective length of the flow path overestimates the distances traveled by the elements of fluid. This happens because four flow paths entering the pore body overlap each other in the vicinity of its center. To eliminate this double-counting of a momentum loss in a pore body, we simply shorten the lengths of all the flow paths (tubes) in the packing by the same relative amount. Qualitative geometric analysis for the pore throat between two ideal tetrahedral cells (four grains in contact with each other) yields a shortened value of the effective length of about 0.7 of the distance between cell centers. Indeed, the radius of the sphere, inscribed within such a cell, is about 0.2 in dimensionless units (when grain radius is equal to 1.0), and the distance between centers of two inscribed spheres is about 0.6. If we assume that intersection of flow paths occurs within the volumes of inscribed spheres, we need to take the distance between the *surfaces* of spheres instead of the distance between their *centers* as the effective length of the flow path. In this case this distance is about 0.4, or about 0.7 of the distance between the centers of inscribed spheres.

Taking into account qualitative considerations above, we compute the effective lengths of the given pore throat in the following way: first, we compute the distance between the centers of the corresponding pore bodies and then take 0.7 of this distance as the value of the effective length. This procedure applies at any value of saturation during both drainage and imbibition for any pore throat in consideration. No adjustable parameters therefore enter the calculations. Such a choice of effective radii and lengths of pore throats results in computed value of absolute permeability of unconsolidated Finney pack of about 1.5×10^{-3} in units of square grain radii. For the comparison, absolute permeability of different glass bead packs is about 2.7×10^{-3} square grain radii [13, 18].

Detailed description of the permeability calculation, argumentation and discussion regarding the choice of effective radii, lengths and approximations, can be found in [18]. We extended the approach presented in these papers for the presence of pendular rings and applied it for the simulation of two-phase flow during both drainage and imbibition with the detailed calculation of phases' geometries, as described above.

4.2 Model of Electric Current Flow

In order to estimate the water content and quality in formations containing water and another fluid (air, oil, natural gas), electrical measurements are often used. The prediction of the dependence between electrical resistivity of the rock and its saturation is therefore of great practical interest.

To model electric current flow through the fluid-filled porous media, we use the same approach that was described above (section 4.1) to compute relative permeabilities of two-phase flow. It is necessary to define whether W or NW phase is conductive (or, in other words, to specify whether the rock is water- or oil-wet, since we consider water (brine) to be conductive and oil (air) and solid grains to be insulators). We assume that no conduction occurs on the grain surfaces. The total electrical conductance (see section 4.1) is computed in the network, extracted from the Finney pack.

The electrical conductance of the bond (pore throat) is computed similarly to its hydraulic conductance (section 4.1.2). We approximate current I through the pore throat as the current flowing through the conduit of length l having constant cross-sectional area A:

$$I = \frac{A\sigma_w}{l}\Delta V, \tag{69}$$

where ΔV – voltage drop across the pore throat; σ_w – conductivity of conducting fluid; A – cross-sectional area of conduit; l –length of the conduit.

As the cross-sectional area of conduit we take cross-sectional area of the narrowest constriction at the pore throat (triangle ABC, Figs. 63 and 64). It is natural to take the effective length used in two-phase flow simulation (section 4.1.2) as the effective length of the conduit for the electric current flow in order to avoid double-counting of the path lengths followed by the current. Eq. (69) still assumes that the flow paths have constant cross-section, which is not the case for tetrahedral cells – cross-sectional area increases along the pore throat as it approaches cell center. Fortunately, in most Delaunay cells in the Finney pack the change in cross-sectional area is small [18].

Pendular rings, which exist at grain contacts, also contribute to the electrical conductance of the packing. If the conductive phase is the NW phase (oil-wet rock) then pendular rings simply decrease the cross-sectional area of the pore throat, available for the flow of electric current (similar to two-phase flow, see Figs. 63 and 64). If the conductive phase is the W phase, then pendular rings provide connections between the pores filled with the W phase, even if these pores are not immediate neighbors and are not connected directly by the pore throats (Fig. 65).

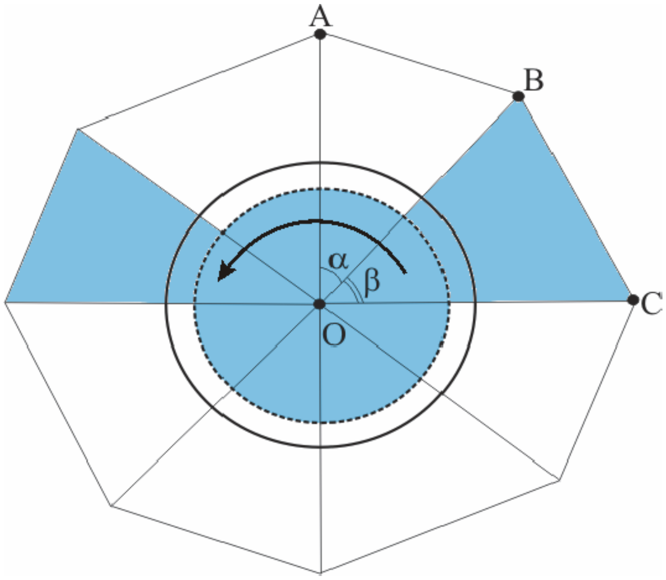

Fig. 65 Illustration of the electrical conductance via pendular ring. Spherical grain contour is shown by the solid black line; pendular ring contour – by dotted line. The view corresponds to the projection onto the *YOZ* plane in Fig. 17. Pores around the grain contact are shown schematically by triangles; pore throats – by their edges (OA, OB and OC). The W phase is shown by blue color. The conductive path via pendular ring is shown by the arrow.

Fig. 65 illustrates the conductance of pendular rings. Each grain contact in the packing is contained in several tetrahedral pores as the edge common to those tetrahedra (see Fig. 3); or, in other words, several pores exist around each grain contact. Fig. 65 shows the grain contact (cf. Fig. 17; in Fig. 65 grain contact is depicted in two-dimensional view, corresponding to the coordinate plane *YOZ* in Fig. 17), pendular ring at this grain contact, and several pores around this grain contact.

If more than two pores, filled with the W phase, exist around the grain contact (Fig. 65), there is a path for the flow of electric current between them via the pendular ring (see Fig. 65, the W phase is shown by blue color, the conductive path – by the arrow). This is true even though NW phase fills the pores between two W-phase-filled pores. This is different from the situation described above for fluid flow, in which throats only allowed flow between pores containing the same phase. At small W phase saturations this effect is potentially important, so we approximate such a conductance in the following way. Each pore throat, associated with a grain contact such as that shown in Fig. 65 and connecting two pores, at least one of which contains NW phase, is assigned a nonzero value of electrical conductance. (Recall that pore throats, defined by the faces of the Delaunay tetrahedra, Fig. 3, are shown in Fig. 65 by the corresponding projections (lines OA, OB and OC)). First, we compute the two-dimensional cross-sectional area A_{ring} in the narrowest constriction of the corresponding pore throat, occupied by the pendular ring (see also Fig. 16). Then we compute the dihedral angles between the planes that contain the considered pore throat (OB in Fig. 65) and neighboring pore throats (OA and OC). These angles are denoted in Fig. 65 as α and β. The conductance of the pore throat is then approximated by the formula

$$C_{throat} = \frac{A_{throat}}{b\left(\frac{\alpha+\beta}{2}\right)}, \tag{70}$$

where b is the *liquid neck* of the pendular ring (its value is equal to the distance between the point A and the X-axis in Fig. 17). The value of b is determined by the geometry of the grain contact and the curvature, as described in section 2.2.1.

The methodology described above results in computed value of dimensionless formation factor (Eq. (71)), normalized by the brine conductivity, for unconsolidated Finney pack of about 4.0 in dimensionless units (grain radius equal to 1). For the comparison, formation factor of different glass bead packs is about 3.4 in dimensionless units [16].

4.3 Concept of Electrical Efficiency

Electrical properties of porous media are usually reported in terms of *formation factor* (for fully saturated media) and *resistivity index* (for partially saturated media) [121]. The first is defined as

$$F = \frac{C_w}{C_0}, \tag{71}$$

where C_w is the conductivity of the conductive phase (brine) and C_0 is the conductivity of the fully saturated sample. The resistivity index is defined as

$$I_R = \frac{1/C_t}{1/C_0}, \tag{72}$$

where C_t is the conductivity of partially saturated sample.

The basis for the resistivity log interpretation is empiric Archie's equations [4, 121, 129], which relate properties of interest (porosity and brine saturation of the formation) to the measured electrical properties:

$$F = \frac{a}{\phi^m}, \tag{73}$$

$$I_R = S_w^{-n}. \tag{74}$$

Here ϕ is the formation porosity and S_w – its brine saturation. Empirical constants m and n are called *cementation* and *saturation* exponents correspondingly and a is an empirical constant usually assumed to be equal to 1 [121].

Although widely applied, Eqs. (73) and (74) are simply the generalization of some experimental facts. They do not have any underlying physical basis and do not provide any insight into the influence of pore geometry on electrical properties of porous media.

In order to quantify the influence of pore geometry on electrical properties of porous media, Herrick and Kennedy [63] suggested the concept of *electrical efficiency* instead of resistivity index correlated with water content by Eq. (74).

For a rock sample, fully saturated with the conductive phase, electrical efficiency is defined as a ratio of sample conductivity to the conductivity of the most efficient pore geometry: a cylindrical capillary tube, having the same amount of pore space [63]:

$$E_0 = \frac{C_0}{C_w \phi} \ . \tag{75}$$

Thus defined, electrical efficiency of the sample (E_0) depends only on pore space geometry and is equal to 1 for the most efficient geometry, i.e. that of a cylindrical tube.

When hydrocarbons are present, (75) should be modified as [63]

$$C_t = C_w S_w \phi E_t \, , \tag{76}$$

where C_t – conductivity of partially saturated rock sample, E_t – its electrical efficiency, which can be expressed as a product of two factors: $E_t = e_t E_0$, where e_t corrects electrical efficiency of fully saturated media (Eq. (75)) for the presence of hydrocarbons. Detailed description of this concept and physical basis underlying it can be found in [63].

Herrick and Kennedy [63] also presented experimental data for different sandstones and carbonates, which suggest that the relationship between electrical efficiency and porosity (for a fully saturated media) and efficiency and water saturation (partially saturated porous media) is linear. Thus, one of our objectives in this work is to find out whether the modeling of electric current flow in the Finney pack is able to represent these experimental trends and investigate what underlies these linear relationships.

4.4 Results: Fully Saturated Packing

4.4.1 Relationship between Permeability and Porosity

The simulations of single phase flow in the Finney pack were performed with the methodology described above. Fig. 66 presents the results of these simulations as the dependence between the porosity and permeability of the packing for different types of cementation (see section 1.5).

Fig. 66 shows the dependence between permeability and porosity for the uniform isopachous cement (that is, the radii of the grains are increased uniformly by the same value) and random isopachous cement (each grain radius is increased by the random value; the corresponding distribution of radii is taken uniform in the specified interval). As one can see from Fig. 66, the dependence between permeability and porosity is the same for both these cases. This demonstrates the independence of the macroscopic property (i.e. permeability) of the porous media on the details of cementation; the important is the type only (i.e. isopachous cement).

Another interesting observation in Fig. 66 is that the pore-filling cement, occurring in clusters of one single pore, decreases the permeability of the packing more rapidly, than the isopachous cement. But, on the other hand, if pore-filling cement occurs in clusters of larger size, its effect on reducing permeability can be comparable or even smaller than the effect of isopachous cementation. The reason for this is that these two types of cement (isopachous and pore-filling) reduce porosity in a qualitatively different way. Isopachous cement uniformly diminishes sizes of pores and pore throats; pore-filling cement reduces connectivity of the pore network (see also sections 3.4 and 3.5 for the influence of these two types of cement on the capillary pressure curves). Moreover, pore-filling cement blocks the pore space more effectively if the size of maximal allowed cluster of cemented pores is small. Permeability for the case of clusters of single pore vanishes at porosity of about 15%; for the case of clusters of 10 pores – of about 10%.

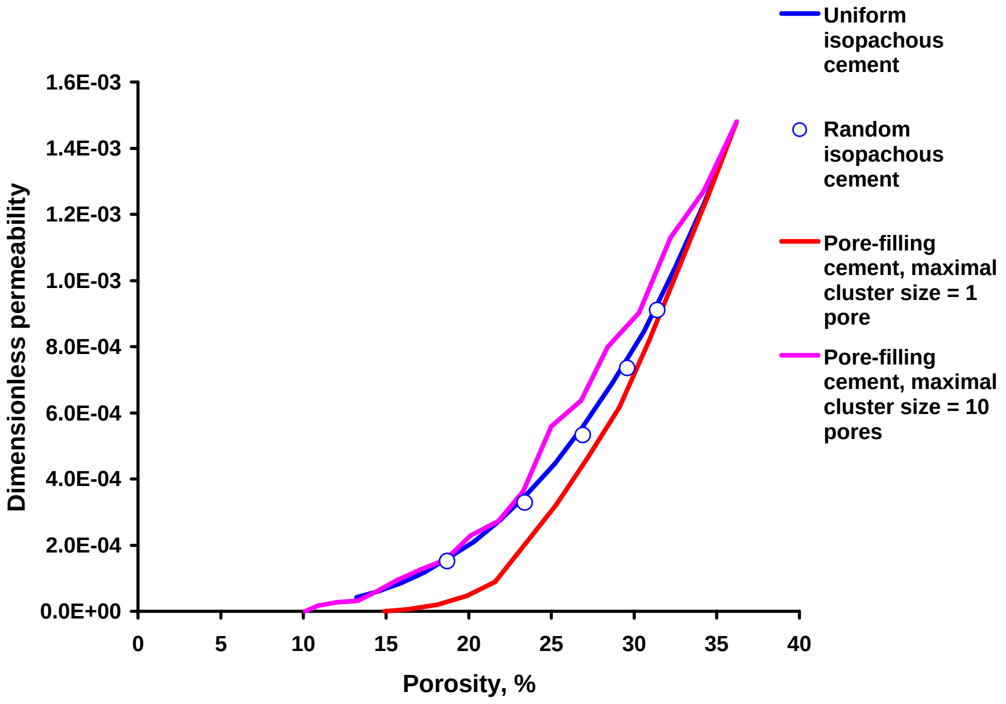

Fig. 66 Simulation of single phase flow for different types of cementation in the Finney pack. Permeability – porosity relationship.

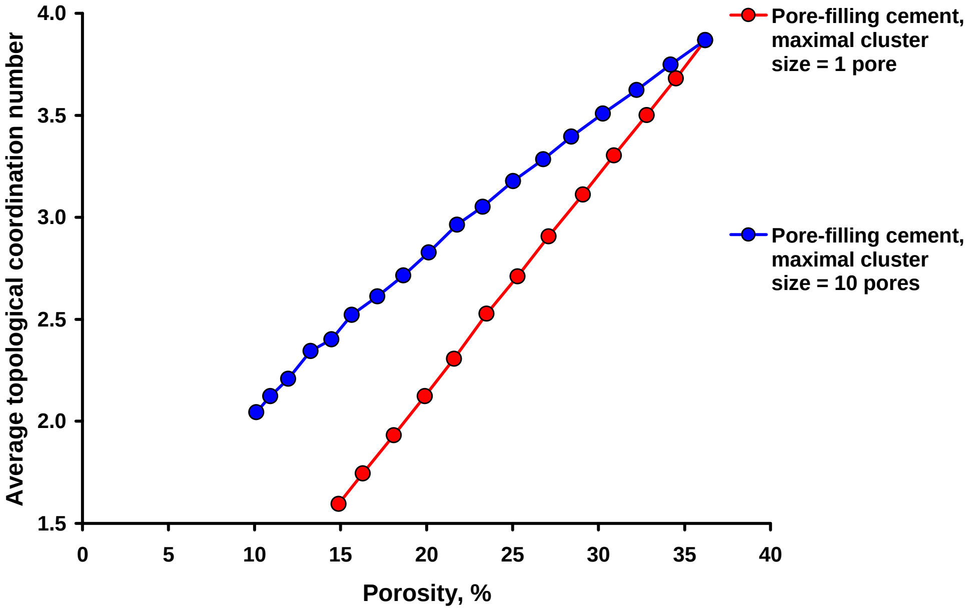

Fig. 67 Average topological coordination number of non-cemented pores as a function of porosity for pore-filling cement.

In order to illustrate the impact of maximal allowed cluster size on the network connectivity and its percolation properties, we show in Fig. 67 average topological coordination number of non-cemented pores in the packing as a function of porosity for pore-filling cement with clusters of one and 10 pores. This parameter is the same as was described in section 3.2.5; here we consider non-cemented pores and compute their average topological coordination number rather than pores with the W phase as described in section 3.2.5.

It can be seen from Fig. 67 that the impact of cement with clusters of one pore on the pore network connectivity is much larger – it reduces average topological coordination number much faster with porosity than cement with clusters of 10 pores. This result is intuitively clear – when the same number of cemented pores is distributed randomly throughout the packing (clusters of one pore), it blocks more pore throats than if these pores are tend to be clustered together. The influence of the first type on single-phase flow is therefore higher (Fig. 66).

For the case of uniform isopachous cement an extensive description of the methodology used and results for the Finney pack together with the comparison with experimental data of permeability–porosity relationship can be found in Bryant *et al* [17].

4.4.2 Relationship between Electrical Properties and Porosity

Figs. 68 – 69 present results of simulations of electric current flow in the Finney pack for different types of cement (isopachous and pore-filling).

Fig. 68 shows the dependence between electrical efficiency of the packing and its porosity. Although trends are not linear (as may be expected from the experimental data by Herrick and Kennedy [63], see preceding section) for all ranges of porosity, they can be accurately approximated as linear when porosity is sufficiently large. For example, in the case of uniform isopachous cementation blue solid line (Fig. 68) represents the deviation of the trend from linearity as porosity decreases (grain radius increases). This behavior allows a simple explanation. Indeed, for the case of uniform isopachous cement, both porosity and efficiency are continuous functions of grain radius increase (Fig. 6, shown by orange), which we denote here as δR. Thus they can be written as a Taylor expansion series with small variable δR. All the non-linear terms in the expansion are negligible in comparison with the linear term when δR is sufficiently small and so the function is linear with its argument. The implication of this is that electrical efficiency as a function of porosity has linear trend when grain radius increase δR is sufficiently small but starts to deviate from linearity when non-linear terms of Taylor series expansion become comparable with the linear term.

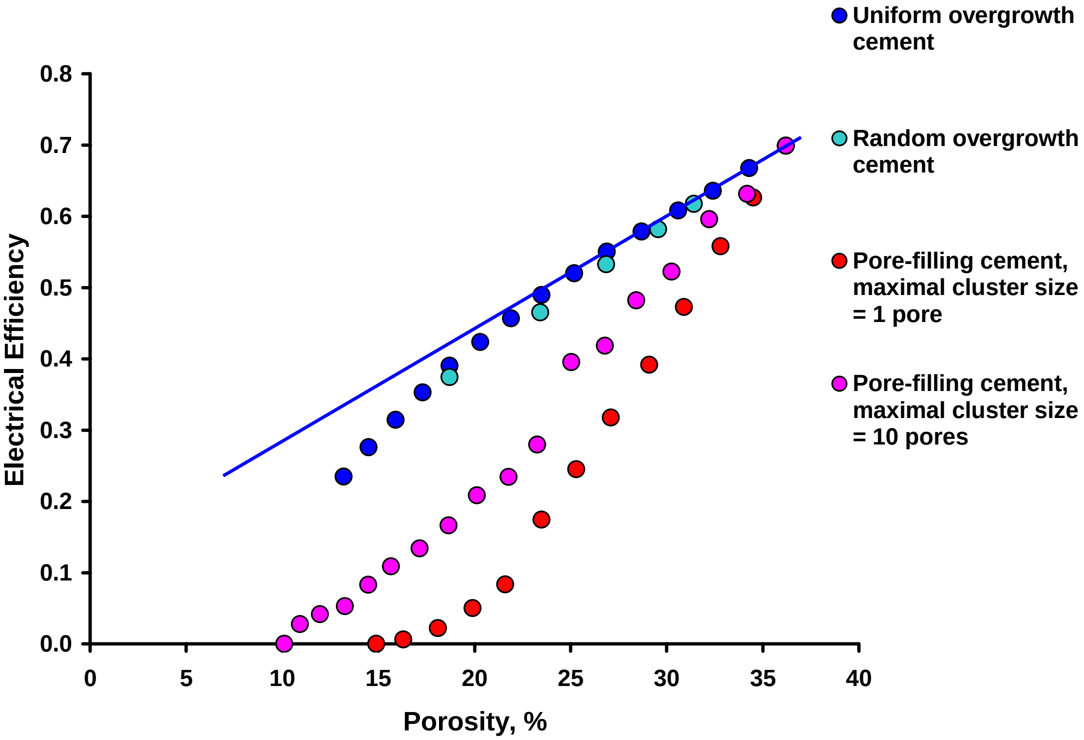

Fig. 68 Simulation of electric current flow for different types of cementation in the Finney pack. Electrical efficiency – porosity relationship.

Similar to the permeability – porosity relationship, both uniform and random isopachous cementation produce similar results for the dependence between efficiency and porosity. It is worth noting also that in the case of electric current flow, pore-filling cement reduces electrical efficiency much faster (as porosity decreases) in comparison with isopachous cement. This statement is true even for large pore-filling clusters (Fig. 68), unlike for the case of single phase flow (Fig. 66). This is explained by the fact that the effect of pore-filling cementation is similar for both single phase and electric current flow, being simply the exclusion of some bonds from the network (shown in Fig. 4). Isopachous cementation, on the other hand, has qualitatively different influence on single phase flow (the conductance of the pore throat is given by Eq. (67) and depends on its effective radius as r^4) and electric current flow (the conductance of the pore throat is given by Eq. (69) and depends linearly on its cross-sectional area, that is, it depends on its effective radius roughly as r^2). The latter influence therefore is much smaller.

Fig. 69 presents the results of the simulation of the flow of electric current in its most common form – the relationship between dimensionless formation factor (Eq. (71)), normalized by the brine conductivity, and porosity of the packing. The results are shown on the logarithmic scale. Although such way of presenting electrical data is widely used in order to obtain linear correlation between formation factor and porosity and then use empirical Archie's equation (73), this way is certainly not the best. The measurement error at small conductances accentuates the error in formation factor at small porosities, making this part of plot in Fig. 69 unreliable. Also, as was pointed out above, Eq. (73) is purely empirical and does not have any physical basis underlying it. Moreover, the linearity between log formation factor and log porosity, as Eq. (73) assumes, is not always true. This is evident from the results, shown in Fig. 69, especially when the cementation type strongly affects electrical properties of the packing (pore-filling cement with maximal cluster of one pore).

Taking into account all mentioned above, we believe that the concept of electrical efficiency, being the one that takes into account the influence of pore geometry on electrical properties, should be used when analyzing electrical data.

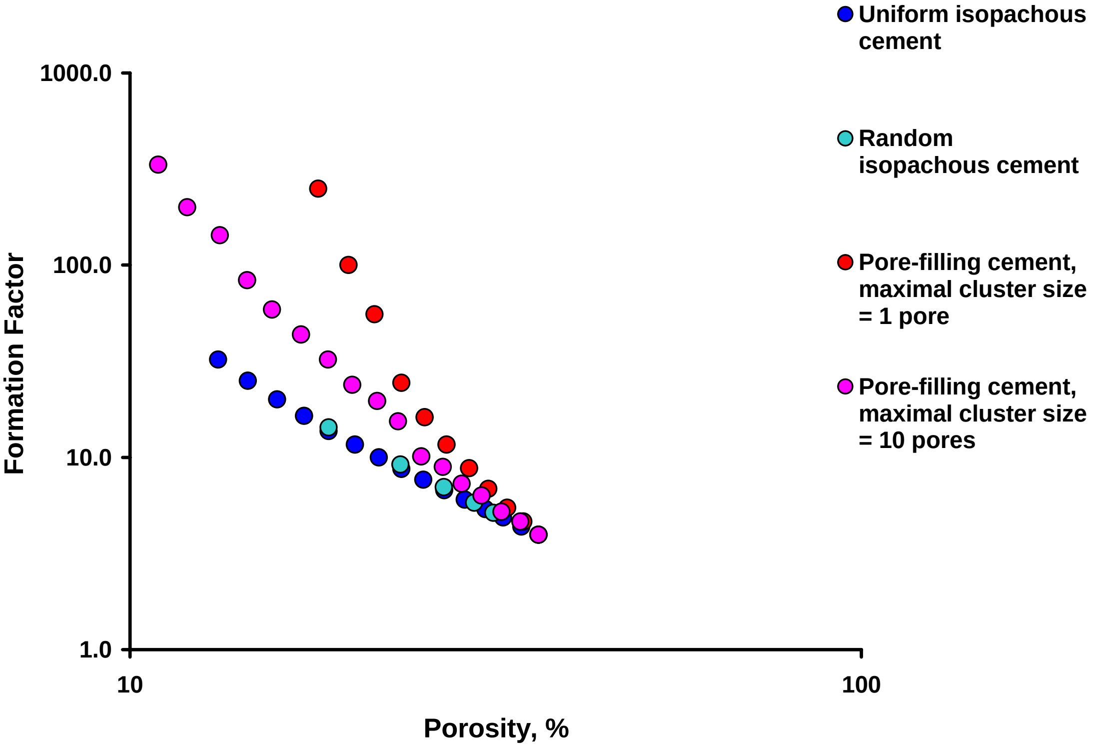

Fig. 69 Simulation of electric current flow for different types of cementation in the Finney pack. Dependence between log formation factor and log porosity.

4.5 Results: Partially Saturated Packing

4.5.1 Comparison between Predicted Relative Permeabilities and Experimental Data

Using the technique, described above, we compute relative permeabilities of two-phase flow during both drainage and imbibition in the Finney packing for the whole range of saturations.

First, we compare the results of the predictions for the relative permeabilities of two-phase flow in the unconsolidated Finney pack with existing experimental data. Fig. 70 presents such a comparison. We simulated two-phase flow in the unconsolidated Finney pack, value of contact angle = 0 degrees, number of entrance pores is equal to 9. Experimental data for the comparison is taken from the paper by Naar *et al* [105]. The experiments were performed for both drainage and imbibition in a binary mixture of glass spheres. The authors reported strong water-wet behavior of their system, so we compare their data with the simulations for the contact angle = 0 degrees. Fig. 70 illustrates good agreement between predictions and experiments for both relative permeabilities to the W and NW phases during drainage, thus providing additional support to the methodology. The deviation for the relative permeability to the NW phase at intermediate saturations can be attributed to overestimation of the influence of pendular rings at grain contacts and lenses of the W phase at pore throats. This discrepancy is the subject of future research.

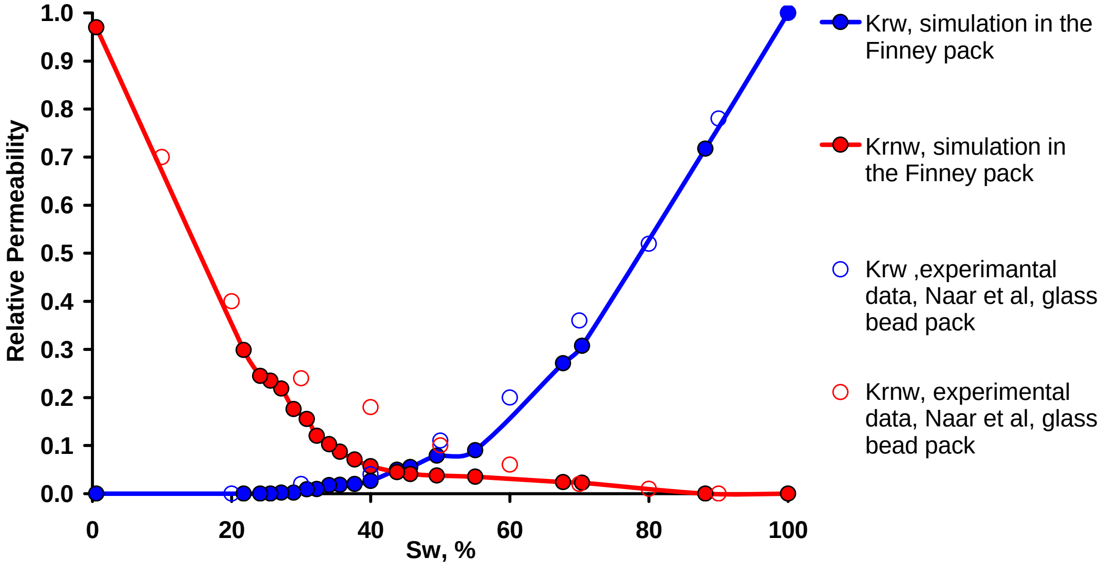

Fig. 70 Comparison between predicted relative permeabilities of two-phase flow during drainage in the unconsolidated Finney pack (contact angle = 0 degrees, 9 entrance pores) and experimental data by Naar *et al* [105] for glass bead pack.

The extensive analysis of the simulations of two-phase flow in the Finney pack during drainage and comparison with experimental data can be found in Bryant and Blunt [13].

Fig. 71 presents a comparison between predictions and experiments for imbibition. We simulated two-phase flow in the unconsolidated Finney pack, value of contact angle = 0 degrees, number of entrance pores is equal to 11. Experimental data for the comparison is taken from the paper by Naar *et al* [105]. Similarly to drainage (Fig. 70), the agreement between simulations and experiment is good, although the predictions for the relative permeability to the NW phase give consistently lower values than the experiment. But since there is an uncertainty in wettability conditions (the contact angle value was not measured independently during experiment, although authors report strong water-wet conditions) and bead size influence (binary mixture of glass beads was used in the experiments, and the Finney pack consists of the spheres of equal size), some deviation may be expected.

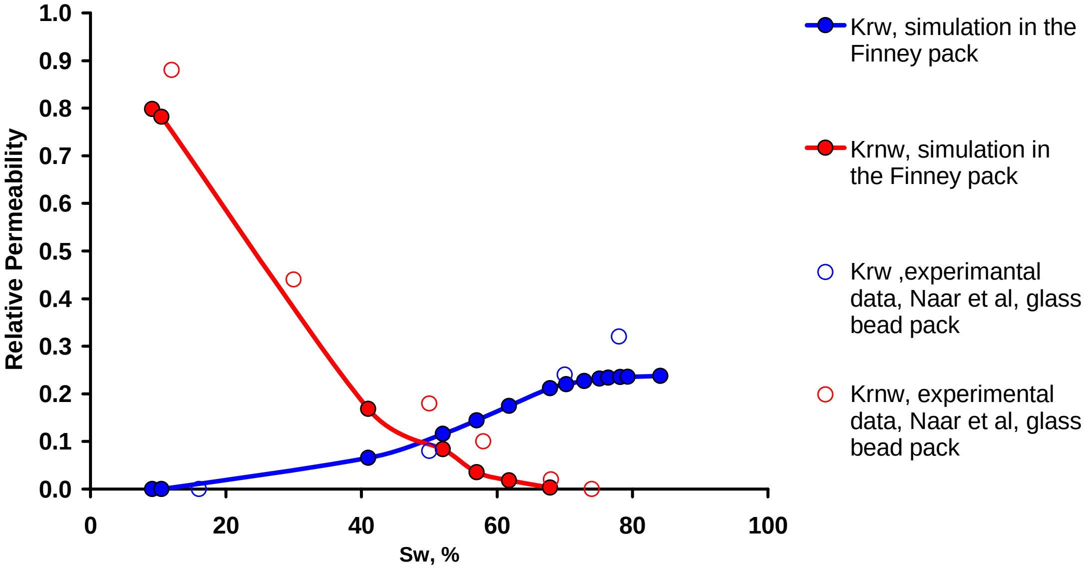

Fig. 71 Comparison between predicted relative permeabilities of two-phase flow during imbibition in the unconsolidated Finney pack (contact angle = 0 degrees, 11 entrance pores) and experimental data by Naar *et al* [105] for glass bead pack.

4.5.2 Influence of Wettability on Relative Permeabilities

It is interesting to quantify the effect of wettability, specified by the value of contact angle, on relative permeabilities of two-phase flow. The results of two-phase flow simulations during drainage in the unconsolidated Finney pack for different wettability conditions are shown in Fig. 72. Relative permeabilities to both phases were computed for the values of contact angle of 0, 10 and 30 degrees. The number of entrances was chosen to be 200 pores in order to approach percolation threshold smoothly and compute more points for relative permeabilities. It must be noted here that in order to maintain consistency between simulations and make a fair comparison between them, we choose exactly the same boundary conditions (namely, 200 entrance pores) for all simulations, regardless of wettability conditions and cementation type and degree. However, when the value of contact angle is large, the percolation during imbibition is very rapid (even with 200 entrance pores), which prevents computing values of relative permeabilities at intermediate saturations. This is the reason why there are hardly any curves for relative permeabilities, for example, in Fig. 73 (contact angle = 30 degrees); the same explanation holds for other predictions (and for electrical properties as well, see below), when there are no points at intermediate saturations for large values of contact angle.

From Fig. 72 one can see that the influence of wettability on relative permeabilities during drainage is negligible. This result is readily explained by the drainage criteria used (Haines' face insphere, Eq. (2), see section 2.1.2), which does not assume the change in the sequence of pore-level events and phase morphologies when the value of contact angle changes (cf. also with the influence of wettability on drainage capillary pressure curves, section 3.1.2). The small deviation between the curves in Fig. 72 is due to the difference in the shapes of the interfaces (pendular rings and menisci) for the different values of contact angle. Therefore, it is not instructive to present the results of simulations for the influence of wettability on drainage relative permeabilities, since the considerations mentioned above apply for any condition that we are able to model (i.e. different types of cement). We will omit the figures with the influence of wettability on drainage relative permeabilities in further discussion.

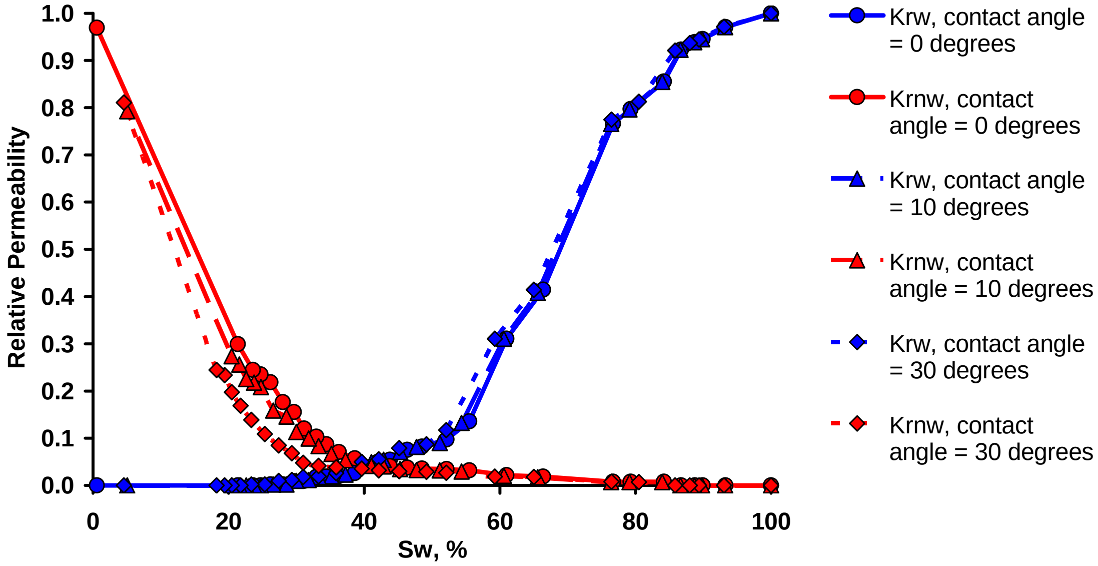

Fig. 72 Influence of wettability on relative permeabilities of two-phase flow during drainage in the unconsolidated Finney pack.

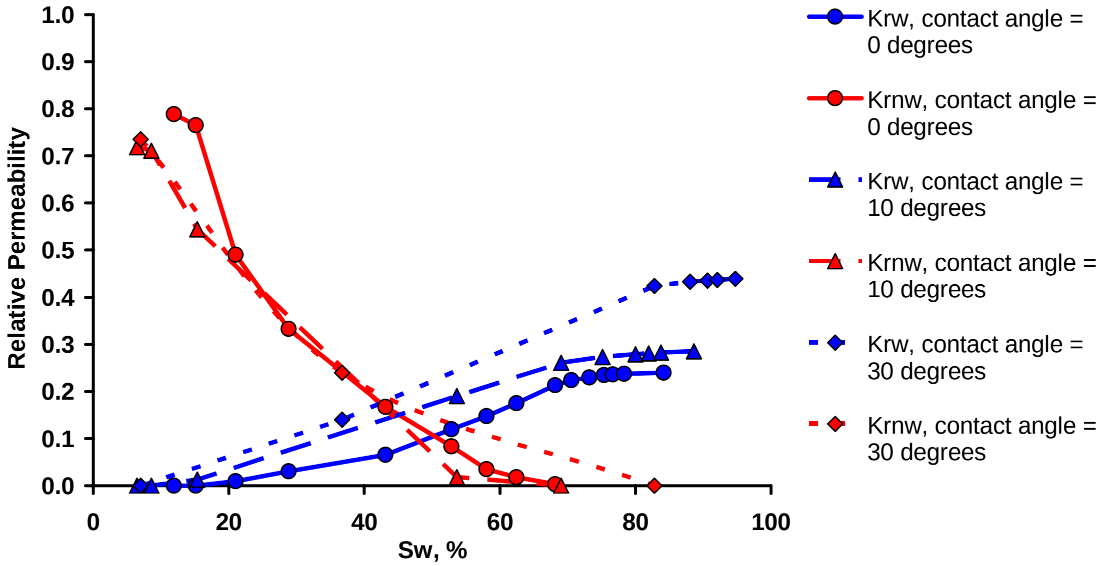

Fig. 73 Influence of wettability on relative permeabilities of two-phase flow during imbibition in the unconsolidated Finney pack.

Fig. 73 presents the results of two-phase flow simulations in the unconsolidated

Finney pack for different wettability conditions during imbibition. Relative permeabilities to both phases were computed for the values of contact angles of 0, 10 and 30 degrees. The number of entrances was chosen to be 200 pores.

It can be seen from Fig. 73 that relative permeability to the NW phase is not very sensitive to the wettability of the system, though its decrease for low W phase saturation for the case of contact angle, equal to zero, is slower, than for other values of contact angle. This is a result of qualitatively different character of imbibition in strongly wet system (contact angle is zero) and weakly wetted system (non-zero contact angle). Since W phase is completely connected in strongly wetted system, pendular rings grow simultaneously throughout the whole packing, and the W phase saturation increases correspondingly; the decrease of relative permeability to the NW phase is also associated with this growth of rings and the corresponding decrease of the cross-sectional pore throat areas, available for the flow of the NW phase. For the case of non-zero contact angle pendular rings are disconnected from the bulk W phase and cannot grow, thus W phase saturation increases only as a result of the imbibition of the pores. Imbibition of pores has a stronger effect on the NW connectivity and thus its relative permeability. The endpoint of the NW relative permeability corresponds to the value of residual NW saturation and thus is strongly sensitive to wettability, as explained in Chapter III.

Relative permeability to the W phase at the same time is very sensitive to the wettability (Fig. 73). As the contact angle increases, relative permeability to the W phase also increases, and this happens for the whole range of saturation. This effect is caused by the different *morphology* of the W phase for different wettabilities, and was qualitatively predicted in section 3.2.5 from the influence of wettability on W phase topological coordination number.

Qualitative empirical support for the predictions of this character concerning influence of wettability on relative permeabilities during imbibition is provided by Owens and Archer [108] and Hamon and Bennes [58]. Owens and Archer [108] performed series of experiments to quantify the influence of wettability on relative permeabilities of two-phase flow in sandstones. Unfortunately, they normalized their data to relative permeability at irreducible W phase saturation, which makes direct comparison impossible. Qualitatively, though, their results are similar to our predictions, namely, the increase of relative permeability to the W phase during imbibition with the increase of contact angle. Hamon and Bennes [58] present experimental data for imbibition in samples from West Africa sandstone reservoir. They observed strong correlation between relative permeability to water (W phase) at oil residual saturation and height above water-oil contact. Namely, their data show that relative permeability to the W phase increases with the height. The latter is the measure of the reservoir wettability, since wettability to water decreases as the elevation above water-oil contact increases. The observations therefore are qualitatively consistent with our predictions shown in Fig. 73.

We are not aware however of the existence of the data with the strong influence of small contact angles on imbibition relative permeabilities. This trend remains the subject of future research.

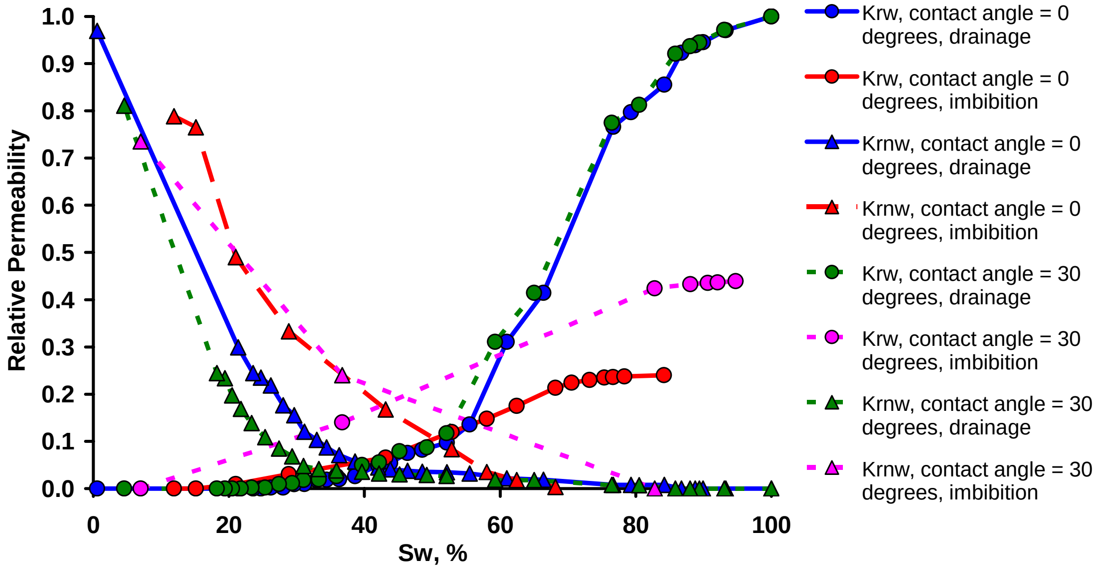

Fig. 74 Hysteresis in relative permeabilities of two-phase flow in the unconsolidated Finney pack. Influence of wettability.

Finally, for reference Fig. 74 shows the existence of hysteresis in relative permeabilities of two-phase flow in the unconsolidated Finney pack and the influence of wettability on such hysteresis. Presented are the results of simulations for the values of contact angle of 0 and 30 degrees for both drainage and imbibition.

4.5.3 Relative Permeabilities: Media with Isopachous Cement

We illustrate in Figs. 75 – 80 the influence of isopachous cementation on relative permeabilities of two-phase flow during drainage (Figs. 75 – 77) and imbibition (Figs. 78 – 80) for different wettability conditions. This type of cementation was modeled as described in section 1.5 (see Figs. 5 and 6) by uniform increase of grain radii until the desired porosity was reached.

It is interesting that isopachous cementation has no effect on drainage relative permeabilities for any value of contact angle (Figs. 75 – 77). The reason for this is again the use of Haines' insphere criterion for the modeling of drainage, which yields exactly the same sequence of pore-level events during drainage in the Finney pack regardless of its degree of cementation, since cement grows uniformly for all grains in the packing and therefore reduces pore throat sizes by the same value. This leads to the same morphology of phases, distributed in the network, used for the simulation of two-phase flow (section 4.1.1) and therefore results in similar values of relative permeabilities.

On the other hand, there is a strong influence of isopachous cement on imbibition relative permeabilities (Figs. 78 – 80). The more cemented the packing is, the smaller are the values of relative permeabilities to both phases consistently for the whole range of saturations and any value of contact angle. For example, relative permeability to the W phase at residual saturation becomes smaller than 0.1 for highly cemented packing (porosity 18.7%, Figs. 78 – 80). It turns out that the presence of uniform layers of isopachous cement changes the sequence of local imbibition events, which happen according to Melrose criterion of imbibition (see section 2.3.1), in such a way that average topological connectivity of the W phase (see section 3.2.5 for its definition) decreases in comparison with non-cemented packing. In this sense the influence of isopachous cementation has an opposite effect to that of wettability (see results in section 3.2.5). The reason for this is that Melrose criterion for imbibition has purely geometrical nature. Both the presence of isopachous cement and change in contact angle result in the change in the shapes of pendular rings and menisci, which, in turn, changes the character of imbibition according to Melrose criterion. In highly cemented packing pores become small, and geometry of rings and menisci is defined almost exclusively by geometry of cemented pore space; change in contact angle does not change much shapes of rings and menisci. This is the reason why influence of contact angle disappears in a highly cemented packing (see below, Figs. 81 – 82). This effect once again emphasizes strong relation of Melrose criterion to the pore space geometry.

This qualitative prediction of the influence of isopachous cement provides yet another independent tool of checking the consistency of Melrose criterion for imbibition. We are not aware of any experimental data that can be directly compared to these predictions, though. Overall, the results of this section are subject to future research.

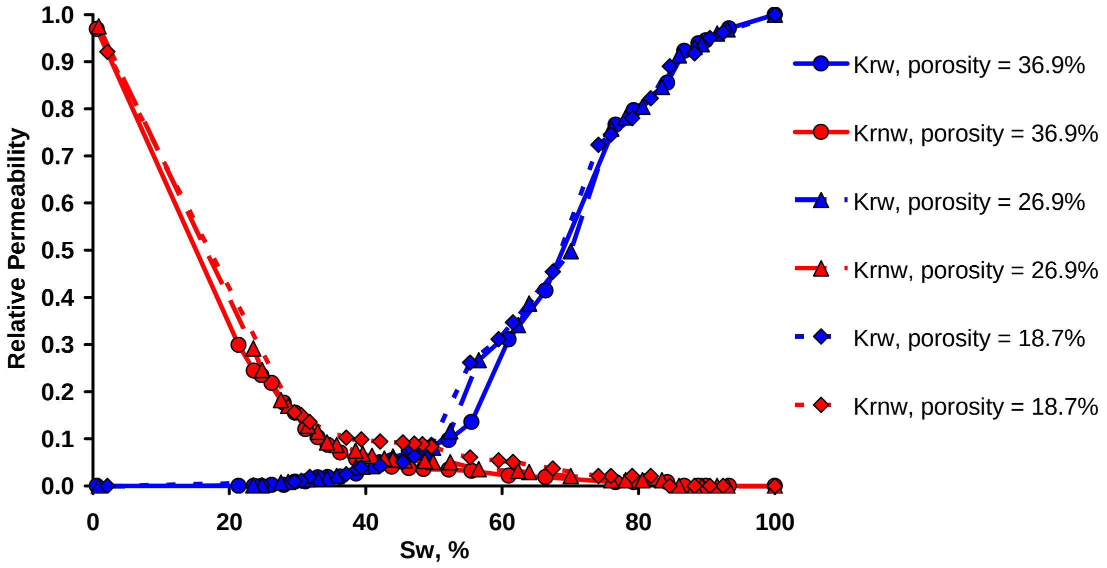

Fig. 75 Influence of isopachous cementation on drainage relative permeabilities in the Finney pack. Contact angle =0 degrees.

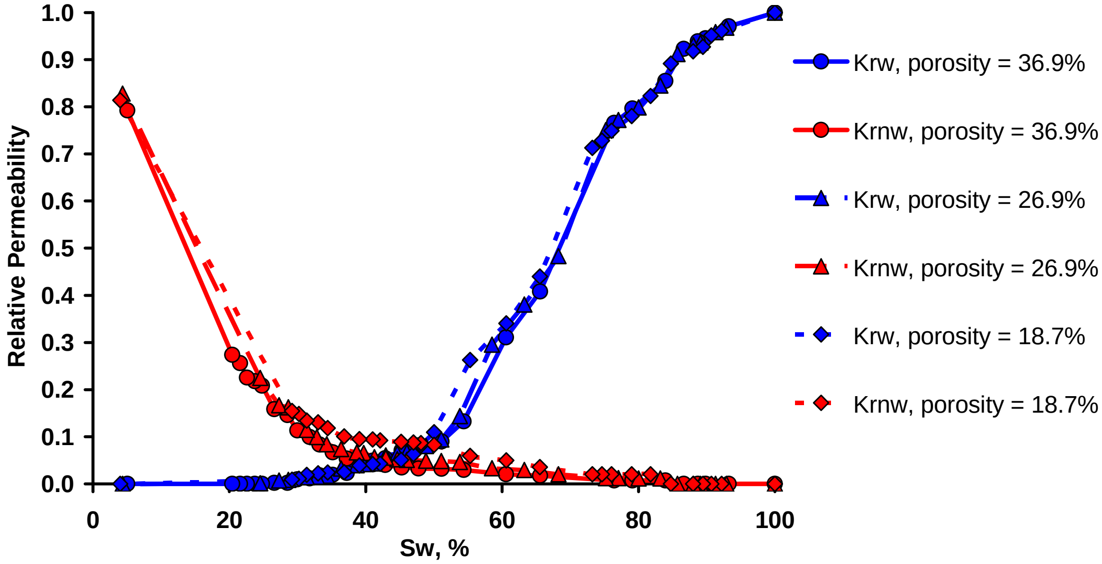

Fig. 76 Influence of isopachous cementation on drainage relative permeabilities in the Finney pack. Contact angle =10 degrees.

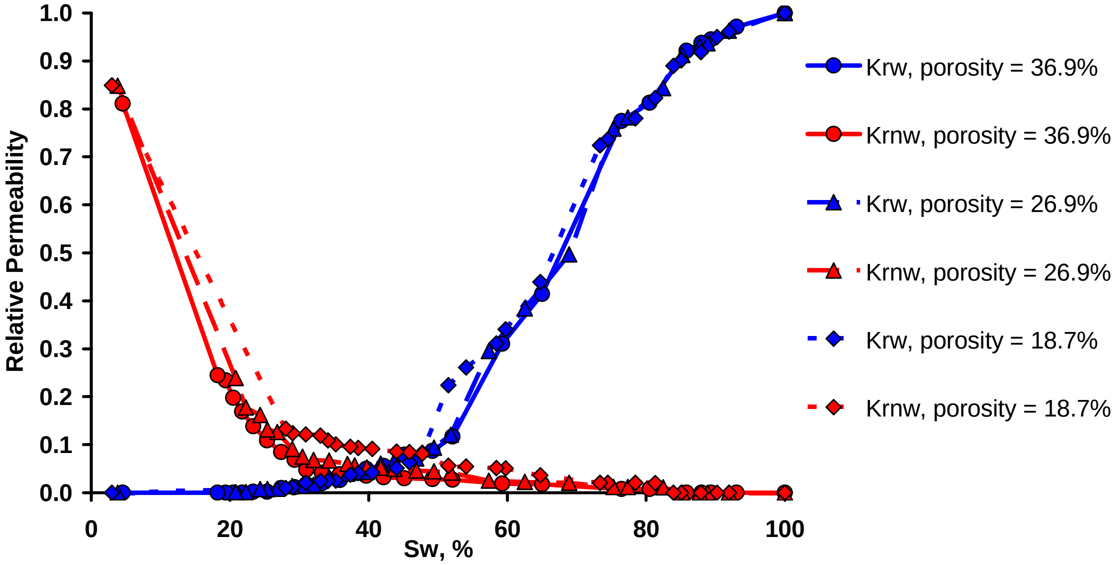

Fig. 77 Influence of isopachous cementation on drainage relative permeabilities in the Finney pack. Contact angle =30 degrees.

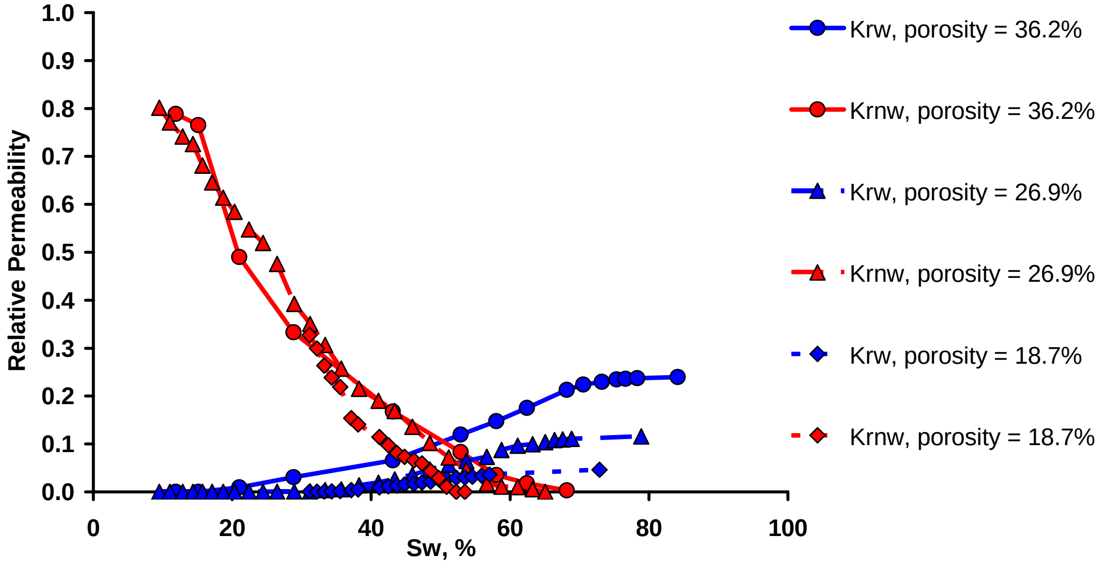

Fig. 78 Influence of isopachous cementation on imbibition relative permeabilities in the Finney pack. Contact angle = 0 degrees.

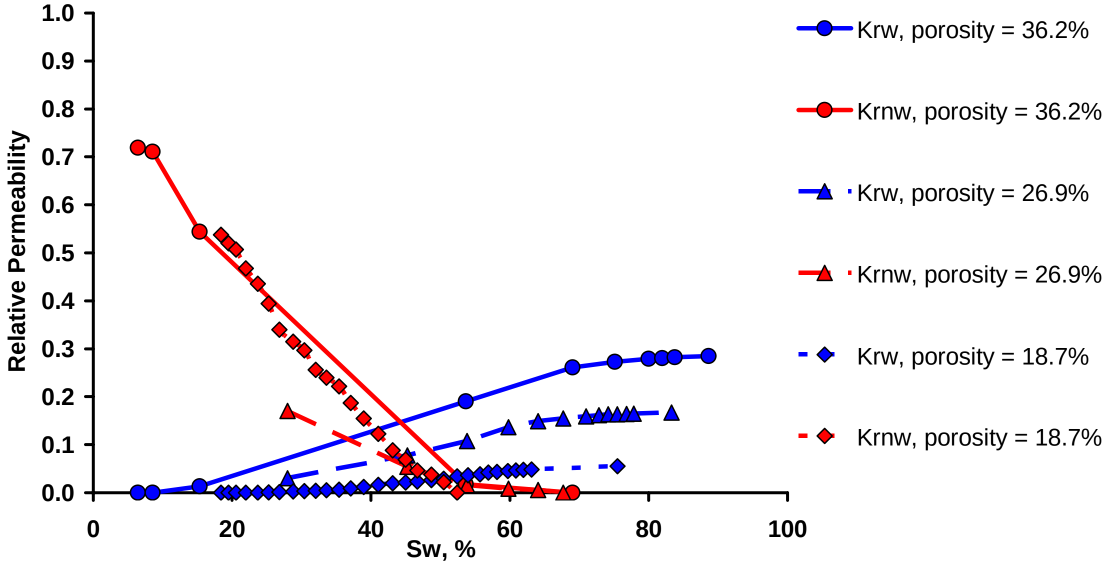

Fig. 79 Influence of isopachous cementation on imbibition relative permeabilities in the Finney pack. Contact angle =10 degrees.

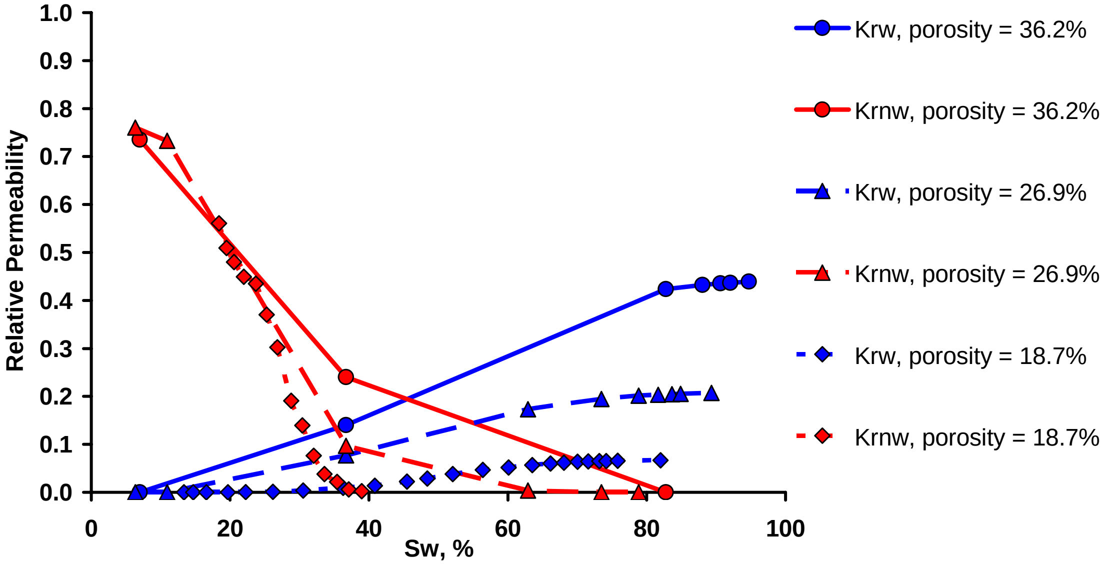

Fig. 80 Influence of isopachous cementation on imbibition relative permeabilities in the Finney pack. Contact angle =30 degrees.

It is interesting also to quantify the influence of wettability (specified by the value of contact angle) on relative permeabilities of two-phase flow during imbibition in the Finney pack with isopachous cement (the influence of wettability on drainage relative permeabilities is negligible, see section 4.5.2). Figs. 81 and 82 show imbibition relative permeabilities for different wettability conditions (contact angle is equal to 0, 10 and 30 degrees) in the packing with different amount of isopachous cement (Fig. 81 – porosity 26.9%, Fig. 82 – porosity 18.7%). The influence of wettability is qualitatively the same as for the case of unconsolidated packing (Fig. 73), although the effect is less pronounced for highly cemented packing (Fig. 82). The influence of cementation in this case is dominant.

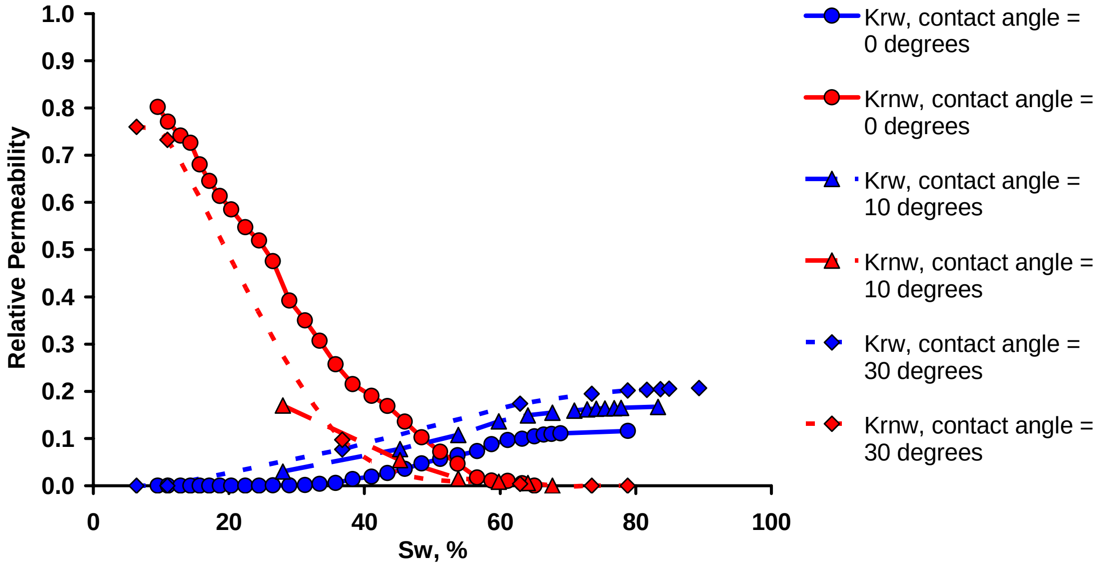

Fig. 81 Influence of wettability on imbibition relative permeabilities in the cemented Finney pack. Isopachous cement, porosity = 26.9%.

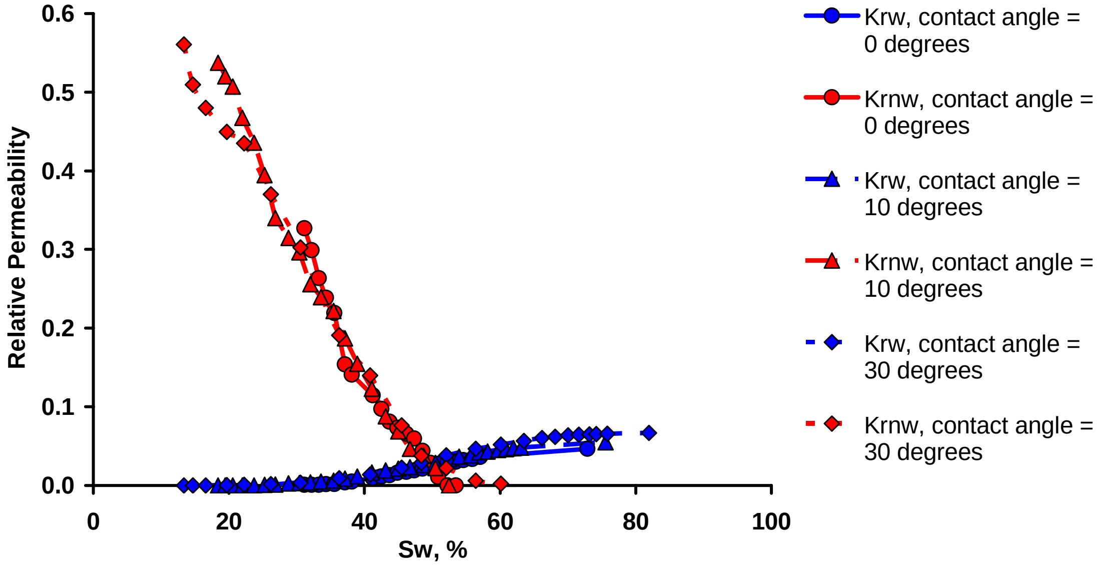

Fig. 82 Influence of wettability on imbibition relative permeabilities in the cemented Finney pack. Isopachous cement, porosity = 18.7%.

4.5.4 Relative Permeabilities: Media with Pore-Filling Cement

We illustrate in Figs. 83 – 88 the influence of pore-filling cementation on relative permeabilities during drainage (Figs. 83 – 85) and imbibition (Figs. 86 – 88) for different wettability conditions. This type of cementation was modeled as described in section 1.5 (see Figs. 5 and 6). The maximal size of pore-filling cluster was specified to be 10 pores. The effect of pore-filling cement is similar to the effect of isopachous cement (Figs. 75 – 80). It is interesting to note that relative permeability to the W phase in highly cemented packing (porosity 18.6%) and small contact angle (0 degrees) (Fig. 86) is essentially zero for the whole range of saturations. It means that this case is highly degenerated: since at small contact angle W phase imbibes the packing as dendritic branches (section 3.2.5), and about half the pores are filled with cement at porosity of 18.6%, the W phase in the middle core of the packing (these pores are defined as the inlet for the flow, see section 4.1.1) never becomes connected to the surface via continuous path of pores containing W phase. On the other hand, imbibition can still proceed since the W phase enters the packing from the entrance pores at the surface of the packing (see section 2.1.4).

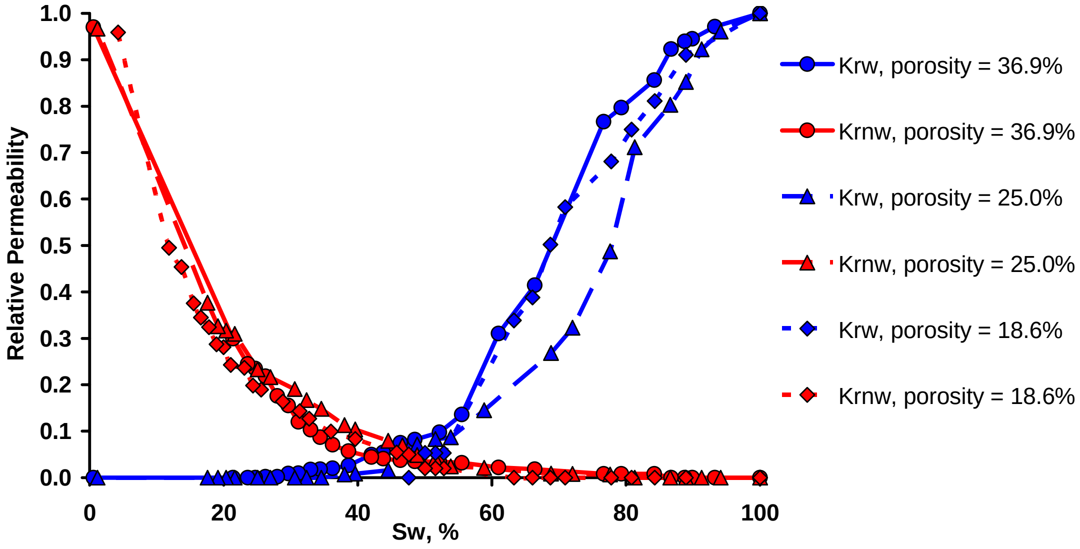

Fig. 83 Influence of pore-filling cementation on drainage relative permeabilities in the Finney pack. Contact angle =0 degrees.

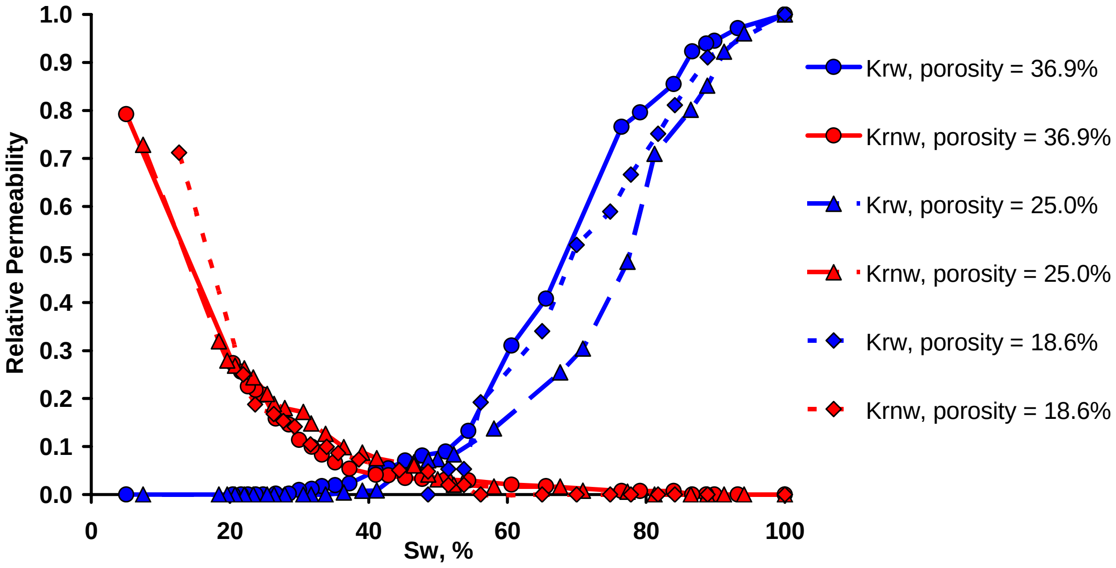

Fig. 84 Influence of pore-filling cementation on drainage relative permeabilities in the Finney pack. Contact angle =10 degrees.

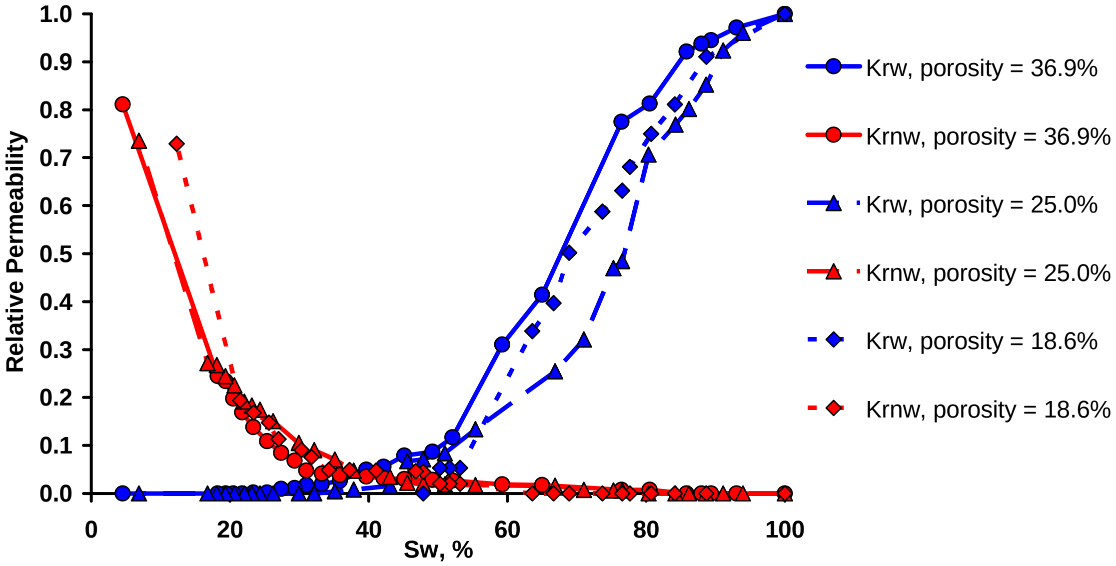

Fig. 85 Influence of pore-filling cementation on drainage relative permeabilities in the Finney pack. Contact angle =30 degrees.

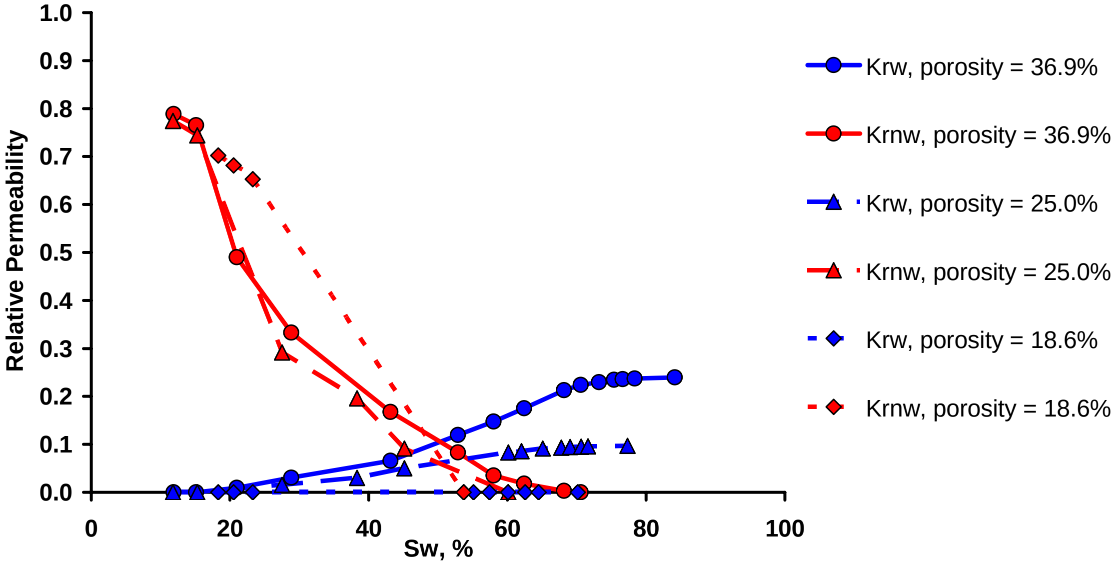

Fig. 86 Influence of pore-filling cementation on imbibition relative permeabilities in the Finney pack. Contact angle =0 degrees.

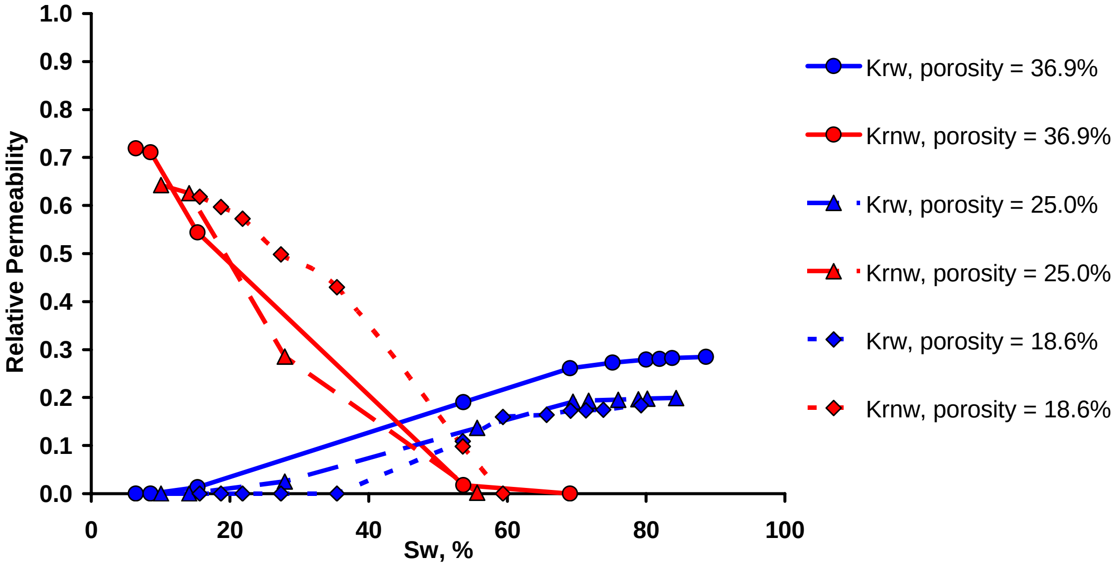

Fig. 87 Influence of pore-filling cementation on imbibition relative permeabilities in the Finney pack. Contact angle =10 degrees.

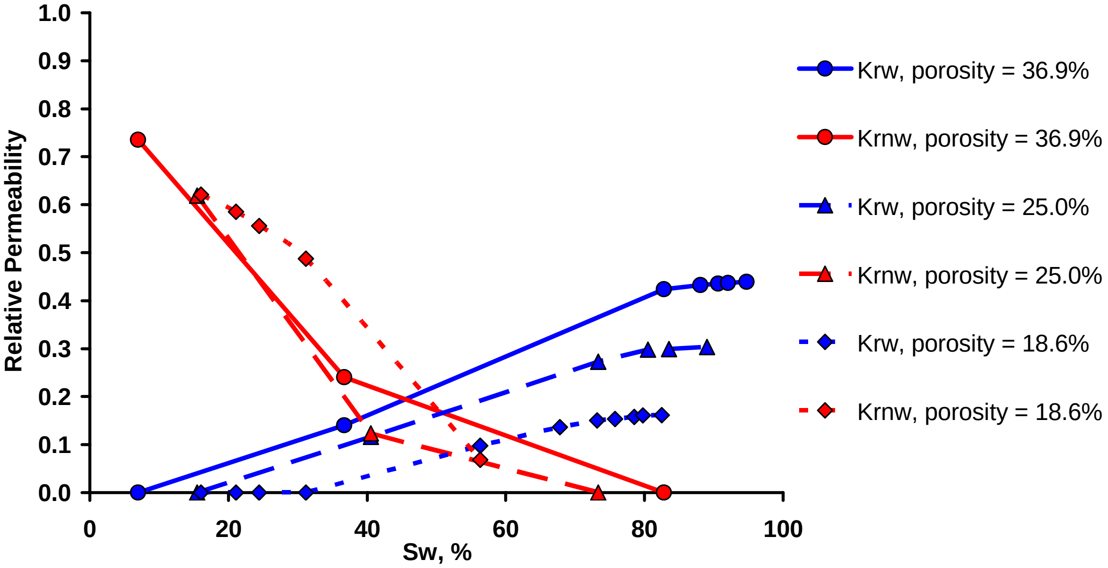

Fig. 88 Influence of pore-filling cementation on imbibition relative permeabilities in the Finney pack. Contact angle =30 degrees.

It is also interesting to see the influence of wettability (specified by the value of contact angle) on relative permeabilities of two-phase flow during imbibition in the Finney pack with pore-filling cement. Figs. 89 and 90 show imbibition relative permeabilities for different wettability conditions (contact angle is equal to 0, 10 and 30 degrees) in the packing with different amount of pore-filling cement (Fig. 89 – porosity 25.0%, Fig. 90 – porosity 18.6%). Qualitatively, the effect is similar to the case of unconsolidated packing (Fig. 73) and isopachous cement (Figs. 81 and 82).

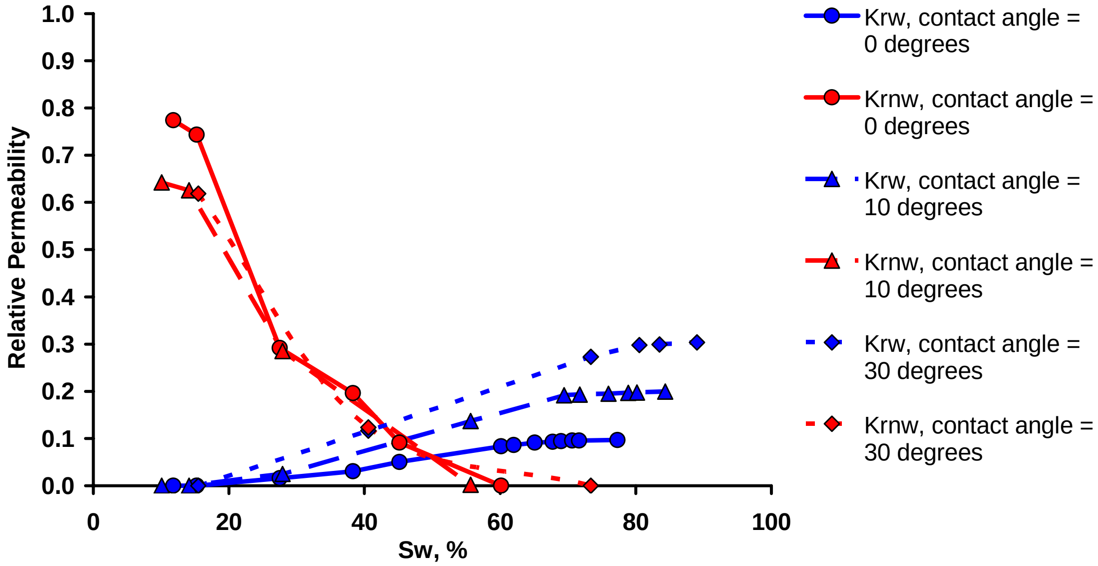

Fig. 89 Influence of wettability on imbibition relative permeabilities in the cemented Finney pack. Pore-filling cement, porosity = 25.0%.

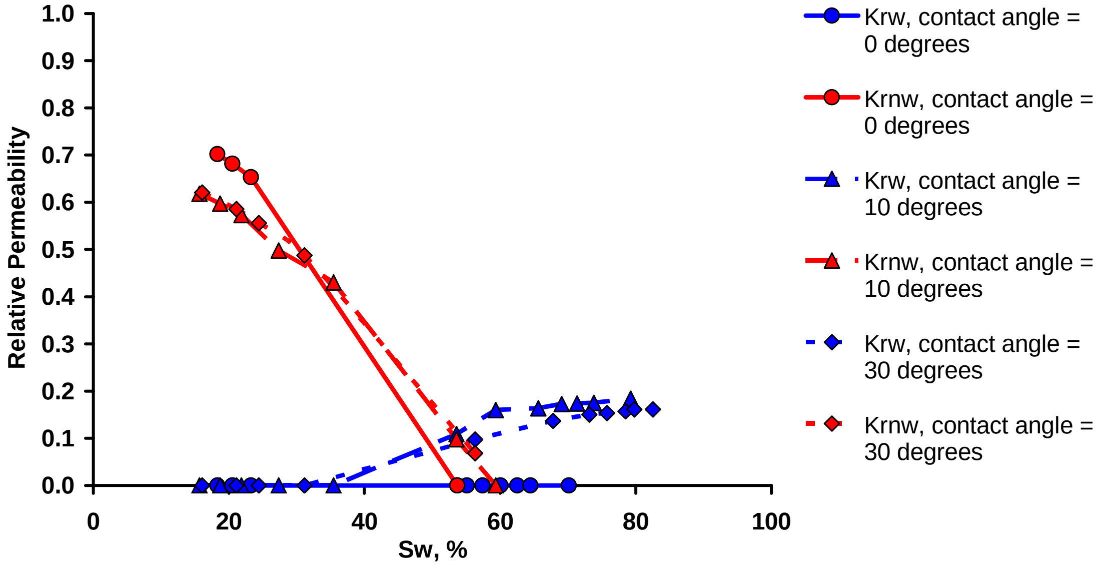

Fig. 90 Influence of wettability on imbibition relative permeabilities in the cemented Finney pack. Pore-filling cement, porosity = 18.6%.

4.5.5 Electrical Properties: Comparison with Experimental Data

We present results of the simulation of electric current flow during both drainage and imbibition as both resistivity index and electrical efficiency.

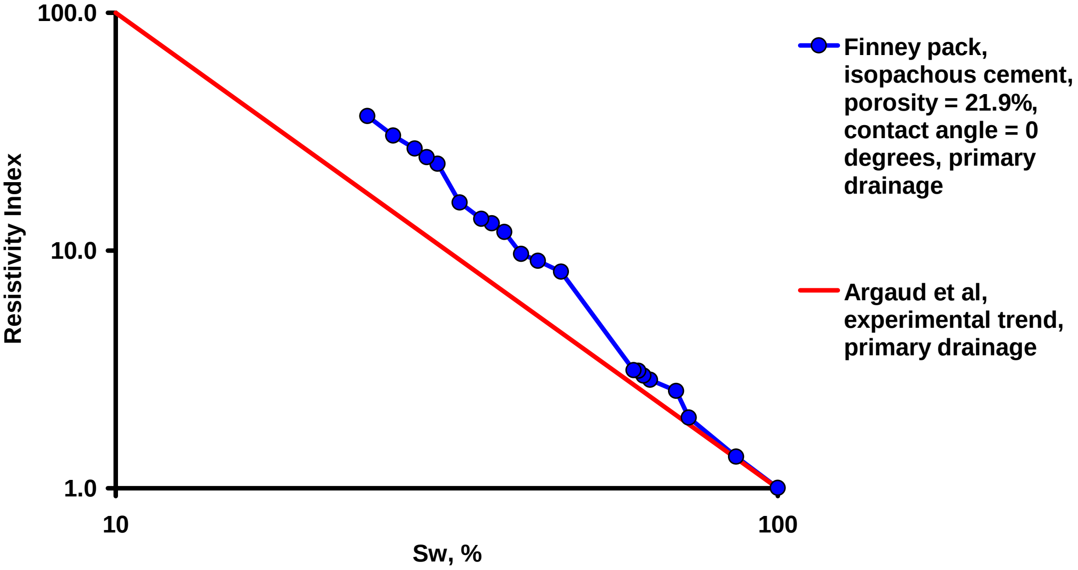

Fig. 91 Comparison between predictions of resistivity index during drainage in the cemented Finney packing (isopachous cement, porosity = 21.9%, contact angle = 0 degrees, 9 entrance pores) and experimental trend (clean Cretaceous sandstone, porosity 21.9%, Argaud *et al* [5]).

Fig. 91 shows a comparison between simulated resistivity index during drainage and experimental data for the drainage in clean Cretaceous sandstone by Argaud *et al* [5]. Simulation of electric current flow was computed in the Finney pack with uniform isopachous cementation, so that its porosity reached the same value as that of the experimental sample (21.9%). The value of contact angle is 0 degrees (strongly water-wet system); number of entrances is 9 pores. The smaller experimental values of resistivity index may probably be attributed to the presence of conductive thin films of W phase on grain surfaces, the contribution of which was neglected in our model.

Fig. 92 presents a comparison between two predicted electrical efficiency trends during drainage in the unconsolidated and cemented (isopachous cement, porosity =

21.9%) Finney pack (value of contact angle is 0 degrees (water-wet), number of entrances is 9 pores) and experimental data for the drainage in two sandstones and one carbonate formation (Herrick and Kennedy, [63]). Fig. 92 shows that predicted trends for the model rocks lie in the same range of efficiencies and are similar to the experimental trends. This allows concluding that the simulations adequately capture the influence of one type of diagenetic alteration (isopachous cement) on electrical efficiency.

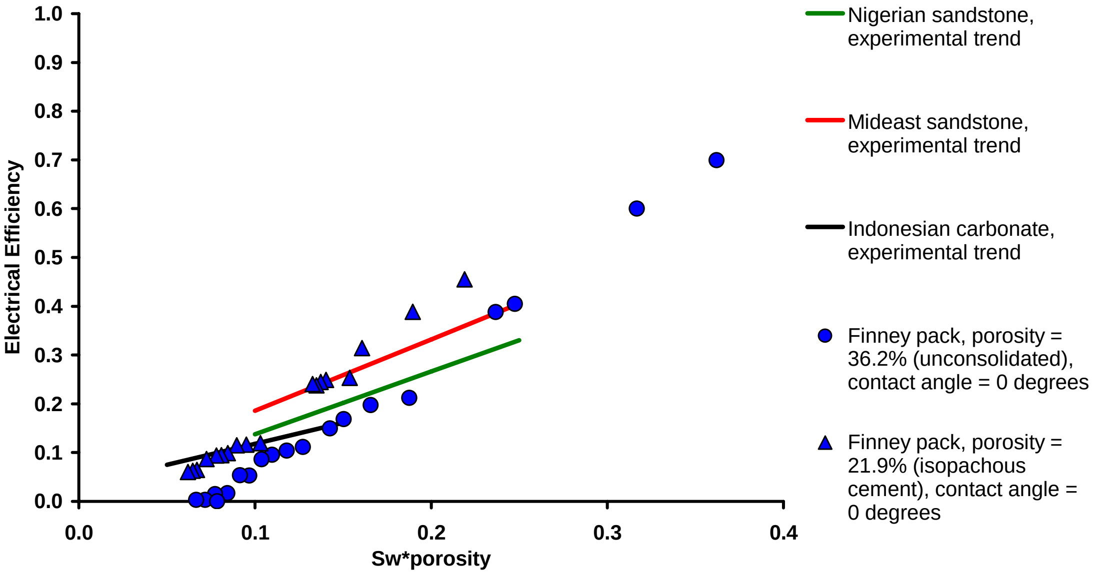

Fig. 92 Comparison between predictions of electrical efficiency during drainage in the Finney packing and experimental trends (Herrick and Kennedy, [63]).

4.5.6 Electrical Properties: Unconsolidated Media

Figs. 93 – 96 present the predicted hysteresis in resistivity index (Figs. 93 and 94) and electrical efficiency (Figs. 95 and 96) in the Finney pack for different values of contact angle (0, 10 and 30 degrees). It is important to distinguish between two cases: water- (brine) wet conditions and oil-wet conditions. Since we consider brine to be the conductive phase, and oil along with solid grains to be insulators, these two cases are qualitatively different. In the water-wet sample the W phase is conductive (brine), in the oil-wet sample NW phase is conductive. Therefore, when plotting electrical data against *water* (brine) saturation (denoted as S_w on Figs. 93-128 below), we must be aware that this saturation corresponds to the W phase saturation in water-wet sample and NW phase saturation in oil-wet sample.

It should be noted also that in the simulations, shown in Figs. 93 – 128, the number of entrance pores was chosen to be 200 in order to approach percolation threshold smoothly and compute more points for relative permeabilities. Similarly to the case of two-phase flow (sections 4.5.2 – 4.5.4), in order to maintain consistency between simulations and make a fair comparison between them, we choose exactly the same boundary conditions (namely, 200 entrance pores) for all simulations. However, when the value of contact angle is large, the percolation during imbibition is very rapid (even with 200 entrance pores), which prevents computing values of electrical properties at intermediate saturations.

The undesirable consequence of relatively large number of entrances (200 pores) is the presence of edge effects – for example, the part of the drainage electrical efficiency curve in Fig. 95 at high S_w, which shows an increase in electrical efficiency as saturation decreases. This part should be absent for the measurements of sufficiently large real samples and simulations that give strong percolation threshold behavior (cf. Fig. 92).

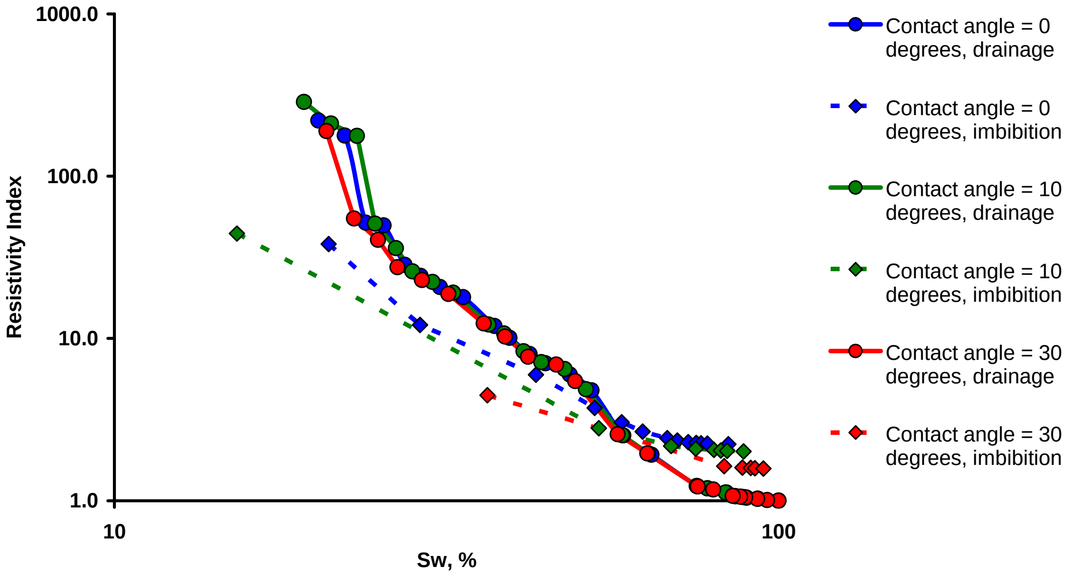

Fig. 93 Hysteresis in resistivity index in the unconsolidated Finney pack. Water-wet conditions.

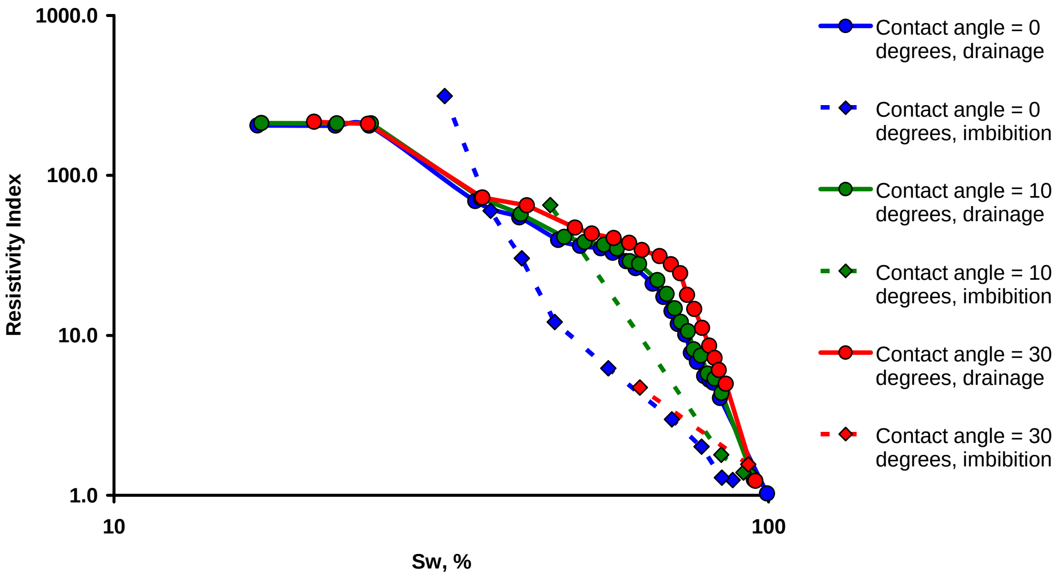

Fig. 94 Hysteresis in resistivity index in the unconsolidated Finney pack. Oil-wet conditions.

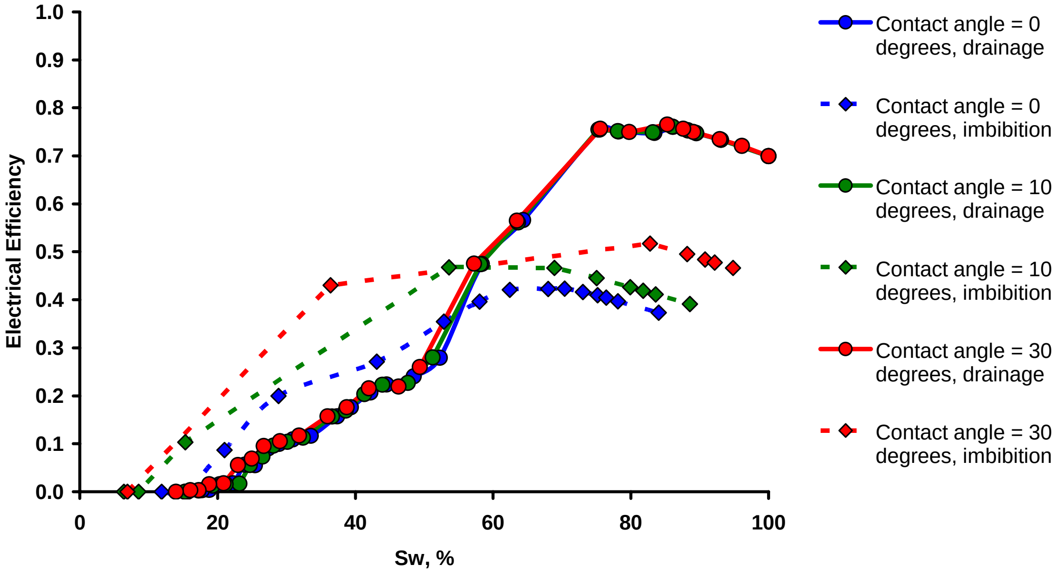

Fig. 95 Hysteresis in electrical efficiency in the unconsolidated Finney pack. Water-wet conditions.

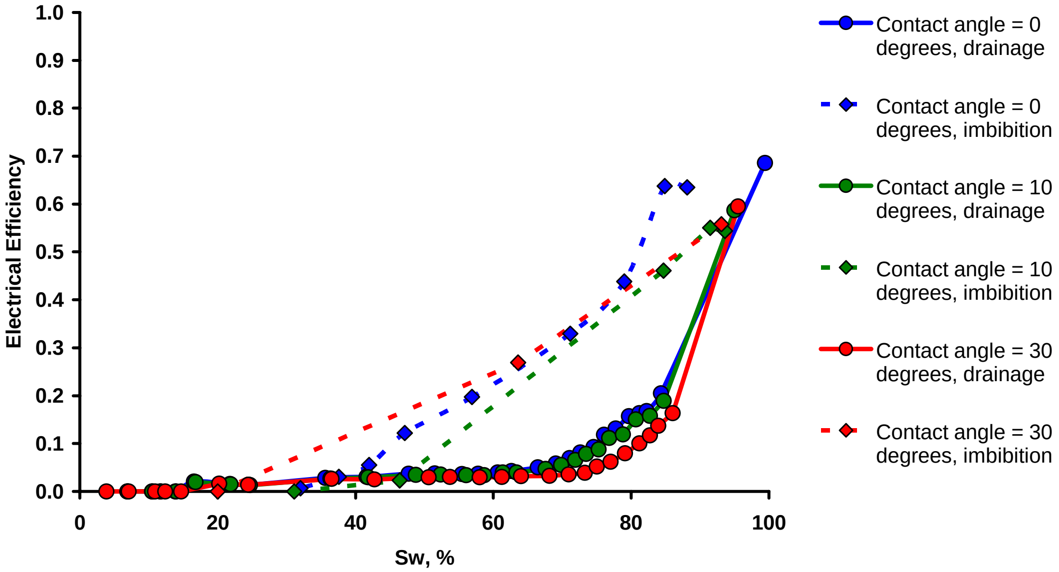

Fig. 96 Hysteresis in electrical efficiency in the unconsolidated Finney pack. Oil-wet conditions.

We can notice two important results: 1) imbibition is more electrically efficient than drainage; 2) influence of wettability on electrical properties during drainage is negligibly small (see section 4.5.2 for similar results regarding drainage relative permeabilities), but has a great effect during imbibition. The latter result is due to the fact that for the modeling of drainage we use Haines' face insphere criterion, which is linear with cosine of contact angle (Eq. (4)) and does not change the sequence of pore-level events. The morphology of the W phase is exactly the same for any contact angle and the difference between two curves is due to the change in the shapes of pendular rings. To model imbibition, though, we use Melrose criterion, which is inseparable from the pore space geometry and spatial correlations within it [18, 20, 112, 131]. Change in wettability conditions leads to the change in the behavior of W phase invasion during imbibition. This effect is caused by the different *morphology* of the W phase for different wettabilities, and was qualitatively predicted in section 3.2.5 from the influence of wettability on W phase topological coordination number.

The existence of hysteresis in electrical properties of water wet samples is qualitatively supported by the measurements of Knight [76]. Knight measured resistivity of different sandstones during both drainage and imbibition and observed hysteresis in the electrical resistivity of the samples. On the other hand, several other authors [41, 103, 121] did not observe any hysteresis in resistivity index during displacement cycle for glass beads [121] as well as for different sandstones. This contradictory behavior may be attributed to the measurement technique [41, 134] or to the presence of conductive films of W phase on grain surfaces [121]. We speculate that the absence of hysteresis in electrical properties is due to the presence of thin films of the W phase. The thickness of these films can be estimated as 10^{-4} of grain radius in dimensionless units (about 100 Å for the beads of 0.1 mm radius [121]). The conductive thin films cover grain surfaces continuously during earlier stages of drainage but disappear at drainage end-point and do not contribute to electrical conductivity during imbibition. Such behavior would possibly eliminate the predicted hysteresis in electrical properties of water-wet rocks (Fig. 93 and 95) if the conductivity of such films is large enough. Overall, this question is subject to further investigation.

For the oil-wet sample the effect of wettability is qualitatively different. The hysteresis in electrical properties of oil-wet rocks is attributed to the fact that during imbibition the NW phase is trapped within porous media and the bulk connectivity of the conductive phase (brine, which is the NW phase in oil-wet case) is very low. Therefore the resistivity can be very high for some finite value of brine saturation. This effect leads to the observed hysteresis in electrical properties of oil-wet rocks for small saturations [121, 134, 136]. The predictions shown in Fig. 94 are qualitatively consistent with these experimental observations (see the curves corresponding to the contact angle of 0 degrees on Fig. 94 for small saturation).

4.5.7 Electrical Properties: Media with Isopachous Cement

We illustrate in Figs. 97 – 104 the influence of isopachous cementation on hysteresis in resistivity index (water-wet conditions, Figs. 97 – 98; oil-wet conditions, Figs. 99 - 100) and electrical efficiency (water-wet conditions, Figs. 101 – 102; oil-wet conditions, Figs. 103 – 104) for different values of contact angle. This type of cementation was modeled as described in section 1.5 (see Figs. 5 and 6) by uniform increase of grain radii until the desired porosity was reached. Overall, the influence of isopachous cement on electrical properties is similar to the predictions for relative permeabilities (section 4.5.3). The effect of hysteresis in resistivity index for oil-wet case is consistent with the observed trends [121, 134] (see preceding section), when imbibition resistivity index is higher than the drainage resistivity index for small W phase saturation (Figs. 99 and 100). For the cemented media this effect is much clearer than for the unconsolidated packing (Fig. 94), due to the fact that the residual NW phase saturation is larger for the cemented pack (Figs. 52-54). Figs. 101-104 illustrate that the effect of isopachous cementation is to reduce the efficiency of the conductive phase for both drainage and imbibition. This might be expected in advance: if we consider a capillary tube with converging-diverging geometry and will grow uniform layers of cement on its walls, this cement will have stronger effect on the sizes of converging sections of capillary tube (its smallest constrictions, or “pore throats”) than on the sizes of diverging sections (“pore bodies”). Thus, as cement grows, electrical conductivity of such capillary tube will decrease faster than its porosity. This leads to decrease in electrical efficiency.

Data presented as electrical efficiency is much more convenient in analyzing trends and drawing conclusions than the data presented as resistivity index. Moreover, electrical efficiency is directly connected to the geometry of pore space and therefore provides useful physical insight.

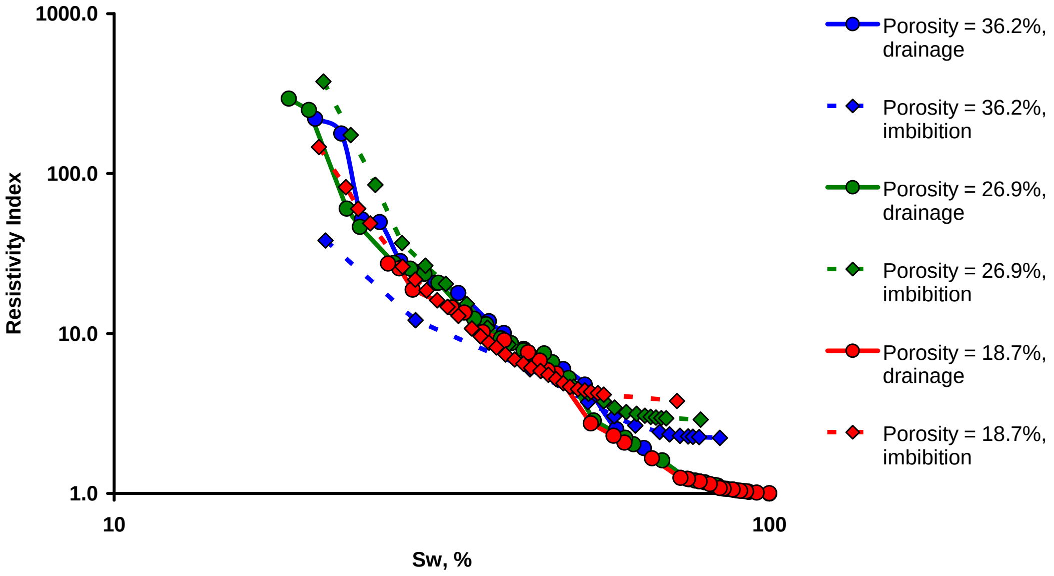

Fig. 97 Influence of isopachous cementation on hysteresis in resistivity index. Water-wet conditions. Contact angle = 0 degrees.

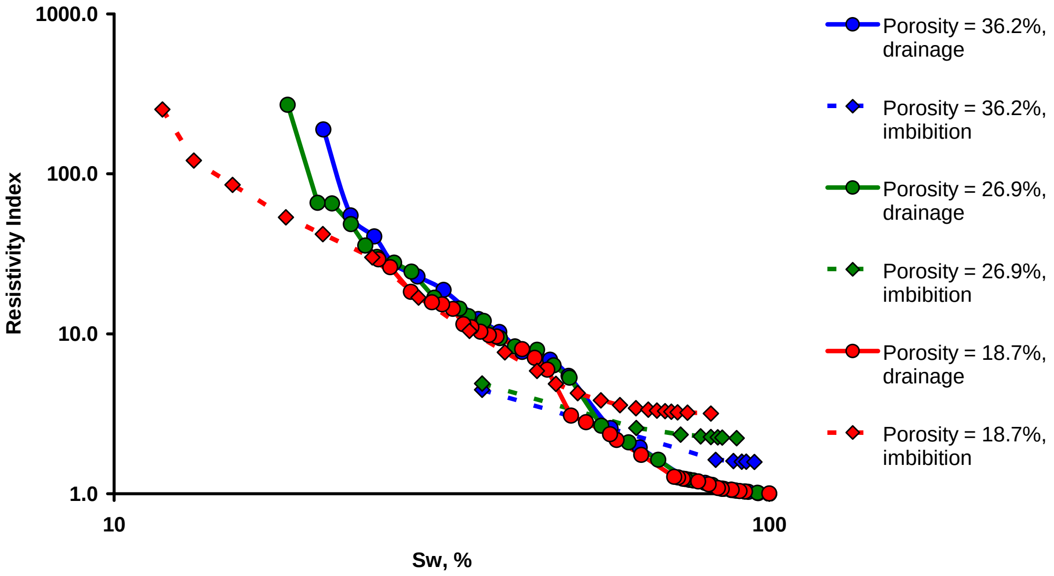

Fig. 98 Influence of isopachous cementation on hysteresis in resistivity index. Water-wet conditions. Contact angle = 30 degrees.

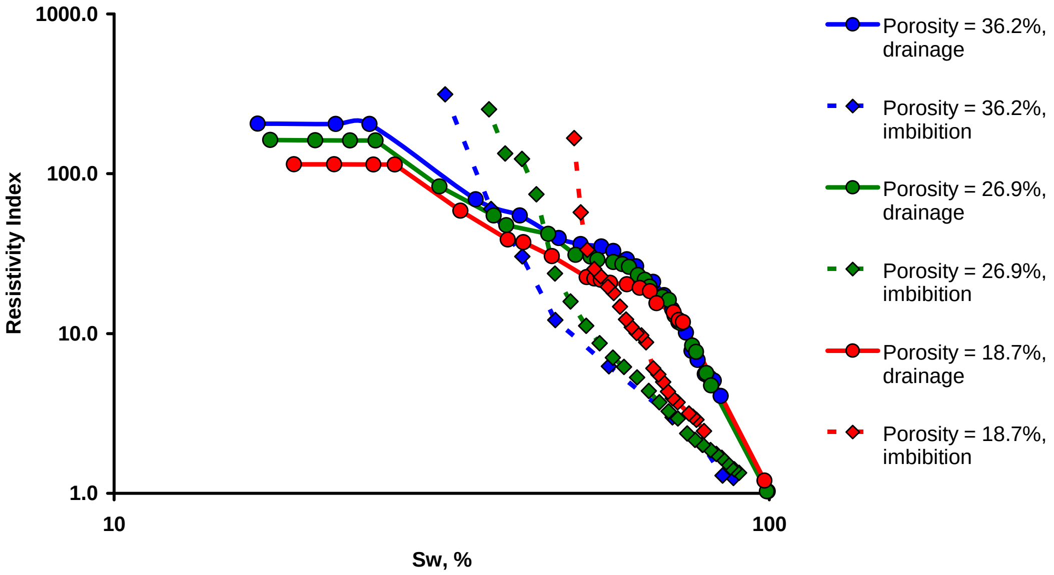

Fig. 99 Influence of isopachous cementation on hysteresis in resistivity index. Oil-wet conditions. Contact angle = 0 degrees.

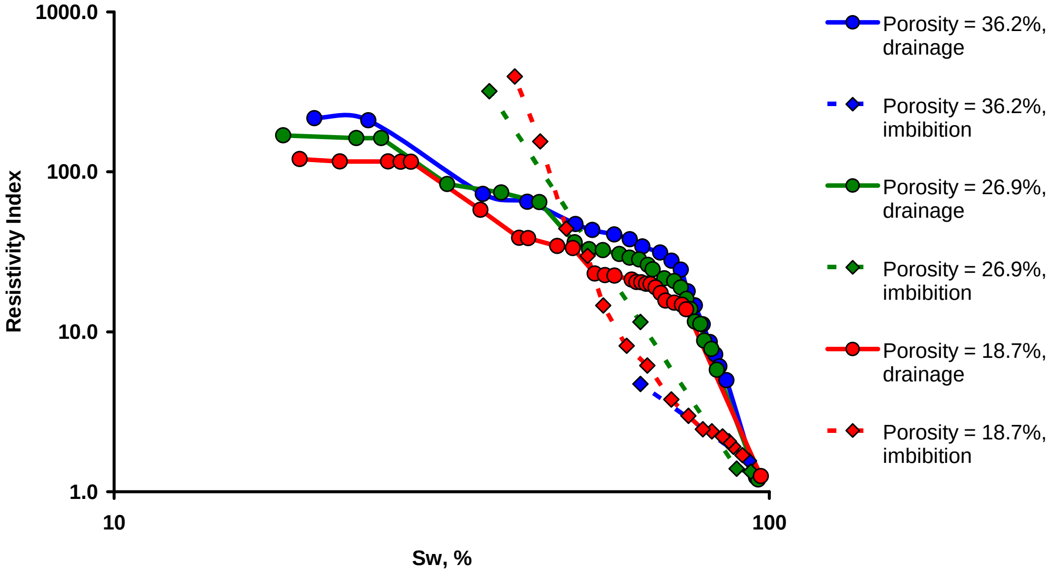

Fig. 100 Influence of isopachous cementation on hysteresis in resistivity index. Oil-wet conditions. Contact angle = 30 degrees.

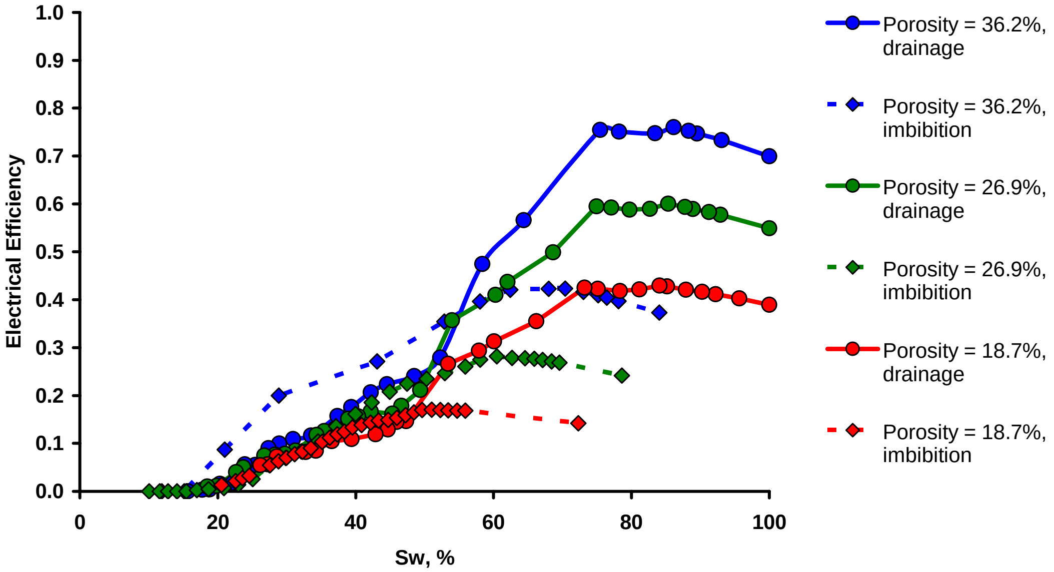

Fig. 101 Influence of isopachous cementation on hysteresis in electrical efficiency. Water-wet conditions. Contact angle = 0 degrees.

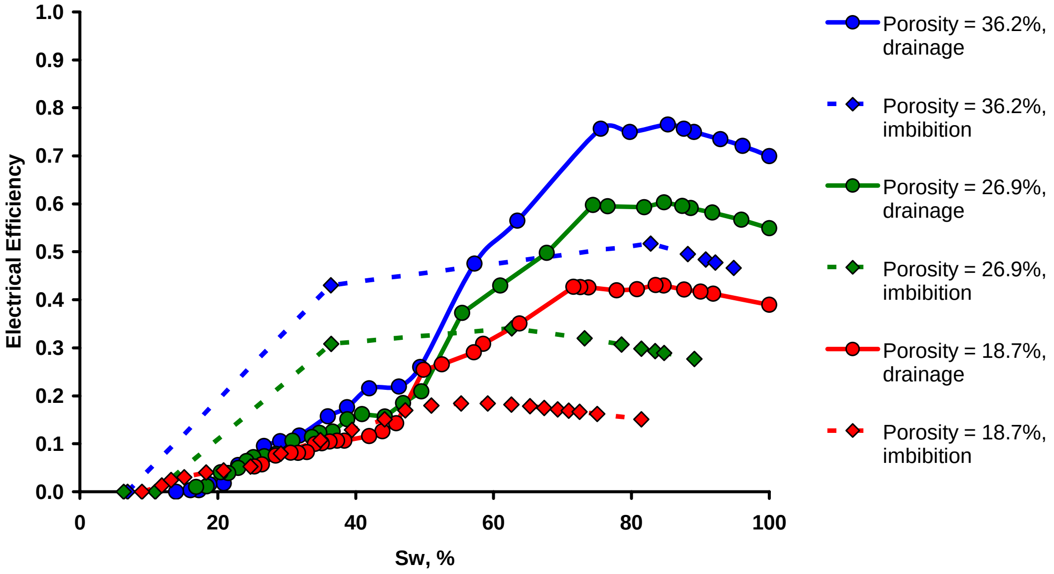

Fig. 102 Influence of isopachous cementation on hysteresis in electrical efficiency. Water-wet conditions. Contact angle = 30 degrees.

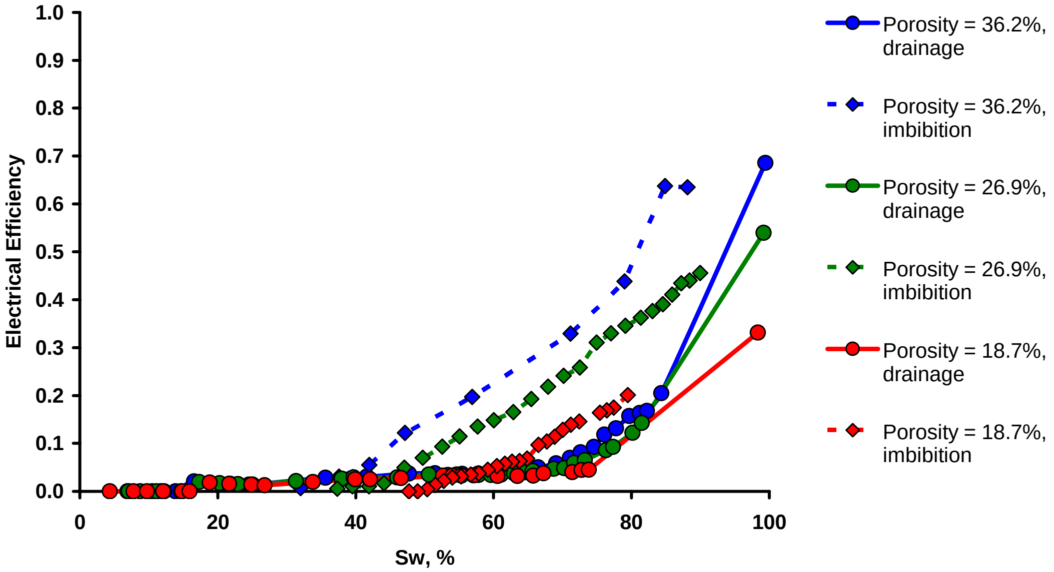

Fig. 103 Influence of isopachous cementation on hysteresis in electrical efficiency. Oil-wet conditions. Contact angle = 0 degrees.

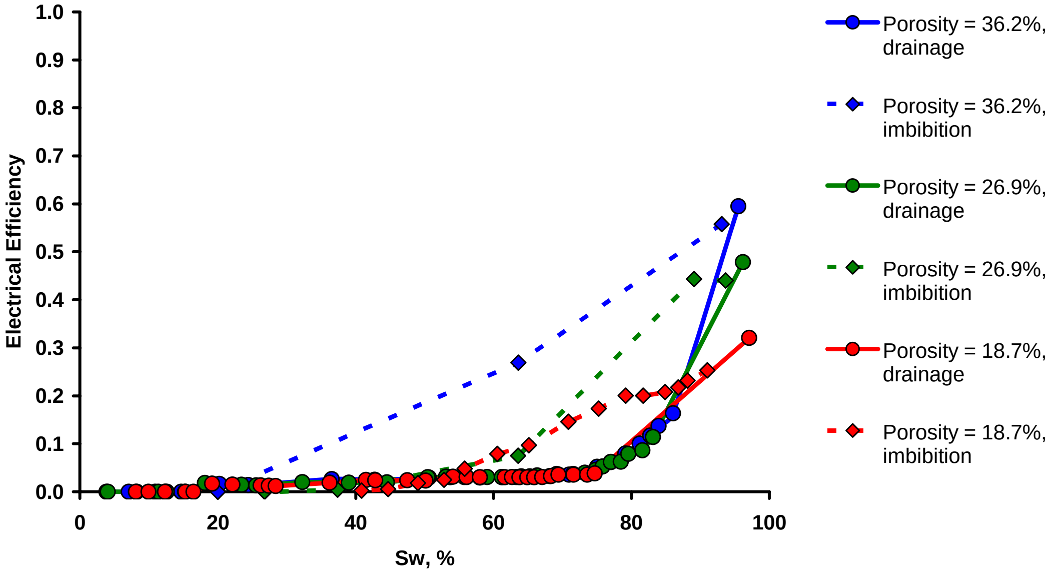

Fig. 104 Influence of isopachous cementation on hysteresis in electrical efficiency. Oil-wet conditions. Contact angle = 30 degrees.

We show in Figs. 105 – 112 the influence of wettability on hysteresis in resistivity index (water-wet conditions, Figs. 105 – 106; oil-wet conditions, Figs. 107 - 108) and electrical efficiency (water wet conditions, Figs. 109 – 110; oil-wet conditions, Figs. 111 - 112) for different values of isopachous cement (values of porosity 26.9% and 18.7%). Qualitatively the effect of wettability is the same as for the case of unconsolidated packing (Figs. 93-96). It is interesting that the influence of contact angle becomes smaller with the decrease in porosity (cf. Figs. 109 and 110, for example) and is negligible for the highly cemented packing (Fig. 110). In this case the influence of high cementation seems to be dominant (see also results of section 4.5.3 for relative permeabilities). Another interesting observation is that hysteresis in electrical properties between drainage and imbibition disappears for highly cemented media (at least at intermediate saturations, compare again Figs. 109 and 110). These qualitative predictions might be readily used in formation evaluation, when estimating water content of reservoir using electrical measurements. For example, comparison of Figs. 109 and 110 suggests that in a sample with high degree of isopachous cement value of contact angle is not an issue; on the other hand, in a lightly cemented rock its wettability (value of contact angle) has to be measured independently and taken into account in order to estimate water content accurately.

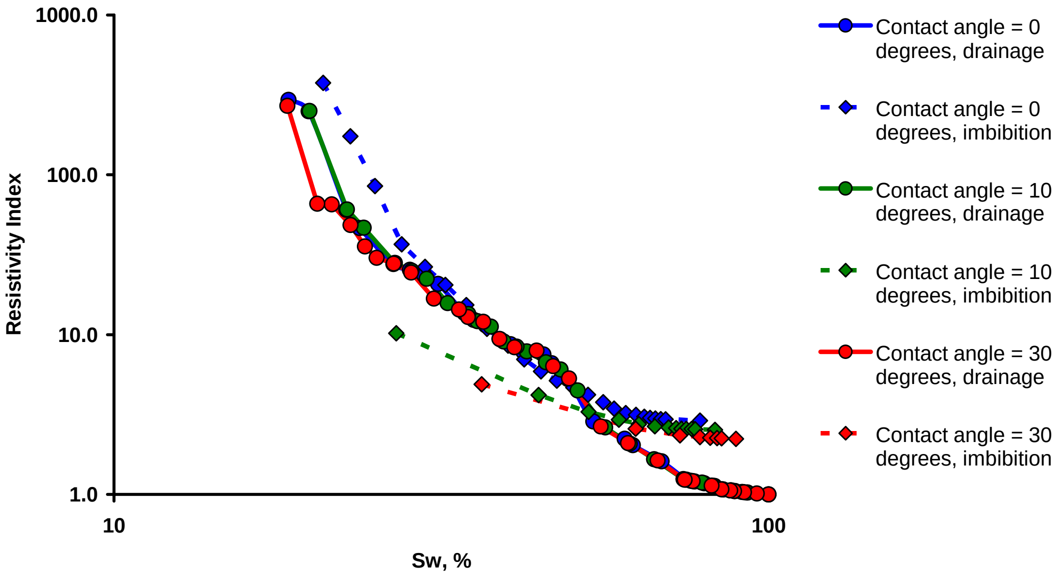

Fig. 105 Influence of wettability on hysteresis in resistivity index. Isopachous cement, porosity = 26.9%. Water-wet conditions.

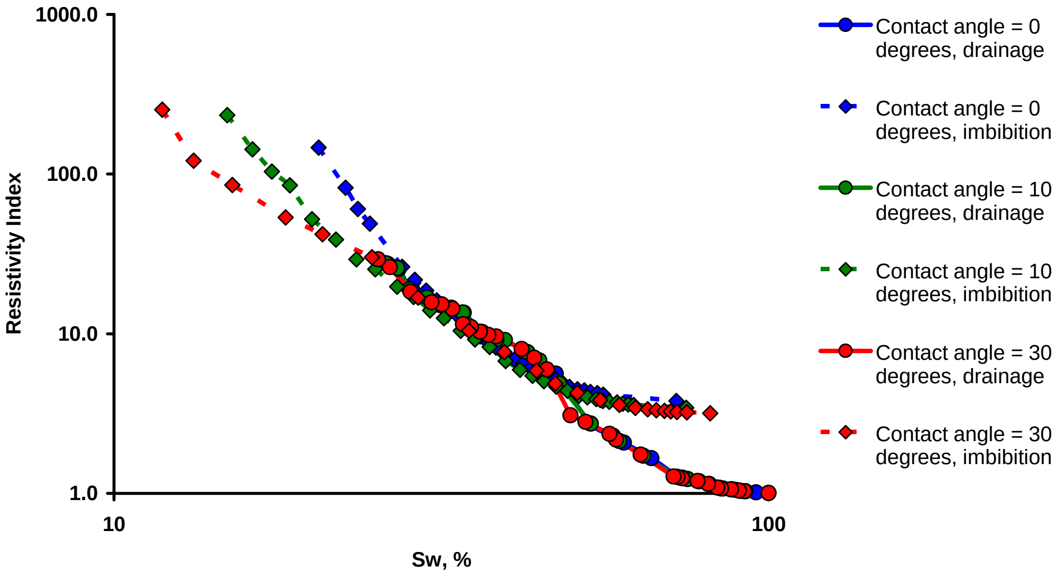

Fig. 106 Influence of wettability on hysteresis in resistivity index. Isopachous cement, porosity = 18.7%. Water-wet conditions.

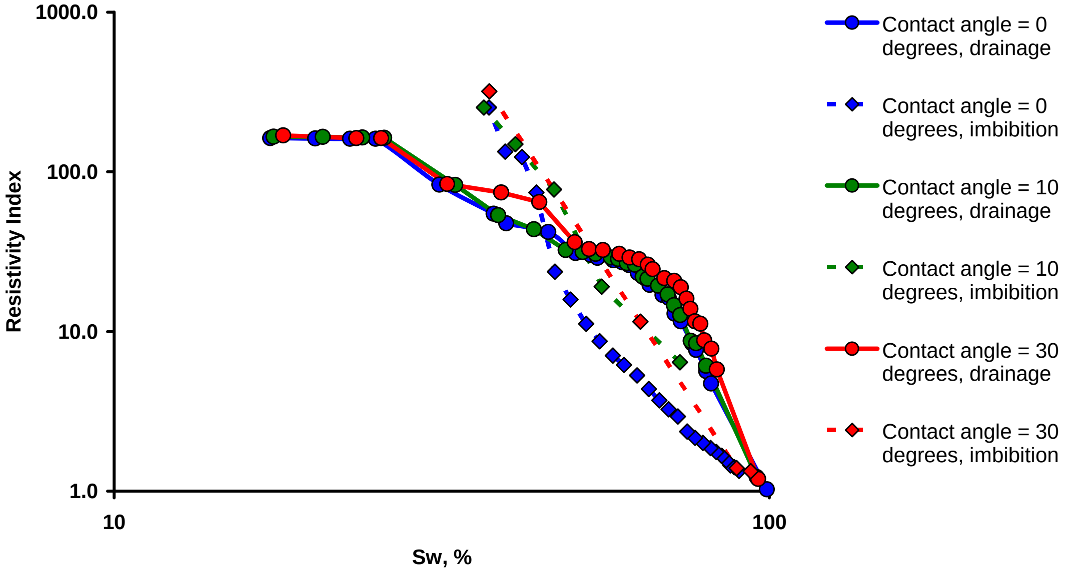

Fig. 107 Influence of wettability on hysteresis in resistivity index. Isopachous cement, porosity = 26.9%. Oil-wet conditions.

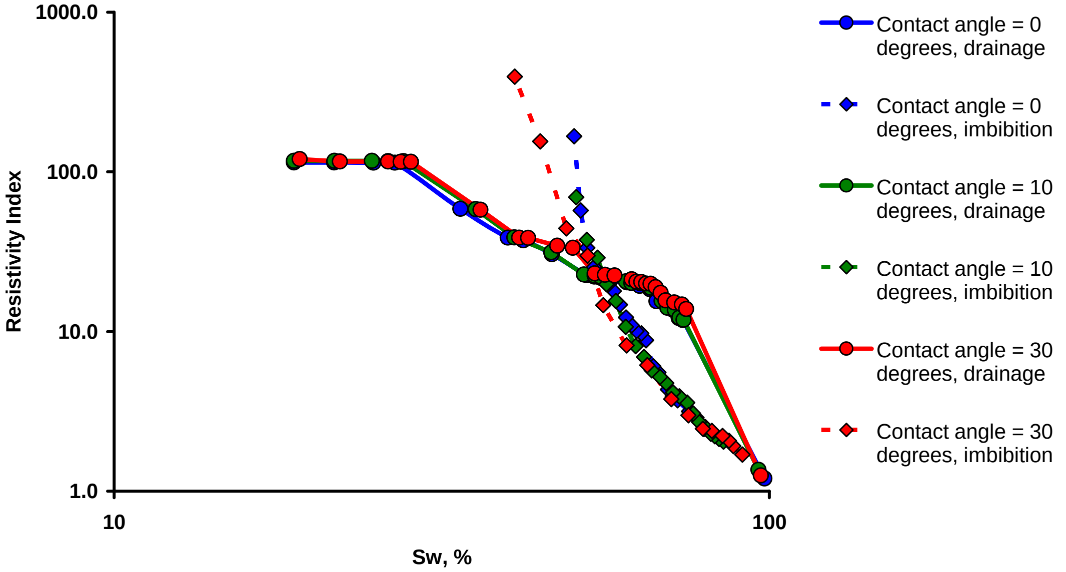

Fig. 108 Influence of wettability on hysteresis in resistivity index. Isopachous cement, porosity = 18.7%. Oil-wet conditions.

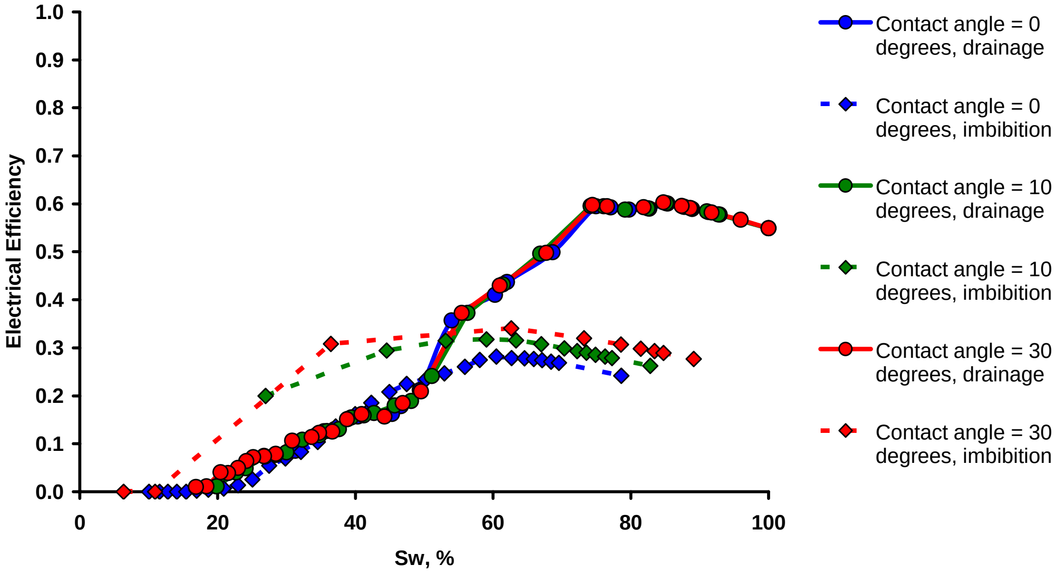

Fig. 109 Influence of wettability on hysteresis in electrical efficiency. Isopachous cement, porosity = 26.9%. Water-wet conditions.

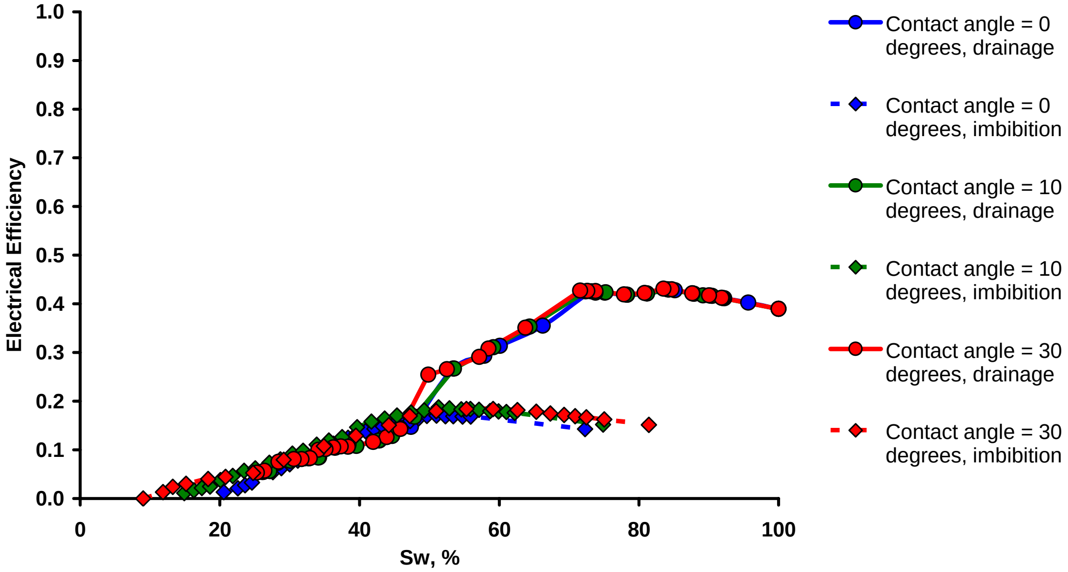

Fig. 110 Influence of wettability on hysteresis in electrical efficiency. Isopachous cement, porosity = 18.7%. Water-wet conditions.

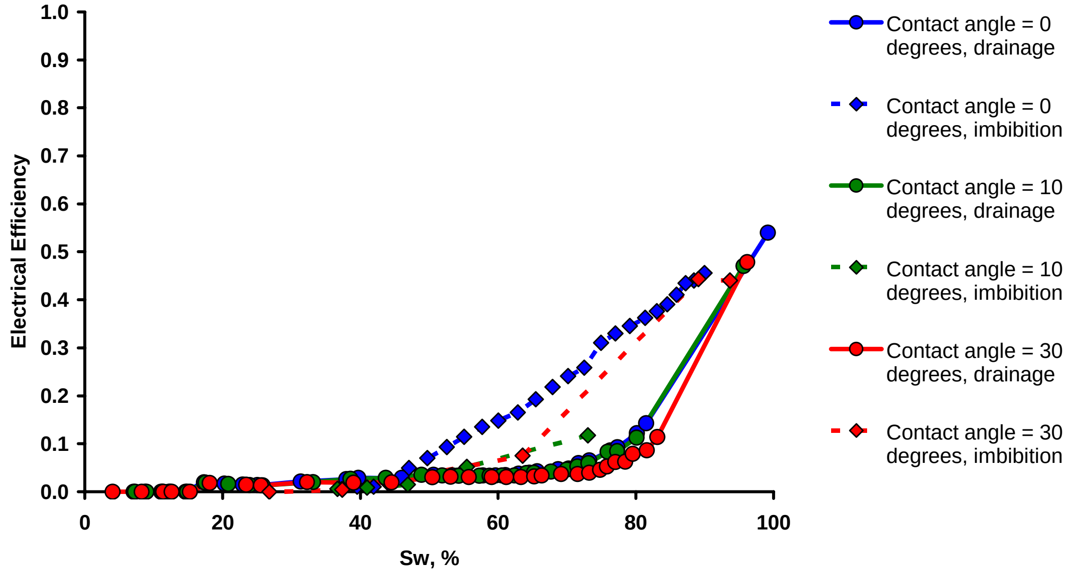

Fig. 111 Influence of wettability on hysteresis in electrical efficiency. Isopachous cement, porosity = 26.9%. Oil-wet conditions.

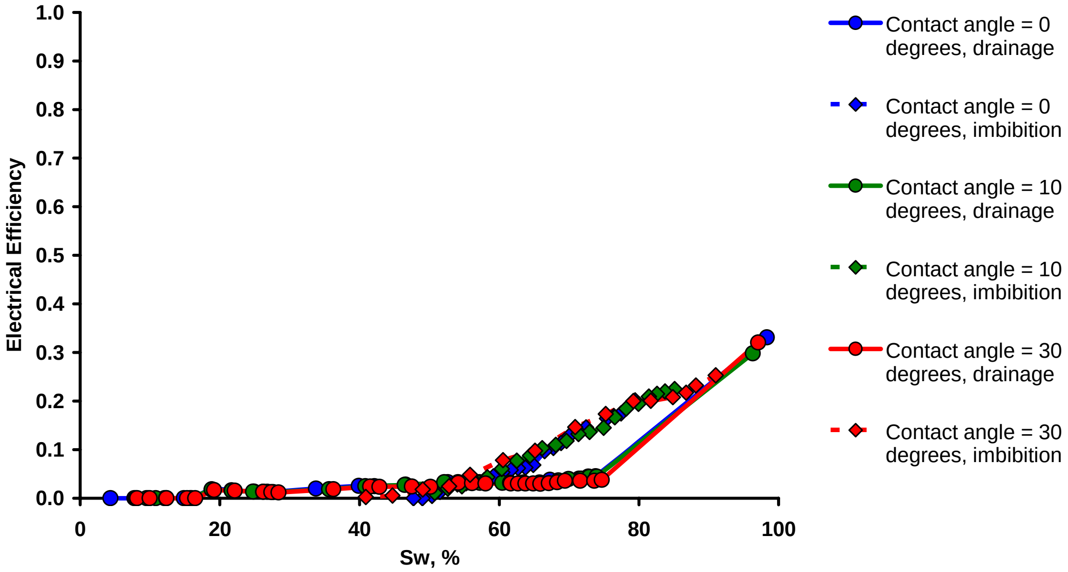

Fig. 112 Influence of wettability on hysteresis in electrical efficiency. Isopachous cement, porosity = 18.7%. Oil-wet conditions.

4.5.8 Electrical Properties: Media with Pore-Filling Cement

We illustrate in Figs. 113 – 120 the influence of pore-filling cementation on hysteresis in resistivity index (water-wet conditions, Figs. 113 – 114; oil-wet conditions, Figs. 115 – 116) and electrical efficiency (water-wet conditions, Figs. 117 – 118; oil-wet conditions, Figs. 119 – 120) for different values of contact angle. This type of cementation was modeled as described in section 1.5 (see Figs. 5 and 6). The maximal cluster size of pore-filling cement is 10 pores. Qualitatively, the effect is similar to the case of isopachous cement (see preceding section).

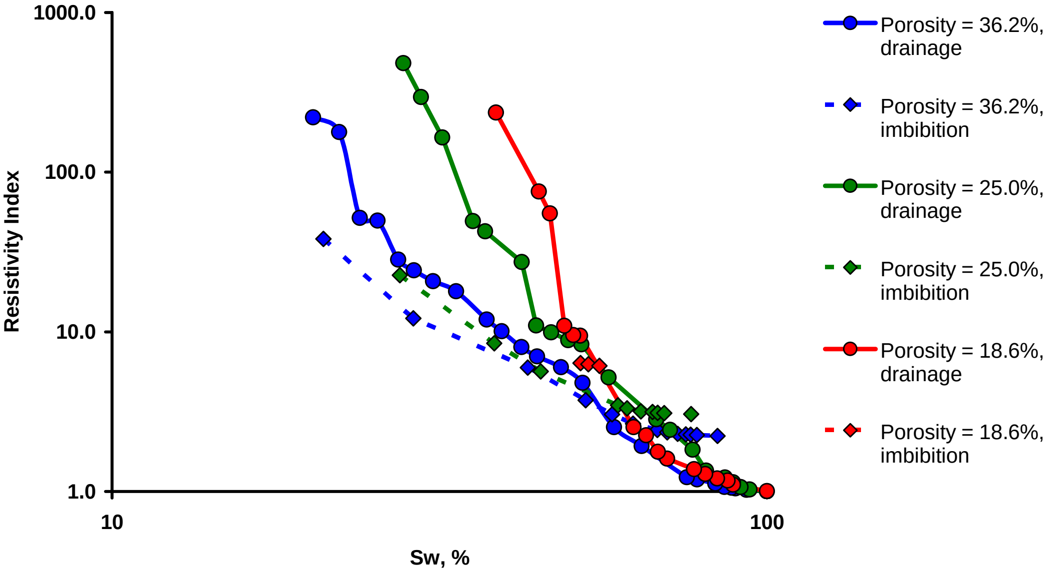

Fig. 113 Influence of pore-filling cementation on hysteresis in resistivity index. Water-wet conditions. Contact angle = 0 degrees.

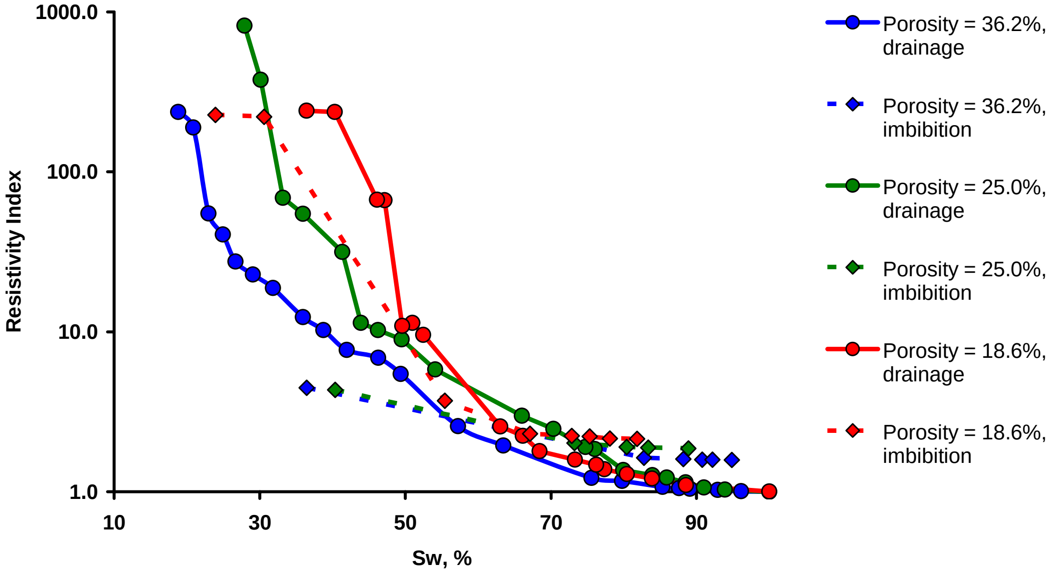

Fig. 114 Influence of pore-filling cementation on hysteresis in resistivity index. Water-wet conditions. Contact angle = 30 degrees.

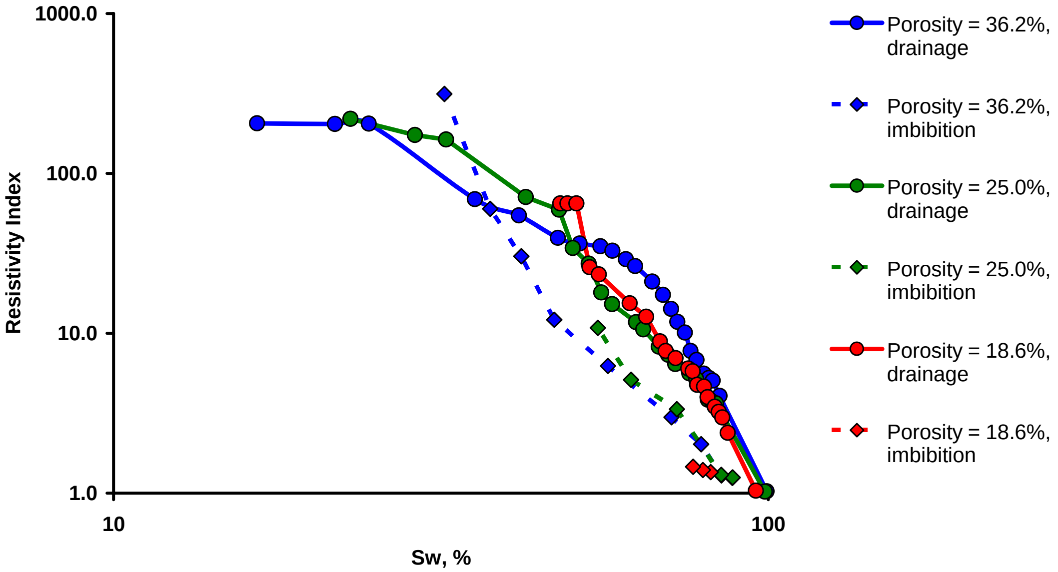

Fig. 115 Influence of pore-filling cementation on hysteresis in resistivity index. Oil-wet conditions. Contact angle = 0 degrees.

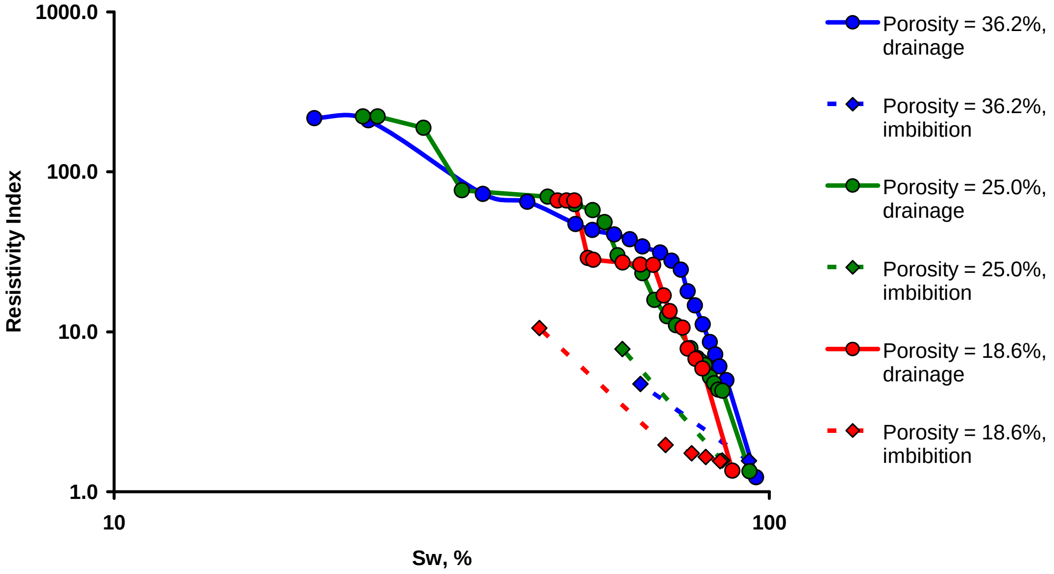

Fig. 116 Influence of isopachous cementation on hysteresis in resistivity index. Oil-wet conditions. Contact angle = 30 degrees.

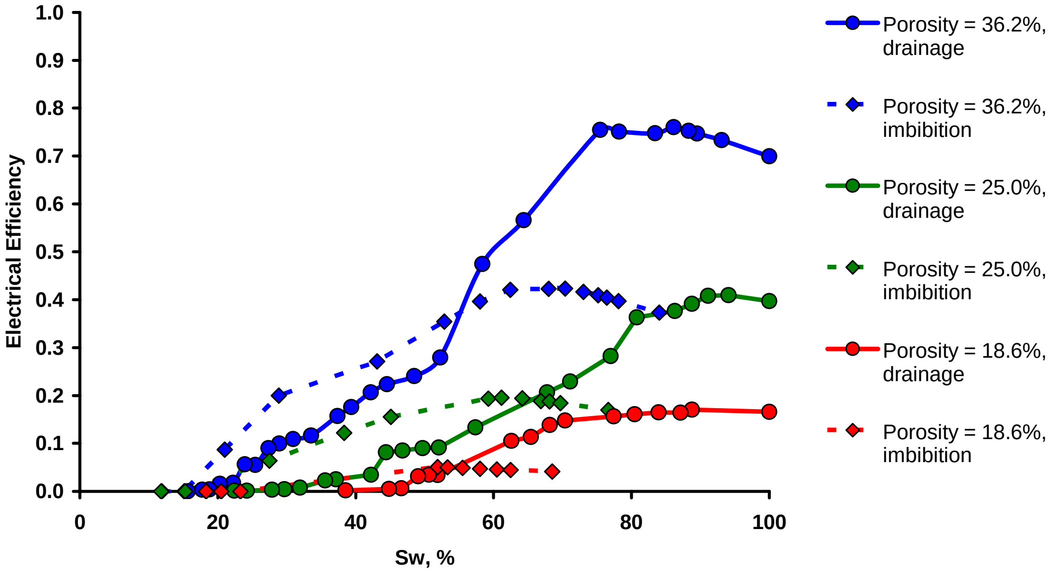

Fig. 117 Influence of pore-filling cementation on hysteresis in electrical efficiency. Water-wet conditions. Contact angle = 0 degrees.

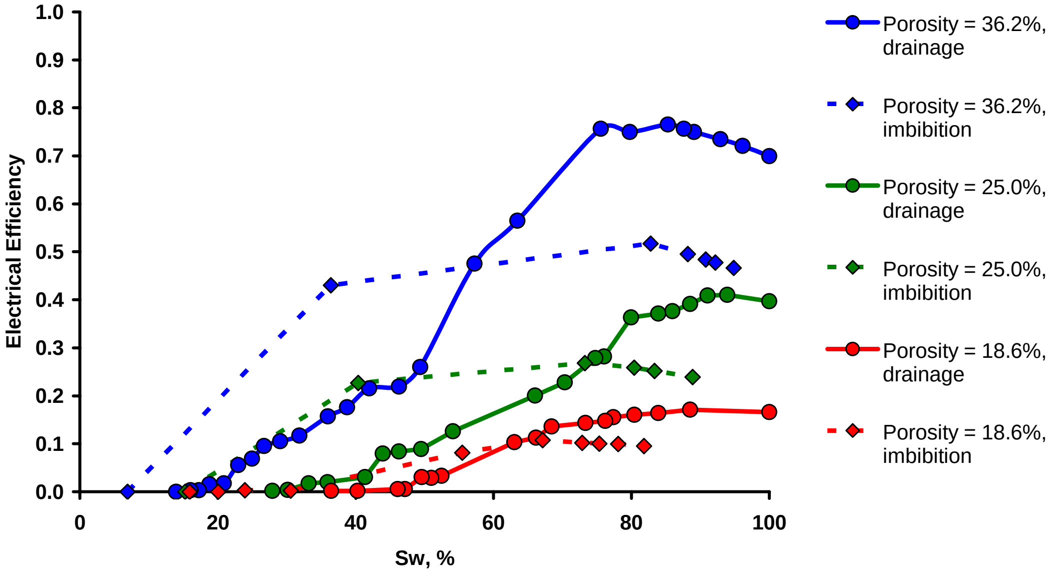

Fig. 118 Influence of pore-filling cementation on hysteresis in electrical efficiency. Water-wet conditions. Contact angle = 30 degrees.

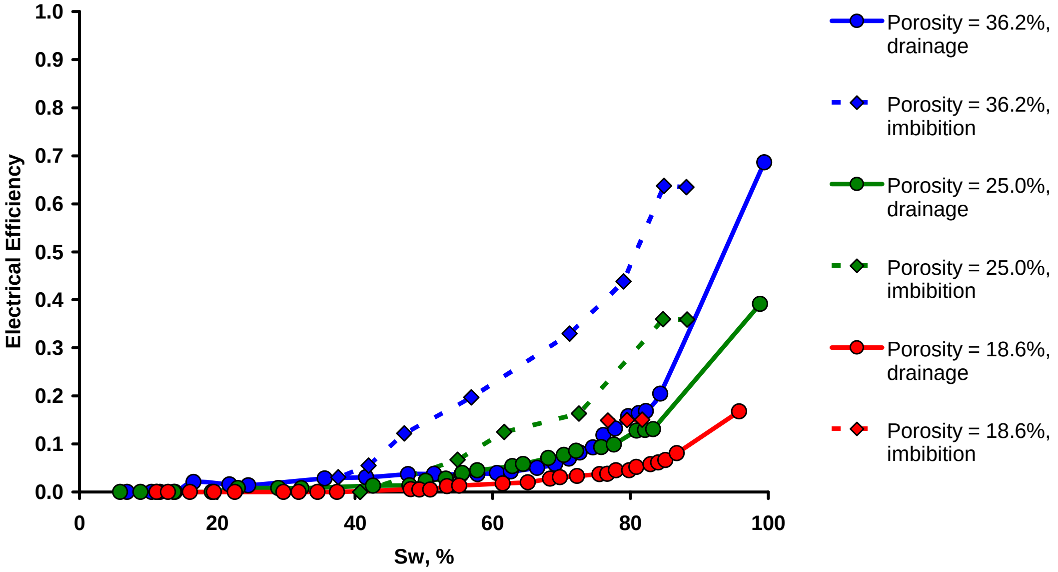

Fig. 119 Influence of pore-filling cementation on hysteresis in electrical efficiency. Oil-wet conditions. Contact angle = 0 degrees.

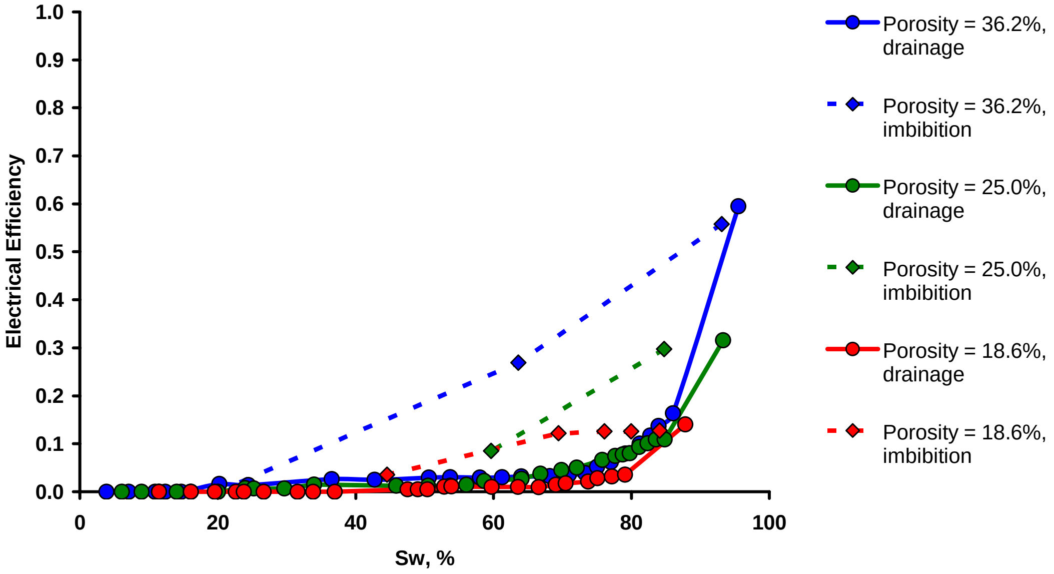

Fig. 120 Influence of pore-filling cementation on hysteresis in electrical efficiency. Oil-wet conditions. Contact angle = 30 degrees.

Figs. 121 – 128 depict the influence of wettability on hysteresis in resistivity index (water-wet conditions, Figs. 121 – 122; oil-wet conditions, Figs. 123 – 124) and electrical efficiency (water-wet conditions, Figs. 125 – 126; oil-wet conditions, Figs. 127 – 128) for different values of pore-filling cement (values of porosity 25.0% and 18.6%). Qualitatively, the effect of wettability is similar to the case of unconsolidated packing (Figs. 93 – 96) and isopachous cement (preceding section).

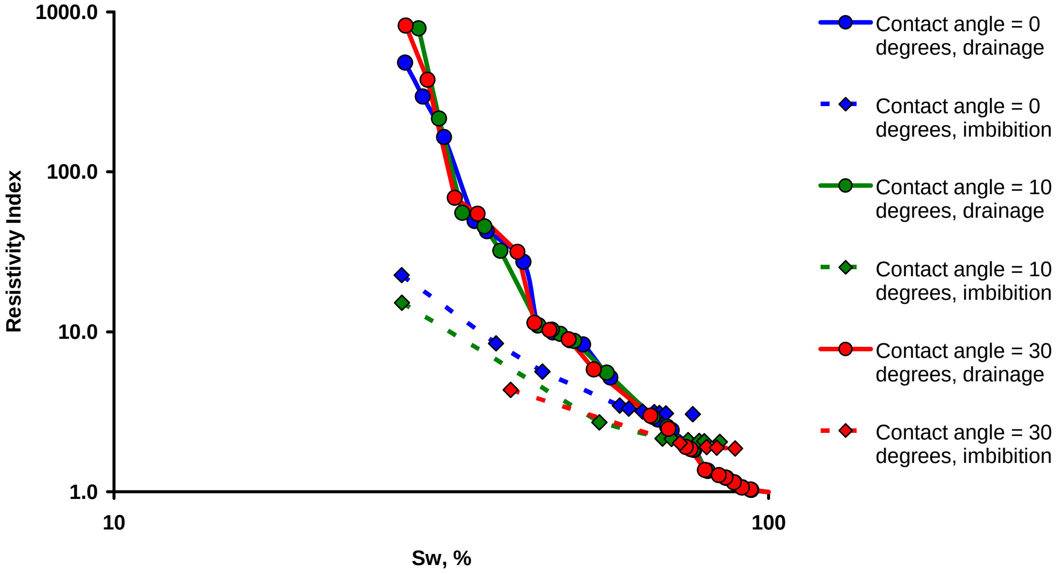

Fig. 121 Influence of wettability on hysteresis in resistivity index. Pore-filling cement, porosity = 25.0%. Water-wet conditions.

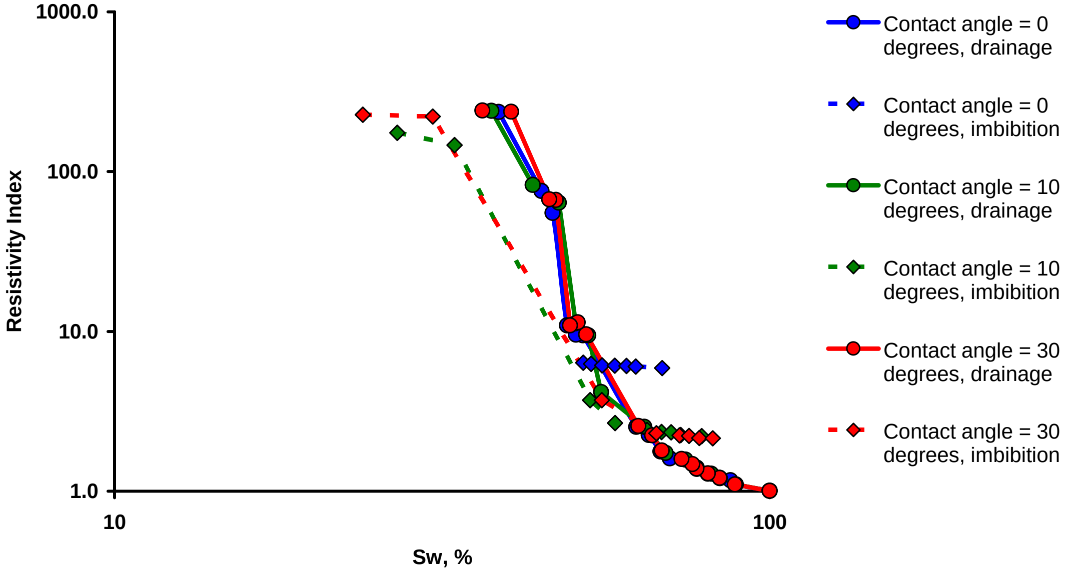

Fig. 122 Influence of wettability on hysteresis in resistivity index. Pore-filling cement, porosity = 18.6%. Water-wet conditions.

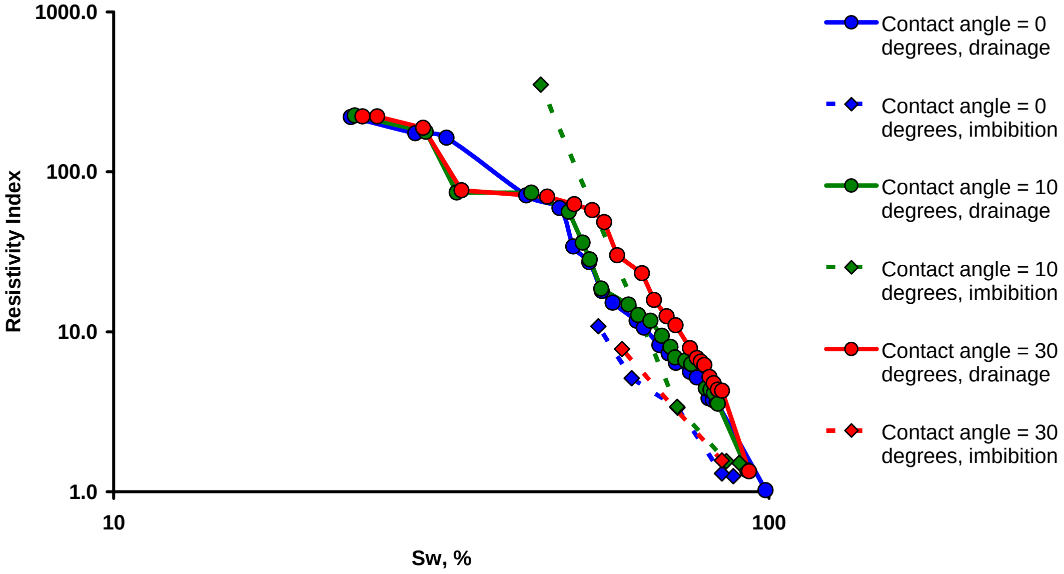

Fig. 123 Influence of wettability on hysteresis in resistivity index. Pore-filling cement, porosity = 25.0%. Oil-wet conditions.

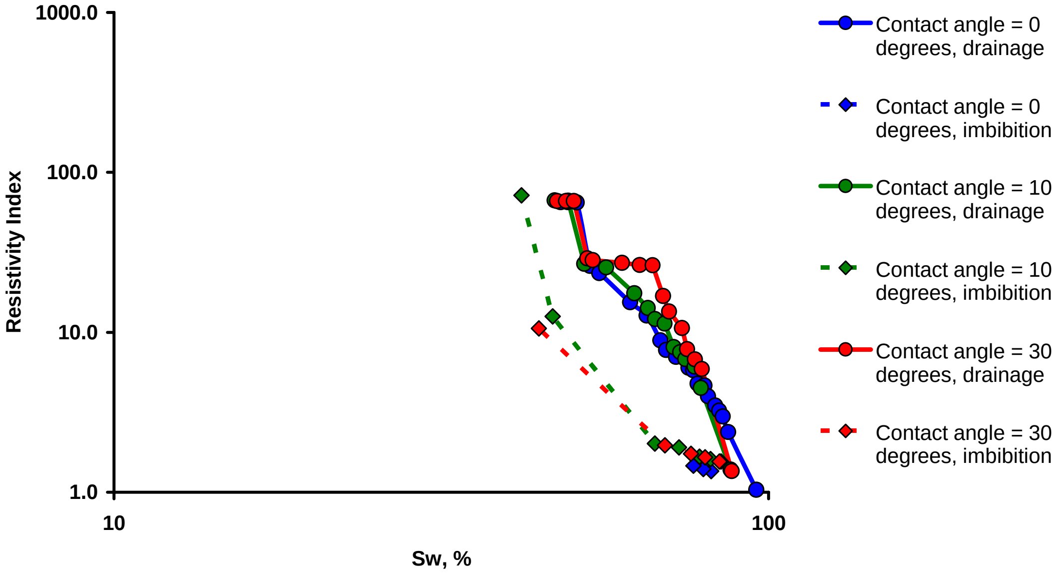

Fig. 124 Influence of wettability on hysteresis in resistivity index. Pore-filling cement, porosity = 18.6%. Oil-wet conditions.

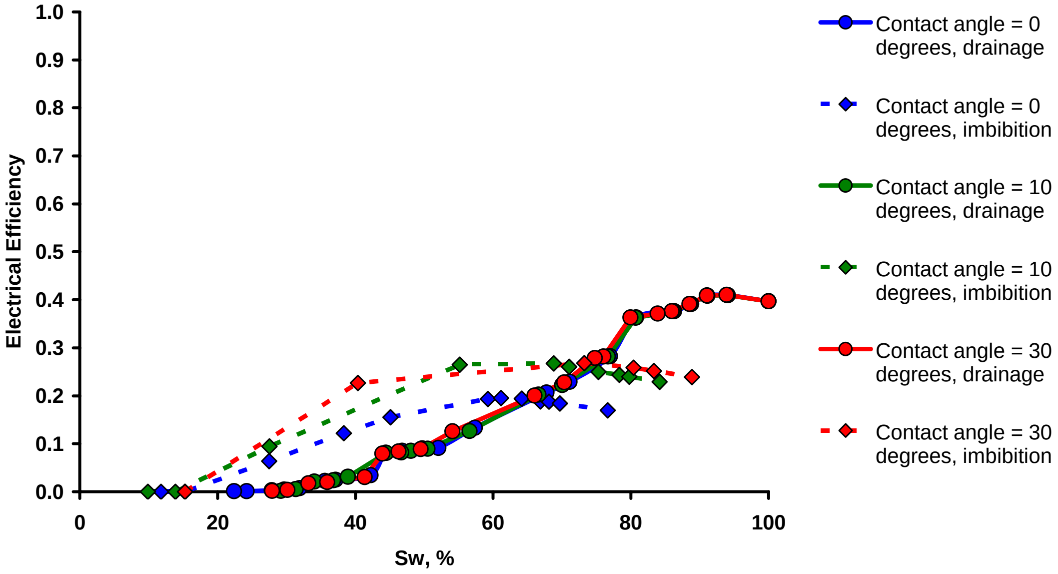

Fig. 125 Influence of wettability on hysteresis in electrical efficiency. Pore-filling cement, porosity = 25.0%. Water-wet conditions.

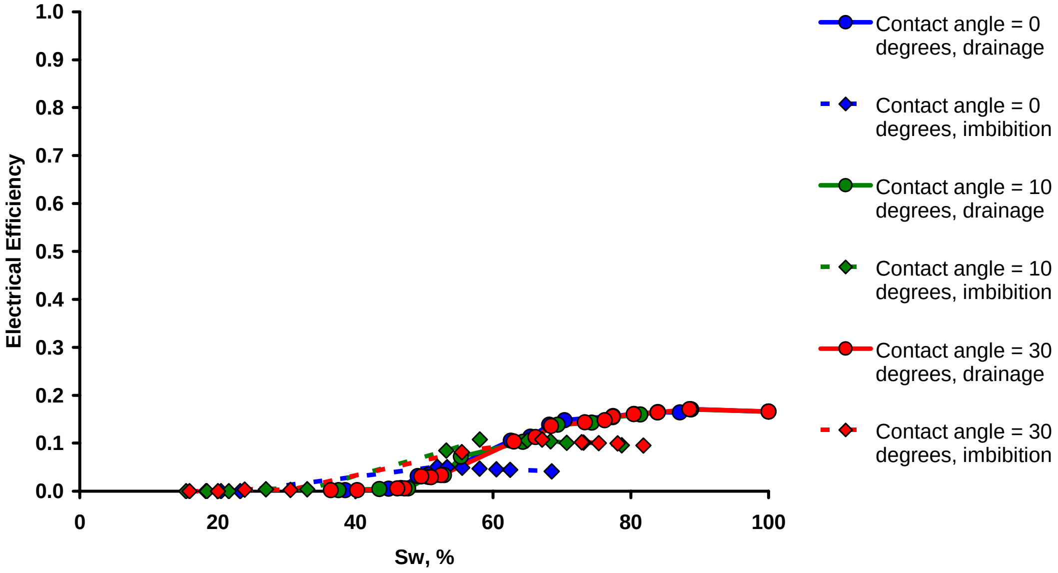

Fig. 126 Influence of wettability on hysteresis in electrical efficiency. Pore-filling cement, porosity = 18.6%. Water-wet conditions.

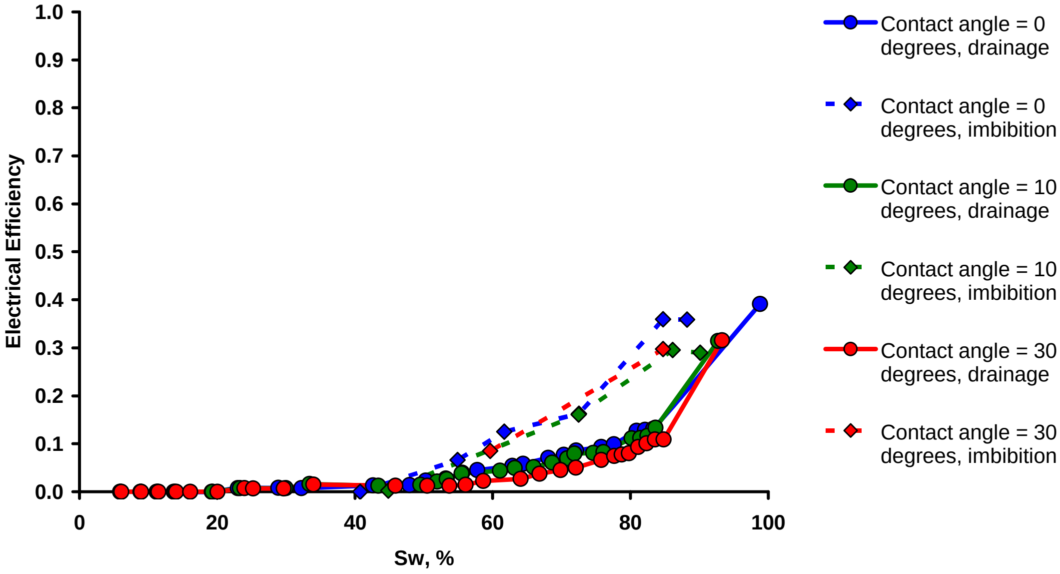

Fig. 127 Influence of wettability on hysteresis in electrical efficiency. Pore-filling cement, porosity = 25.0%. Oil-wet conditions.

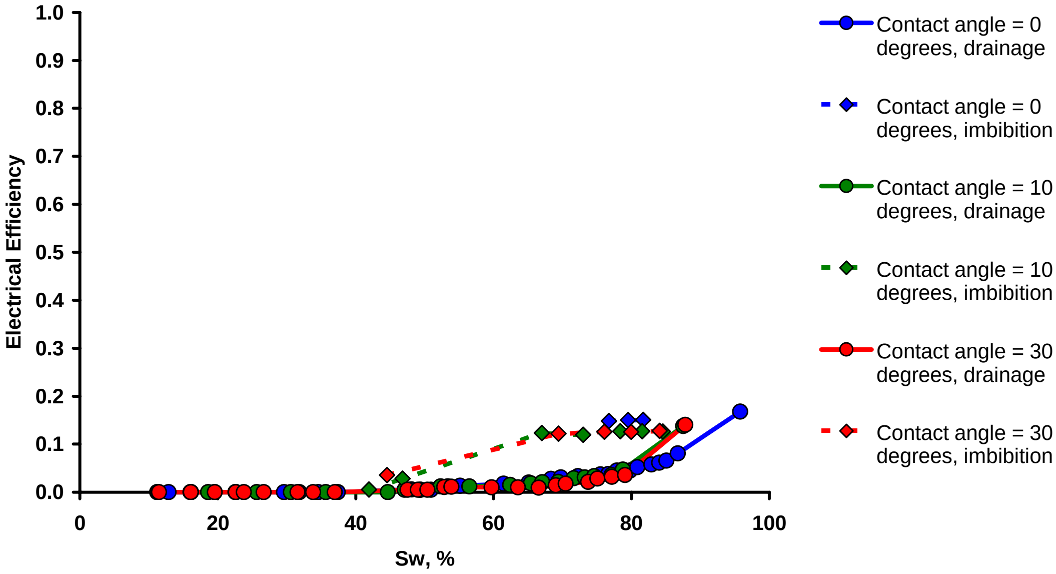

Fig. 128 Influence of wettability on hysteresis in electrical efficiency. Pore-filling cement, porosity = 18.6%. Oil-wet conditions.

Chapter V

In order to better understand and quantify fluid flow and transport processes in porous media, it is important to have knowledge of interfacial areas. Mass transfer rates for processes such as adsorption, dissolution, and volatilization are proportional to solid-fluid and fluid-fluid interfacial areas. The air-water interfacial area plays a critical role in remediation processes like soil-vapor extraction in vadose zone. Air-water interfaces also serve as sorption sites for colloids and bacteria, subsequently retarding their transport in unsaturated media. Similarly, knowledge of liquid-liquid interfacial area is important in estimating the contaminant flux between non-aqueous phase liquids and water. Liquid-liquid and liquid-solid interfacial areas are often included as independent parameters in theories of multiphase flow [50, 51, 60], which allows relating parameters of the flow (i.e. relative permeabilities) to independently measured interfacial area.

Most models for fluid transport in porous media employ a "lumped" parameter for interphase mass transport, (e.g. Powers *et al*, [111]). The lumped parameter includes an interfacial area and a mass transfer coefficient. This circumvents the difficulty of measuring independently the interfacial area on which or through which the adsorption, dissolution etc. is occurring. If interfacial area were constant, interpreting the lumped parameter is straightforward. Experiments show that interfacial area varies with phase saturation [68], however, and this complicates the analysis of mass transfer rates.

The importance of interface area has motivated the development of several techniques for measuring interfacial areas. Some experimental measurements of air-water interfacial area in unsaturated porous media as a function of saturation have been reported. Karkare and Fort [73] used a hydrophobic surfactant (1-tetradecanol) to study its impact on water movement and then calculated air-water interfacial area as the number of molecules of surfactant required to initiate water movement multiplied by area of each surfactant molecule. Kim *et al* [75] developed a miscible displacement technique using interfacial tracers to measure the interfacial areas. Many other researchers have also reported results with this technique. Faisal Anwar *et al* [33] developed a method to measure air-water interfacial area using the surfactant adsorption concept. Magnetic resonance imaging (MRI) has also been used to image the geometry of the fluids in pore space; algorithms can be applied to the images to identify the interface and characterize the liquid-liquid interfacial area, along with volume and shape of the NW phase trapped in the porous media [3, 71]. Recent theoretical and numerical approaches include the methodologies developed by Costanza-Robinson and Brusseau [27], Bradford and Leij [11], Berkowitz and Hansen [8] and Dalla *et al* [29]. These different approaches sometimes exhibit different qualitative trends of interfacial area as a function of saturation, and in some cases display considerable variation in the magnitude of the area (see Bryant and Johnson, [14] and Gladkikh and Bryant, [43], for a summary). Thus it is useful to introduce theoretical constraints on the possible range of behavior in order to evaluate a particular measurement and to compare different techniques.

It is also useful to have a theoretical basis for understanding different contributions to interfacial area, which is a strong function of the morphology of fluids in the porous media. One type of interface is that between the disconnected (also referred to as residual) volumes of one fluid phase and the connected bulk volume of the other. The isolated phase has different morphologies. Trapped W phase can exist as pendular rings at grain contacts after surrounding pores have been drained, as lenses left in pore throats and as "islands" occupying one (or more) pore(s). Computationally we treat lenses like double-sided menisci (see section 2.2.3). Trapped NW phase exists as blobs in pores surrounded by W phase. The ratio of area to volume differs significantly for these morphologies.

The second type of interface is the meniscus present between the bulk connected W and bulk connected NW phases. The third type of the interface is the film of W phase on grains in pores containing NW phase. The film area in drained pores is very large compared to the area of the interface between bulk connected phases. However, film area often does not contribute to mass transfer applications because film volumes are small sources/sinks for mass transfer. Because most experimental measurement techniques do not discriminate between the different morphologies, understanding the contribution of each morphology can lead to a better understanding of the experimental technique, as well as the application of the measurements.

5.1. Thermodynamic Analysis of Interfacial Area Behavior during Drainage and Imbibition

In this section we summarize classical thermodynamic treatments of interfacial areas in porous media between two immiscible fluids. These allow simple inferences regarding the magnitude and behavior of areas as functions of saturation. These inferences also provide insight into measurements of areas in porous media of different wettability, and this proves crucial when interpreting the experiments.

To understand the trends of measured interfacial area in a drainage or imbibition experiment, we need to know what type of area the method is measuring and how the areas of the interfaces between phases in porous media (solid grains, W and NW phase) change qualitatively. Presented below is a simple thermodynamic analysis of changes in these areas. The analysis closely follows the works of Adamson [1], Israelichvili [67], Leverett [81], Melrose [95], Morrow [99], Hirasaki [65], Gray and Hassanizadeh [50, 51], Hassanizadeh and Gray [60] and others; our objective is to use these classical ideas to understand the contribution of films and grain surfaces to interfacial area.

The key parameter that affects the behavior of the porous medium during drainage or imbibition is the *spreading coefficient*.

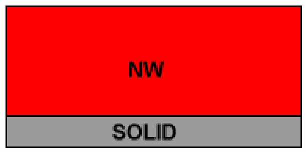

Fig. 129 NW phase on solid surface.

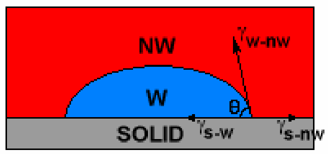

Fig. 130 Non-spreading W phase: the drop of W phase remains intact on solid surface, surrounded by NW phase.

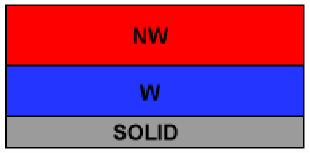

Fig. 131 Spreading W phase: the W phase spreads over solid surface, displacing NW phase.

Consider the NW phase on solid surface (S) (Fig. 129). If a drop of W phase is introduced into the system, either W will stay on the surface as a drop, forming contact angle θ (Fig. 130), or W will spread over the solid surface, displacing NW (Fig. 131, see also section 2.1.5). For the second case we have for the change in interfacial energy between initial stage (Fig. 130) and final stage (Fig. 131):

$$\Delta G = (\gamma_{WS} + \gamma - \gamma_{NS})\Delta A\,, \tag{77}$$

where γ_{WS} – interfacial tension between W and S; γ_{NS} – between NW and S; γ – between W and NW and ΔA is the area of solid surface.

In order for the W to spread, we must have

$$\gamma_{WS} + \gamma - \gamma_{NS} < 0\,, \quad \text{or} \quad \frac{\gamma_{WS} + \gamma}{\gamma_{NS}} < 1\,. \tag{78}$$

The fraction in (78) we will call *spreading coefficient* ***k***. So, if ***k***<1, then W will spread over solid surface, and we will call such a condition *strongly wetting*. In porous media it means that W will form *thin films* on the surfaces of solid grains, because the same simple analysis is valid for the case of a spherical surface also. Moreover, these thin films will not be destroyed during drainage or imbibition, because energetically films are the preferable state for the system. If ***k***>1, then W will remain on the solid surface in the form of the drop, and we need to use the contact angle equation instead:

$$\gamma_{NS} = \gamma_{WS} + \gamma \cos\theta . \qquad (79)$$

In porous media ***k***>1 means that W will not form thin films on the grain surfaces in the presence of NW. Instead there is a possibility of existence of W-drops on solid grains, which complicates the configuration of interfaces. We will call such a condition *weakly wetting*. Also, we need to consider displacement of W from the grain surfaces by NW during drainage and the opposite displacement during imbibition.

5.1.1 Strongly Wetted System: Primary Drainage

Consider a dense random packing of equal spheres as a model porous medium. Because ***k***<1, thin films of W will cover the sphere surfaces all the time.

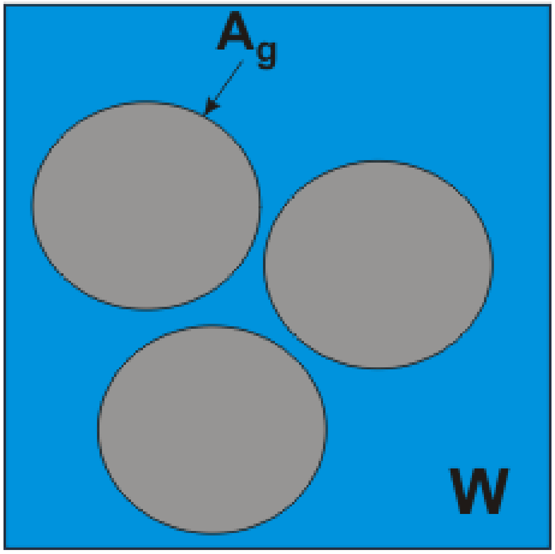

Fig. 132 Initial stage of primary drainage. Strongly wetted system (*k*<1).

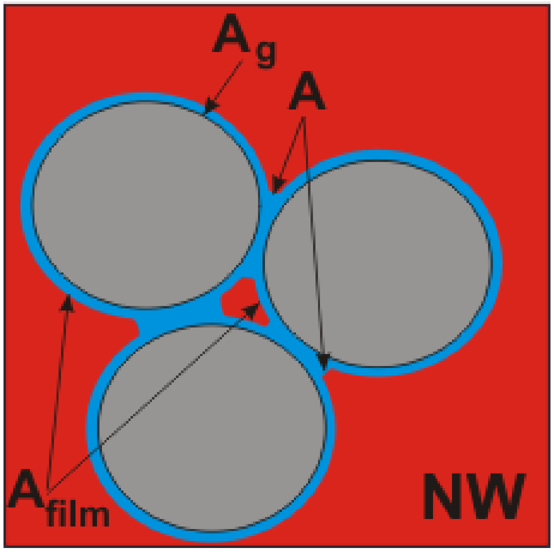

Fig. 133 Final stage of primary drainage. Strongly wetted system (*k*<1).

The schematic of primary drainage is presented in Figs. 132 and 133. In this figure and everywhere below the colors of phases correspond to the colors in Figs. 129 – 131. In the initial stage (Fig. 132) we have only W-S interface, the area of which is exactly the *total grain area* A_g. So, for the initial interfacial energy we have:

$$E_0^{dr} = A_g \gamma_{WS}, \tag{80}$$

and in the final stage (Fig. 133) we have:

$$E_f^{dr} = A_g \gamma_{WS} + A\gamma + A_{film}\gamma, \tag{81}$$

where A – area of *bulk* W-NW interface (e.g. surface area of menisci and pendular rings), and A_{film} – area of thin films alone (e.g. area of W-NW interface, which exists in the form of thin film).

Thus, for the change in energy during primary drainage we have:

$$\Delta E = E_f^{dr} - E_0^{dr} = (A + A_{film})\gamma. \tag{82}$$

This change in energy is positive. This is consistent with the fact that work is done *on* the system during drainage as the meniscus is pushed into the pore space: $W = \int P_c dV_{nw}$.

Moreover, an energy balance shows that during *any* process the work done on the system cannot exceed the increase of its free energy:

$$-W = \int_0^f P_c dV_w \leq E_0^{dr} - E_f^{dr} = -\Delta E. \tag{83}$$

The behavior of drainage curve (capillary pressure remains positive as W saturation decreases) shows that the work is done *on* the system. From the energetic point of view the inequality in Eq. (83) can be described as follows: work, done on the system by the surroundings, is expended; part of the work goes toward increasing the free energy of the system, and part of this work is lost due to irreversibility. We note that this thermodynamic analysis *does not demand reversibility* of the processes, nor does it presume quasi-static displacements. In the case of a reversible drainage process we will have zero losses of the work done; in the case of a reversible imbibition process (see next section) we will have zero losses of the energy released. In these cases inequality in (83) will become equality. Also, in this section we are not yet trying to consider microscopic behavior of the system and estimate losses of energy due to spontaneous microscopic events such as Haines jumps [56, 99]. The analysis is valid in the *macroscopic* sense, when we can estimate the work by integrating capillary pressure curve.

As in Fig. 133, the *total* interfacial area of W-NW interface consists of two parts: bulk (meniscus and pendular rings) contribution, A, plus thin films area A_{film}. According to Eqs. (83) and (84), the sum of these parts must *increase* monotonically during drainage if the drainage curve is monotonic. (Drainage curves measured in the laboratory are invariably monotonic.) Moreover the sum must be bounded from above by total grain area A_g. To see this, consider the limits of A and A_{film} as W saturation S_w goes to zero: $A \to 0$ and $A_{film} \to A_g$. Furthermore, the area of thin films must inevitably increase during drainage, because films are continually created as each pore drains. Thus the behavior of the bulk interfacial area is not constrained, in the following sense: it can increase or decrease during drainage, but any decrease must be less in absolute value than a concomitant increase in the area of thin films. For connected W, A must eventually decrease during drainage as S_w approaches zero. The possible trends are shown schematically in Fig. 134. In this figure trends for the areas are shown asymptotically when W phase saturation is going to zero. Such a behavior is possible theoretically in a strongly wet system: when capillary pressure increases to infinity, it is possible to displace all macroscopic volumes of W phase from the media, since the W phase is assumed to be hydraulically connected through thin films. At the end of such process (infinite capillary pressure) only thin films remain in the system. Their macroscopic volume and therefore contribution to W phase saturation is negligible, and W phase saturation is essentially zero.

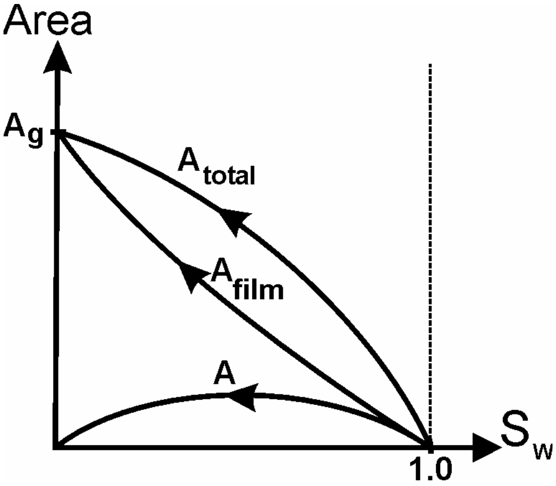

Fig. 134 Schematic trends of interfacial areas during primary drainage for strongly wetted system (*k*<1).

Thus, if we assume that the technique for determining W-NW interfacial area measures *total* area, we expect that obtained trend should be increasing, as shown in Fig. 134, with the limitation that total interfacial area *cannot exceed total grain area.* If experimental results deviate from this behavior widely, it means that the method measures something else, not the total W-NW interfacial area.

5.1.2 Strongly Wetted System: Imbibition

Now, let us consider imbibition in the case ***k***<1. Similarly to drainage, here we also have thin films of W on grain surfaces during the whole process.

The schematic of imbibition is presented in Figs. 135 and 136. We assume that the initial stage of imbibition (Fig. 135) coincides with the final stage of drainage (Fig. 133). (This assumption corresponds to a common situation in practice, but it is not essential for our analysis.) In this case total area of W-NW interface also consists of two components: bulk area and thin films area. For the initial interfacial energy we have:

$$E_0^{imb} = E_f^{dr} = A_g \gamma_{WS} + A\gamma + A_{film}\gamma \,, \tag{84}$$

and in the final stage (Fig. 136) we have:

$$E_f^{imb} = A_g\gamma_{WS} + A'\gamma + A'_{film}\gamma\,, \tag{85}$$

where A' – area of the interface between trapped NW and W in the bulk; A'_{film} – area of thin films, which are contained within trapped clusters of NW.

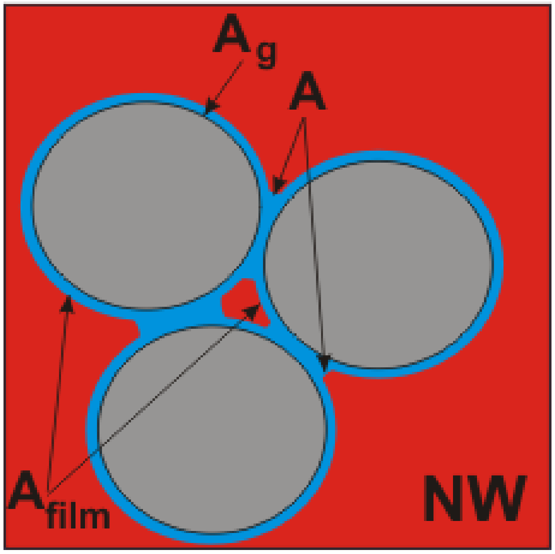

Fig. 135 Initial stage of imbibition – the same as final stage of drainage (cf. Fig.133). Strongly wetted system (k<1).

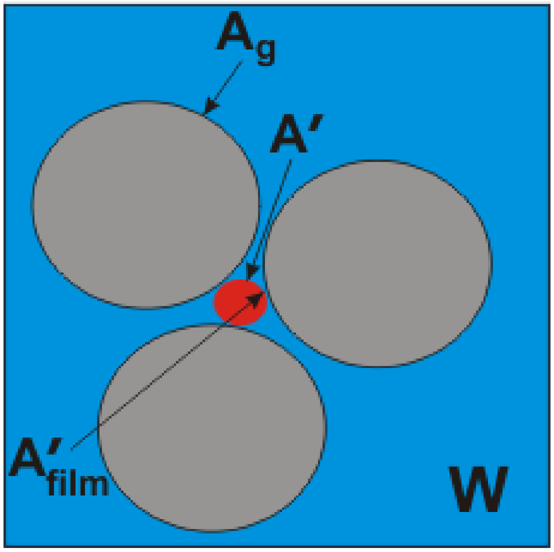

Fig. 136 Final stage of imbibition. Strongly wetted system (k<1). Thin films of W phase exist around grains within trapped clusters of NW phase.

Thus, for the change in energy during imbibition we have:

$$\Delta E = E_f^{imb} - E_0^{imb} = (A' + A'_{film} - A - A_{film})\gamma\,. \tag{86}$$

Note that $A'_{film} - A_{film}$ is negative, since films are being destroyed as each pore imbibes wetting phase. From the behavior of imbibition capillary curve (capillary pressure remains positive as W saturation increases) it follows that the work is done *by* the system. Thermodynamics demands that this work cannot exceed the decrease of the free energy of the system:

$$0 < W = \int_0^f P_c dV_w \le E_0^{imb} - E_f^{imb} = -\Delta E \,. \tag{87}$$

Equation (87) implies that the change in free energy during imbibition must be negative. From the energetic point of view the process can be described as follows: the system tends to achieve the state with the lower free energy. The accompanying decrease in energy is spent in two ways: as work done by the system on the surroundings, and as energy lost during irreversible changes. Again, as in the case of drainage, for the reversible process inequality in (87) becomes equality.

So, the change in *total* interfacial area of W-NW interface also consists of two parts: destruction of thin films in the pores in which W displaces NW, and change of the interfacial area between the bulk phases due to destruction of some rings and menisci and trapping of NW. The change in total interfacial area must have *decreasing* character during imbibition and be bounded from above by total grain area A_g. (This upper bound exists because the initial area is bounded by this value; the argument is completely analogous to that for drainage discussed above). Furthermore, since the area of thin films must inevitably decrease during imbibition, the behavior of the bulk interfacial area is not constrained. That is, A' could be greater than A, if the magnitude of the increase A'-A were less than a concomitant decrease in the film area $A'_{film} - A_{film}$. The possible schematic trends are shown in Fig. 137.

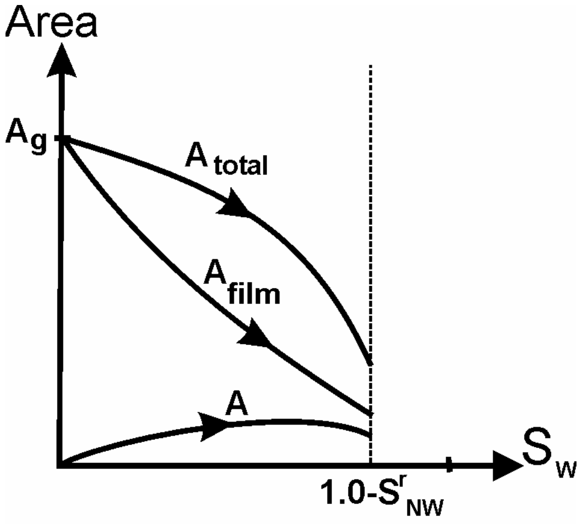

Fig. 137 Schematic trends of interfacial areas during imbibition. Strongly wetted system (k<1).

Thus, if we assume that the technique for determining W-NW interfacial area measures *total* area, we expect that obtained trend should be decreasing, as shown in Fig. 137, with the limitation that total interfacial area *cannot exceed total grain area.* If experimental results deviate from this behavior widely, it means that method measures something else, not the total W-NW interfacial area.

5.1.3 Weakly Wetted System: Primary Drainage

Now let's consider primary drainage in the case ***k***>1. In this case there are no thin films of W on grain surfaces, but drops of W can exist there instead.

The schematic of primary drainage is presented in Figs. 138 and 139. The initial stage (Fig. 138) corresponds to the initial stage of primary drainage for ***k***<1, Fig. 132. For the initial interfacial energy we have:

$$E_0^{dr} = A_g \gamma_{WS} , \tag{88}$$

and for the final stage (Fig. 139) we have:

$$E_f^{dr} = A_g^w \gamma_{WS} + A_g^{nw} \gamma_{NS} + A\gamma , \tag{89}$$

where A_g^w – area of solid grains in contact with W; A_g^{nw} – area of solid grains in contact with NW; A – area of W-NW interface.

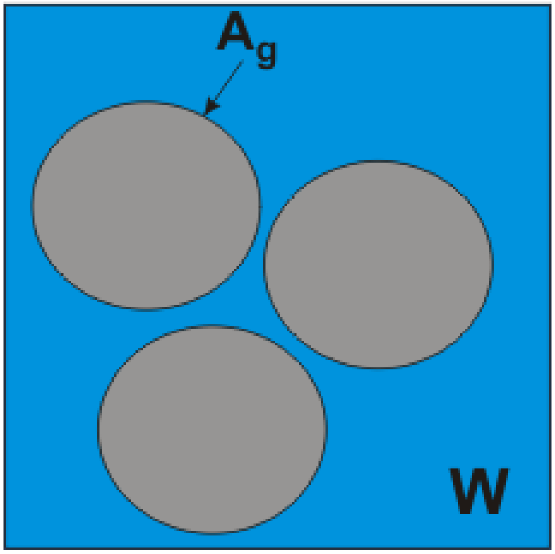

Fig. 138 Initial stage of primary drainage. Weakly wetted system (k>1).

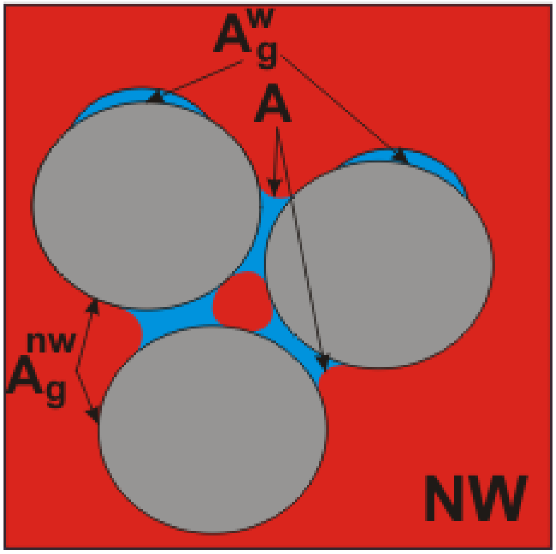

Fig. 139 Final stage of primary drainage. Weakly wetted system (k>1).

Thus, for the change in energy during primary drainage we have:

$$\begin{aligned} 0 < \Delta E = E_f^{dr} - E_0^{dr} &= A_g^w \gamma_{WS} + A_g^{nw} \gamma_{NS} + A\gamma - A_g \gamma_{WS} = \\ &= A_g^{nw}(\gamma_{NS} - \gamma_{WS}) + A\gamma = (A_g^{nw} \cos\theta + A)\gamma. \end{aligned} \tag{90}$$

Here the third equality holds because $A_g = A_g^w + A_g^{nw}$ and the last equality follows from (79). From the same considerations, as in the case of ***k***<1 this change in energy must be positive, and the quantity in the last brackets in (90) must be also positive.

So, in this case the *total* interfacial area of W-NW interface is the bulk interfacial area (area of menisci and pendular rings) plus surface area of possible drops of W on solid surface. Since ${A_g}^{nw}$ must inevitably increase during drainage, the behavior of the second component (bulk interfacial area A) is not constrained. But the limitation that this W-NW interfacial area A cannot exceed total grain area still remains at any intermediate point of drainage, because ${A_g}^{nw}$ is bounded from above by total grain area (to see this, consider drainage in the limit of S_w going to zero). The possible schematic trends are shown in Fig. 140.

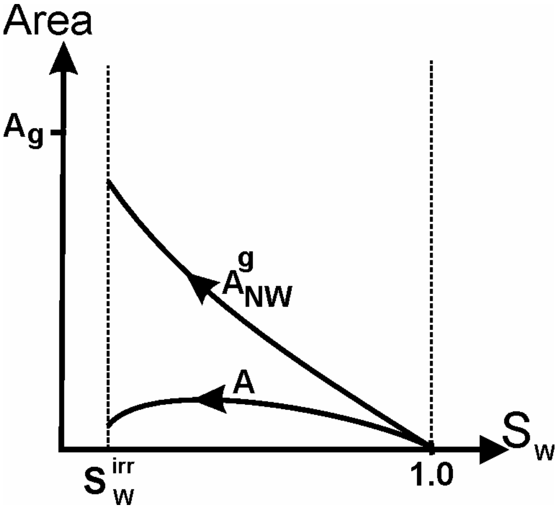

Fig. 140 Schematic trends of interfacial areas during primary drainage. Weakly wetted system (*k*>1).

So in experiments for which ***k***>1, we don't expect monotonic behavior of the measured W-NW interfacial area. Nevertheless, simple considerations of the endpoints (S_w = S_{wirr} (irreducible W saturation) and S_w = 1.0) show that this area should increase from zero at S_w = 1.0, reach a maximum, then decrease to zero as S_w is going to zero, as shown in Fig. 140. The only limitation is that *the W-NW area A cannot exceed total grain area.*

If experimental results give values of interfacial area, which is higher than total grain area, it means that method measures something else, not the total W-NW interfacial area. In this case, however, we need to be careful in defining total grain area. A rough grain can have an area greatly exceeding the nominal area of the corresponding smooth sphere of the same diameter. This was not the case for ***k***<1 discussed above, because then there were thin films of W on grain surfaces. At the capillary pressures typical of imbibition and drainage experiments, the curvature of these films will not follow grain roughness, and so the shape of grains, surrounded by thin films of W, should be very close to spherical.

5.1.4 Weakly Wetted System: Imbibition

Finally, let us consider imbibition in the case ***k***>1. There are no thin films of W on grain surfaces in this case also, but drops of W can exist there instead.

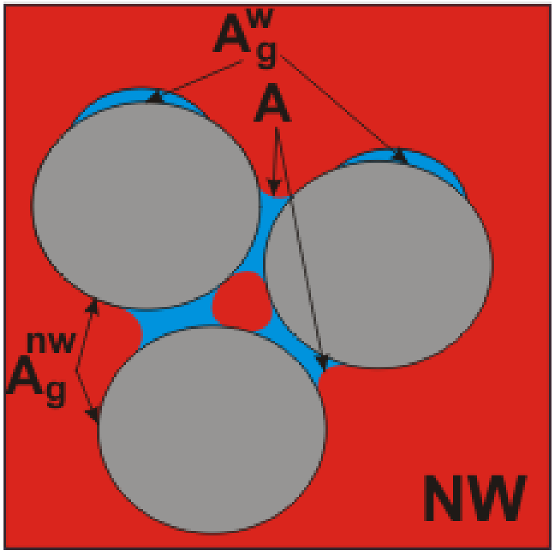

Fig. 141 Initial stage of imbibition – the same as final stage of drainage (cf. Fig. 139). Weakly wetted system (k>1).

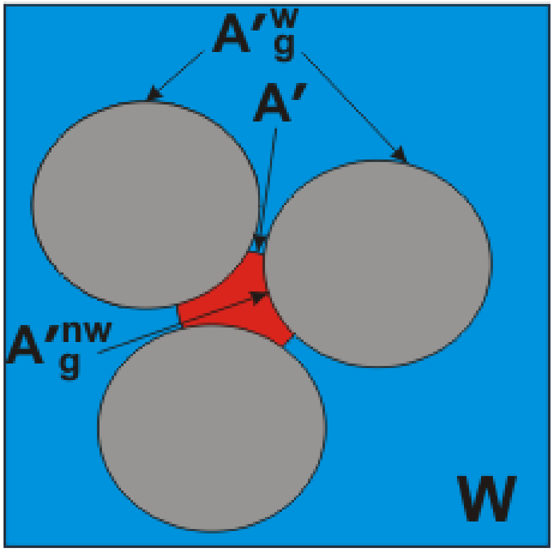

Fig. 142 Final stage of imbibition. Weakly wetted system (k>1).

The schematic of imbibition is presented in Figs. 141 and 142. Initial stage (Fig. 141) coincides with the final stage of primary drainage (Fig. 139), so for the initial interfacial energy we have:

$$E_0^{imb} = E_f^{dr} = A_g^{w}\gamma_{WS} + A_g^{nw}\gamma_{NS} + A\gamma\,, \tag{91}$$

and for the final stage (Fig.141) we have:

$$E_f^{imb} = A_g'^{w}\gamma_{WS} + A_g'^{nw}\gamma_{NS} + A'\gamma\;. \tag{92}$$

In (91)-(92) we have the same notations for the areas as in (88)-(90), and the variables with the stroke correspond to the areas in the final stage of imbibition (Fig. 142).

At any intermediate point of imbibition the following must hold:

$$A_g^w + A_g^{nw} = A_g'^w + A_g'^{nw} = A_g \,. \tag{93}$$

Using (91)-(93) and (79), we obtain for the change in energy during imbibition:

$$0 > \Delta E = E_f^{imb} - E_0^{imb} = (\Delta A_g^{nw} \cos\theta + \Delta A)\gamma \,, \tag{94}$$

where ΔA_g^{nw} – change in the area of contact between NW and solid grains; ΔA – change in the area of W-NW interface $A' - A$. From the same considerations as in the case of $\boldsymbol{k}<1$ this change in energy must be negative, and the quantity in the brackets in (94) must be also negative.

So, in this case, as during drainage, the *total* interfacial area of W-NW interface is the bulk interfacial area plus surface area of possible drops of W on solid surface. Since A_g^{nw} must inevitably decrease during imbibition, the behavior of the second component (bulk interfacial area) is not constrained. That is, it can increase or decrease, but the magnitude of any increase cannot exceed the change $A'^g_{nw} - A^g_{nw}$. As in the other cases, this W-NW interfacial area cannot exceed total grain area at any intermediate point of imbibition, because the initial value of A_g^{nw} is bounded from above by total grain area. The possible schematic trends are shown in Fig. 143.

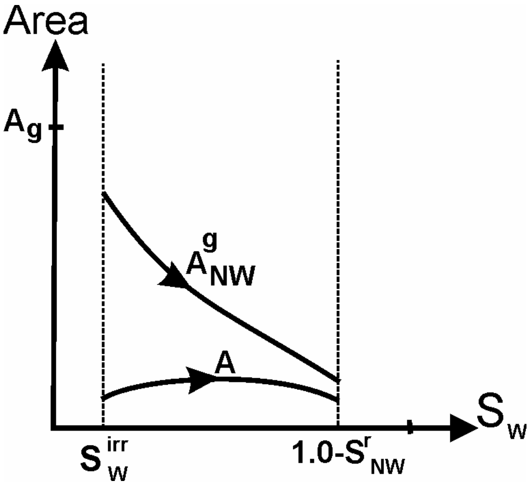

Fig. 143 Schematic trends of interfacial areas during imbibition. Weakly wetted system (k>1).

So, we can expect similar trends for imbibition, as for the case of drainage. We do not expect the increasing or decreasing character of the measured W-NW interfacial area, but at least in simple porous media it should have character as shown in Fig. 143. The only limitation again is that *neither of these areas can exceed total grain area.* Other remarks remain the same as for the case of drainage.

5.2 Results: Predictions of Interfacial Area

5.2.1 Interfacial Area: Comparison between Predictions and Experimental Data

Using the algorithms described above, we compute interfacial area between phases in the Finney pack during both drainage and imbibition. The methodology for computing volumes and surface areas of pendular rings was described in section 2.2.1; for menisci – in section 2.2.3. These simulations are consistent with the thermodynamic analysis, presented in the preceding section. All the results of the simulations shown below were computed simultaneously with capillary pressure curves, shown in sections 3.3 – 3.5.

First, we show the comparison between model predictions and experimental data for both drainage (Fig. 144) and imbibition (Fig. 145).

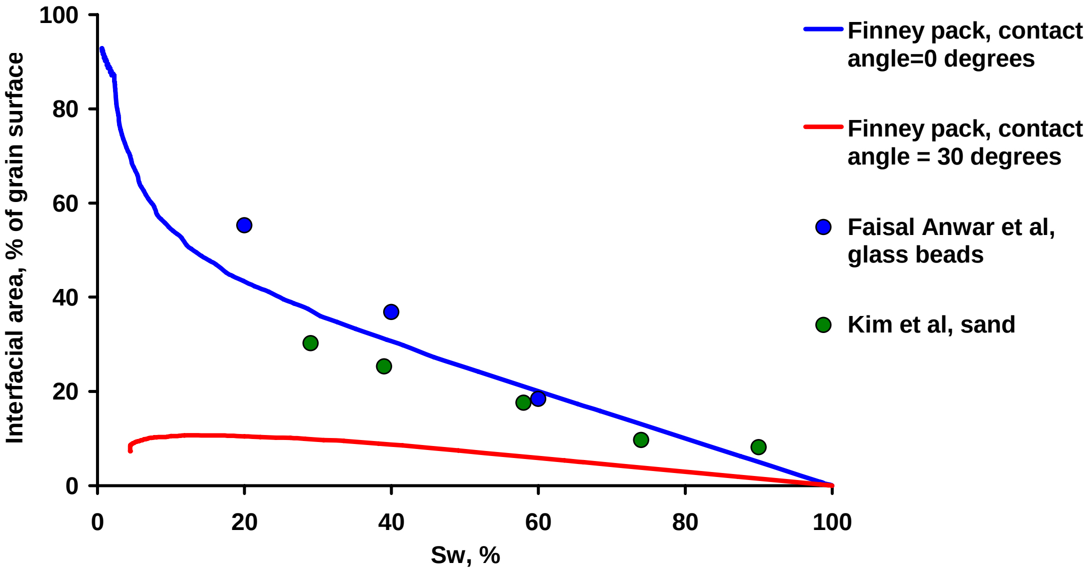

Fig. 144 Comparison between predictions in the unconsolidated Finney pack and experimental data for the behavior of interfacial area during drainage.

Fig. 144 presents results for interfacial area during simulations of drainage in the unconsolidated Finney pack for the values of contact angle of 0 and 30 degrees and experimental data from Faisal Anwar *et al* [33] (glass beads) and Kim *et al* [75] (unconsolidated sand). The agreement between predictions for zero contact angle and experimental data is good (similar monotonic behavior of interfacial area, cf. also with Fig. 134). Note that predicted curves in Fig. 144 corresponding to the values of contact angles of 0 (strongly wetted system) and 30 (weakly wetted system) degrees are qualitatively different (cf. to the thermodynamic analysis above – Figs. 134 and 140). For the extensive analysis of the behavior of interfacial area during drainage and comparison with experimental data, see also Bryant and Johnson [14].

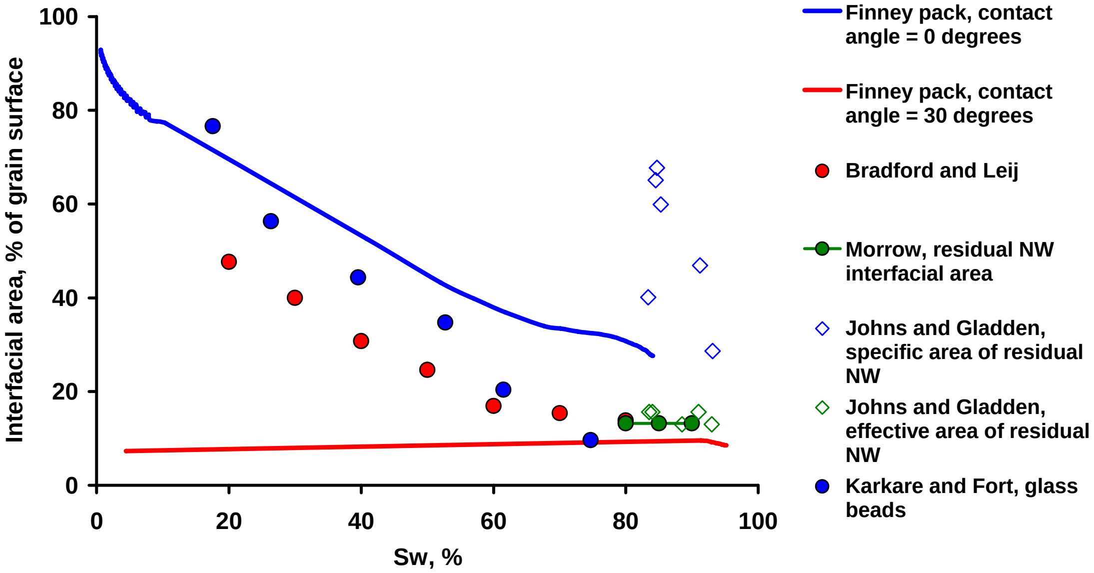

Fig. 145 Comparison between predictions in the unconsolidated Finney pack and experimental data for the behavior of interfacial area during imbibition.

Fig. 145 presents results of interfacial area simulations during imbibition in the unconsolidated Finney pack for the values of contact angle of 0 and 30 degrees and different experimental data.

Morrow [99] measured area of residual NW-phase in random packing of 3-mm beads, using visual investigation of 2D – cross sections after the phase configurations were “frozen” by *in situ* polymerization reactions. His value was 13.2% of total solid area. Unfortunately, he did not report his residual NW-phase saturation, so this result is plotted in the Fig. 145 as a line of constant value 0.132 of total solid area in the range of residual NW-phase saturations 0.1 – 0.2 of pore volume, a typical range for bead packs. Johns and Gladden [71] explored dissolution of octanol ganglia in random packings of glass ballotini and measured residual NW-phase area by magnetic resonance imaging (MRI). They reported values of “specific” area, which corresponds to our total interfacial area (includes solid-NW interface), and “effective” area, which corresponds to the bulk W – NW phase interface. For the former, they obtained values in the range from 0.3 to 0.7 expressed as a fraction of total solid surface; their residual NW – phase saturation ranged from 7 – 17%. For the latter, they reported values of about 0.15 for the same range of residual NW – phase saturation. These direct measurements of Morrow and values of "effective" area, obtained by Johns and Gladden, agree well with the predictions. As for the values of "specific" area, they represent the total interfacial area including solid – NW-phase area, so the difference between "specific" and "effective" areas is exactly the area of this solid – NW-phase interface. In some cases the values of these differences are about twice as large as maximal possible solid – NW-phase area for the Finney packing. The reason for this discrepancy remains puzzling, especially in light of the otherwise good agreement with predictions.

Karkare and Fort [73] proposed a measuring technique based on the adsorption of insoluble surfactant. They measured air-water interfacial area as a function of W-phase saturation for both glass bead packings and sand columns, but they used preliminary interfusion of the sample with water-surfactant mixture, so their process was not equivalent to imbibition. As shown in Fig. 145, they obtained the same decreasing trend in the interfacial area, from about 0.8 of total solid surface area at low W-phase saturation to 0.1 at high saturations. Comparison with predictions and thermodynamic analysis suggests that the solid – NW-phase area (thin films) is included in their measurements.

Bradford and Leij [11] computed interfacial area from imbibition data (capillary pressure vs. W-phase saturation) in an oil-air-sand system (oil wetted sand particles completely), based upon a thermodynamic approach [81, 99]. For consistency with other data in the Fig. 145 their measurements have been normalized by the specific surface area of the mixture of sands used in their experiments, reported by them as 650 cm^{-1}. They also obtained a monotonic decrease in area. Their areas are smaller than our predictions, especially at the beginning of the process. This could be explained by the fact that they used mixtures of sands with a wide distribution of particle sizes, so that their irreducible W-phase saturation was larger than the value for our monodisperse packing. The interfacial area would be correspondingly smaller. Their residual NW-phase saturation was about 20% of pore volume.

Note that the predicted curves in Fig. 145 corresponding to the values of contact angles of 0 (strongly wetted system) and 30 (weakly wetted system) degrees are qualitatively different (cf. to the thermodynamic analysis above – Figs. 137 and 143).

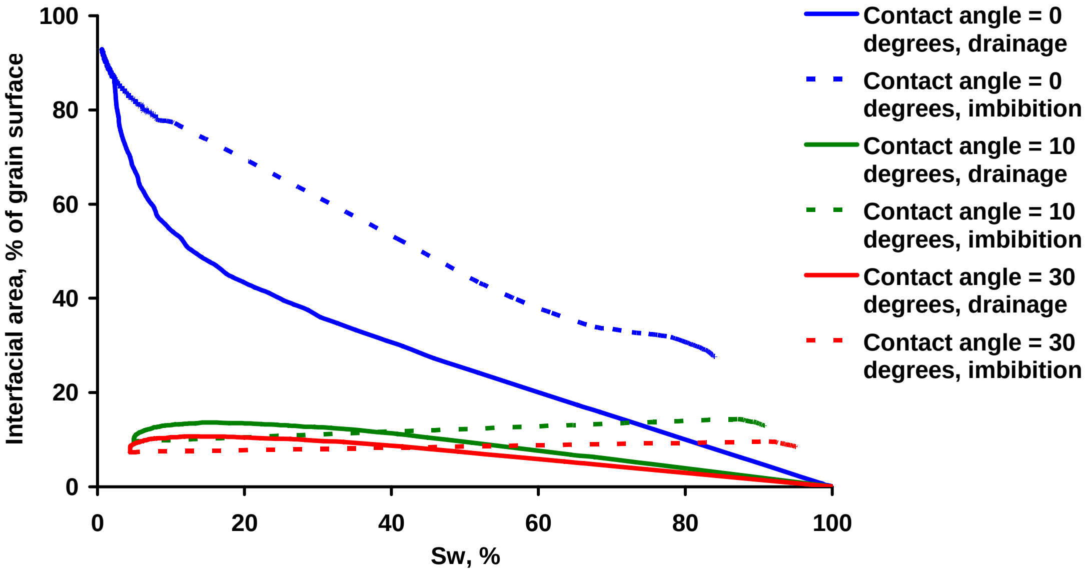

Fig. 146 Simulation of the hysteresis in interfacial area during displacement processes in the unconsolidated Finney pack.

Fig. 146 illustrates the presence of hysteresis in interfacial area for both weakly wet (contact angles = 10 and 30 degrees) and strongly wet (contact angle = 0 degrees) conditions during drainage and imbibition in the unconsolidated Finney pack. It is interesting to note two important results in Fig. 146: 1) interfacial area during imbibition in strongly wet system is larger than during drainage; 2) interfacial area do not change much in weakly wet system and is about the same for both drainage and imbibition for intermediate W phase saturations. Both these results are explained if we consider contributions from different morphologies (pendular rings, menisci, films of W phase) to total liquid-liquid interfacial area, shown on Fig. 146. The behavior of different contributions for both drainage and imbibition is shown in Figs. 147 (strongly wet system, contact angle = 0 degrees) and 148 (weakly wet system, contact angle = 30 degrees).

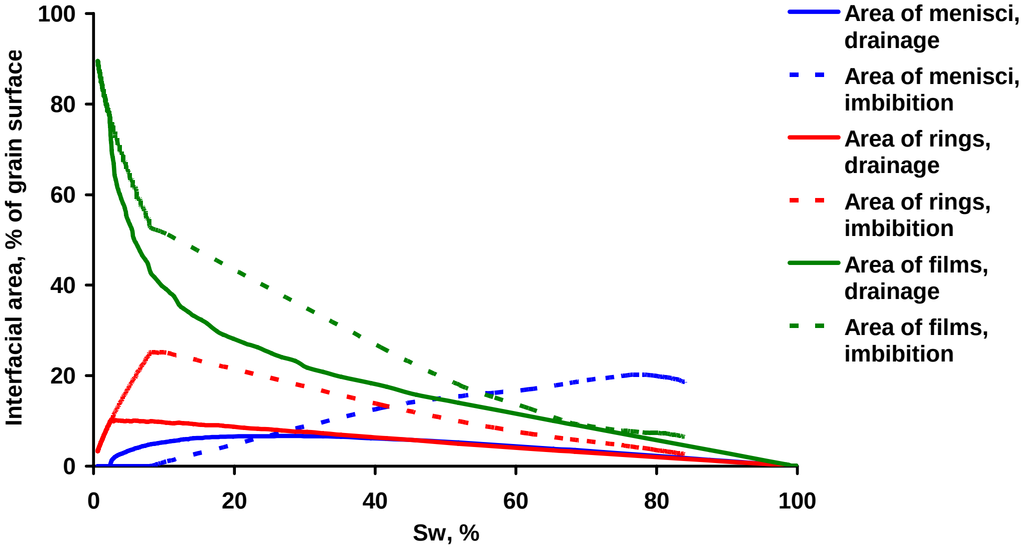

Fig. 147 Contributions from different interface morphologies to total W-NW interfacial area (shown in Fig. 146) during both drainage and imbibition. Strongly wet system, contact angle = 0 degrees.

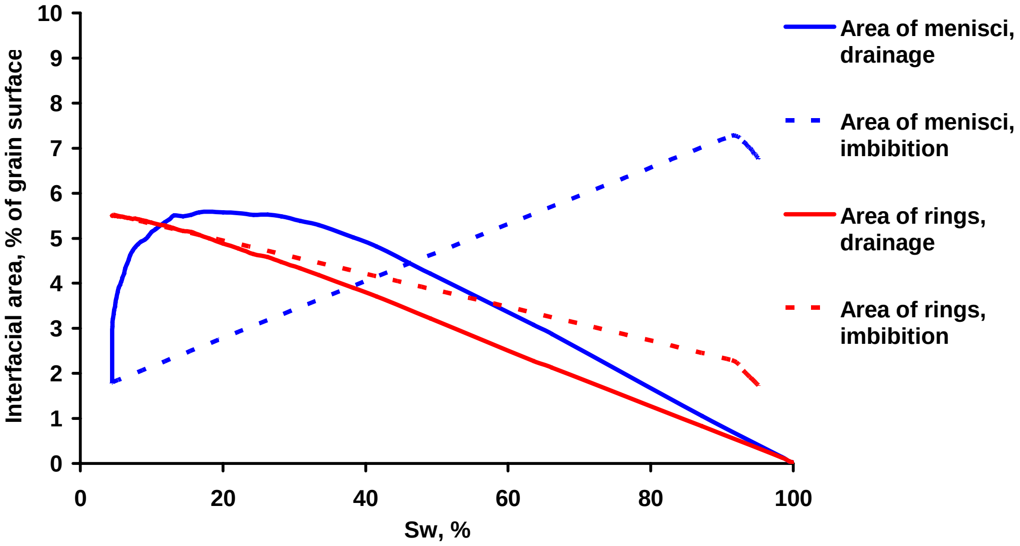

Fig. 148 Contributions from different interface morphologies to total W-NW interfacial area (shown in Fig. 146) during both drainage and imbibition. Weakly wet system, contact angle = 30 degrees.

Fig. 147 illustrates the behavior of all three components of W-NW interface: pendular rings, menisci (including lenses), and thin films of W phase on grain surfaces (since this is strongly wet system). The larger values of total interfacial area during imbibition (Fig. 146) are due to the contribution from pendular rings, as Fig. 147 shows.

Imbibition proceeds at smaller curvatures than drainage, and in a strongly wet system all pendular rings are assumed to be connected to the bulk. Therefore at low saturations during imbibition rings adjust their shapes to the current curvature and can grow larger in size than during drainage (see the part of the curve corresponding to the rings contribution during imbibition for saturations between 5 and 10%, Fig. 147). This results in larger surface area of rings during imbibition and therefore to larger total W-NW interfacial area. The same saturation in late stages of drainage and early stages of imbibition is achieved in a qualitatively different way: since pendular rings during imbibition occupy larger volumes, this additional contribution to saturation must be contained in non-drained pores during drainage. Therefore contribution from thin films is also qualitatively different: in late stages of drainage it increases because W phase leaves pore bodies; in early stages of imbibition it decreases because of growing pendular rings. It turns out that in unconsolidated packing the second process is slower (Fig. 147) and this results in larger values of area of thin films during imbibition. At high saturations larger values of total interfacial area are due to residual clusters of NW phase – all three contributions at the end of imbibition have non-zero values.

Fig. 148 depicts the behavior of two components of W-NW phase interface (pendular rings and menisci) during drainage and imbibition for contact angle of 30 degrees. Thin films of W phase are absent in a weakly wet system. During initial stages of drainage both pendular rings and menisci are created and their surface area increases (Fig. 148). During late stages of drainage and the whole imbibition the sum of these two components (which is total W-NW interfacial area, Fig. 146) remains approximately constant - when menisci disappear (late stages of drainage), rings are created; during imbibition the trend is opposite (new menisci appear, surface area of pendular rings is decreased by the W phase in imbibed pores).

The detailed analysis of the behavior of interfacial area during imbibition, contribution from different W phase morphologies, and comparison with experimental data, is presented Gladkikh and Bryant [43].

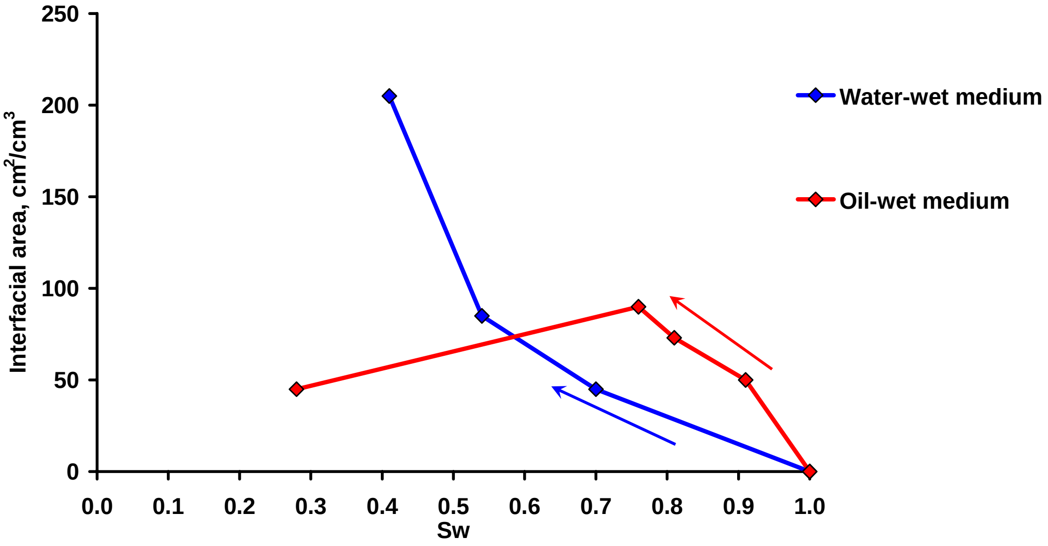

Fig. 149 Total interfacial area during drainage for water-wet and oil-wet bead packs. Experimental data by Jain *et al* [68]. Arrows show the trends in area during drainage experiment.

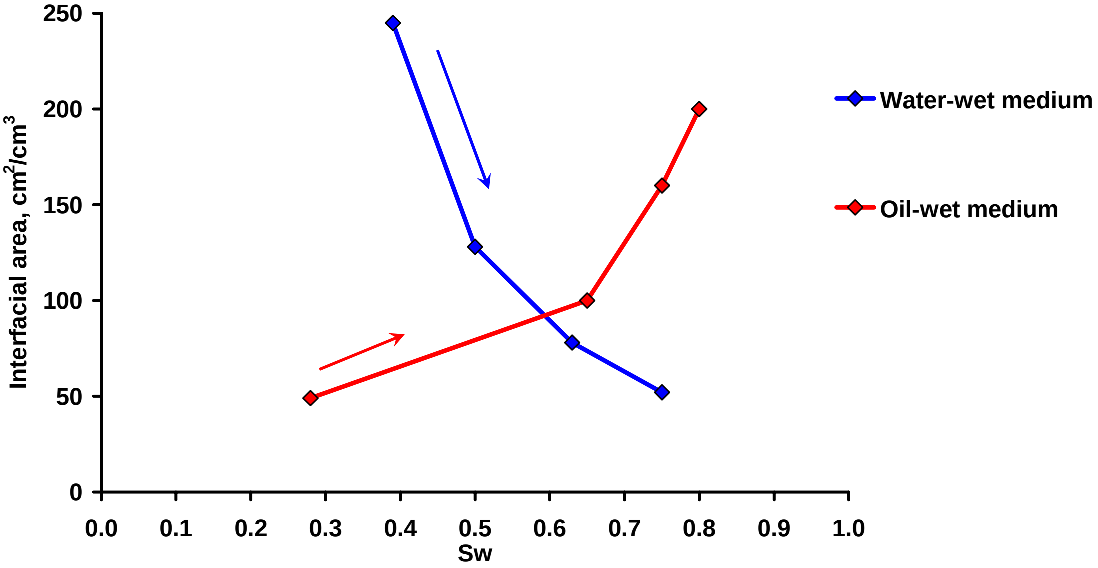

Fig. 150 Total interfacial area during imbibition for water-wet and oil-wet bead packs. Experimental data by Jain *et al* [68]. Arrows show the trends in area during imbibition experiment.

Experimental support for the predictions given above is provided by the measurements of Jain *et al* [68]. They used interfacial tracer technique for measuring areas during drainage and imbibition in glass bead packs for both water-wet and oil-wet conditions. Their results for drainage are presented in Fig. 149 and for the imbibition in Fig. 150. The trend in the dependence between interfacial area and W saturation for the water-wet medium during drainage is consistent with the *total* interfacial area ($A + A_{film}$) in a strongly wetted system (cf. Fig. 134). In contrast the trend for the oil-wet medium is consistent with the behavior of the *bulk* interfacial area A in a weakly wetted system (cf. Fig. 140). The observed trends and measured values of areas are similar to the above predictions and so the discrepancy between water-wet and oil-wet data can be explained by the degree of wettability. In the strongly wetted system, the film of W phase on grains forms an interface with the NW in drained pores, and the interfacial tracer sorbs at this interface. This contribution will be of order of the grain surface area, which is about an order of magnitude greater than the area of the interface between macroscopic volumes of fluid. In the weakly wetted system though, there are no thin films of W, and thus the only fluid/fluid interface in the system is that between macroscopic volumes of the phases (bulk interfacial area). The observed measurements and simple thermodynamic analysis, presented above, suggest strong wettability (existence of thin films of W phase) for the water-wet system and weak wettability (absence of thin films of W phase) for the oil-wet system.

In the imbibition experiments (Fig 150) the results obtained for the water-wet system are consistent with the trend for total area in the case of strongly wetted system (cf. Fig. 137), which agrees well with the behavior of the drainage curve in the same system. Presumably, films of W make the dominant contribution to the total interfacial area. For the oil-wet system though, the measurement shows a monotonic *increase* in interfacial area during imbibition. Assuming that the system was weakly wetted in this case as in the corresponding drainage experiment, we would expect the trend represents the behavior of *bulk* interfacial area and thus need to exhibit a maximum, similar to that of Fig. 143. It is conceivable that a decrease in interfacial area would be observed if it were possible to reduce the NW saturation further. Nevertheless this behavior does not violate the thermodynamic requirement of Eq. (94). That constraint would simply require a larger compensating change in the area of the grains in contact with the NW. We have no experimental data to check this possible explanation, however.

Several other factors can affect measured interfacial area during experiments, both in the physical process and in the technique of measurements itself. This complicates the interpretation of the observed trends. One such complication is the abnormal behavior just described (namely, monotonic increase of the measured interfacial area during imbibition in the oil-wet system). Another is the magnitude of the measured interfacial area, which is much larger than the total grain surface. The nominal grain surface area in the experiments of Jain *et al* [68] was 90 cm^{-1}, and this value should be close to the actual area since glass beads were used as the column packing. Yet the measured interfacial area was as high as 250 cm^{-1} (cf. Figs. 149 and 150). These high values suggest the influence of surface roughness on the behavior, but at the capillary pressures prevailing in these experiments the W/NW interface should not have been strongly affected by roughness. Another possibility is the experimental technique itself (for example, the tracer no longer adsorbs as a monolayer). Also of particular note are the values of interfacial area at residual NW saturation during imbibition in the oil-wet system (Fig. 150). These greatly exceed the nominal grain area and also the areas observed at residual NW saturation in the water-wet packing (Fig. 150). The areas measured in the oil-wet system cannot correspond only to bulk interfaces (i.e. menisci and pendular rings). If they did, we should observe comparable values in the water-wet system at residual NW saturation. Evidently the oil-wet experiment is subject to other effects. One possibility is the presence of drops of NW phase, which remain on rough grain surfaces after W phase imbibes into the pore.

Costanza-Robinson and Brusseau [27] measured air-water interfacial areas in sand columns, uniformly mixed with water for the low water saturations (5-20%) with the gas-phase interfacial tracer. They observed very large values of the interfacial area at the W saturations less than 5%, which were close to the BET-measured surface area of the sand, and suggested, that different techniques measure areas of different *interfacial domains.* Namely, gas-phase tracer will see not only area of bulk interface and pendular rings, but also the area of thin films. At very low W phase saturation (which also means very high capillary pressure), thin films will no longer be smooth and W phase will occupy microcapillaries, microfractures and micropores of the grains themselves, so the interfacial area, measured by gas-phase tracer, will tend to achieve BET-surface area of the porous media. Aqueous-phase tracers, though, cannot access thin films, especially at low W saturations, when almost all W-phase is isolated. So there is not only a difference in the behavior of the porous media itself, due to its wettability, but also a difference due to different measurements' techniques.

Figs. 144 – 150 illustrate qualitatively different behavior of interfacial area in strongly/weakly wetted system. These plots emphasize the importance to distinguish between strongly or weakly wetted behavior, as was pointed out in the preceding thermodynamic analysis. Without such explicit distinction, the model would be unable to predict qualitatively different trends, as shown in Figs 144 – 150. Moreover, during experiments one should be aware of the possibility to obtain qualitatively different trends of data and be able to draw conclusions about the wettability of the system from such difference.

5.2.2 Interfacial Area: Media with Isopachous Cement

We illustrate in Figs. 151 – 153 the influence of isopachous cementation on the hysteresis in interfacial area for different wettability conditions. This type of cementation was modeled as described in section 1.5 (see Figs. 5 and 6) by uniform increase of grain radii until the desired porosity was reached. We present simulations for porosities of 26.9% and 18.7%. The total grain surface area of the packing is about 28,000 in dimensionless units for porosity of 26.9% and about 24,000 for porosity of 18.7%. For comparison, total grain surface area of unconsolidated packing is about 30,400 in dimensionless units. So, considered isopachous cementation results in total grain surface area of about 92% (porosity 26.9%) and 79% (porosity 18.7%) of total grain surface area of unconsolidated packing.

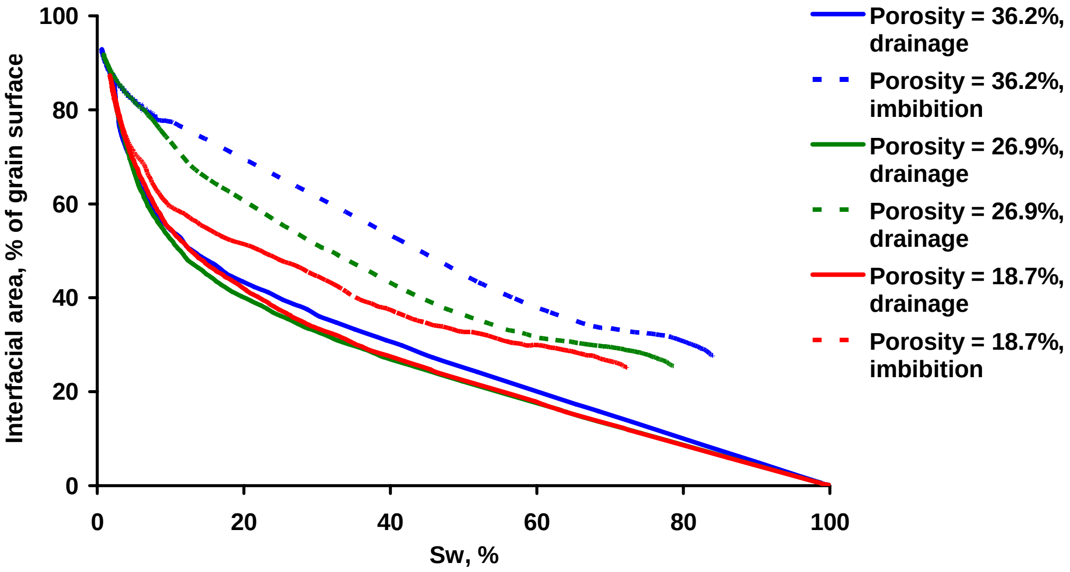

Fig. 151 Influence of isopachous cementation on the hysteresis in interfacial area in the Finney pack. Contact angle =0 degrees.

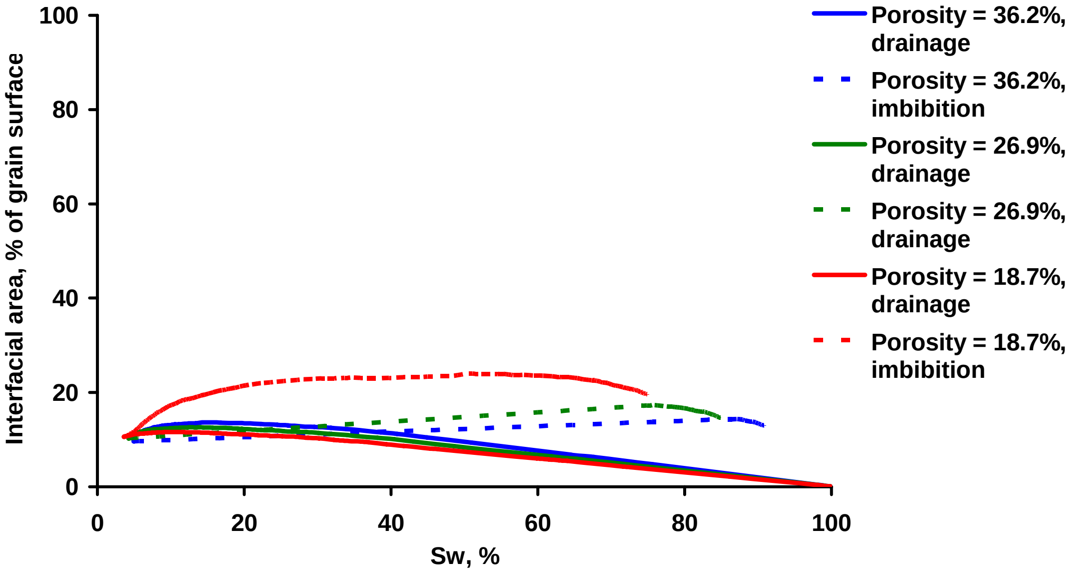

Fig. 152 Influence of isopachous cementation on the hysteresis in interfacial in the Finney pack. Contact angle =10 degrees.

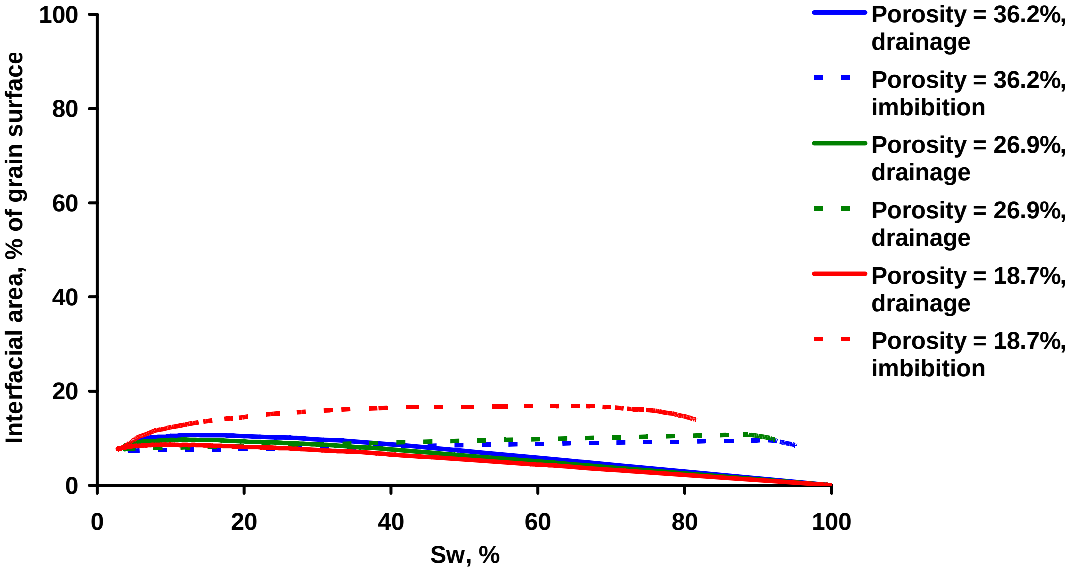

Fig. 153 Influence of isopachous cementation on the hysteresis in interfacial area in the Finney pack. Contact angle =30 degrees.

Figs. 151 – 153 illustrate an interesting result: isopachous cementation in strongly wet system (Fig. 151) decreases the hysteresis between drainage and imbibition interfacial areas. At the same time, in weakly wetted system this type of cement increases the difference (Figs. 152 and 153) between interfacial areas during drainage and imbibition. This effect might have a direct consequence to the theories of multiphase flow (see, for example, [50, 51]), which use liquid-liquid interfacial area as an independent variable in order to compute parameters of two-phase flow (i.e. relative permeabilities). This trend is explained by the behavior of different contributions to total W-NW interfacial area in cemented media (Figs. 154 – 155).

Strongly wet system (Fig. 154) exhibits behavior, similar to unconsolidated case (cf. Fig. 147). All ideas used to explain trends of contributions from different morphologies in Fig. 147 are valid here. The only exception is the behavior of surface area of thin films, which in highly cemented packing becomes smaller during imbibition than during drainage (simulations in Fig. 147 for unconsolidated pack exhibit the opposite trend). It turns out that cementation changes the pore space in such a way that growing rings in early stages of imbibition decrease area of thin films faster, than W phase that leaves pore bodies during late stages of drainage increases it.

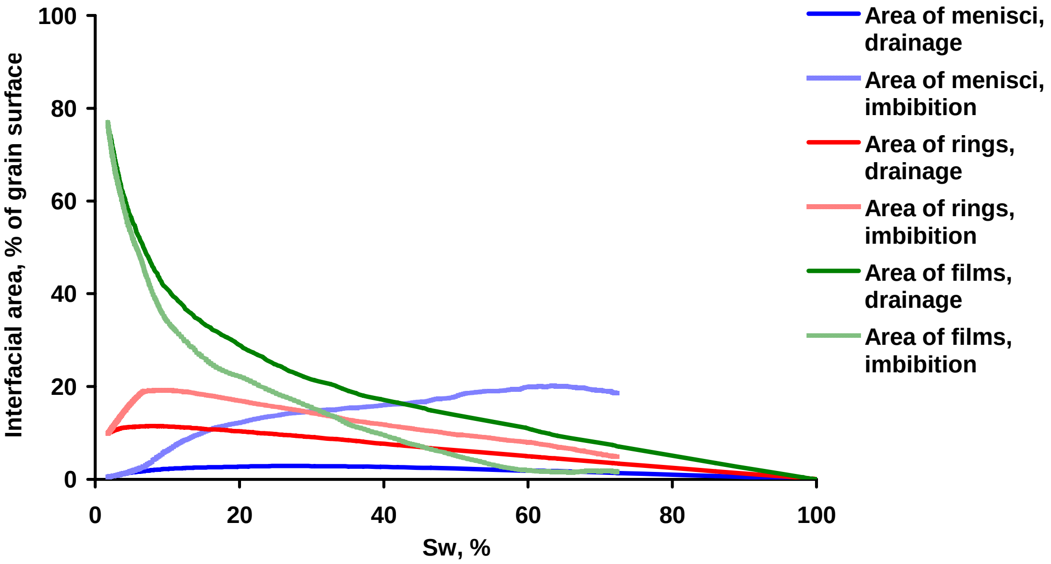

Fig. 154 Contributions from different interface morphologies to total W-NW interfacial area (shown in Fig. 151) during both drainage and imbibition in cemented packing (isopachous cement, porosity = 18.7%). Strongly wet system, contact angle = 0 degrees.

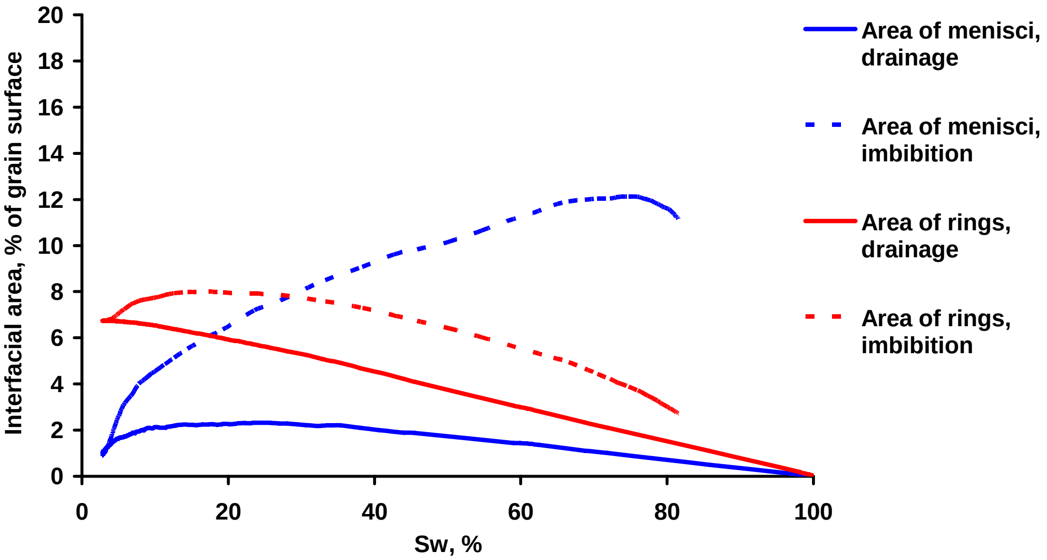

Fig. 155 Contributions from different interface morphologies to total W-NW interfacial area (shown in Fig. 153) during both drainage and imbibition in cemented packing (isopachous cement, porosity = 18.7%). Weakly wet system, contact angle = 30 degrees.

In weakly wet system (Fig. 155) contributions to total W-NW interfacial area from both menisci and pendular rings are consistently larger during imbibition, than during drainage. This difference is larger than for the unconsolidated case (Fig. 148). This is due to the character of imbibition in cemented packing, which results in much larger number of menisci, than in unconsolidated media, and also increases residual NW phase saturation (see corresponding capillary pressure curves in Figs. 52 – 54).

It is also interesting to quantify the influence of wettability (specified by the value of contact angle) in the Finney pack with isopachous cement. Figs. 156 and 157 show hysteresis in interfacial area for different wettability conditions (contact angle is equal to 0, 10 and 30 degrees) in the packing with different amount of isopachous cement (Fig. 156 – porosity 26.9%, Fig. 157 – porosity 18.7%).

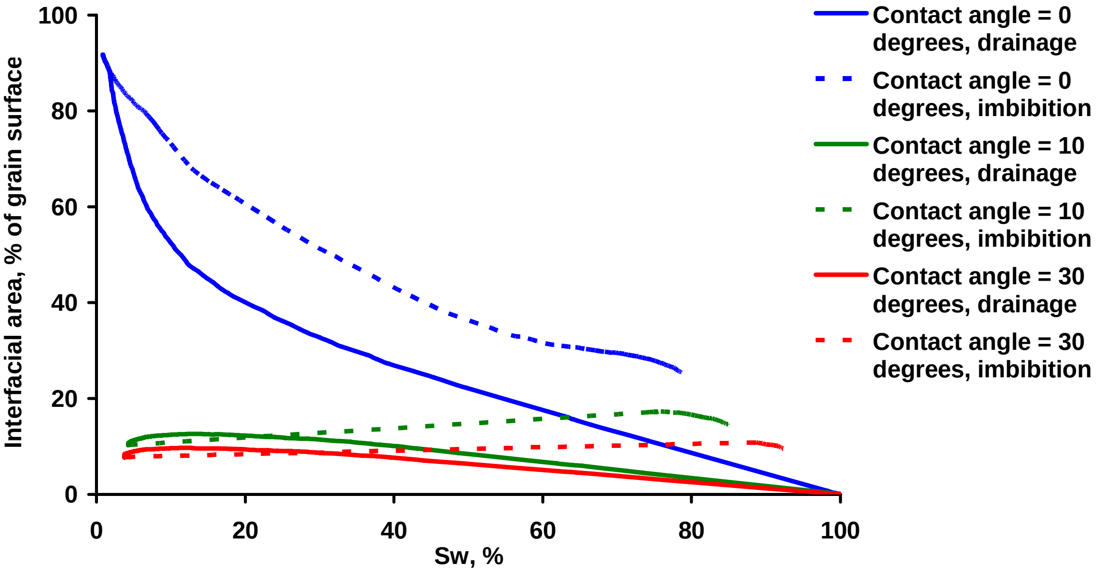

Fig. 156 Influence of wettability on the hysteresis interfacial area in the cemented Finney pack. Isopachous cement, porosity = 26.9%.

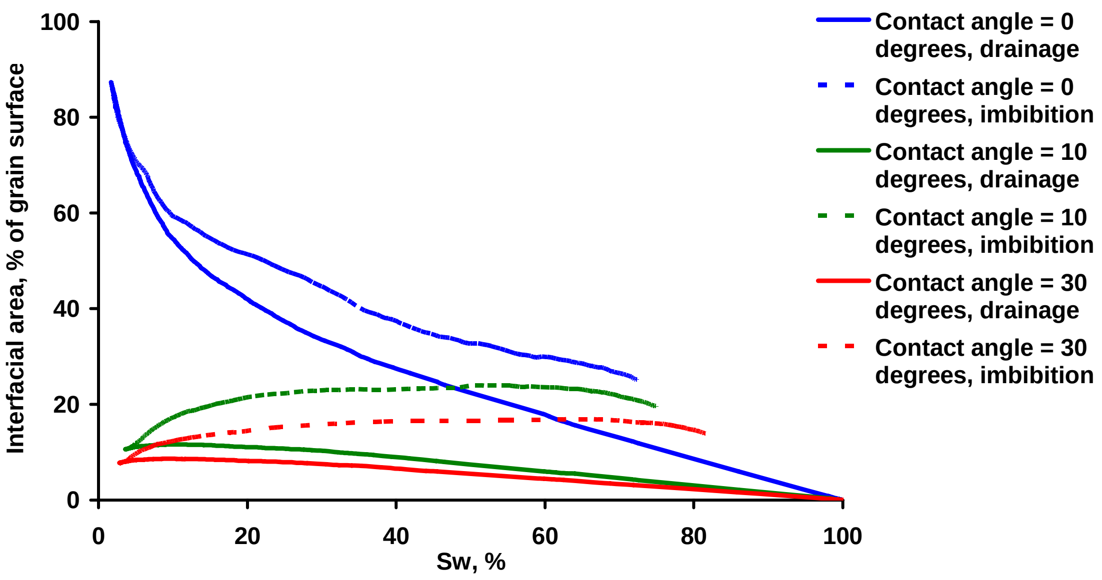

Fig. 157 Influence of wettability on the hysteresis in interfacial area in the cemented Finney pack. Isopachous cement, porosity = 18.7%.

5.2.3 Interfacial Area: Media with Pore-Filling Cement

We illustrate in Figs. 158 – 160 the influence of pore-filling cementation on the hysteresis in interfacial area for different wettability conditions. This type of cementation was modeled as described in section 1.5 (see Figs. 7 and 8). The maximal cluster size of pore-filling cement was specified to be 10 pores. We present simulations for porosities of 25.0% and 18.6%. The total grain surface area of the packing is about 24,000 in dimensionless units for porosity of 25.0% and about 19,400 for porosity of 18.6%; which is about 79% and 64% of total grain surface area of unconsolidated packing correspondingly.

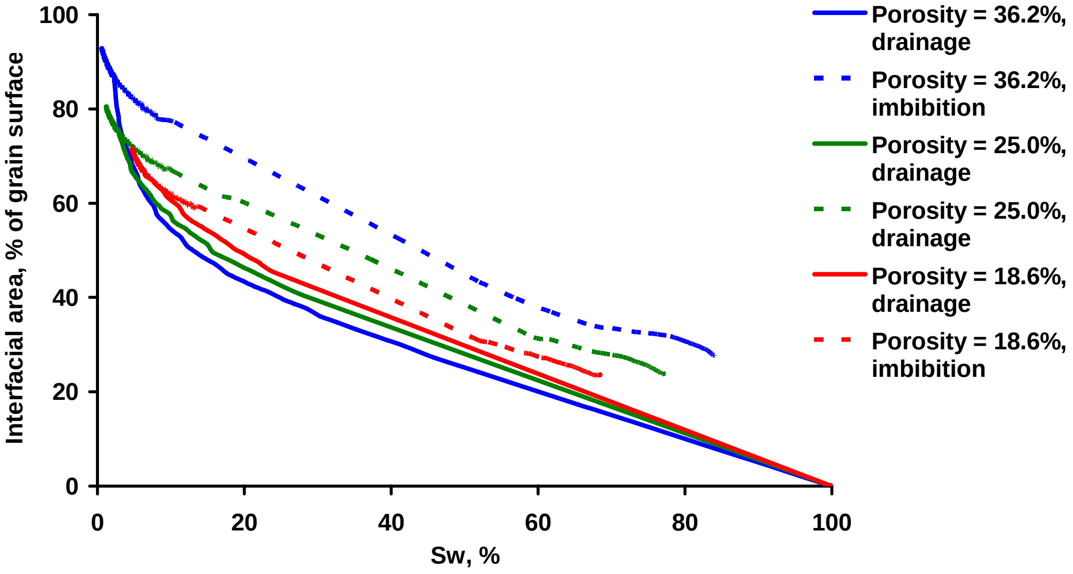

Fig. 158 Influence of pore-filling cementation on the hysteresis in interfacial area in the Finney pack. Contact angle =0 degrees.

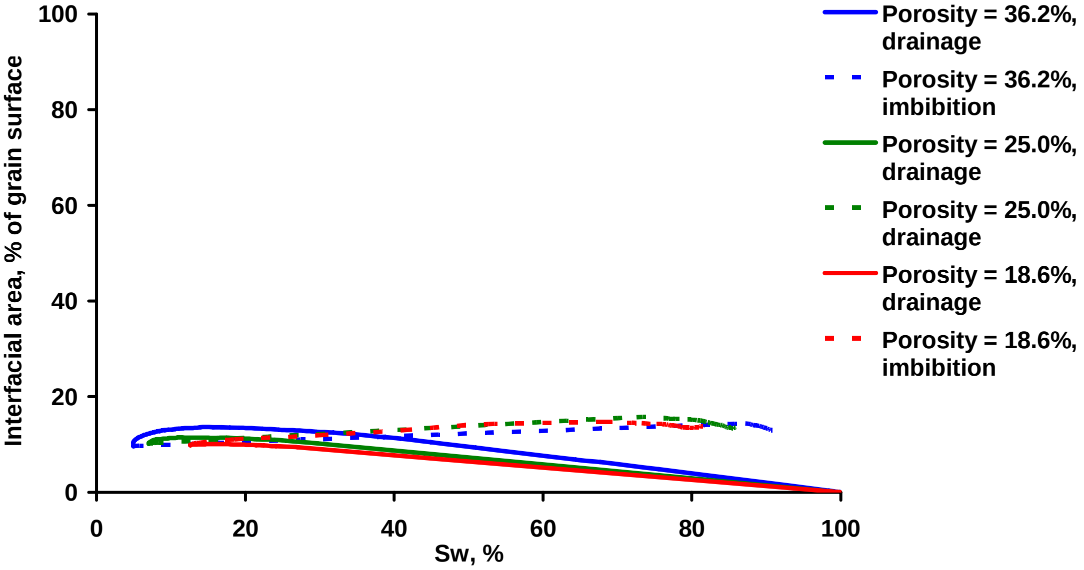

Fig. 159 Influence of pore-filling cementation on the hysteresis in interfacial area in the Finney pack. Contact angle =10 degrees.

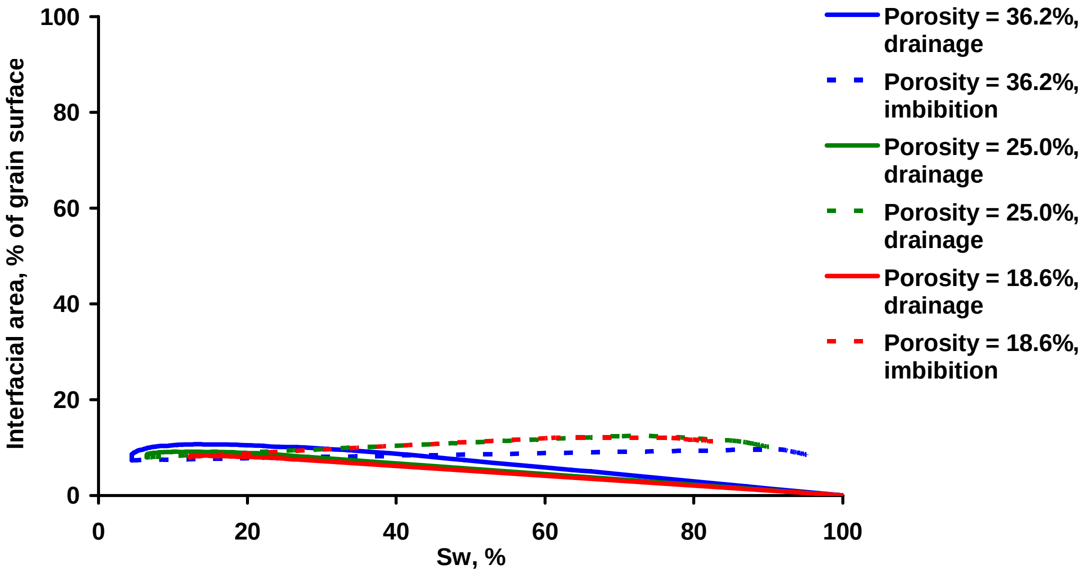

Fig. 160 Influence of pore-filling cementation on the hysteresis in interfacial area in the Finney pack. Contact angle =30 degrees.

Figs. 158 – 160 suggest that when pore-filling cement is introduced in the packing, interfacial areas do not change much. A direct consequence of this concerns theories of multiphase flow [50, 51, 60], which establish functional dependence between relative permeabilities of two-phase flow and independently measured interfacial areas. Trends in Figs. 158 – 160 suggest that relative permeabilities also would not change when pore-filling cement is introduced. However, our simulations show that this is not the case – see the influence of pore-filling cementation on imbibition relative permeabilities in Figs. 58 – 60.

It is also interesting to quantify the influence of wettability (specified by the value of contact angle) in the Finney pack with pore-filling cement. Figs. 161 and 162 show hysteresis in interfacial area for different wettability conditions (contact angle is equal to 0, 10 and 30 degrees) in the packing with different amount of pore-filling cement (Fig. 161 – porosity 25.0%, Fig. 162 – porosity 18.6%).

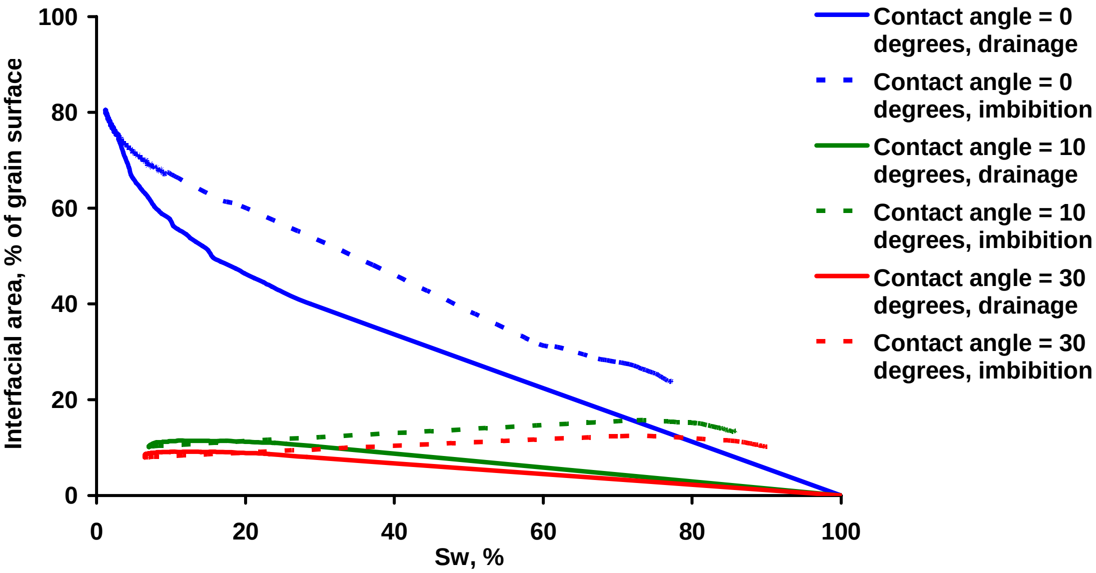

Fig. 161 Influence of wettability on the hysteresis interfacial area in the cemented Finney pack. Pore-filling cement, porosity = 25.0%.

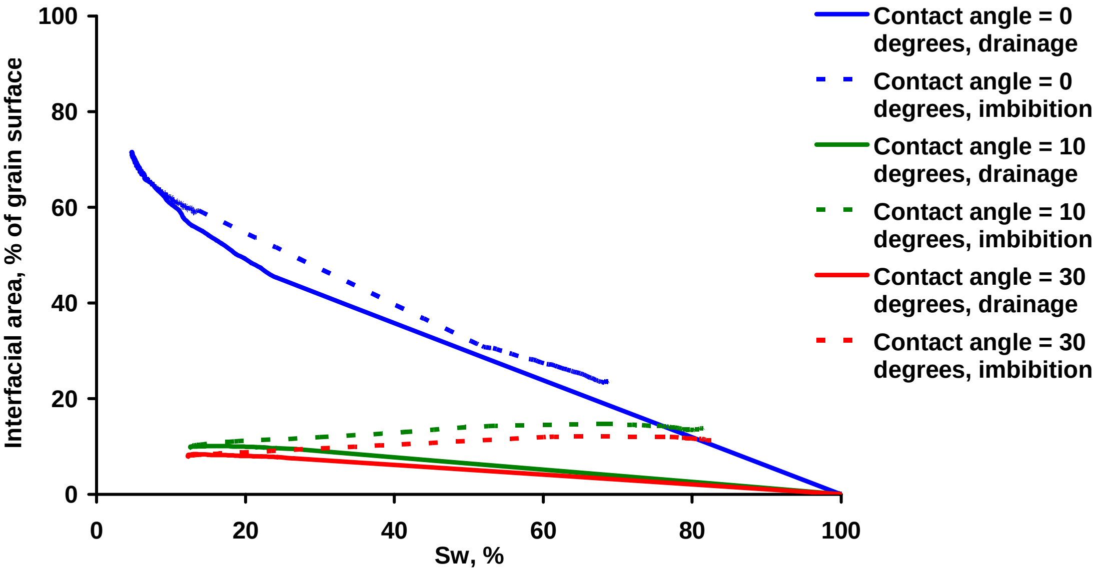

Fig. 162 Influence of wettability on the hysteresis in interfacial area in the cemented Finney pack. Pore-filling cement, porosity = 18.6%.

Chapter VI

6.1 Directions for Future Work and Concluding Remarks

The methodology considered in this work was applied to make *a priori* predictions of macroscopic properties of sedimentary rocks containing two immiscible fluids, such as capillary pressure curves, relative permeabilities of two-phase flow and electrical properties, during a displacement cycle (drainage followed by imbibition) in the pore space. The predictions were made for model sedimentary rocks of different geological features (i.e. amount and type of cementation) and different physical conditions (i.e. wettability, specified by the value of contact angle). The influence of pore-level events, such as entrapment of NW phase and snap-off at pore throats (treated as the coalescence of pendular rings) during imbibition was considered using for the first time an entirely mechanistic approach. Major achievements of this work include the successful predictions of imbibition capillary pressure curves and of the influence of wettability on measurements of interfacial area, both of which are unprecedented.

A physically consistent dynamic criterion due to Melrose [95] was applied for the imbibition of a single pore. Comparison between predicted capillary pressure curves and experimental data, presented in the literature, provides strong support for the Melrose criterion. The influence of wettability predicted by means of this criterion is in a good agreement with experimental data by Morrow *et al* [102] and Hamon and Bennes [58]. This behavior cannot be predicted by imbibition criteria that are derived from the behavior of cylindrical capillary tubes and only account for the linear dependence between capillary pressure and cosine of contact angle. Moreover, investigation of the behavior of different parameters during imbibition (such as W phase topological coordination number and structure of residual NW phase) shows that Melrose criterion acts inseparably from the pore space geometry and its spatial correlations. The Melrose criterion is also dynamic, in the sense that the curvature at which any given pore imbibes will depend on which pore throat the meniscus happens to enter. It follows that critical curvatures for imbibition cannot be pre-computed for pores, even when the local geometry is well characterized, nor could the distribution of critical curvatures realized during imbibition be used in a traditional uncorrelated network-of-conduits model. The inadequacy of classical network models even as a conceptual basis for understanding imbibition is an important implication of this research.

The *a priori* predictions of macroscopic properties of sedimentary rocks made in this work are in a good qualitative and quantitative agreement with existing experimental data. This provides the confidence in the predictive power of the proposed methodology, in spite of the fact that some serious simplifications (locally spherical shape) in the mathematical description of menisci between W and NW phases were made.

The most important findings that concern predictions of these macroscopic properties are:

1) non-linear dependence between contact angle and capillary pressure during imbibition (as was pointed out above, this dependence can not be obtained from the behavior of cylindrical capillary tubes);
2) decrease in residual NW phase saturation with increase in contact angle (this effect has direct practical application in soil cleansing, for example, if NW phase is a contaminant; and in petroleum engineering, when the value of residual oil remaining in the reservoir after waterflooding is of primary interest);
3) increase in residual NW phase saturation when isopachous cement is introduced into the model rock (the practical applications are the same as in the previous item, this trend is supported by experimental data by Morrow *et al* [95] and by Hamon and Bennes [58]);
4) increase in relative permeability to the W phase during imbibition with increase in contact angle (the immediate practical application is for oil-wet reservoirs; this trend is supported by experimental data by Owens and Archer [102] and Hamon and Bennes [58];
5) decrease in relative permeability to the W phase when isopachous cement is

introduced into the model rock;

6) hysteresis in electrical properties (resistivity index and electrical efficiency) for both water-wet and oil-wet media (this result suggests that the use of the same value of Archie's exponent for drainage and imbibition to estimate water content of reservoir from measured electrical properties is unwarranted);
7) influence of contact angle on electrical properties disappears for the packing with high degree of isopachous cementation (this effect has direct application in formation evaluation, because it suggests that in a sample with high degree of isopachous cement value of contact angle is not an issue; on the other hand, in a lightly cemented rock its wettability (value of contact angle) has to be measured independently and taken into account in order to estimate water content accurately);
8) qualitatively different behavior of interfacial area in strongly/weakly wetted system (this is important for models of multiphase flow where interfacial area is used as an independent variable; predicted qualitatively different trends are supported by experimental data by Jain *et al* [68]).

Theoretical analysis of the stability of two-dimensional liquid wedges is presented in this work and its results are suggested as support for Melrose imbibition criterion. The condition for the instability of two wedges in contact with each other is derived. Though it cannot be concluded that any intersection between two pendular rings or between ring and meniscus during imbibition in the Finney pack will always lead to the instability of the interface, it is most likely that some condition, similar to that of 2D liquid wedges, has to be derived for the actual 3D geometry. Whether derivation of such condition is theoretically possible remains uncertain; in order to approach this problem it is necessary first to resolve criterion for the stability of pendular ring in isolation.

Several possible extensions of the approach may be proposed as the directions of future work. First, the methodology for the computation of geometrical features of menisci may be developed to find true shape of the meniscus in the pore throat formed by three grains instead of the locally spherical approximation used. The problem however might be intractable rigorously, but its numerical solution should be possible. Second, more complex models of sedimentary rocks need to be considered, including the distribution of grain sizes, compaction and some other types of cementation. In order to make better comparisons with experimental data, there is also a need to create samples of different geometry than the spherical conglomerate of the Finney pack. Finally, based on the successful predictions in uniformly wetted media, we expect that future applications of the Melrose criterion will provide insight into the behavior of mixed wet media as well.

Simulating imbibition by tracking meniscus movement at the grain scale provides significant predictive power, but it must be performed in sufficiently detailed grain-scale geometry. We have illustrated its application in a model porous medium physically representative of simple sedimentary rocks. The approach could also be applied to models of complicated consolidated and compacted materials with angular grains and to high resolution 3D CT images of samples. The algorithm in this case may require some extensions. It will be necessary to define “grain contacts” and “pore throats” in the image where the interfaces which correspond to pendular rings and menisci in the case of spherical grains would exist. It will also be necessary to compute the shapes of these interfaces locally, in order to apply Melrose criterion for imbibition as instability of the when these interfaces intersect.

Bibliography

[1] Adamson, A.W., 1990. Physical Chemistry of Surfaces. Wiley, New-York.

[2] Al-Gharbi, M.S., and Blunt, M.J., 2004. 2D dynamic pore-scale network model of imbibition. Proceedings, Computational Methods in Water Resources XV Conference, Chapel Hill, NC, June 13 – 17, 2004.

[3] Annable, M.D., Jawitz, J.W, Rao, P.S.C., Dai, D.P., Kim, H.K., Wood A.L., 1998. Interfacial and partitioning tracers for characterization of effective NAPL - water contact areas. Ground Water, 36(3), 495-502.

[4] Archie, G.E., 1942. The electrical resistivity log as an aid in determining some reservoir characteristics. Trans AIME, 146, 54 – 62.

[5] Argaud, M., Giouse, H., Straley, C., Tomanic, J. and Winkler, K., 1989. Salinity and saturation effects on shaly sandstone conductivity. SPE paper 19577. Presented at 64th Ann Tech Conf Exhib, SPE, San Antonio, TX, 1989.

[6] Bakke, S. and Øren, P.E., 1997. 3-D pore-scale modeling of sandstones and flow simulations in the pore networks. SPEJ, 2, 136-149.

[7] Bell, W.K., van Brakel, J., and Heertjes, P.M., 1981. Mercury penetration and retraction hysteresis in closely packed spheres. Powder Technology, 29, 75 – 88.

[8] Berkowitz, B. and Hansen, D.P., 2001. A numerical study of the distribution of water in partially saturated porous rock. Transport in Porous Media, 45, 303 – 319.

[9] Bernal, J., Mason, J., 1960. Coordination of randomly packed spheres. Nature, 188, 910-911.

[10] Blunt, M.J., Jackson, M.D., Piri, M., and Valvatne, P.H., 2002. Detailed physics, predictive capabilities and macroscopic consequences for pore-network models of multiphase flow. Adv Water Resources, 25, 1069 – 1089.

[11] Bradford, S.A., Leij, F.J., 1997. Estimating interfacial areas for multi-fluid soil systems. J Cont Hydr, 27, 83-105.

[12] Brown, H.W., 1951. Capillary pressure investigations. Pet Trans AIME, 192, 61 – 74.

[13] Bryant, S.L. and Blunt, M., 1992. Prediction of relative permeability in simple porous media. Phys Rev A, 46, 2004-2011.

[14] Bryant, S.L., and Johnson, A.S., 2001. Theoretical evaluation of the interfacial area between two fluids in a model soil. ACS Symp Series 806, Chem In the Env, 26 – 41.

[15] Bryant, S.L., and Johnson, A.S., 2003. Wetting phase connectivity and irreducible saturation in simple granular media. J Coll Int Sci, 263(2), 572 – 579.

[16] Bryant, S.L., and Pallatt, N., 1996. Predicting formation factor and resistivity index in simple sandstones. J Pet Sci Eng, 15, 169-179.

[17] Bryant, S.L., Cade, C. and Mellor, D.W., 1993. Permeability prediction from geologic models. AAPG Bulletin, 77 (8), 1338-1350.

[18] Bryant, S.L., King, P.R. and Mellor, D.W., 1993. Network model evaluation of

permeability and spatial correlation in a real random sphere packing. Transport in Porous Media, 11, 53-70.

[19] Bryant, S.L., Mellor, D.W. and Cade, C.A., 1993. Physically representative network models of transport in porous media. AIChE J, 39, 387-396.

[20] Bryant, S.L., Mason, G. and Mellor, D.W., 1996. Quantification of spatial correlation in porous media and its effect on mercury porosimetry. J Coll Int Sci, 177, 88-100.

[21] Cassiani, G., Dalla, E., Brovelli, A., and Pitea, D., 2004. Pore-scale modeling of electrical conductivity in unsaturated sandstones. Proceedings, Computational Methods in Water Resources XV Conference, Chapel Hill, NC, June 13 – 17, 2004.

[22] Celia, M.A., Dahle, H.K., and Hassanizadeh, S.M., 2004. Dynamic effects in capillary pressure relationships for two-phase flow in porous media: insights from bundle-of-tubes models and their implications. Proceedings, Computational Methods in Water Resources XV Conference, Chapel Hill, NC, June 13 – 17, 2004.

[23] Chatzis, I., and Dullien, F.A.L., 1983. Dynamic immiscible displacement mechanisms in pore doublets: theory versus experiment. J Coll Int Sci, 91(1), 199 – 222.

[24] Chatzis, I., Morrow, N.R., and Lim, H.T., 1983. Magnitude and detailed structure of residual oil saturation. SPE Paper 10681.

[25] Chen, S.Y., Zhang, D.X., and Kang, Q.J., 2004. Pore-scale simulations of flow, transport, and reaction in porous media. Proceedings, Computational Methods in Water Resources XV Conference, Chapel Hill, NC, June 13 – 17, 2004.

[26] Coles, M.E., Hazlett, R.D., Spanne, P., Soll, W.E., Muegge, E.L., Johns, K.W., 1998. Pore level imaging of fluid transport using synchrotron X-ray microtomography. J Pet Sci Eng, 19, 55 – 63.

[27] Costanza-Robinson, M.S. and Brusseau, M.L., 2002. Air-water interfacial areas in unsaturated soils: Evaluation of interfacial domains. Water Resources Research, 38(10), 13-1 – 13-17.

[28] Cousin, I., Levtiz, P. and Bruand, A., 1996. Three-dimensional analysis of loamy-clay soil using pore and solid chord distributions. Eur J Soil Sci, 47, 439-452.

[29] Dalla E., Hilpert, M., and Miller, C.T., 2002. Computation of the interfacial area for two-fluid porous medium systems. J Cont Hydr, 56, 25 – 48.

[30] Dullien, F.A.L., Dhawan, G.K., 1975. Bivariate pore-size distribution of some sandstones. J Coll Int Sci, 52(1), 129-135.

[31] Dullien, F.A.L., Zarcone, C., Macdonald, I.F., Collins, A. and Bochard, R.D.E., 1989. The effects of surface roughness on the capillary pressure curves and the heights of capillary rise in glass bead packs. J Coll Int Sci, 127 (2), 362 – 272.

[32] Erle, M.A., Dyson, D.C., Morrow, N.R., 1971. Liquid bridges between cylinders, in a torus, and between spheres. AIChE J, 17, 115 – 121.

[33] Faisal Anwar, A.H.M., Bettahar, M. and Matsubayashi, U., 2000. A method for determining air- water interfa-cial area in variably saturated porous media. J Cont Hydr, 43, 129 – 146.

[34] Fatt I., 1956. The network model of porous media I. Capillary pressure characteristics. Trans AIME, 207, 144-159.

[35] Fatt I., 1956. The network model of porous media II. Dynamic properties of a single size tube network. Trans AIME, 207, 160-163.

[36] Fatt, I., 1956. The network model of porous media III. Dynamic properties of networks with tube radius distribution. Trans AIME, 207, 164-181.

[37] Fenwick, D.H. and Blunt M.J., 1998. Three-dimensional modeling of three phase imbibition and drainage. Adv Water Resources, 21, 121 – 143.

[38] Finney, J.L., 1970. Random packings and the structure of simple liquids. I. The geometry of random close packing. Proceedings of the Royal Society of London, Ser A, Math and Phys Sci, 319 (1539), 479 – 493.

[39] Fischer, U. and Celia, M., 1999. Prediction of relative and absolute permeabilities for gas and water retention curves using a pore-scale network model. Water Resources Research, 35, 1089-1100.

[40] Fisher, R.A., 1926. On the capillary forces in an ideal soil; correction of formulae given by W. B. Haines. J Agric Sci, 16, 492.

[41] Fleury, M. and Longeron, D., 1998. Combined resistivity and capillary pressure measurements using micropore membrane technique. J Pet Sci Eng, 19, 73 – 79.

[42] Gielen, T., Hassanizadeh, S.M., Celia, M. A., Dahle, H.K., and Leijnse, A., 2004. A pore-scale network approach to investigate dynamic effects in multiphase flow. Proceedings, Computational Methods in Water Resources XV Conference, Chapel Hill, NC, June 13 – 17, 2004.

[43] Gladkikh, M. and Bryant, S.L., 2003. Prediction of interfacial areas during imbibition in simple porous media. Adv Water Resources, 26, 609-622.

[44] Gladkikh, M. and Bryant, S.L., 2004. Influence of Wettability on Petrophysical Parameters during Imbibition in Simple Porous Media. Proceedings of the 8th International Symposium on Reservoir Wettability, May 16-18, 2004, Houston, TX, USA

[45] Gladkikh, M. and Bryant, S.L., 2004. Prediction of Imbibition in Simple Porous Media. Proceedings of the XVth International Conference on Computational Methods in Water Resources, June 13-17, 2004, Chapel Hill, NC, USA.

[46] Gladkikh, M. and Bryant, S.L., 2004. Mechanistic Prediction of Capillary Imbibition Curves. SPE paper 90333. Proceedings of the SPE Annual Technical Conference and Exhibition, September 26-29, 2004, Houston, TX, USA.

[47] Gladkikh, M. and Bryant, S.L., 2005. Prediction of Imbibition from Grain-Scale Interface Movement. To appear in Adv Water Resources.

[48] Gladkikh, M. and Bryant, S.L., 2005. Prediction of Imbibition in Unconsolidated Granular Materials. J Coll Int Sci, (2005), in press; doi:10.1016/j.jcis.2005.03.029.

[49] Gladkikh, M., Jain, V., Bryant, S., and Sharma, M., 2003. Experimental and theoretical basis for a wettability-interfacial area-relative permeability relationship. SPE Paper 84544.

[50] Gray, W. G., Hassanizadeh, S.M., 1991. Paradoxes and realities in unsaturated flow theory. Water Resources Research, 27(8), 1847 – 1854.

[51] Gray, W. G., Hassanizadeh, S.M., 1991.Unsaturated flow theory including interfacial phenomena. Water Resources Research, 27(8), 1847 – 1854.

[52] Gvirtzman, H. and Roberts, P.V., 1991. Pore scale spatial analysis of two immiscible

fluids in porous media. Water Resources Research, 27(6), 1165 – 1176.

[53] Gvirtzman, H., Magaritz, M., Klein, E., and Nadler, A., 1987. A scanning electron microscopy study of water in soil. Transport in Porous Media, 2, 83 –93.

[54] Hackett, F.E. and Strettan, J.S., 1928. The capillary pull of an ideal soil. J Agric Sci, 18, 671 – 681.

[55] Haines, W.B., 1925. Studies in the physical properties of soils. II. A note on the cohesion developed by capillary forces in an ideal soil. J Agric Sci, 15, 529 – 535.

[56] Haines, W.B., 1927. Studies in the physical properties of soils. IV. A further contribution to the theory of capillary phenomena in soil. J Agric Sci, 17, 264 – 290.

[57] Haines, W.B., 1930. Studies in the Physical Properties of Soil. V. The hysteresis effect in capillary properties and the modes of moisture distribution associated therewith. J Agric Sci, 20, 97 – 116.

[58] Hamon, G. and Bennes, M., 2004. Two-phase flow rock typing: another approach. Petrophysics, 45(5), 433 – 444.

[59] Harris, C.C., Jowett, A. and Morrow, N.R., 1963. Effect of contact angle on the capillary properties of porous masses. Trans Inst Min Metall, 73, Part 5, 335-351.

[60] Hassanizadeh, S.M. and Gray, W.G., 1990. Mechanics and thermodynamics of multiphase flow in porous media including interphase boundaries. Adv Water Resources, 13, 169 – 186.

[61] Hazlett, R. D., 1995. Simulation of capillary-dominated displacements in microtomographic images of reservoir rocks. Transport in Porous Media, 20, 21 – 35.

[62] Held, R.J. and Celia, M.A., 2001. Pore – scale modeling extension of constitutive relationships in the range of residual saturations. Water Resources Research, 37(1), 165 – 170.

[63] Herrick, D.C. and Kennedy, W.D., 1994. Electrical efficiency – a pore geometric theory for interpreting the electrical properties of reservoir rocks. Geophysics, 59(6), 918-927.

[64] Hilpert, M. and Miller, C.T., 2001. Pore-morphology-based simulation of drainage in totally wetting porous media. Adv Water Resources, 24, 243-255.

[65] Hirasaki, G.J., 1990. Thermodynamics of thin films and three-phase contact regions. Interfacial Phenomena in Petroleum Recovery, Marcel Drekker, New-York, 23 – 76.

[66] Ioannidis, M.A., Chatzis, I., Payatakes, A.C., 1991. A mercury porosimeter for investigating capillary phenomena and microdisplacement mechanisms in capillary networks. J Coll Int Sci, 143(1), 22-36.

[67] Israelachvili, J, 1992. Intermolecular and Surface Forces. Academic Press, London.

[68] Jain, V., Bryant, S.L. and Sharma, M.M., 2003. Influence of wettability and saturation on liquid - liquid interfacial area in porous media. Env Sci and Technology, 37(3), 584-591.

[69] Jerauld, G.R. and Salter, S.J., 1990. The effect of pore – structure on hysteresis in relative permeability and capillary pressure: pore – level modeling. Transport in Porous Media, 5, 103 – 151.

[70] Jin, G., Patzek, T.W., and Silin, D.B., 2003. Physics-based reconstruction of sedimentary rocks. SPE paper 83587. SPE Western Regional/AAPG Pacific Section

Joint Meeting, Long Beach, CA, 19-24 May, 2003.

[71] Johns, M.L. and Gladden, N.F., 1999. Magnetic resonance imaging study of the dissolution kinetics of octanol in porous media. J Coll Int Sci, 40, 261 – 270.

[72] Johnson, A.S., 2001. Pore Level modeling of interfacial area in porous media. MS Thesis, The University of Texas at Austin.

[73] Karkare, M.V. and Fort, T., 1996. Determination of the air –water interfacial area in wet "unsaturated" porous media. Langmuir, 12, 2041 – 2044.

[74] Kenmotsu, K., 2003. Surfaces with constant mean curvature. Translations of Mathematical Monographs, Vol. 221. American Math Soc.

[75] Kim, H., Rao, P.S.C. and Annable, M.D., 1997. Determination of effective air-water interfacial area in par-tially saturated porous media using surfactant adsorption. Water Resour Research, 33(12), 2705-2711.

[76] Knight, R., 1991. Hysteresis in the electrical resistivity of partially saturated sandstones. Geophysics, 56(12), 2139 – 2147.

[77] Lian, G., Thornton, C., and Adams, M.J., 1993. A theoretical study of the liquid bridge forces between two rigid spherical bodies. J Coll Int Sci, 161, 138 – 147.

[78] Lindquist, W.B. and Lee, S., 1996. Medial axis analysis of void structure in three-dimensional tomographic images of porous media. J Geophys Res, 101, 8297-8310.

[79] Lindquist, W.B., Venkatarangan, A., Dunsmuir, J., and Wong, T.F., 2000. Pore and throat size distributions measured from synchrotron X-ray tomographic images of Fontainebleau sandstones. J Geophys Res, 105B, 21508-21528.

[80] Lenormand, R. and Zarcone, C., 1984. Role of roughness and edges during imbibition in square capillaries. SPE paper 13264.

[81] Leverett, M.C., 1941. Capillary behavior in porous solids. AIME Pet Trans, 142, 152 – 169.

[82] Lowry, M.I. and Miller, C.T., 1995. Pore-scale modeling of nonwetting-phase residual in porous media. Water Resources Research, 31, 455-473.

[83] Man, H.N. and Jing, X.D., 2000. Pore network modeling of electrical resistivity and capillary pressure characteristics. Transport in Porous Media, 41, 263 – 286.

[84] Mani, V. and Mohanty, K.K., 1998. Pore-level network modeling of three-phase capillary pressure and relative permeability curves. SPEJ, 3, 238 – 248.

[85] Mason, G.J., 1971. A model of the pore space in a random packing of equal spheres. J Coll Int Sci, 35, 279-287.

[86] Mason, G.J. and Clark, W.C., 1965. Liquid bridges between spheres. Chem Eng Sci, 20, 859 – 866.

[87] Mason, G.J. and Mellor, D.W., 1995. Simulation of drainage and imbibition in a random packing of equal spheres. J Coll Int Sci, 176, 214 – 225.

[88] Mason, G. and Morrow, N.R., 1984. Coexistence of menisci and the influence of neighboring pores on capillary displacement curvatures in sphere packings. J Coll Int Sci, 100(2), 519 – 535.

[89] Mason, G. and Morrow, N.R., 1987. Meniscus configurations and curvatures in non-axysimmetric pores of open and closed uniform cross sections. Proc Roy Soc London, 414A, 111-133.

[90] Mason, G., Morrow, N.R., and Walsh, T.J., 2000. Interaction between menisci in

adjacent pores. Studies in Surface Science and Catalysis, 128, 495 – 504.

[91] Mayer, A.S. and Miller, C.T., 1992. The influence of porous medium characteristics and measurement scale on pore-scale distributions of residual nonaqueous-phase liquids. J Cont Hydr, 11, 189-213.

[92] Mayer, R.P. and Stowe, R.A., 1965. Mercury porosimetry: breakthrough pressure for penetration between packed spheres. J Coll Int Sci, 20, 893-911.

[93] McClure, J.E., Pan, C., Adalsteinsson, D., Gray, W.G., and Miller, C.T., 2004. Estimating interfacial areas resulting from lattice Boltzmann simulation of two-fluid-phase flow in a porous medium. Proceedings, Computational Methods in Water Resources XV Conference, Chapel Hill, NC, June 13 – 17, 2004.

[94] Mellor, D.W., 1989. Random close packing (RCP) of equal spheres: Structure and implications for use as a model porous medium. PhD Thesis, Open University, Milton Keynes, UK.

[95] Melrose, J.C., 1965. Wettability as related to capillary action in porous media. SPEJ, 5, 259 – 271.

[96] Melrose, J.C., Wallick, G.C., 1967. Exact geometrical parameters for pendular ring fluid. J Phys Chem, 71, 3676-3677.

[97] Mogensen, K., and Stenby, E.H., 1998. A dynamic two-phase pore-scale model of imbibition. Transport in Porous Media, 32, 299-327.

[98] Mohanty, K.K., and Salter, S.J., 1982. Multiphase flow in porous media: II. Pore level modeling. SPE Paper 11018.

[99] Morrow, N.R., 1970. Physics and thermodynamics of immiscible displacement in porous media. Ind Eng Chem, 62, 32-56.

[100] Morrow, N.R., 1971. Irreducible wetting-phase saturations in porous media. Chem Eng Sci, 25, 1799 – 1815.

[101] Morrow, N.R. and Mungan, N., 1971. Moullabilite et capillarite en milieux poreux. Revue Inst Francais du Petrole, 26, 629-650.

[102] Morrow, N.R., Cram, P.J., McCaffery, F.G., 1973. Displacement studies in dolomite with wettability control by octanoic acid. SPEJ, 255, 221-232.

[103] Moss, A.K., Jing, X.D., and Archer, J.S., 1999. Laboratory investigation of wettability and hysteresis effects on resistivity index and capillary pressure characteristics. J Pet Sci Eng, 24, 231 – 242.

[104] Myshkis, A.D., Babskii, V.G., Kopachevskii, N.D., Slobozhanin, L.A., Tyuptsov, A.D., 1987. Low-Gravity Fluid Mechanics. Springer-Verlag, Berlin.

[105] Naar, J., Wygal, R. and Henderson, J., 1962. Imbibition relative permeability in unconsolidated porous media. SPEJ, 13, 131.

[106] Øren, P.E. and Bakke, S., 2002. Process based reconstruction of sandstones and prediction of transport properties. Transport in Porous Media, 46, 311 – 343.

[107] Øren, P.E., Bakke, S. and Arntzen, O.J., 1998. Extending predictive capabilities to network models. SPEJ, 3, 324 – 336.

[108] Owens, W.W. and Archer, D.L., 1971. The effect of rock wettability on oil-water relative permeability relationships. J Petroleum Technology, 23, 873-878.

[109] Pan, C., Luo, L.-S., and Miller, C.T., 2004. An evaluation of lattice Boltzmann equation methods for simulating flow through porous media. Proceedings,

Computational Methods in Water Resources XV Conference, Chapel Hill, NC, June 13 – 17, 2004.

[110] Patzek, T.W., 2001. Verification of a complete pore network simulator of drainage and imbibition. SPEJ, 6 (2), 144 – 156.

[111] Powers, S.E., Loureiro, C.O., Abriola, L.M. and Weber, W.J. Jr., 1991. Theoretical study of the significance of nonequilibrium dissolution on nonaqueous phase liquids in subsurface systems. Water Resources Research, 27(4), 463.

[112] Prince, C.M., Ehrlich, R., and Anguy, Y., 1995. Analysis of spatial order in sandstones II: grain clusters, packing flaws, and the small-scale structure of sandstones. J Sedimentary Research, A65(1), 13 – 28.

[113] Princen, H.M., 1969. Capillary phenomena in assemblies of parallel cylinders. II. Capillary rise in systems with more than two cylinders. J Coll Int Sci, 30(3), 359-371.

[114] Prodanovic, M., Lindquist, W.B., and Seright, R.S., 2004. 3D microtomographic study of fluid displacement in rock cores. Proceedings, Computational Methods in Water Resources XV Conference, Chapel Hill, NC, June 13 – 17, 2004.

[115] Purcell, W.R., 1949. Capillary pressures - their measurement using mercury and the calculation of permeability therefrom. Pet Trans AIME, 186, 39 – 48.

[116] Rajaram, H., Ferrand, L.A. and Celia, M.A., 1997. Prediction of relative permeabilities for unconsolidated soils using pore-scale network models. Water Resources Research, 33, 43-52.

[117] Reeves, P.C. and Celia, M.A., 1996. A functional relationship between capillary pressure, saturation, and interfacial areas as revealed by a pore-scale network model. Water Resources Research, 32, 2345-2358.

[118] Rose, W., 1958. Volumes and surface areas of pendular rings. J Appl Phys, 29(4), 687 – 691.

[119] Rothman, D.H. and Zaleski, S., 1997. Lattice-gas cellular automata: simple models of complex hydrodynamics. Cambridge, Cambridge University Press.

[120] Schaap, M.G. and Lebron, I., 2004. An evaluation of permeability of statistically reconstructed three-dimensional pore structures with Lattice Boltzmann simulations. Proceedings, Computational Methods in Water Resources XV Conference, Chapel Hill, NC, June 13 – 17, 2004.

[121] Sharma, M.M., Garrouch, A. and Dunlap, H.F., 1991. Effects of Wettability, Pore Geometry and Stress on Electrical Conduction in Fluid-Saturated Rocks. The Log Analyst, 32, 511-526.

[122] Slichter, C., 1899. Theoretical investigations of the motions of groundwaters. US Geol Surv Ann Rept, 306.

[123] Stegemeier, G.L., 1974. Relationship of trapped oil saturation to petrophysical properties of porous media. SPE paper 4754.

[124] Swanson, B.F., 1977. Visualizing pores and non-wetting phase in porous rock. SPE paper 6857.

[125] Thompson, K.E. and Fogler, H.S., 1997. Modeling flow in disordered packed beds from pore-scale fluid mechanics. AIChE J, 43, 1377-1389.

[126] Valvatne, P.H. and Blunt, M.J., 2003. Predictive pore-scale network modeling. SPE

paper 84550, proceedings of the SPE Annual Meeting, Denver, CO, 5-8 October, 2003.

[127] van Dijke, M.I.J. and Sorbie, K.S., 2003. Pore-scale modeling of three-phase flow in mixed-wet porous media: multiple displacement chains. J Pet Sci Eng, 39, 201 – 216.

[128] Vogel, H.J. and Roth, K., 2001. Quantitative morphology and network representation of soil pore structure. Adv Water Resources, 24, 233-242.

[129] de Waal, J.A., Smits, R.M.M., de Graaf, J.D., and Schipper, B.A., 1991. Measurement and evaluation of resistivity-index curves. The Log Analyst, 32, 583 – 594.

[130] Wang, X., Thauvin, F. and Mohanty, K.K., 1999. Non-Darcy flow through anisotropic porous media. Chem Eng Sci, 54, 1859-1869.

[131] Wardlaw, N.C., 1976. Pore geometry of carbonate rocks as revealed by pore casts and capillary pressure. AAPG Bulletin, 60(2), 245-257.

[132] Wardlaw, N.C. and McKellar, M., 1981. Mercury porosimetry and interpretation of pore geometry in sedimentary rocks and artificial models. Powder Technology, 29, 127 – 143.

[133] Wardlaw, N.C., Li, Y. and Forbes, D., 1987. Pore-throat size correlation from capillary pressure curves. Transport in Porous Media, 2, 597 – 614.

[134] Wei, J.-Z. and Lile, O.B., 1991. Influence of wettability on two- and four-electrode resistivity measurements on Berea sandstone plugs. SPE Formation Evaluation, December, 470 – 476.

[135] Wilkinson, D. and Willemsen, J.F., 1983. Invasion percolation: a new form of percolation theory. J Phys A: Math Gen, 16, 3365-3376.

[136] Zhou, D., Arbabi, S., and Stenby, E.H., 1997. A percolation study of wettability effect on the electrical properties of reservoir rocks. Transport in Porous Media, 29, 85 – 98.

Vita

Mikhail Nikolaevich Gladkikh was born in Tula, Russia on December 7, 1977, the son of Nikolay and Elena Gladkikh. He received a Bachelor of Science degree in Applied Mathematics and Physics at Moscow Institute of Physics and Technology in May 1999. He graduated from Moscow Institute of Physics and Technology in May 2001 with the degree of Master of Science. In August 2001 he entered the Graduate School of The University of Texas at Austin and received Master of Science degree in Computational and Applied Mathematics in August 2003.

Permanent Address: Suvorova 20, kv. 31, Korolev, Mosk. Obl., Russia, 141070

This dissertation was typed by the author.